ISSN 1983-4195

IBRACON

IBRACON Structures and Materials Journal

Revista IBRACON de Estruturas e Materiais

Volume 16, Number 2
April 2023

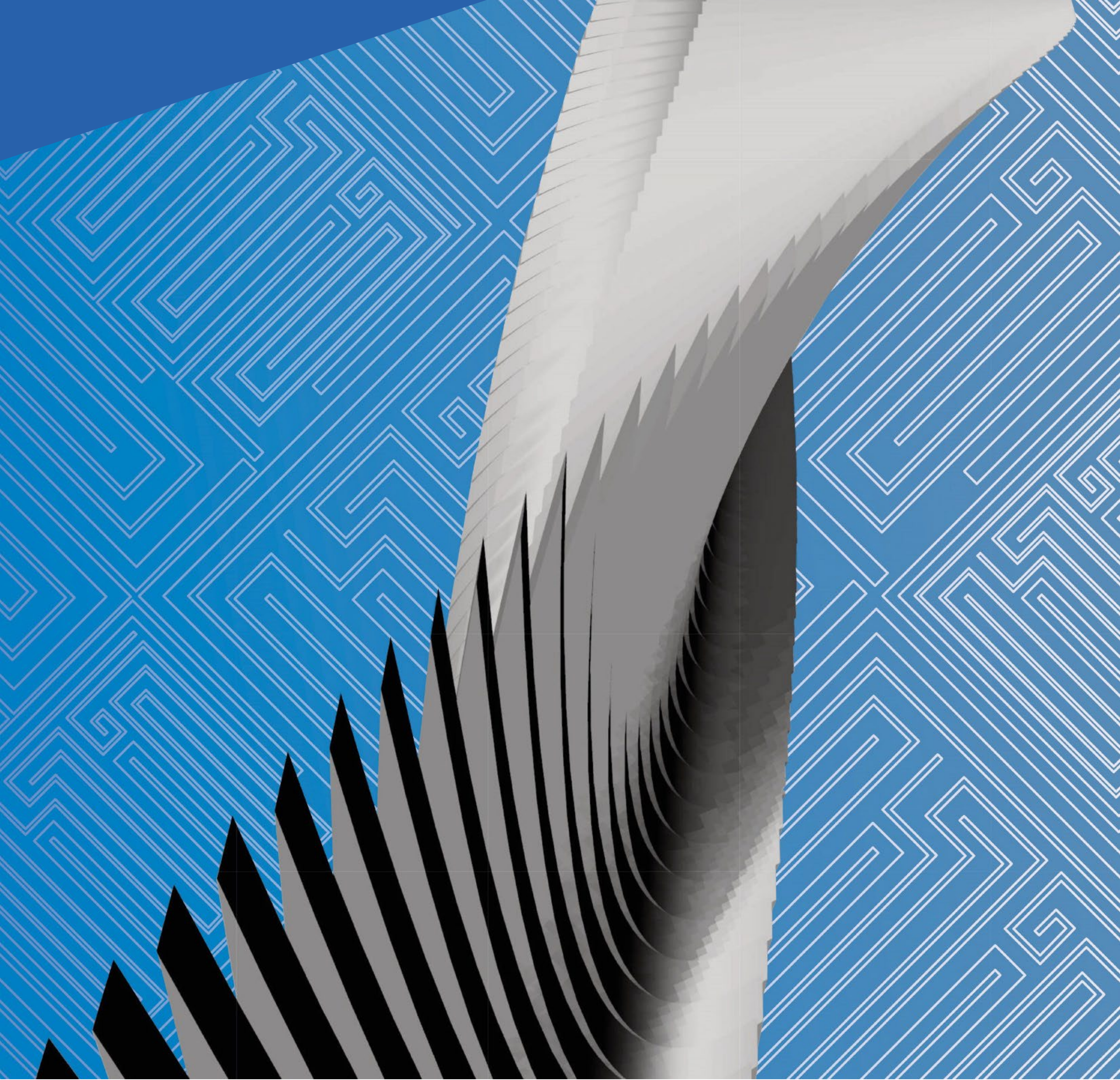

ISSN 1983-4195
Volume 16, Number 2
April 2023

IBRACON Structures and Materials Journal
Revista IBRACON de Estruturas e Materiais

Contents

Cover: Parametric Tower

Courtesy: Marcela Noronha P. de O. e Sousa

IBRACON

Ibracon Structures and Materials Journal is published bimonthly. (February, April, June, August, October, and December) by IBRACON.

IBRACON
Instituto Brasileiro do Concreto Founded in 1972

Av. Queiroz Filho, nº 1700 — sala 407/408
Torre D — Villa Lobos Office Park
CEP 05319-000 — São Paulo, SP — Brazil
Phone: +55 11 3735-0202
Fax: +55 11 3733-2190
E-mail: riem@ibracon.org.br
Website: http://www.ibracon.org.br

Cover design & Layout: Editora Cubo www.editoracubo.com.br

Support: Wallison Angelim Medeiros

Aims and Scope

Aims and Scope

The IBRACON Structures and Materials Journal (in Portuguese: Revista IBRACON de Estruturas e Materiais) is a technical and scientific divulgation vehicle of IBRACON (Brazilian Concrete Institute), published every two months. Each issue has 12 to 15 articles and, possibly, a technical note and/or a technical discussion regarding a previously published paper. All contributions are reviewed and approved by professionals with recognized scientific competence in the area. The IBRACON Structures and Materials Journal is an open access Journal, free of charges for authors and readers.

Objectives

The IBRACON Structures and Materials Journal´s main objectives are:

- Present current developments and advances in concrete structures and materials.
- Make possible the better understanding of structural concrete behavior, supplying subsidies for a continuous interaction among researchers, producers, and users.
- Stimulate the development of scientific and technological research in the areas of concrete structures and materials, through papers peer-reviewed by a qualified Editorial Board.
- Promote the interaction among researchers, constructors and users of concrete structures and materials and the development of Civil Construction.
- Provide a vehicle of communication of high technical level for researchers and designers in the areas of concrete structures and materials.

Submission Procedure

The procedure to submit and revise the contributions, as well as the formats, are detailed in the Journal Website (ismj.org).

The papers and the technical notes are revised by at least two reviewers indicated by the editors. Discussions and replies are accepted for publication after a review by the editors and at least one member of the Editorial Board. In case of disagreement between the reviewer and the authors, the contribution will be sent to a specialist in the area, not necessarily linked to the Editorial Board. Conflict of interests is carefully handled by the Editors.

Contribution Types

The Journal will publish original papers, short technical notes, and paper discussions. Original papers will be accepted if they are in accordance with the objectives of the Journal and present quality of information and presentation. A technical note is a brief manuscript. It may present a new feature of research, development, or technological application in the areas of Concrete Structures and Materials, and Civil Construction. This is an opportunity to be used by industries, companies, universities, institutions of research, researchers, and professionals willing to promote their works and products under development.

A discussion is received no later than 3 months after the publication of the paper or technical note. The discussion must be limited to the topic addressed in the published paper and must not be offensive. The right of reply is granted to the Authors. The discussions and the replies are published in the subsequent issues of the Journal.

The submission file should be in accordance with the paper template available at the Journal Website. It is recommended that the length of the papers does not exceed 25 pages. Where available, URLs for the references should be provided.

The IBRACON Structures and Materials Journal will conduct the review process for manuscripts submitted in English. Titles, abstracts, and keywords are presented in English, and in Portuguese or Spanish. Articles and technical notes are peer-reviewed and only published after approval of the reviewers and the Editorial Board.

Once accepted, an article is typeset according to the journal layout. The author will be required to review and approve the galleys before publishing. At this stage only typesetting errors will be considered.

Internet Access

The IBRACON Structures and Materials Journal Webpage is available at http://ismj.org.

Sponsors

The funds for the maintenance of the Journal are currently obtained from the IBRACON. The Journal is not supposed to be maintained with funds from private sponsorship, which could diminish the credit of the publications.

Photocopying

Copyright

IBRACON

Av. Queiroz Filho, 1700 – sala 407/408 – Torre D
Villa Lobos Office Park
05319-000 – Vila Hamburguesa
São Paulo – SP
Phone: +55 (11) 3735-0202
E-mail: riem@ibracon.org.br

Disclaimer

Papers and other contributions and the statements made, or opinions expressed therein are published on the understanding that the authors of the contribution are the only responsible for the opinions expressed in them and that their publication does not necessarily reflect the views of IBRACON or of the Journal Editorial Board.

Editorial Board

Direction

Rev. IBRACON Estrut. Mater., vol. 16, no. 2, e16201, 2023

IBRACON Structures and Materials Journal
Revista IBRACON de Estruturas e Materiais
ISSN 1983-4195 ismj.org

ORIGINAL ARTICLE

Evaluation of concrete self-healing by encapsulated sodium metasilicate in perlite and expanded clay

Avaliação de concreto autocicatrizante através do encapsulamento de metasilicato de sódio em perlita e argila expandidas

Fernanda Pacheco[a]
Cláudio Henrique Boscaini[b]
Thaize Nascimento Gauto[b]
Vinicius Müller[c]
Hinoel Zamis Ehrenbring[a]
Regina Célia Espinosa Modolo[c]
Bernardo Fonseca Tutikian[c]

[a]Unisinos, Escola Politécnica, itt Performance, São Leopoldo, RS, Brasil
[b]Unisinos, Escola Politécnica, Graduação em Engenharia Civil, São Leopoldo, RS, Brasil
[c]Unisinos, Escola Politécnica, Pós-graduação em Engenharia Civil, São Leopoldo, RS, Brasil

Received 31 December 2021
Accepted 01 July 2022

Abstract: Investigating the behavior of self-healing cementitious composites is necessary to know alternatives that can be applied in structures increasing their life service. Therefore, this study evaluated concrete self-he aling from the use of expanded perlite (EP) and expanded clay (EC) capsules impregnated with a sodium metasilicate solution. These materials were used to substitute natural aggregates in concrete in proportions of 0 wt·%, 15 wt·% and 30 wt·% which were cured in humid or submerged environments. Cracking was induced with a flexural test and a closing with cicatrization product. was evaluated and measured visually with a software. Capillary absorption tests indicated a reduction in the porosity of samples which incorporated self-healing materials, considering it as an important property related to durability. Samples with EP achieved 100% self-healing with 15% substitution. Crack filling was achieved in cracks up to 0.43 mm wide. Samples with EC achieved 50% crack recovery under humid curing and 90% under submerged curing. It was concluded that incorporating the sodium silicate allowed improvements to fissure sealing and it is an alternative to produce self-healing concrete in Brazil. EP was more effective than EC as encapsulating material. Despite that, the EP did not impact the compressive strength due to its small size and better packing of the mixture, Also, EP presented higher healing percentage when comparing with samples containing EC.

Keywords: concrete, self-healing, expanded perlite, sodium meta-silicate.

Resumo: Investigar o comportamento de compósitos cimentícios autocicatrizantes é necessário para conhecer alternativas que possam ser aplicadas em estruturas aumentando a sua vida útil. Portanto, este estudo avaliou a cicatrização do concreto a partir do uso de cápsulas de perlita expandida (PE) e argila expandida (AE) impregnadas com solução de metassilicato de sódio. Esses materiais foram utilizados em substituição aos agregados naturais no concreto nas proporções de 0%, 15% e 30% em relação à massa. Os exemplares foram curados em ambientes úmidos ou submersos. A fissura foi induzida pelo teste de flexão e a cicatrização foi avaliada visualmente e medida por meio de software. Testes de absorção capilar indicaram redução da porosidade das amostras que incorporaram materiais autocurantes, sendo esta uma importante propriedade relacionada à durabilidade do conjunto. As amostras com PE alcançaram 100% de cicatrização com 15% de substituição. O preenchimento da fissura foi obtido em fissuras de até 0,43 mm de largura. Amostras com AE alcançaram 50%

Corresponding author: Bernardo Fonseca Tutikian. E-mail: bftutikian@unisinos.br
Financial support: The authors would like to thank Unisinos, Performance Technological Institute a(itt) and CNPq for the financial support granted to Bernardo Fonseca Tutikian with the Productivity Research Scholarship.
Conflict of interest: Nothing to declare.
Data Availability: The data that support the findings of this study are available from the corresponding author, FP, upon reasonable request.

de recuperação de fissura sob cura úmida e 90% sob cura submersa. Conclui-se que incorporar a solução de metassilicato de sódio proporcionou melhorias consideráveis na selagem de fissuras e esta solução torna-se uma alternativa eficiente para concretos autocicatrizantes a serem produzidos no Brasil. A incorporação de PE foi mais eficaz do que o AE como material encapsulante. Além disso, o uso de PE não impactou na resistência à compressão em decorrência de sua reduzida dimensão de partícula e empacotamento. Ainda, a EP apresentou maior percentual de cicatrização comparando-se com as amostras contendo AE.

Palavras-chave: concreto, autocicatrização, perlita expandida, metassilicato de sódio.

How to cite: F. Pacheco et al. "Evaluation of concrete self-healing by encapsulated sodium metasilicate in perlite and expanded clay", *Rev. IBRACON Estrut. Mater.*, vol. 16, no. 2, e16201, 2022, https://doi.org/10.1590/S1983-41952023000200001

1 INTRODUCTION

Concrete is widely used worldwide due to its well-known properties. Hardened concrete has its durability linked to its main property of mechanical strength [1]. The U.S. Geological Survey [2] estimated a world production of cement of 4.1 billion metric tonne in 2019. In 2021, world cement production achieved 4.4 billion metric tonne [3]. Cement emissions amount to 1 t CO_2 / t of cement produced [4]. In 2019, worldwide CO_2 emissions were 36.8 ± 1.8 Gt [5], of which an estimated 11.1 ± 0.5% can be attributed to cement production, and thus, is required to increase the lifespan of construction elements that use cement.

Structural concrete is highly susceptible to the formation of cracks. This is a result of low resistance to tension and other mechanisms such as contraction from drying, thermal cycling and shifting, overloading, reinforcement corrosion etc [6]. The reduced durability due to cracks, repair and recovery cost of structures [7] and environmental impact of cement production are driving motivations to the development of self-healing types of concrete, which operates [8]–[11] under the same principle as a human body: injuries cause the release of healing agents which induce regeneration [12]. As noted succinctly by Van Tittelboom et al. [13], there are 3 types of concrete self-healing processes or mechanisms: autogenous, autonomous and vascular.

Autogenous self-healing is a natural phenomenon of concrete, related to delayed cement hydration and/or pozzolan addition. Autonomous healing is obtained from the addition of micro-capsules impregnated with healing agents. When exposed to the environment, these agents induce healing and they are not commonly used in concrete. Lastly, vascular healing also makes use of healing agents but in hollow tubes that connect the external environment to the inside of the structure. Studies have demonstrated that autogenous self-healing materials were limited to small cracks and were thus restricted and less reliable since they could not repair multiple cracking phenomena [13], [14]. As an example, the range of values in which cicatrization happens is between 50μm and 200μm [13].

Autonomous self-healing can be classified as bacterial precipitation or healing induced by chemical agents [12]. Among the chemical healing agents, there is a prevalence in the use of sodium metasilicate (Na_2SiO_3) [6], [7], [15]. This material reacts with calcium hydroxide ($Ca(OH)_2$) inside concrete to produce calcium silicate hydrate (C-S-H) gel which binds to the concrete, partially filling the crack and recovering the strength of the material [16].

For an effective healing process, capsules must remain intact after fresh cement has been mixed, resisting impact from the concrete mixer and other aggregates. It has been noted that spherical capsules were more resistant and influenced the least the workability of concrete under mixing [17]. Capsule wall thickness was also an important factor since thinner walls could result in premature rupture while thicker walls might impede the agent release [12]. Sisomphon et al. [18] made use of expanded clay (EC) capsules with a protective coating of cement. The cement coating was completely cured prior to mixing and the final result was a much improved concrete quality with self-healing properties. Zhang et al. [6] made use of capsules between 2 mm and 4 mm in diameter impregnated with *Bacillus cohnii* and coated in a geopolymer produced from metakaolin and sodium metasilicate.

Aggregates are used as capsules for healing agents but while more capsules increase the probability that a crack might rupture them, too many capsules could increase the cost and compromise the strength of the resulting material [19]. The width of the crack healed varied with respect to the encapsulating method. In the case of spherical capsules, their diameter must be large enough to store and release the healing agent into the crack. This recommended diameter varied between 5 μm and 5 mm. If the crack were too wide, the capsule healing agent could be rapidly expanded [13].

Another factor in the encapsulated healing agent was the local pressure during the manufacturing process. Sisomphon et al. [18] used sodium monofluorophosphate (Na_2PO_3F) in EC capsules 4 mm in diameter. In this case, the absorption rate under natural pressure conditions was lower when compared to absorption in a vacuum. Results showed that the use of a vacuum chamber was a necessity to allow higher agent absorption. Sisomphon et al. [18] also demonstrated that sodium monofluorophosphate healed the samples and significantly improved the quality of concrete in the carbonation region.

Alghamri et al. [20] used light aggregate capsules impregnated with sodium metasilicate. Cracking tests demonstrated an 80% recovery in load-bearing capacity when compared to a control sample. Capillary water absorption was also improved, indicating a reduction in cracking and an expected longer durability of the material.

Pelletier et al. [16] used polyurethane capsules also impregnated with sodium metasilicate. This light aggregate was used as 2% substitution in volume of concrete. Healed samples had strengths up to 10% higher than reference samples. Tan et al. [7] also used polymer capsules with a silica solution at its core. The resulting material had an increase of 7.5% in strength and flexural resistance.

The viscosity of the healing agent is an essential parameter to prevent its absorption into the concrete matrix since it could allow it to flow from inside the capsules. Dry, apud Van Tittelboom et al. [21] concluded that the healing agent viscosity must remain between 100 mPa·s and 500 mPa·s but other studies have noted that lower viscosity agents were able to fill both micro and macro-cracks. Methyl methacrylate was an example of an inappropriate low viscosity agent: cracks might be left open since its curing time was of approximately 30 mins, which was sufficient time for concrete to absorb or leak out part of it. Van Tittelboom and De Belie [22] increased the viscosity of the healing agent with the addition of poly(methyl methacrylate) as a thickening agent to hold the chemical inside the capsule. Viscosity was also associated with the SiO_2/Na_2O molar ratio (also known as the silica modulus). Higher silica modulus indicated a more viscous agent and, for most healing agents, varied between 1.60 to 3.75 [23].

The most used encapsulating aggregate is expanded clay (EC) since it is readily available and of low cost but with low mechanical resistance. Another light aggregate is expanded perlite (EP) which is also readily available and less expensive than other aggregates such as vermiculite, pumice etc [24]. The use of EC as encapsulating material for bacterial spores was tested by Jonkers [25]. It was determined that cracks of up to 0.46 mm were healed after 100 days curing in water immersion. While viable, this technique also increased the porosity of concrete and reduced its resistance. In the case of 50 wt·% aggregate substitution with EC, samples presented a 50% reduction in resistance after 28 days of curing, which was not recommended for structural applications [12], [24].

Further studies were conducted to improve autonomous self-healing capacity. Zhang et al. [6] compared the use of EC and EP as capsules for Bacillus cohnii bacteria. After 28 days curing, EP and EC were able to recover cracks up to 0.79 mm and 0.45 mm wide, respectively.

Sisomphon et al. [18] demonstrated that self-healing with microencapsulated sodium monofluorophosphate delayed water penetration and increased concrete strength. In more detail, the healing agent increased strength for concrete subjected to a high stress environment which included freezing/unfreezing cycles and exposure to salinity. Sodium, phosphorus and fluorine were also detected in the concrete matrix which proved the successful release of the healing agent from the capsules.

Even knowing that several studies have already been performed in this area, the present study compares the use of sodium silicate when using percentages of 10, 20 e 30% of expanded perlite and expanded clay. The aim is to evaluate procedures viable to be applied on a large scale for real concrete procedures. The present study used EC and EP as transport media for the healing agent. Perlite is a volcanic silicate glass which can expand as much as 20x in volume when rapidly heated, leaving several internal void spaces [19]. Expanded clay has been widely studied and is already used in structural concrete [26]. Nevertheless, EC has enough void spaces to be used in self-healing concrete [27]. The chosen healing agent was sodium metasilicate encapsulated in either EC or EP and an outer protective coating. Evaluation techniques included examination of the microstructure of both aggregates and varying the type of curing: samples were immersed in water while others were exposed to a humid environment. Mechanical and physical tests were conducted and the formation of healing products verified with scanning electronic microscopy (SEM).

2 MATERIALS AND METHODS

The methodology consisted of the production of 5 compositions: a reference concrete and concretes with 15 wt·% and 30% wt·% substitution of sand with EP and EC aggregates impregnated with sodium metasilicate.

2.1 Materials and composition

The Portland cement used was of type III as defined in ASTM C150 [28]. Fine aggregate was locally sourced river quartz sand. Sand bulk density was 1,411 kg/m^3 while specific mass was 2,595 kg/m^3, as determined from ASTM C29 [29] and ASTM C128 [30] procedures, respectively. The granulometric distribution of the sand was determined following ASTM C33 [31] procedures and is shown in Figure 1. The resulting fineness modulus was 3.07 and the maximum dimension was 2.36 mm.

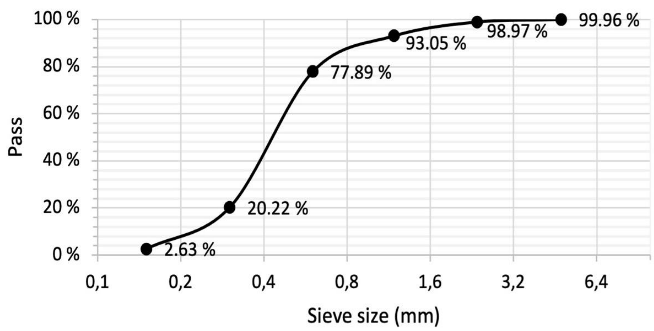

Figure 1 - Granulometric distribution of fine aggregate

The EP used had granulometry between 1.2 mm and 4.8 mm with bulk density of 110.1 kg/m^3. The EP aggregate showed a mass of 94.36 kg/m^3 in the natural state and after being impregnated with chemical solution the value was 475.50 kg/m^3. No further granulometric distributions were examined since fine aggregate substitution was based on the % diameter of sand removed. The EP used was of two types: one with granulometry between 1.2 mm and 4.75 mm and the other between 2.4 mm and 12.5 mm. Substitute aggregate microstructure and chemical composition were evaluated with a Zeiss-brand scanning electronic microscope with energy-dispersive spectroscopy (SEM/EDS). Samples were pre-dried and coated in gold prior to testing and the results are shown in Figure 2.

The SEM/EDS results of Figure 2 show that EP had a more porous surface more likely to absorb the healing agent efficiently. In contrast, EC had a more compact and dense structure than the samples used by Ahmad et al. [32] and Bogas et al. [33] in addition to being fundamentally different from EP. Chemical compositions obtained from EDS in the same regions where the images were taken are shown in Table 1.

Table 1 shows that both substitute aggregates were composed mainly of oxides and silicates, as identified by the O and Si contents, respectively. Both also contained sodium but in less than 3 wt·% which makes it improbable that they contained naturally formed sodium metasilicate. This confirmed the need to impregnate the substitute aggregates with a chemical solution to promote C-S-H formation.

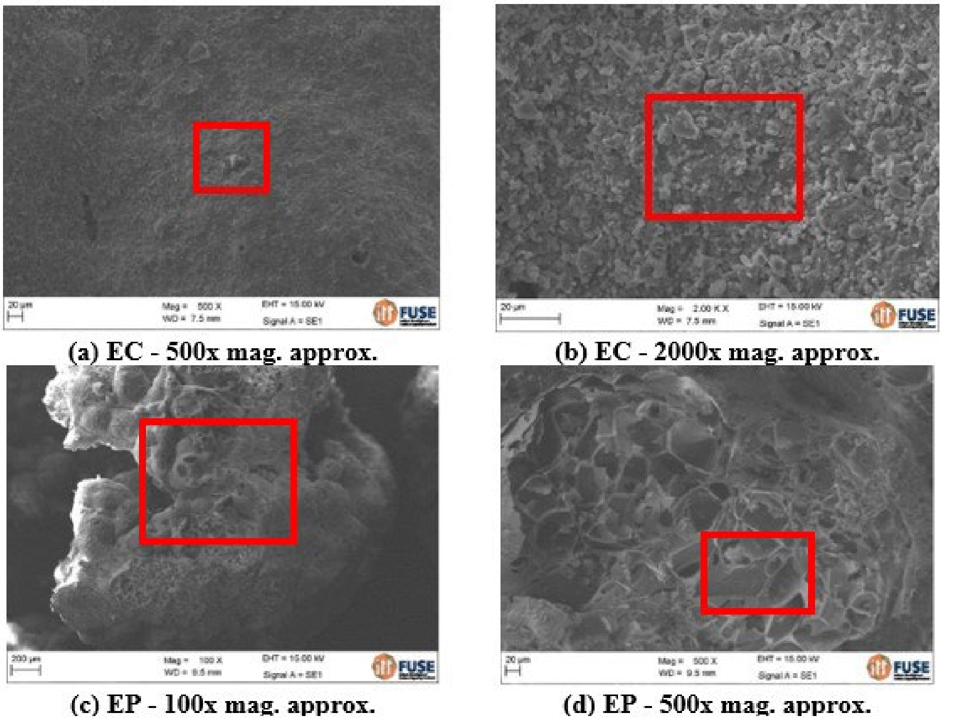

Figure 2 - SEM/EDS images for EC (a,b) and EP (c,d)

Table 1 - EDS semiquantitative chemical analysis of substitute aggregates

Element	EC (%)		EP (%)	
	Weight	Atomic	Weight	Atomic
O	42.80	58.92	43.05	57.65
Na	0.43	0.41	2.27	2.12
Mg	1.78	1.61	0.00	0.00
Al	10.23	8.35	7.18	5.70
Si	30.87	24.22	40.70	31.04
K	4.48	2.52	4.76	2.61
Ca	1.16	0.64	0.62	0.33
Ti	1.15	0.53	0.00	0.00
Fe	7.10	2.80	1.41	0.54
Total	100.00		100.00	

The EC was also applied in replacement of natural fine aggregate. In accordance with its manufacturer, the EC is divided into small and large, considering the specific mass of 850 kg/m^3 and 600 kg/m^3, respectively. Coarse aggregate used was basaltic gravel of granulometry between 4.8 mm and 9.5 mm. The same characterization procedures applied to the quartz river sand fine aggregate were applied to the gravel. The bulk density and specific mass were determined as 1,641 kg/m^3 and 2,480 kg/m^3, respectively. The granulometric distribution of the coarse aggregate is shown in Figure 3. The fineness modulus was determined as 2.57 and the maximum characteristic dimension was 9.5 mm.

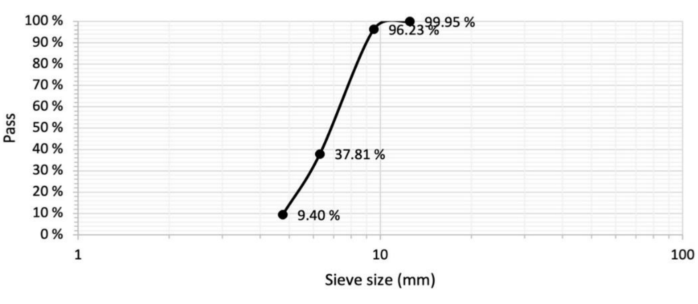

Figure 3 - Granulometric distribution of coarse aggregate (basaltic gravel)

The healing agent used in this study was the same sodium metasilicate (Na_2SiO_3) used in other reference studies [6], [7], [22]. The sodium silicate is from Simoquímica brand, with original concentration of 50%, diluted in water also by 50% The molar ratio SiO_2/Na_2O is 3.27. The healing agent was used in liquid form with 50 wt·% dilution in deionized water. The vacuum impregnation technique of Sisomphon et al. [18] was used to impregnate the healing agent in the substitute aggregates. The original healing agent had viscosity of 496 mPa·s and a SiO_2/Na_2O ratio of 3.27. Other properties are shown in Table 2, through data collected from the manufacturer, and were in accordance with reference work [21].

Table 2 - Sodium metasilicate properties

Property	This work	Reference value
Appearance	Viscous liquid	
Baumé scale (ºBé)	38.50 - 41.50	39.92
Specific mass (g/cm^3)	1.37 - 1.42	1.38
Viscosity (mPa·s)	250 - 500	496
Sodium oxide (%)	8.0 - 9.20	8.43
Silicon dioxide (%)	26.00 - 29.50	27.65
SiO_2/Na_2O molar ratio	3.00 - 3.35	3.27
pH	10.5-12.2	11.2

2.2 Healing agent encapsulation

Healing agent encapsulation consisted of 4 steps:

Step 1: sodium metasilicate was separated according to granulometric size and diluted in 50-wt·% deionized water. Substitute aggregate capsules were submersed in this solution for 6 h to induce pre-saturation;

Step 2: the substitute aggregate capsules and sodium metasilicate solution were exposed to a vacuum for 2 h in a glass desiccator;

Step 3: substitute aggregate capsules were weighted and coated in Portland cement for mechanical protection as described in Sisomphon et al. [18]. The before and after visual aspects are shown in Figure 4ab for EC and Figure 4cd for EP;

Step 4: substitute aggregate capsules were cured in a humidity chamber at 100% humidity for 5 days for later molding.

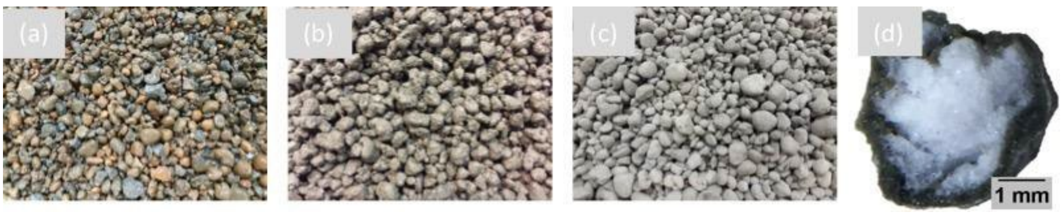

Figure 4 - Before and after cement coating application on substitute aggregate capsules for EC (a, b) and EP (c, d)

2.3 Mixing, Curing and Molding

The samples and mixing ratios used are shown in Table 3. Sand substitution was performed by removing the target wt·% and replacing it with an equivalent volume of aggregate.

Table 3 - Samples and mixing mass ratios used in the study

Material	Sample and Mixing ratio				
	REF	**EP 15**	**EP 30**	**EC 15**	**EC 30**
Cement	1	1	1	1	1
Sand	1.5	0.89	0.73	0.89	0.73
Perlite	-	0.16	0.32	-	-
Clay	-	-	-	1.4	2.8
Gravel	3	3	3	3	3
Water	0.48	0.48	0.48	0.48	0.48
Additive superplasticizer	2.0%	1.3%	1.2%	1.5%	2.0%

The water/cement relation is in accordance with Brazilian standard for concrete design. The class of slump was achieved with the use of a superplasticizer based on polycarboxylate, named tecflow 800, from GCP Applied Technologies brand. The proportions of EP and EC were defined as defined by Pacheco et al. [34].

Molding was performed in cylindrical (10 cm x 20 cm) and prismatic (6 cm x 6 cm x 18 cm) molds. Throughout the process, slump tests were conducted in accordance with ASTM C143 [35] and found to yield between 50 mm and 100 mm. Samples were cured both in a humidity chamber and submerged. Both curing processes were conducted under strict climate-controlled conditions with air and water temperatures of 23 ± 2ºC and relative humidity conditions of 95 ± 5%. Molding followed procedures of ASTM C470 [36].

For the prismatic samples, a 5 mm diameter CA60 steel bar segment was inserted to promote cracking in lieu of subjecting the sample to a flexural test until failure. Since the sample was 6 cm in height, the bar segment was inserted to depths of 2 cm from the base and 4 cm from the top. The prismatic samples were applied only to allow the analysis of concrete healing. Cylindrical samples were submitted to two tests: water absorption and compressive strength.

2.4 Sample Characteristics and Crack Formation

Compression strength tests were performed according to ASTM C39 [37] procedures after 7 days, 28 days and 56 days of aging with 2 samples each time.

In prismatic specimens, cracks were obtained from a flexural test according to ASTM C348-97 [38] in 7-day samples. In this case, load was applied until crack formation. The load was applied to crack formation until the value of 1.1 kN, aiming to achieve an opening of 0.3mm. After the sample's cracking, Capillary absorption tests followed the procedures of RILEM TC 116 PCD [39] after 7 days, 28 days and 56 days of aging. Test times used were of 10 min, 20 min, 30 min, 40 min, 50 min, 1 h, 2 h, 3 h, 4 h and 24 h. Also, after the crack formation, the cracks were optically evaluated with a Starret® Galileo AV 300+ Automatic model 3-D measuring apparatus. Images generated had amplifications of 62x and 164x and were post-processed in ImageJ software. Starting from calibrated values, a reference line segment of known length was created on ImageJ. This allowed the measurement of open and healed crack widths (mm) and the calculation of regenerated percent area (mm^2), as established by Wiktor and Jonkers [40]. Through the Equation 1 from the mentioned authors, it was possible to determine the healing percentage from the specimens.

$$HP(\%) = \left(\frac{w_i - w_t}{w_i}\right) \times 100 \quad (1)$$

Where:
HP (%): Healing percentage
w_i : crack initial width;
w_t : crack width in a time t.

3. RESULTS AND DISCUSSION

3.1 Mechanical strength

Table 4 presents the results of individual and potential strength resistance. As noted by Sengul et al. [24], strength decreased as EP substitution increased: a reported substitution of 20% yielded a decreased strength of around 40%. Jedidi et al. [41] also reported similar results with a 65% decrease in strength with a 30% EP substitution. Leyton-Vergara et al. [42] indicated that a maximum 40% substitution was the limit for a viable adequate concrete strength while Alazhari et al. [43] set this substitution limit at 20%.

Table 4 - Strength test results

Sample	Compressive strength (MPa)					
	7 days		28 days		56 days	
	Ind.	Potential	Ind	Potential	Ind	Potential
REF	46.5	46.5	48.5	49.0	52.6	52.6
	46.3		49		49.9	
EP 15	40.2	43.5	51.1	55.9	52.8	54.3
	43.5		55.9		54.3	
EP 30	34.8	36.6	37.6	42.3	45	45.0
	36.6		42.3		44.4	
EC 15	27.2	29.4	35.7	35.7	40.5	40.5
	29.4		34.9		34.9	
EC 30	32.1	33.6	37.2	37.2	37	37.0
	33.6		35.7		36.5	

However, for this study, 30% EP substitution resulted in a decrease in strength of approximately 13% after 28 days. Furthermore, 15% EP substitution resulted in a strength superior to the reference sample, which was rather anomalous when compared to the results of the other substitution samples. It was believed that for this case the healing agent might have filled void spaces and pores within the matrix for this sample, which would explain the increase in strength. The remaining samples agreed with the general result with the largest substitution resulting in the largest decrease in strength. It should be noted that after 56 days, the strength of the EP15 sample was very close to REF. Rashad [19] noted that EP substitution commonly had a negative impact in concrete mechanical properties but, since it was a powdered substance, might result in a gain in compaction in the final material.

In relation to compressive strength results from samples EP15 comparing with reference samples, it is noticed that they are similar. At 7 and 56 days, the potential compressive strength from EP15 samples is slightly higher than the reference. It is possible to relate those differences not only due to perlite usage, but also to the standard deviation common in cement compositions. However, the impact of perlite usage is more evident with samples named as EP30, with larger EP percentage. In all ages, the results from EP30 remain with a potential strength of up to 21% below the REF, which is higher than the applicable deviation values for concrete.

Comparing the results from EP and EC, the EP results were higher than EC samples in all ages and percentages of use, due to the lower dimension of EP. It can be pointed out that the aggregate's resistance to be used as capsules is reduced and it is not applied to enhance the composite compressive strength. EP and EC were considered as porous aggregates to be used in concrete for self-healing [6] and without the encapsulating agent works as voids inside concrete matrix. However, it is worth noting that EP presented better behavior considering the distribution of the aggregates inside concrete and also the packing analysis. Pacheco et al. [34]. Thus, due to the quality, dimension and distribution of EC, may have affected the concrete microstructure, damaging its compressive strength.

In terms of EC substitution, Shafigh et al. [44] obtained a small alteration in strength after 7 days which demonstrates a stabilizing trend. This result was observed in this study with 30% EC substitution. Despite this detrimental effect, Alghamri et al. [20] noted that light aggregates impregnated with sodium metasilicate were able to recover 80% of the resistance after cracking. This resonated well with the EP15 samples having strengths superior to REF and EC30 samples having strengths superior to EC15. Pelletier et al. [16] also observed mechanical recovery of samples containing healing agents 11% superior to reference. These results showed that, while light aggregates might impact mechanical strength negatively, post-cracking strength recovery of healing agents was superior to conventional concrete.

3.2 Capillary water absorption

Figures 5, 6 and 7 present average results of capillary water absorption after 7 days, 28 days and 56 days, respectively. The values are pointed out in Table 5. It should be noted that days were counted after the appearance of cracks from flexural tests.

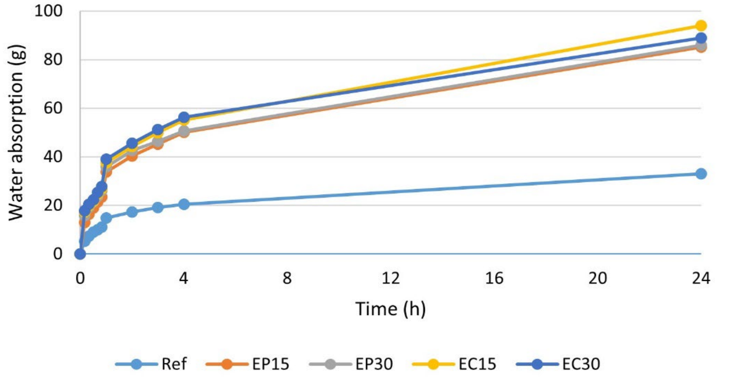

Figure 5 - Capillary water absorption after 7 days

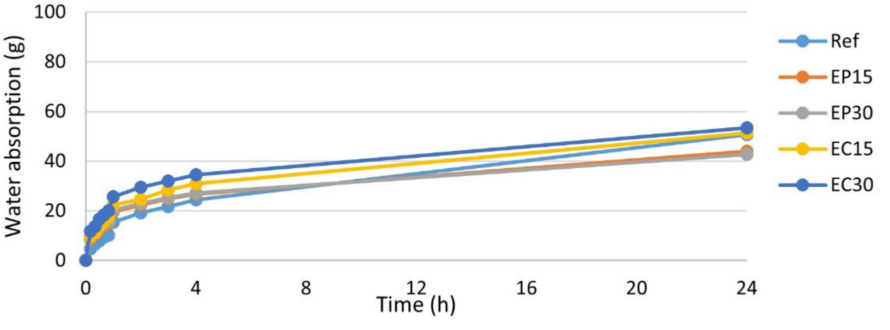

Figure 6 - Capillary water absorption after 28 days

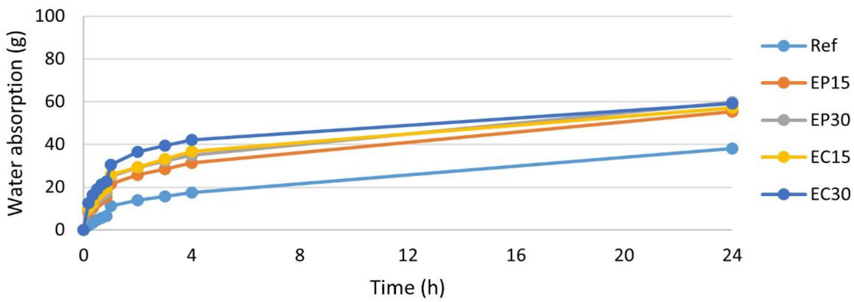

Figure 7 - Capillary water absorption after 56 days

Table 5- Water absorption (g)

T	7 days					28 days					56 days				
	R	EP		EC		R	EP		EC		R	EP		EC	
		15	30	15	30		15	30	15	30		15	30	15	30
0	0	0	0	0	0	0	0	0	0	0	0	0	0	0	0
10m	5.2	13	15.8	17.2	17.8	4.7	8.7	9.8	9.8	11.8	1.9	8.4	9.4	10.1	12.6
20m	7.4	16.4	19.2	19.9	20.5	6.5	10.6	11.6	11.2	13.8	3.3	10.3	11.9	12.5	16.3
30m	9	19	21.3	21.7	22.4	7.8	12.5	13.3	13.9	16.7	4.7	12.9	14.4	15.9	19.1
40m	10	21.4	23.7	24.6	25.4	9.2	13.9	14.7	15.6	18.3	5.5	14.4	15.9	17.9	21.2
50m	11	23.5	26	26.9	27.8	10.1	14.9	15.7	17.3	20	6.4	15.5	17.5	19.4	22.6
1	14.9	33.8	35.8	37.6	39	15.3	19.5	20.2	22.3	25.6	11.2	21.5	25	25.8	30.4
2	17.2	40.3	42.6	44.3	45.6	19.1	22.4	22.9	24.7	29.4	13.9	25.8	29	29.3	36.4
3	19.1	45.3	46.4	49.9	51.2	21.7	24.8	25.2	28.5	32	15.7	28.4	32.2	33.1	39.5
4	20.5	50	50.6	55.1	56.2	24.5	26.8	27.2	30.9	34.5	17.4	31.4	34.9	36.8	42
24	33.1	85.2	85.9	93.9	88.9	50.7	44	42.7	51.4	53.4	38	55.4	59.8	57.1	59.2

As seen in Figures 5 through 7 and in Table 5, all substitution samples presented higher water absorption than the reference sample (R). This could be explained as the substitute aggregates contained void spaces which, even though the material was impregnated with healing agent, acted as water storage spaces. All substitution samples also presented the same trends with an initial absorption followed by saturation as expected [14]. As pointed out by Pacheco et al. [34] by 3D microtomography, EC mixes presented a higher void ratio when comparing with EP samples and reference mixture. In the same context, it could be noted that EP samples had less water absorption than EC samples, likely due to void spaces and packing characteristics of each mixing ratio. It was noted that from 7 to 56 days, there was a reduction of around 30% in the water absorption of the samples with healing agents. For comparison, the reference samples had an increase of around 15% in the water absorption in the same period. When comparing identical concrete samples, it should be noted that capillary water absorption naturally decreased with age. This was a result of the complete hydration of concrete samples which increased density and decreased void spaces [1], [44].

Alghamri et al. [20] obtained a reduction in absorption of 50% in samples with self-healing agents. However, it was also determined that self-healed materials were able to completely recover their permeability. This confirmed the property of sodium metasilicate to improve absorption and reduce permeability. This was likely the result of healing agent deposition.

Tan et al. [7] initially compared capillary absorption in samples without cracks and found that self-healing concrete had absorption of 0.70% while normal concrete was 1.7%. However, post-cracking, absorptions were of 0.70% and 3.54% for self-healing and normal concrete, respectively. This demonstrated that self-healing concrete maintained its initial absorption despite the crack while normal concrete increased absorption considerably. It should be noted that the use of light aggregates, even in self-healing concrete, might have increased water content inside the material.

3.3 Visual Analysis

It is worth mentioning that the results from visual analysis were obtained by superficial tests, and thus, they do not include the crack depth.

Visual analysis did not yield any healing results 7 days after cracking. However, after 28 days, samples EP15 and EP30 were observed to have healing activity and were examined with 3-D measuring equipment. Figure 8 compares the initial condition of sample EP15 (Figure 8a) with the areas to be analyzed for cracking closure percentage (Figure 8b).

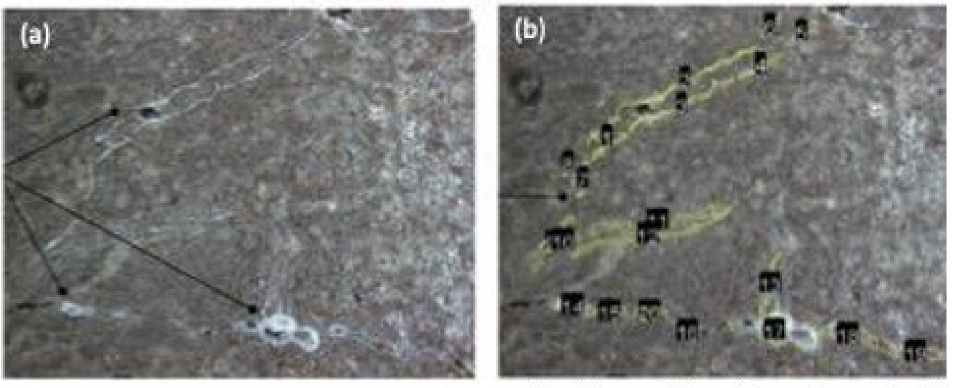

(a) First signs of healing of the crack **(b) Signs of healing of cracks during measurement**

Figure 8 - Original cracking and healing activity areas to be analyzed in EP15

Close examination of cracks shown in Figure 9 further identified healing activity after 28 days in EP samples.

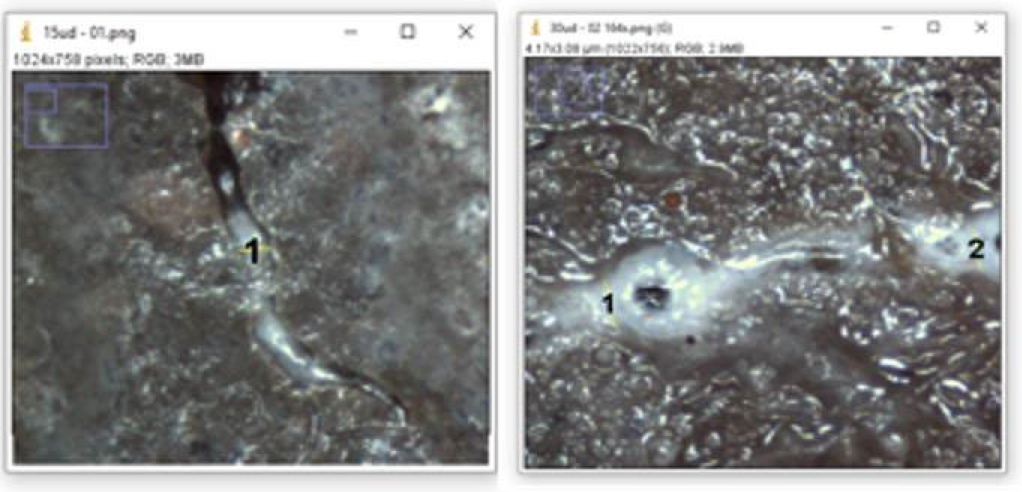

Figure 9 - Detail image of crack and healing product formation in EP15

Table 6 presents a compilation of results of initial crack opening, healing and healing percentage with respect to sample and curing conditions. The EP achieved the most healing activity at 15% substitution and that submerged curing was superior to humid curing, achieving close to total healing. In comparison, a 30% EP substitution yielded results like the other test samples. When compared to EC, EP was more efficient – a likely result of the substitute aggregate size and necessary fracture tension for the release of the healing agent. The best results of EP use in comparison to EC were aligned with the results of Zhang et al. [6]. Reductions in absorption and visual crack healing were also observed by Alazhari et al. [43] for a bacterial solution encapsulated in EP. Considering EC only, results were similar for all EC samples regardless of the degree of substitution, but it was noted that submersed EC curing yielded better results since no humid curing sample achieved more than 51% healing.

Table 6 - Cracking, healing and healing % obtained for each sample

Sample	Curing conditions	Initial crack opening (mm^2)	Healing (mm^2)		Healing percentage (%)	
			28 days	56 days	28 days	56 days
REF	Humid	0.085	0.000	0.033	0.00	38.82
REF	Submerged	0.160	0.000	0.075	0.00	46.88
EP15	Humid	0.066	0.038	0.038	57.58	57.58
EP15	Humid	0.092	0.079	0.082	85.87	89.13
EP15	Submerged	0.125	0.076	0.125	60.80	100.00
EP15	Submerged	0.141	0.118	0.134	83.69	95.04
EP30	Humid	0.109	0.106	0.109	97.25	100.00
EP30	Humid	0.106	0.000	0.088	0.00	83.02
EP30	Submerged	0.056	0.056	0.056	100.00	100.00
EP30	Submerged	0.201	0.000.	0.172	0.00	85.57
EC15	Humid	0.137	0.000	0.047	0.00	34.31
EC15	Humid	0.095	0.000	0.012	0.00	12.63
EC15	Submerged	0.036	0.025	0.032	69.44	88.89
EC15	Submerged	0.099	0.060	0.089	60.61	90.00
EC30	Humid	0.105	0.000	0.020	0.00	19.05
EC30	Humid	0.147	0.065	0.075	44.22	51.02
EC30	Submerged	0.073	0.060	0.065	82.19	89.00
EC30	Submerged	0.103	0.088	0.095	85.44	92.23

Zhang et al. [6] made similar use of image amplification equipment on 4 samples and observed crack recovery of up to 0.79 mm at 28 days. Figure 10 presents comparisons of healing progress of some samples of this study after 28 days and 56 days. As seen in Figure 10, some samples presented healing in some cracks likely due to formation of calcium silicate hydrate (C-S-H) gel. Yow and Routh [45] reported similar healing and confirmed by Alghamri et al. [20] and Sisomphon et al. [18]. Some cracks presented elevated healing potential but since the depth of the cracks was unknown, the true efficiency of healing could not be assessed.

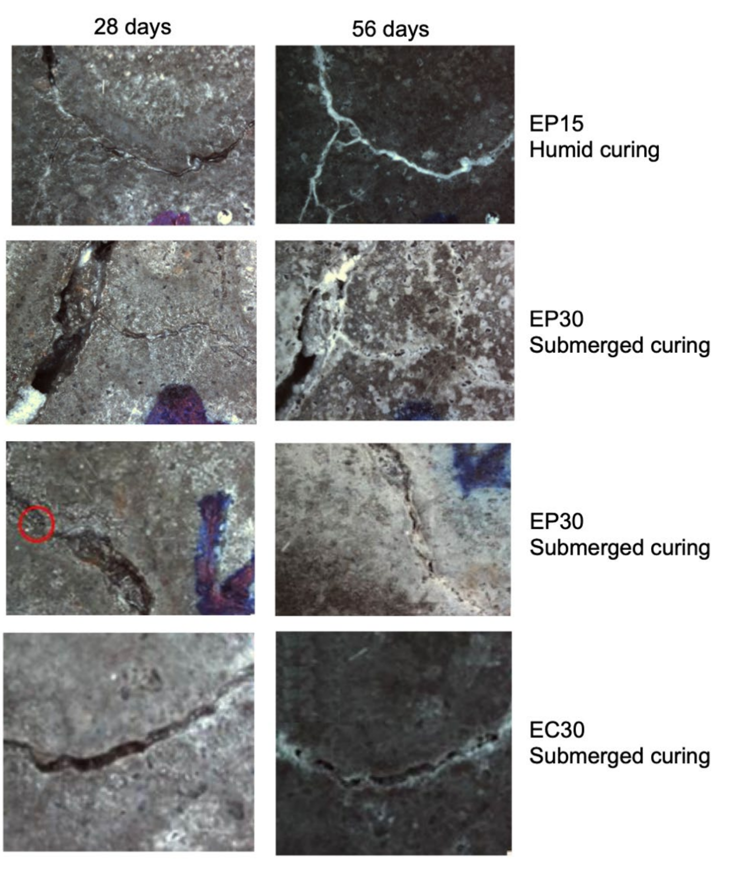

Figure 10 - Healing progress comparison at 28 days and 56 days

The images of Figure 10 suggested the possible reaction of sodium metasilicate with humidity to form products that contribute to the curing process. However, there appeared to be no linearity to the healing which, according to Van Tittelboom et al. [13], could be because healing occurred only at locations where healing material was available. In this case, locations with no visible healing activity might be the result of insufficient healing agent absorption in the substitute aggregate or a lack of rupturing to release it.

It should be noted that concrete with light aggregates tended to crack at the aggregates and not in the transition zone. This was a result of light aggregates being more susceptible to tension than compression as this relation was inversely proportional to particle size [46]. Consequently, in this study, if a crack appeared along a region of smaller particles, there was a chance that the substitute aggregate did not fracture and sodium metasilicate was not exposed to humidity. Those results of cicatrization occurrence being affected by the crack area, the surface characteristics, and the healing product availability were also pointed out by Pacheco et al. [34] and Muller et al. [47]. Overall, EP substitution achieved between 57.58% and 100% healing of the crack while EC substitution achieved between 12.63% and 90% healing. Of the 3 EP samples that achieved 100% healing, there were no observable cracks on the surface as it was completely covered in healing chemical products. As a caveat, it should be noted that optical measurements were taken at selected locations and, for most cases, did not cover the full length of the cracks present.

4. CONCLUSIONS

Substitute aggregate EP15 achieved higher mechanical strength than the reference sample for periods equal or longer than 28 days. This was likely due to crack matrix regeneration since light aggregates usually resulted in less resistance. When comparing EP and EC substitution, EP samples had superior resistances at all mixing ratios.

Capillary absorption of samples containing the healing agent was approximately 30% lower in between aging periods while the reference sample presented an increase of 15% for the same intervals. These results indicated that not only there was healing activity in the matrix but also that it had a high probability of occurring.

Optical analysis showed 100% crack area healing in 3 samples with EP substitution. The largest cracks healed were 0.056 mm for EP and 0.103 mm for EC with the latter achieving 90% healing.

Comparing both types of substitute aggregate, it was determined that EP was more efficient in absorbing sodium metasilicate so that more material is available to react with calcium hydroxide and produce C-S-H vital to concrete and its properties.

REFERENCES

[1] F. Pacheco, R. P. Souza, R. Christ, A. G. Rocha, L. Silva, and B. F. Tutikian, "Determination of volume and distribution of pores of concretes according to different exposure classes through 3d microtomography and mercury intrusion porosimetry," *Struct. Concr.*, vol. 19, no. 5, pp. 1419–1427, 2018, http://dx.doi.org/10.1002/suco.201800075.

[2] U.S. Geological Survey, *Mineral Commodity Summaries 2020*. Reston, VA: U.S. Geological Survey, 2020, https://doi.org/10.3133/mcs2020

[3] M. Garside "Cement production in the United States from 2010 to 2021(in million metric tons)". Statista. March 2022. https://www.statista.com/statistics/219343/cement-production-worldwide/ (accessed Dec. 31, 2021).

[4] H. V. Oral and H. Saygin, "Simulating the future energy consumption and greenhouse gas emissions of Turkish cement industry up to 2030 in a global context," *Mitig. Adapt. Strategies Glob. Change*, vol. 24, no. 8, pp. 1461–1482, 2019, http://dx.doi.org/10.1007/s11027-019-09855-8.

[5] P. Friedlingstein et al., "Global Carbon Budget 2019," *Earth Syst. Sci. Data*, vol. 11, no. 4, pp. 1783–1838, 2019, http://dx.doi.org/10.5194/essd-11-1783-2019.

[6] J. Zhang et al., "Immobilizing bacteria in expanded perlite for the crack self-healing in concrete," *Constr. Build. Mater.*, vol. 148, pp. 610–617, 2017, http://dx.doi.org/10.1016/j.conbuildmat.2017.05.021.

[7] N. P. B. Tan, L. H. Keung, W. Choi, W. C. Lam, and H. N. Leung, "Silica-based self-healing microcapsules for self-repair in concrete," *J. Appl. Polym. Sci.*, vol. 133, no. 12, 2016, http://dx.doi.org/10.1002/app.43090.

[8] N. Nain, R. Surabhi, N. V. Yathish, V. Krishnamurthy, T. Deepa, and S. Tharannum, "Enhancement in strength parameters of concrete by application of bacillus bacteria," *Constr. Build. Mater.*, vol. 202, pp. 904–908, 2019, http://dx.doi.org/10.1016/j.conbuildmat.2019.01.059.

[9] C. S. T. Reddy and A. Ravitheja, "Macro mechanical properties of self-healing concrete with crystalline admixture under different environments," *Ain Shams Eng. J.*, vol. 10, no. 1, pp. 23–32, 2019, http://dx.doi.org/10.1016/j.asej.2018.01.005.

[10] A. Al-Tabbaa, C. Litina, P. Giannaros, A. Kanellopoulos, and L. Souza, "First UK field application and performance of microcapsule-based self-healing concrete," *Constr. Build. Mater.*, vol. 208, pp. 669–685, 2019, http://dx.doi.org/10.1016/j.conbuildmat.2019.02.178.

[11] S. S. Lucas, C. Moxham, E. Tziviloglou, and H. Jonkers, "Study of self-healing properties in concrete with bacteria encapsulated in expanded clay," *Sci. Technol. Mater.*, vol. 30, Suppl. 1, pp. 93–98, 2018, http://dx.doi.org/10.1016/j.stmat.2018.11.006.

[12] S. Gupta and H. W. Kua, "Encapsulation technology and techniques in self-healing concrete," *J. Mater. Civ. Eng.*, vol. 25, no. 12, pp. 864–870, 2016, http://dx.doi.org/10.1061/(ASCE)MT.1943-5533.

[13] K. Van Tittelboom, E. Gruyaert, H. Rahier, and N. De Belie, "Influence of mix composition on the extent of autogenous crack healing by continued hydration or calcium carbonate formation," *Constr. Build. Mater.*, vol. 37, pp. 349–359, 2012, http://dx.doi.org/10.1016/j.conbuildmat.2012.07.026.

[14] S. Gupta, S. D. Pang, and H. W. Kua, "Autonomous healing in concrete by bio-based healing agents – a review," *Constr. Build. Mater.*, vol. 146, pp. 419–428, 2017, http://dx.doi.org/10.1016/j.conbuildmat.2017.04.111.

[15] K. Sisomphon, O. Copuroglu, and E. A. B. Koenders, "Self-healing of surface cracks in mortars with expansive additive and crystalline additive," *Cement Concr. Compos.*, vol. 34, no. 4, pp. 566–574, 2012.

[16] M. M. Pelletier, R. Brown, A. Shukla, and A. Bose, "Self-healing concrete with a microencapsulated healing agent," *Cement Concr. Res.*, vol. 8, pp. 1015, 2011.

[17] K. Van Tittelboom et al., "Self-healing efficiency of cementitious materials containing tubular capsules filled with healing agent," *Cement Concr. Compos.*, vol. 33, pp. 497–505, 2011, http://dx.doi.org/10.1016/j.cemconcomp.2011.01.004.

[18] K. Sisomphon, O. Copuroglu, and A. Fraaij, "Application of encapsulated lightweight aggregate impregnated with sodium monofluorophosphate as a self-healing agent in blast furnace slag mortar," *Heron*, vol. 56, no. 1–2, pp. 17–36, 2011.

[19] A. M. Rashad, "Lightweight expanded clay aggregate as a building material – an overview," *Constr. Build. Mater.*, vol. 170, pp. 757–775, 2018, http://dx.doi.org/10.1016/j.conbuildmat.2018.03.009.

[20] R. Alghamri, A. Kanellopoulos, and A. Al-Tabbaa, "Impregnation and encapsulation of lightweight aggregates for self-healing concrete," *Constr. Build. Mater.*, 2016, http://dx.doi.org/10.1016/j.conbuildmat.2016.07.143.

[21] K. Van Tittelboom et al., "Comparison of different approaches for self-healing concrete in a large-scale lab test," *Constr. Build. Mater.*, vol. 107, pp. 125–137, 2016., http://dx.doi.org/10.1016/j.conbuildmat.2015.12.186.

[22] K. Van Tittelboom and N. De Belie, "Self-healing in cementitious materials: a review," *Materials (Basel)*, vol. 6, pp. 2182–2217, 2013, http://dx.doi.org/10.3390/ma6062182.

[23] V. M. John, “Cimentos de escória ativada com silicatos de sódio,” Ph.D. dissertation, Universidade de São Paulo, São Paulo, Brasil, 1995.

[24] O. Sengul, S. Azizi, F. Karaosmanoglu, and F. M. A. Tasdemir, "Effect of expanded perlite on the mechanical properties and thermal conductivity of lightweight concrete," *Energy Build.*, vol. 43, no. 2–3, pp. 671–676, 2011, http://dx.doi.org/10.1016/j.enbuild.2010.11.008.

[25] H. M. Jonkers, "Bacteria-based self-healing concrete," *Frankfurter Afrikanistische Blatter*, vol. 8, no. 1, pp. 49–79, 2011.

[26] B. Z. Ahmed, E. Rozière, and A. Loukili, "Plastic shrinkage and cracking risk of recycled aggregates concrete," *Constr. Build. Mater.*, vol. 121, pp. 733–745, 2016, http://dx.doi.org/10.1016/j.conbuildmat.2016.06.056.

[27] E. Tziviloglou, V. Wiktor, H. M. Jonkers, and E. Schlangen, "Bacteria-based self-healing concrete to increase liquid tightness of cracks," *Constr. Build. Mater.*, vol. 122, pp. 118–125, 2016, http://dx.doi.org/10.1016/j.conbuildmat.2016.06.080.

[28] American Society for Testing and Materials, *Standard Specification for Portland Cement,* ASTM C150/C150M, 2020b.

[29] American Society for Testing and Materials, *Standard Test Method for Bulk Density (‘Unit Weight’) and Voids in Aggregate,* ASTM C29/C29M, 2017.

[30] American Society for Testing and Materials, *Standard Test Method for Relative Density (Specific Gravity) and Absorption of Fine Aggregate,* ASTM C128, 2015a.

[31] American Society for Testing and Materials, *Standard Specification for Concrete Aggregates,* ASTM C33/C33M, 2018.

[32] M. R. Ahmad, B. Chen, and S. F. A. Shah, "Investigate the influence of expanded clay aggregate and silica fume on the properties of lightweight concrete," *Constr. Build. Mater.*, vol. 220, pp. 253–266, 2019, http://dx.doi.org/10.1016/j.conbuildmat.2019.05.171.

[33] J. A. Bogas, A. Mauricio, and M. F. C. Pereira, "Microstructural analysis of iberian expanded clay aggregates," *Microsc. Microanal.*, vol. 18, no. 5, pp. 1190–1208, 2012, http://dx.doi.org/10.1017/S1431927612000487.

[34] F. Pacheco et al., "Análise da autorregeneração de matrizes cimentícias através de diferentes métodos de inserção de soluções químicas e bacterianas," *Rev. ALCONPAT*, vol. 12, pp. 32–46, 2022.

[35] American Society for Testing and Materials, *Standard Test Method for Slump of Hydraulic-Cement Concrete,* ASTM C143/C143M, 2020a.

[36] American Society for Testing and Materials. *Standard Specification for Molds for Forming Concrete Test Cylinders Vertically,* ASTM C470/C470M, 2015b.

[37] American Society for Testing and Materials, *Standard Test Method for Compressive Strength of Cylindrical Concrete Specimens,* ASTM C39/C39M, 2020d.

[38] American Society for Testing and Materials, *Standard Test Method for Flexural Strength of Hydraulic-Cement Mortars,* ASTM C348, 2020c.

[39] RILEM TC 116-PCD. "Permeability of concrete as a criterion of its durability," *Mater. Struct.*, vol. 32, pp. 174–179, 1999, http://dx.doi.org/10.1007/BF02481509.

[40] V. A. C. Wiktor and H. M. Jonkers, "Quantification of crack-healing in novel bacteria-based self-healing concrete," *Cement Concr. Compos.*, vol. 33, no. 7, pp. 763–770, 2011, https://doi.org/doi:10.1016/j.cemconcomp.2011.03.012

[41] M. Jedidi, O. Benjeddou, and O. C. Soussi, "Effect of expanded perlite aggregate dosage on properties of lightweight concrete," *Jordan J. Civ. Eng.*, vol. 9, no. 3, pp. 278–291, 2015, http://dx.doi.org/10.14525/jjce.9.3.3071.

[42] M. Leyton-Vergara, A. Pérez-Fargallo, J. Pulido-Arcas, G. Cárdenas-Triviño, and J. Piggot-Navarrete, "Influence of granulometry on thermal and mechanical properties of cement mortars containing expanded perlite as a lightweight aggregate," *Materials (Basel)*, vol. 12, no. 23, 2019, http://dx.doi.org/10.3390/ma12234013.

[43] M. Alazhari, T. Sharma, A. Heath, R. Cooper, and K. Paine, "Application of expanded perlite encapsulated bacteria and growth media for self-healing concrete," *Constr. Build. Mater.*, vol. 160, no. January, pp. 610–619, 2018, http://dx.doi.org/10.1016/j.conbuildmat.2017.11.086.

[44] P. Shafigh, L. J. Chai, H. B. Mahmud, and M. A. Nomeli, "A comparison study of the fresh and hardened properties of normal weight and lightweight aggregate concretes," *J. Build. Eng.*, vol. 15, pp. 252–260, Aug 2017, http://dx.doi.org/10.1016/j.jobe.2017.11.025.

[45] H. N. Yow and A. F. Routh, "Formation of liquid core-polymer shell microcapsules," *Soft Matter*, vol. 2, no. 11, pp. 940–949, 2006, http://dx.doi.org/10.1039/b606965g.

[46] G. Li, X. Huang, J. Lin, X. Jiang, and X. Zhang, "Activated chemicals of cementitious capillary crystalline waterproofing materials and their self-healing behaviour," *Constr. Build. Mater.*, vol. 200, pp. 36–45, 2019, http://dx.doi.org/10.1016/j.conbuildmat.2018.12.093.

[47] V. Muller et al., "Analysis of cementitious matrices self-healing with bacillus bacteria," *Rev. IBRACON Estrut. Mater.*, vol. 15, no. 4, pp. e15404, 2022, http://dx.doi.org/10.1590/S1983-41952022000400004.

Author's contributions: F.P experimental procedure, materials characterization, writing; C.H.B experimental procedure, materials characterization, writing; T.N.G experimental procedure, materials characterization, writing; V.M experimental procedure, writing, revising; H.Z.E writing, revising; R.C.E.M writing, revising; B.F.T supervision, revising, formal analysis.

Editors: Fernando Pelisser, Guilherme Aris Parsekian.

IBRACON Structures and Materials Journal
Revista IBRACON de Estruturas e Materiais
ISSN 1983-4195 ismj.org

ORIGINAL ARTICLE

CFRP-strengthened RC beams under fire condition: numerical model

Vigas de concreto armado reforçadas com CFRP em situação de incêndio: modelo numérico

Thiago Brazeiro Carlos[a]
Valdir Pignatta e Silva[a]

[a]Universidade de São Paulo – USP, Escola Politécnica, Departamento de Engenharia de Estruturas e Geotécnica, São Paulo, SP, Brasil

Received 29 March 2022
Accepted 20 Jul 2022

Abstract: The Carbon Fiber Reinforced Polymer (CFRP) has excellent flexural performance on strengthening and rehabilitation of reinforced concrete (RC) structures. However, it is known that CFRP strengthening systems are very vulnerable to high thermal exposure. To provide a better understanding of its fire behavior and fulfill gaps in this field, this investigation proposes the development of an accurate three-dimensional (3D) Finite Element (FE) model capable of simulating the CFRP-strengthened RC beams flexural behavior at ambient temperature and under fire conditions. To achieve the goals, thermal and mechanical numerical simulations have been performed to validate the developed FE models. Experimental results reported in two parallel studies were used to model's validation. The numerical model has been satisfactorily validated and the results had a good predictability with the experimental results in terms of thermal and mechanical behavior.

Keywords: fire, reinforced concrete structures, beam, CFRP strengthening, numerical model.

Resumo: Os Polímeros Reforçados com Fibras de Carbono (CFRP) possuem excelente desempenho à flexão no reforço e reabilitação de estruturas de concreto armado. No entanto, sabe-se que os sistemas de reforço de CFRP são muito vulneráveis à alta exposição térmica. Para fornecer uma melhor compreensão do seu comportamento em incêndio e preencher lacunas da área, o estudo propõe o desenvolvimento de um modelo tridimensional de elementos finitos consistente, capaz de simular o comportamento à flexão de vigas de concreto armado, reforçadas com CFRP, sob condições de temperatura ambiente e de incêndio. Para atingir os objetivos, simulações numéricas, térmicas e mecânicas, foram realizadas para validar os modelos desenvolvidos. Resultados experimentais relatados em dois estudos paralelos foram utilizados para a validação do modelo. O modelo numérico foi satisfatoriamente validado e os resultados tiveram uma boa previsibilidade aos resultados experimentais, em termos de comportamento térmico e mecânico.

Palavras-chave: incêndio, estruturas de concreto armado, viga, reforço, CFRP, modelo numérico.

How to cite: T. B. Carlos and V. P. Silva, "CFRP-strengthened RC beams under fire condition: numerical model," *Rev. IBRACON Estrut. Mater.*, vol. 16, no. 2, e16202, 2023, https://doi.org/10.1590/S1983-41952023000200002

1 INTRODUCTION

The temperature variation significantly affects the mechanical performance of the CFRP strengthening system on concrete structures. Thus, the knowledge of the temperature effects is a key factor in the fire design of this type of construction, especially as it develops at the CFRP-concrete bond which is a critical zone very sensitive to thermal exposure.

Corresponding author: Thiago Brazeiro Carlos. E-mail: thiago_brazeiro@hotmail.com
Financial support: CNPq (National Council of Scientific and Technological Development, Brazil) – scholarship number: 152239/2020-0.
Conflict of interest: Nothing to declare.
Data Availability: The data that support the findings of this study are available in Composite Structures, Volume 189, 1 April 2018, Pages 516-528 at https://www.sciencedirect.com/science/article/abs/pii/S0263822317326326#FCANote and in Construction and Building Materials, Volume 193, 30 December 2018, Pages 395-404 https://www.sciencedirect.com/science/article/abs/pii/S0950061818325935, published by this first author.

The failure of bond generally occurs at temperatures near or above the Glass Transition Temperature (T_g)[1] of the adhesive. Glass Transition Temperature is the point at which a material alters state – going from a glass-like rigid solid to a more flexible compound. T_g is normally measured on a Differential Scanning Calorimeter (DSC) piece equipment. However, in some cases, the bond failure happens for temperatures below T_g. The T_g of the adhesive varies usually from 50 and 120 ºC [1]–[5], depending on the polymeric matrix of constituents and the type of resin, among others. The better understanding of the temperature effects on this type of structures makes it possible for reliable and safe design in case of fire. To contribute to this end, few numerical investigations concerning the fire behavior of CFRP-strengthened RC members have been carried out over the last years [6]–[10], as discussed in detail in the next section.

2 STATE OF THE ART

As mentioned in the previous section, recent concerns about the fire influence on CFRP-strengthened RC beams structures have generated few numerical investigations in this area, to better understand their behavior at elevated temperatures. Relevant numerical studies on fire behavior of CFRP-strengthened RC beams structures [6]–[10] are presented in detail below.

Hawileh et al. [6] numerically investigated the fire behavior of thermally insulated EBR-CFRP-strengthened T-section RC beams previously fire-tested by Williams et al. [11] which was described in the previous section. For this purpose, detailed 3D FE models were developed using the commercial software ANSYS [12] to perform a nonlinear transient thermal-stress analysis under fire conditions. The FE models were composed by thermal and structural elements, to enable independent thermal and structural analysis. The temperature-dependence of thermal and mechanical properties of the constituent materials of the specimens were considered, including CFRP and passive fire protection materials. Numerical results were compared with experimental data [11] in terms of temperature evolution in the beam, in the CFRP, in the reinforcements, along the CFRP-concrete interface as well as the deflections of the beams when subjected to fire. The heating was applied only at the bottom surface of the specimens in a transient state according to ASTM E119 [13]. In addition, a sustained uniformly distributed load at the top surface of the T-beam was applied to simulate the serviceability loads during heating. The numerical models presented a good predictability with the experimental results in terms of temperatures. Regarding the predicted mid-span vertical deflections as a function of fire exposure time, the results also showed a good agreement with the ones experimentally measured in the first 33 minutes of test (until the hydraulic pressure was lost accidentally in the experiment). However, the authors were unable to validate the numerical procedure in terms of mechanical response (such as the CFRP debonding phenomenon) due to limited experimental data.

Ahmed and Kodur [7] improved a numerical approach previously developed by Kodur and Ahmed [14] regarding the modelling of the degradation of connections of reinforced RC beams with EBR-CFRP laminates exposed to fire. The main innovation presented by [7] was the simulation of the bond degradation at the CFRP-concrete interface by means of an explicit model by means of the bond-slip laws, which was not considered in the previous study [14]. The numerical procedure was implemented into a macroscopic FE model which is capable of predicting the temperature-dependency of material properties, different fire scenarios, and failure limit states in evaluating fire response of CFRP-strengthened RC beams. The numerical model validity and accuracy was based on the experimental data from fire resistance tests on CFRP-strengthened RC beams performed by Blontrock et al. [15] and Ahmed and Kodur [16]. Moreover, a parametric study has been carried out on another CFRP-strengthened RC beam [17] to simulate the effect of bond degradation and insulation schemes at CFRP–concrete interface response under fire situation. Overall, according to the results a good agreement between the experimental and numerical FE models was obtained in terms of temperatures, as well as the deflections and the instant to CFRP debonding. Regarding to parametric analysis, the results showed a significant bond degradation in moment capacity and stiffness when the temperature at CFRP–concrete interface slightly exceeds T_g of the adhesive (81 ºC), leading to the initiation of CFRP laminate debonding (around 40 min of fire exposure). In addition, the authors concluded that the time the bond degradation in CFRP-strengthened concrete members occurs depends on the fire protection thickness and T_g of the adhesive.

Dai et al. [8] developed the first 3D FE model for the simulation of the thermomechanical behavior of insulated EBR-CFRP-strengthened RC beams under fire conditions. The 3D FE models were developed and validated based on the experimental data and results from fire resistance tests performed by Blontrock et al. [15] and Williams et al. [11], both described in the previous section through the commercial software package Abaqus [18]. The bond degradation with temperature evolution for the internal steel reinforcement, the external CFRP, the temperature-dependence of thermo-physical and mechanical properties of all materials were considered in the simulations. The bond-slip laws recommended in Model Code [19] for ambient temperature were used to represent the interaction between the concrete surface and steel reinforcements. The proposed numerical approach achieved a good accuracy of thermal and structural response of thermally protected EBR-CFRP strengthened RC beams under fire conditions in comparison to the ones obtained in experimental studies (Blontrock et al. [15] and Williams et al. [11]). Numerical results show that the consideration of a perfect bonding between CFRP and concrete leads to underestimations of fire resistance in CFRP-strengthened RC beams, as adopted in most of previous numerical investigations.

Another relevant numerical investigation on the fire behavior of RC beams strengthened with CFRP laminates bonded according to EBR technique was performed by Firmo et al. [9]. Two-dimensional FE models were developed to simulate fire resistance tests of simply supported RC beams strengthened with EBR-CFRP laminates previously studied by Firmo and Correia [20] (described in detail in previous section) and Firmo et al. [21]. The thermomechanical response of models was numerically simulated considering the influence of CFRP anchorage systems and different passive fire protection schemes applied along the bottom surface of the beams and in the anchorage zones. The commercial software package Abaqus [22] was used in the numerical simulations where the temperature variation of the thermomechanical properties of the materials was considered and the CFRP-concrete bond interaction was modelled based on bi-linear bond-slip laws previously calibrated for different temperatures (up to 120 ºC). The numerical results showed a good accuracy in terms of fire behavior of CFRP-strengthened RC beams, including the “cable mechanism” phenomena, the time and temperature at debonding of the strengthening system as observed in the reported experimental results [20], [21]. Furthermore, this numerical study allowed the validation of the proposed bond-slip laws for the CFRP-concrete bond interaction, showing their suitability for simulating the behavior of EBR-CFRP-strengthened RC beams subjected to fire.

A more recent and detailed numerical investigation carried out by Firmo et al. [10] (improving their initial study mentioned above [9]) proposed 3D FE models to simulate the fire response of the RC beams strengthened with CFRP laminates bonded according to the EBR technique. The CFRP-concrete bond interaction was modelled by bi-linear bond-slip laws as well as the one previously validated by Firmo et al. [9] with Abaqus [22] software. According to results, the structural response of the CFRP-strengthened RC beams was achieved with reasonable accuracy when compared with experimental results obtained in fire resistance tests [20], despite some deviations observed. These satisfactory results confirmed that the bond-slip laws for the CFRP-concrete interaction, previously used in the 2D FE model by Firmo et al. [9], can be used for the 3D simulation of EBR-CFRP strengthening systems subjected to fire conditions and allow more complex analyses. Moreover, the possibility of exploring the mechanical contribution of the CFRP in a fire situation by a “cable” behavior with the application of a thicker insulation in the CFRP anchorage zones is highlighted.

The literature review described above shows that the numerical efforts to simulate the fire behavior of CFRP-strengthened concrete beams are very limited. Few numerical studies have considered the CFRP-concrete interface’s thermal degradation and have used 3D models that are theoretically more realistic. Moreover, numerical results have shown that accurate predictions of the fire response of CFRP-strengthened beams require the inclusion of explicit temperature-dependent bond-slip models for the CFRP-concrete interface, which has been neglected in most of the above-cited studies.

In addition to numerical studies on fire behavior of CFRP-strengthened beams, a few analytical and numerical investigations reported in the literature [23]–[28] have focused specially on the behavior of the bond between the CFRP and concrete at elevated temperatures in strengthening systems. However, some gaps in this field were also noted. Most of these studies were limited to the T_g of the adhesive. Moreover, simplifications assumed by the authors on the bond-slip relationships for higher temperatures, such as the consideration that the concrete-adhesive interface is linear elastic, did not provide good results for temperatures above or much higher than T_g (although good accuracy has been observed for temperatures below T_g).

3 JUSTIFICATION AND OBJECTIVES

In the past, the development of research allowed the elaboration and implementation of standards for ambient temperature design of concrete structures that resulted in the elaboration of EN 1992-1-1 [29]. However, for fire design of CFRP-strengthened concrete elements, there is still a lack of research. Currently, the methods presented in EN 1992-1-2 [30] for fire design of concrete structures do not consider the contribution of the CFRP strengthening on the flexural behavior of these elements under fire conditions and do not have consistent methods for fire design. Furthermore, there are other important standards for specific design of externally bonded FRP systems for strengthening existing structures, such as ACI 440.2R-17 [5] and Fib bulletin 14 [31]. Both recognize the inefficiency of CFRP strengthening systems at elevated temperatures, but they do not define any calculation criteria or method that consider the contribution of the CFRP in the case of fire. The ACI and Fib documents [5], [31] are overly conservative when they simply suggest that the fire verification of the structure may be conducted considering that the strengthening is non-existent, i.e., that the contribution of the resistance of the CFRP system to the service conditions verifications is not considered. Therefore, the development of new design methods for concrete structures strengthened with CFRP subjected to fire are urgently and necessary given the substantial current demand for their use in buildings and due to the inherent risks of a composite structural element when subjected to these limit conditions. This research intends to contribute to this purpose.

Despite the investigations carried out over the years (as discussed in Chapter 2), many issues concerning the bond behavior between concrete and CFRP strengthening systems at elevated temperatures remain unclear and need further investigation, especially concerning the limited temperature ranges studied. Thus, the thermal and mechanical response of the CFRP-concrete bond for temperatures higher and much higher than T_g needs further investigation.

Based on the challenges discussed above, it is fundamental the development of accurate models to simulate the CFRP-concrete bond behavior with good predictions for temperatures above T_g and that consider the complexities mentioned above are essential. In this regard, the present research intends to be an important contribution in fire safety engineering, since its objective is the develop an accurate model capable to simulate the fire behavior of CFRP-strengthened concrete beams, based on valuable experimental results reported in two parallel studies by Carlos et al. [32] and by Carlos and Rodrigues [33]. Therefore, this research becomes essential to bring a deep/better understanding and fill the gaps on the fire behavior of this type of composite structures, also contributing to further research. Moreover, the development of the FE model can be used in parametric studies, to assess different parameters not experimentally tested yet and contribute to the advancement of the area.

4 NUMERICAL INVESTIGATION

4.1 Model geometry

The FE models' geometry consisted of a replication of the ones that composes the beams tested in the experimental investigation by Carlos et al. [32] (Figure 1a), as well as for the other elements and materials involved. Three-dimensional FE models of simply supported RC beams flexurally strengthened with EBR-CFRP laminates (Figure 1b) were modelled using the commercial software package Abaqus to simulate the mechanical response at ambient and elevated temperatures. In addition, 3D models of unstrengthened beams were also developed for the mechanical analysis.

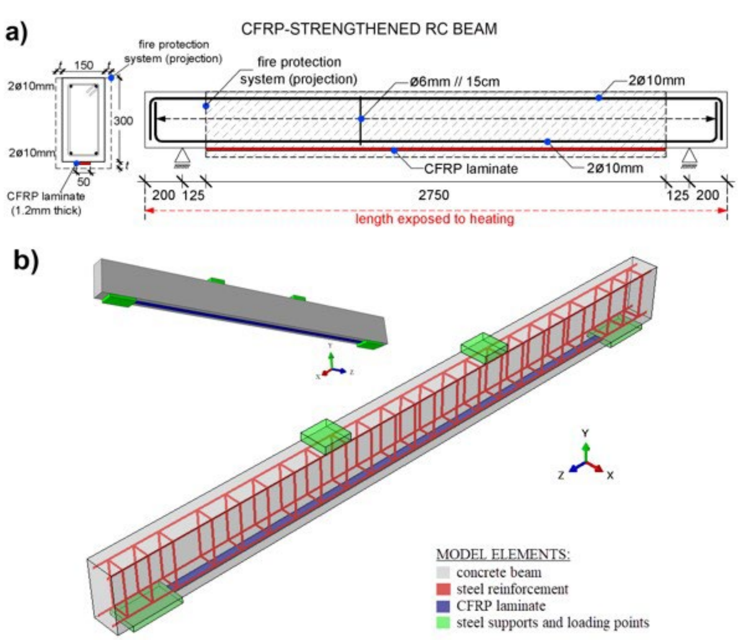

Figure 1. a) Geometry of the beams tested in the experimental investigation by Carlos et al. [32] and b) representative 3D numerical model of the CFRP-strengthened beam for mechanical analysis at ambient and elevated temperatures (not to scale, dimensions in mm).

Two-dimensional (2D) FE models for both type of beams were also developed exclusively for the heat transfer analysis since this is a type of uncoupled analysis. The 2D models were developed based on the tested cross-sections of the beams, including the modelling of the concrete slab cross-section to simulate the thermal interactions between the elements, as intended in the experimental study [32]. The use of three different fire protection materials, the ones previously fire tested in the CFRP-strengthened beams by Carlos et al. [32], were also numerically investigated in terms of thermal response.

The CFRP-strengthened RC beams were protected by three types of fire protection systems composed of the following sprayed materials: Vermiculite-Perlite (VP), ordinary Portland cement with Expanded Clay aggregates (EC) and Ordinary Portland (OP) cement-based mortars. These materials are described in further detail in section 4.3.1.4.

Four representative heat transfer models (Figure 2a-d) were numerically simulated under fire conditions. The nomenclature adopted for the 2D FE models of the beams is analogous to the ones experimentally tested specimens [32]. The unstrengthened and unprotected RC beam is referred to by RC. The predicted results of these simulations were compared with the experimental data obtained by Carlos et al. [32] in terms of temperatures vs. time of fire exposure at different locations of the mid-span cross-section. To allow comparison between results, the same thermocouples arrangement used in the previous experimental study [32] was defined in the current heat transfer analysis, as shown in Figure 3a and Figure 3b for the unstrengthened and CFRP-strengthened beams, respectively.

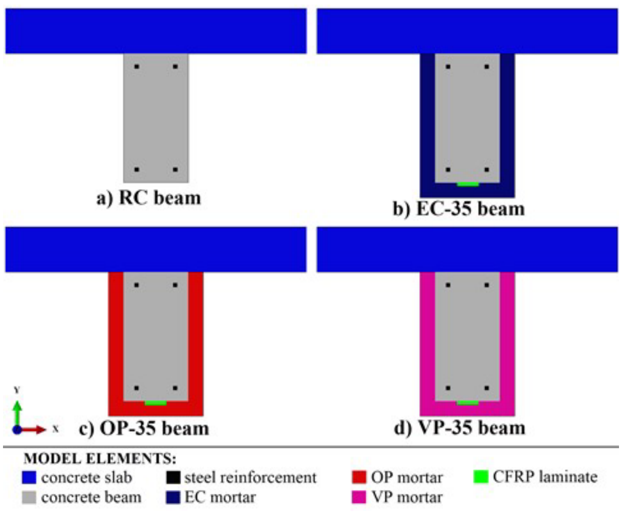

Figure 2. Numerical models for heat transfer analysis: (a) RC beam, (b) EC-35 beam, (c) OP-35 beam and (d) VP-35 beam (not to scale).

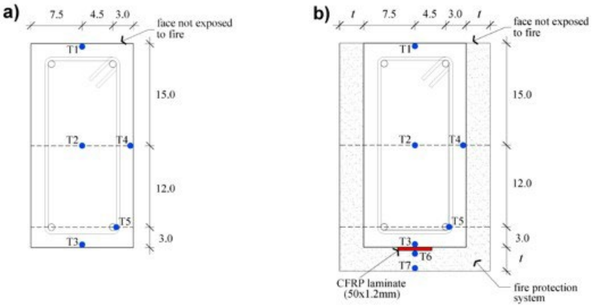

Figure 3. Location and nomenclature of thermocouples at Section S1 of (a) unstrengthened and (b) CFRP-strengthened RC beams (not declared units in cm).

4.2 Finite Element Type

The RC beams were modelled by using solid elements (C3D8R) for the concrete material geometry, steel supports and loading points. The C3D8R finite element was also chosen for modelling the CFRP laminate in the case of strengthened RC beams. The longitudinal steel reinforcement and stirrups were modelled by using truss elements (T3D2).

The C3D8R element (Figure 4) is defined as a three-dimensional, continuum (C), hexahedral and an eight-node brick element with reduced integration (R), hourglass control and first-order (linear) interpolation. These finite elements have three degrees of freedom per node, referring to translations in the three directions X, Y and Z (global coordinates). One of the reasons for using the C3D8R in the current research is because it can be applied in Abaqus for linear analysis and complex nonlinear analyses involving contact, plasticity, and large deformations. Moreover, they are available for stress, heat transfer, acoustic, coupled thermal-stress, coupled pore fluid-stress, piezoelectric, and coupled thermal-electrical analyses [34].

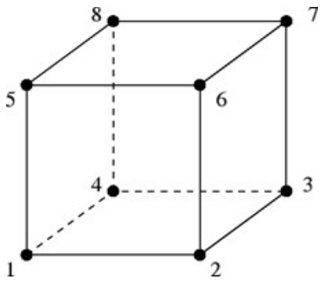

Figure 4. Scheme of the C3D8R element [34]

The selected C3D8R element type uses a reduced (lower-order) integration to form the element stiffness with only one integration location per element. The reduced integration method was chosen because it reduces the amount of CPU time necessary for analysis of the model and avoids shear locking without losing the accuracy of the analysis. Shear locking may occur in elements under pure bending and without reduced integration, because the element edges must remain straight and the angle between the deformed isoparametric lines is not equal to 90º which means that the strain in the thickness direction is not zero (Figure 5). So, this can lead to overestimation of the load capacity in bending dominated problems [35].

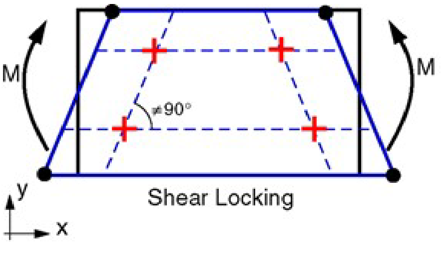

Figure 5. Shear locking in elements without reduced integration points [34]

T3D2 is a three-dimensional and two-node element used to model slender, line-like structures that support loading along the axis only or the centreline of the element (Figure 6). No moments or forces which are perpendicular to the centreline are supported. This element allows defining the cross-sectional area associated with the truss element as part of the section definition. When truss elements are used in large-displacement analysis, the updated cross-sectional area is calculated by assuming that the truss is made of an incompressible material, regardless of the definition of the material being analysed. This assumption is adopted because the most common applications of trusses at large strains involve yielding metal behaviour or rubber elasticity, in which cases the material is effectively incompressible [34].

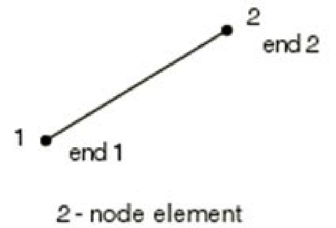

Figure 6. Scheme of the T3D2 element [34]

For the 2D heat transfer analysis, the DC2D4 element was selected. This element type consists of a 4-node linear heat transfer quadrilateral element and was chosen because it presents excellent accuracy to estimate the temperature evolution of different materials in a thermal analysis.

Additional information about the aforementioned finite elements can be seen in detail in [36].

4.3 Material modelling

The properties of the materials used in the FE models were represented in the Abaqus program based on the literature and standardization. So, it was intended to reproduce the thermophysical and mechanical behavior of the tested beams as faithfully as possible, as described in detail in the following sections.

4.3.1 Thermophysical material properties

4.3.1.1 Concrete

In the modelling of the specific heat for concrete (c_p), a higher value of 8.5% for the moisture content was defined according to the humidity conditions of the concrete specimens. Therefore, the $c_{p.peak}$ for the moisture content of 8.5% corresponded to 4040 J/kgºC. This specific heat peak is because the evaporation of the free water from the concrete occurs through endothermic reactions. The evolution of the specific heat value in relation to the temperature adopted for the concrete used in the current investigation was based on the recommendations of Eurocode 2, part 1-2 [30]. The thermal conductivity of ordinary concrete for a given temperature was proposed based on the expressions provided in the National French Annex to NF EN 1992-1-2 [37]. Therefore, the curve established by the French Annex [37] was selected to be applied to the developed model. In the current model, the usual density of the single concrete at 20ºC [ρ (20 ºC)] was defined as 2300 kg/m^3, as suggested in Eurocode 2, part 1-2 [30]. The emissivity of the concrete surface was defined as 0.7 and it was considered constant with temperature evolution, according to Eurocode 2, part 1-2 [30]. The radiative heat flux was calculated using the emissivity coefficients of the electric resistance of the furnace and of the concrete surface, both equal to 0.7, and it resulted in a value of 0.49. A convection coefficient of 15 W/m^2 ºC (also constant with temperature) was adopted as suggested in EN-1992-1-2 [30].

4.3.1.2 Steel reinforcement

In the case of steel reinforcement modelling, the thermophysical material properties were defined based on Eurocode 4, part 1-2 [38] recommendations. The specific heat of steel reinforcement (c_s) at different temperatures in the numerical model was determined by the curve defined in EN 1994-1-2 [38]. The thermal conductivity of the steel was also defined according to EN 1994-1-2 [38]. According to Eurocode 4, part 1-2 [38], the steel reinforcement density (ρ_s) was defined constant with temperature, corresponding to 7850 kg/m^3.

4.3.1.3 CFRP laminate

The CFRP laminates were thermally characterized in the numerical model using experimental data from the literature [39], [40]. The variation of the specific heat of CFRP laminates was modelled based on experimental data reported in the investigation by Griffis et al. [39]. Similarly to the specific heat variation, the proposal presented in Griffis et al. [39] for the evolution of the CFRP thermal conductivity in relation to temperature was adopted. The density of the CFRP was determined based on the relationship of the remaining mass with temperature according to results obtained by Thermogravimetric Analysis (TGA) performed by Firmo et al. [40]. Thus, considering the mass loss relationship determined in [40] and a density of 1550 kg/m^3 at ambient temperature according to the manufacturer [41], the variation of the density in relation to temperature was defined.

4.3.1.4 Fire protection systems

The VP mortar was a commercial mortar made with lightweight expanded perlite and vermiculite aggregates, refractory compounds, cementitious binders, and a ratio water/compounds of 0.67–0.80 l/kg. Also, this fire protection material presents a dry density of 450–500 kg/m3 and a thermal conductivity of 0.0581 W/m·K [42]. The OP mortar, also commercial, was formulated from hydraulic binders, calcareous, siliceous aggregates, and some other non-specified additions, with dry density of 1500–1800 kg/m3, thermal conductivity 0.67 W/m·K and a ratio water/compounds of 0.13–0.15 l/kg [43]. The EC mortar differed from the OP mortar by replacing the calcareous aggregates by expanded clay aggregates. A ratio water/compounds of 0.35–0.40 l/kg was used. The expanded clay is a lightweight aggregate with a granulometry distribution of 0.25–2.0 mm, a dry density of 468–633 kg/m3 and a thermal conductivity of 0.13 W/m·K [44]. This material was incorporated into the mortar mixture in a ratio of 2.6:1 (cement:aggregate). The aforementioned thermal property values are for ambient temperature.

4.3.2 Mechanical material properties

4.3.2.1 Concrete

The mechanical properties of the concrete at ambient temperature were experimentally determined and given in EN 1992-1-1 [29]. Thus, an average cube compressive strength of f_{cm}=30.1 MPa was experimentally obtained in this work by means of compressive strength tests. The average tensile strength (f_{ctm}) was defined as 2.9 MPa according to [29]. Concerning the modulus of elasticity of concrete (E_{cm}), it was calculated for thermal actions (natural fire simulation) in accordance with a mathematical model for stress-strain relationships of concrete under compression at elevated temperatures proposed in EN 1992-1-2 [29]. The E_{cm} was calculated as 17.3 GPa (this value is generally lower than the one defined for concrete at ambient temperature). The reduction of the mechanical properties of the concrete at elevated temperatures were obtained from the relationships suggested in EN-1992-1-2 [30] and EN 1994-1-2 [38]. The Poisson's ratio was defined equal to 0.2 and constant with temperature, according to Eurocode 2, part 1-1 [29] recommendation.

4.3.2.2 Steel reinforcement

The mechanical properties of the steel reinforcement (B500 steel class) were defined according to Eurocode 4, part 1-2 [38]. The mechanical properties of the steel rebars at ambient temperature were as follows: yield stress of 500 MPa, modulus of elasticity of 210 GPa, ultimate tensile strength of 550 MPa and Poisson's ratio (ν) of 0.3. The temperature-dependent behavior of steel was also determined by part 1-2 of Eurocode 4 [38], following the reduction factor proposals presented in this standard. Poisson's ratio was considered constant with temperature. The strain hardening effect on the steel at elevated temperatures was also accounted for in current numerical investigation and was calculated based on the calculation methods proposed by the part 1-2 of Eurocode 4 [38] (allowed by the stress-strain relationships for steel at elevated temperatures).

4.3.2.3 CFRP laminate

Regarding the mechanical behavior of the CFRP laminates, they behave essentially in the longitudinal direction in the present application, hence, as a simplification, the CFRP was modelled as linear elastic isotropic. The temperature influence on mechanical behavior of CFRP laminate in the current model was based on the relations proposed by Wang et al. [45] and Bisby [46] for the tensile strength and modulus of elasticity, respectively. The laminates have an average tensile strength of 2800 MPa, modulus of elasticity of 170 GPa and ultimate strain of 16.0‰ at ambient temperature, according to the manufacturer [41]. The Poisson's ratio is 0.3 (constant with temperature).

4.3.2.4 Fire protection systems

Concerning the fire protection systems, their mechanical contribution was not considered since it is expected to be negligible.

4.4 Finite element mesh

The finite element size significantly influences the behavior of the CFRP-strengthened RC beams. In an analysis based on the finite element method, the accuracy of the results is closely related to two aspects: first, the use of appropriate elements for each type of analyses, based on the structure geometry or material, interpolation degree and integration scheme; second, the correct model discretization defined from a sensitivity study, where a comparison of meshes with different arrangements or densities must be performed.

In the current research, three different mesh densities were studied to verify the effect of the finite element size on the behavior of the unstrengthened and CFRP-strengthened RC beams. The meshes were defined (for both type of beams) based on a relatively coarse, intermediate, and finer refinement level, corresponding to the densities (for the largest element) of 35 x 35 mm, 25 x 25 mm, and 15 x 15 mm.

The mesh study on CFRP-strengthened beams presented a high similarity between the different densities.

Finally, an excellent similarity and simulation stability between the predicted load vs. displacement evolution was obtained by using finite element meshes of 15 x 15 mm and 25 x 25 mm for both types of beams. To save computational time, finite element meshes of 25 x 25 mm were adopted in all models simulated in this research, as presented in Figure 7.

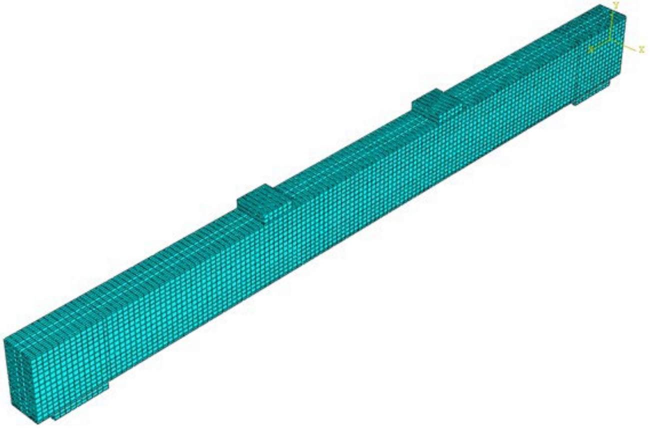

Figure 7. Finite element meshes studied for the CFRP-strengthened and unstrengthened RC beam with maximum densities of 25 mm

4.5 Boundary, loading and contact conditions

To reproduce the real test set-up as reported by Carlos et al. [32], the supports of the beam and the loading were also modelled in the numerical models on rigid plates attached to the beams to distribute possible concentrated forces on them. This representation on a numerical model is shown in Figure 8. The models were subjected to a fixed mechanical load applied to the direction -Y in a four-point bending configuration (see Figure 8) as used in the experimental tests [32]. The preload applied in the simulations (24 kN) correspond to 70% of the design value of the loadbearing capacity of the RC beam at ambient temperature, as defined in the experimental test procedure [32]. Regarding the support system, all degrees of freedom of the nodes located on the bottom surface and at the middle of the respective rigid plate were constrained to simulate the pinned support, whereas for the roller support only the translations in the directions X and Y were constrained. In addition, all nodes located at each end of both supports were constrained to translations in the direction X to prevent their lateral deformation (Figure 8).

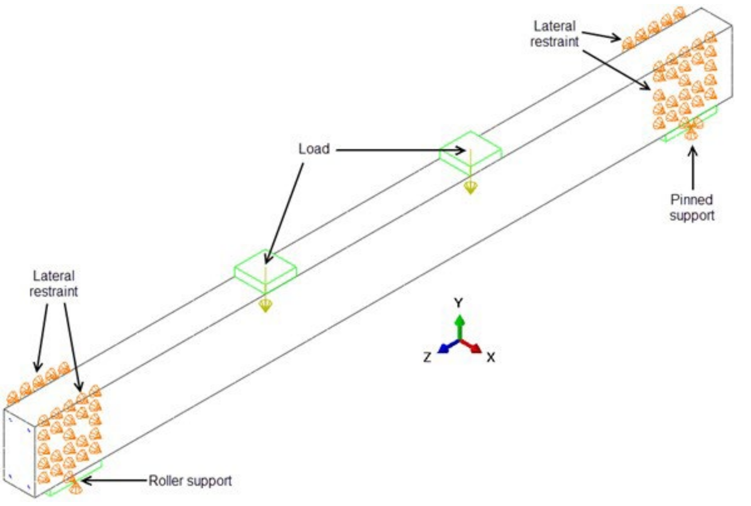

Figure 8. Boundary and loading conditions of 3D numerical models used in the FE analysis.

Concerning the contact conditions, the surface-to-surface contact method was used to simulate the contact between the concrete beam and the other materials. Small-sliding formulation was used in the contact tracking algorithm between the beams and the CFRP laminates. In this case, the geometric nonlinearity is included in the model. A penalty method (damage) was defined as the cohesive contact property between the concrete and CFRP surfaces. Thus, two bond damage criteria were adopted: maximum nominal stress and fracture energy. These values (temperature-dependent) were inputted in the FE model based on the experimental data obtained from the SST tests performed by Carlos and Rodrigues [33].

Finally, the fire action was applied in the 3D model. The heat transfer step was applied after the preloading of the model and performed according to the furnace temperatures registered in the experimental tests to validate the FE model. In these simulations, a 4-node linear heat transfer quadrilateral element (DC2D4) was chosen and a 2D numerical model was developed to estimate the temperature distribution in the cross-sections of the beams. To accurately simulate the experimental test conditions [32], the bottom and lateral surface of the models of the beams were directly exposed to the heating. The upper face of the beam in the model was superposed by a surrounding concrete slab which in turn was submitted to a constant ambient temperature, as adopted in the experimental tests [32]. The initial temperatures of the models were defined based on the measurements recorded in the experimental tests [32]. Radiation and convection heat transfer modes were considered on exposed surfaces. The resultant emissivity was taken as 0.49, considering the emissivity coefficients of the electric resistance of the furnace and the beams both equal to 0.7. A convection coefficient of 15 W/m^2 ºC (constant with temperature) was adopted, as suggested in EN-1992-1-2 [30].

A constant and uniform temperature corresponding to ambient temperature was defined at beam supports and at loading application points, since these elements were fire-protected.

4.6 Analysis method and procedure

Geometrical and material non-linear analysis were employed in the developed FE model. The non-linear equations were solved iteratively using the Newton Raphson's Method. The main advantage of Newton's method is its quadratic convergence rate when the approximation at iteration is within the "radius of convergence", i.e., when the gradients defined by matrix provide an improvement to the solution. The method disadvantage is because the Jacobian matrix must be calculated, and this same matrix must be solved. The solution of the Jacobian matrix can be a problem due to the computational effort involved. The direct solution to linear equations can dominate the entire computational effort, as the complexity of the problem increases. Despite the high computational effort required, Moltubakk [47] states that this method needs few iterations to reach the convergence capable of establishing the final solution.

The prediction of the non-linear concrete behavior was defined considering a plastic damage model: Concrete Damaged Plasticity.

The plastic damage model is the most used model since it has greater convergence capacity compared to the average crack model due to the greater simplicity and robustness of the associated numerical algorithms, which makes the use of this model more attractive in the analysis of more complex structures [48].

The Concrete Damaged Plasticity assumes two mechanisms of concrete failure, tensile cracking and compression crushing. Crack propagation is modeled based on a continuous damage mechanism: Stiffness Degradation.

A sequentially uncoupled thermo-mechanical analysis was adopted to simulate the fire behaviour of the CFRP-strengthened RC beams. A heat transfer analysis was first performed to obtain the temperature distributions along the cross-section of the beam by 2D FE models, followed by a 3D mechanical analysis that considered the thermal data influence provided in the previous step. Therefore, in the Abaqus software the thermo-mechanical response of the specimens (allowed after the uncoupled analysis) was simulated by a two-step analysis. In the first step, the desired loading was applied under displacement control to the FE model at ambient temperature and it was fixed afterwards, inducing an initial deflection (as occurred in the reference experimental model [32]). The loading step was explicitly defined in the Abaqus. In the second step, the temperature distributions in relation to time (previously determined in the thermal analysis) were imposed to the loaded beams for a duration like that observed in the reference fire resistance tests [32]. In the case of validation of models at ambient temperature, only a structural analysis was performed with the purpose of simulating the behavior of unstrengthened and CFRP-strengthened RC beams up to failure.

5 RESULTS AND DISCUSSIONS

5.1 Mechanical response at ambient temperature

Numerical simulations on an unstrengthened and EBR-CFRP-strengthened beam (referred as RC_AT and CFRP_AT, respectively) were performed to assess the ability and accuracy of the 3D FE models described above in predicting the mechanical response of these beams. The results of experimental tests reported in a relevant parallel study by Carlos et al. [32] were used for FE model's validation. Figure 9 shows a comparison of the load vs. vertical mid-span displacement curves for the unstrengthened and CFRP-strengthened RC beams obtained from the experimental tests (Exp.) [32] and FEA (Num.).

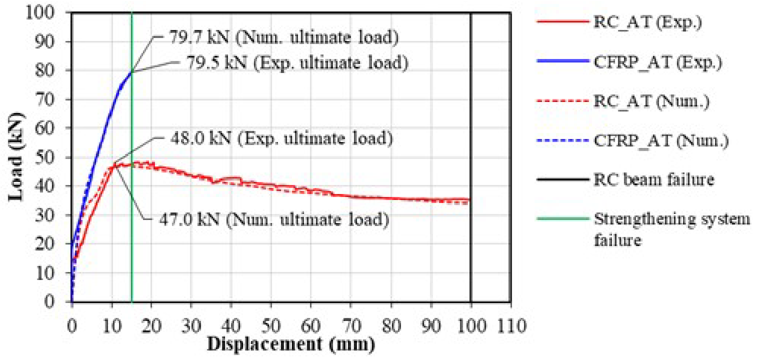

Figure 9. Experimental (Exp.) [32] and predicted (Num.) load vs. mid-span displacement curves for the unstrengthened and CFRP-strengthened RC beams at ambient temperature.

Figure 9 reveals that all predicted results generally fit closely with the experimental curves for both specimens, especially for obtained peak loads (ultimate load). The ultimate predicted load of the RC_AT and CFRP_AT beams was 47.0 kN and 79.7 kN, respectively. The ultimate load experimentally obtained for the unstrengthened and CFRP-strengthened beams was 48.0 and 79.5, respectively. These results were very similar to those obtained numerically for both specimens. Therefore, the values of the predicted-to-experimental loading capacity ratios (P_{NUM} / P_{EXP}) for the RC_AT and CFRP_AT beams correspond to 0.98 and 1.00, respectively. Finally, an excellent agreement and accuracy between the experimental and numerical results was noticed, ensuring a strong validity of the developed FE model in predicting the mechanical response of both RC beams strengthened with EBR-CFRP laminate and unstrengthened RC beam at ambient temperature.

5.2 Mechanical response under fire conditions

The experimental results from fire resistance tests carried out by Carlos et al. [32] on the CFRP-strengthened beam EC-35 were used to validate the mechanical response of the 3D numerical model under fire conditions (see Figure 10b). Furthermore, for the mechanical validation of the FE model that represents the RC beam subjected to fire (see Figure 10a), the experimental data from the unstrengthened specimen (RC) [32] were assigned for comparative purposes. The comparison of the displacement-temperature curves of the simply supported RC beam and CFRP-strengthened beams from the experimental tests and FEA are presented in Figure 10a and Figure 10b, respectively. The results are presented in terms of ultimate failure for the RC beam and strengthening debonding for CFRP-strengthened beam. The mechanical results developed after the strengthening system debonding (ultimate failure of the strengthened beam) is not presented, since it is not relevant to bond analysis.

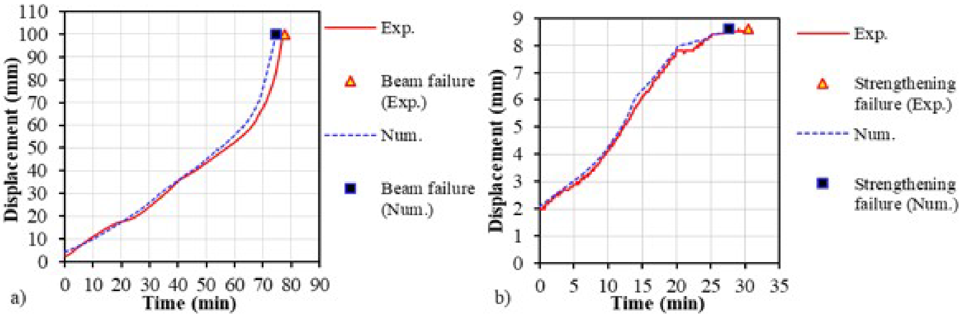

Figure 10. Experimental (Exp.) [32] and predicted (Num.) displacement-temperature curves for the a) unstrengthened and b) CFRP-strengthened RC beams, in terms of ultimate beam failure and strengthening system debonding, respectively

Similar tendencies with an equivalent slope were obtained from the FEA in comparison with the experimental results [32] for both RC beam and CFRP-strengthening system (specimens RC and EC-35, respectively). The experimental curves presented a slightly higher stiffness than the numerical ones, indicating that the respective predicted data is on the safe side. A good agreement between the FEA and experimental [32] analysis in terms of critical fire resistance time for the RC beam (FR_{time}) was obtained, as shown in Table 1. The failure instant of this beam was experimentally achieved at 78.2 min of fire exposure, while for the numerical model a fit close and slight conservative time of 74.5 min was noticed. In the case of strengthened beam, a satisfactory convergence of results between the models was also obtained. The fire resistance time at the CFRP debonding instant ($FR_{time,CFRP}$) for the strengthened beam was quite similar for both experimental and numerical models, corresponding to 30.5 and 27.7 min, respectively, as shown in Table 1. Therefore, the results showed that the differences between experimental and numerical fire resistance times were less than 5% and 10%, respectively for unstrengthened RC beam and CFRP-strengthening system (Table 1). In addition, a relationship between the FR_{time} or $FR_{time,CFRP}$ at different displacements obtained by the numerical and experimental analysis for both types of beams was also presented in Table 1.

Table 1. Experimental (Exp.) [32] and numerical (Num.) fire resistance time at different displacements of unstrengthened beam and CFRP-strengthening system.

unstrengthened RC beam	**FR_{time} at 50 mm displacement (min)**		**FR_{time} at 75 mm displacement (min)**		**FR_{time} at beam failure instant (min)**		**FR_{time} ratio at failure instant of the beam**
	Exp. [32]	**Num.**	**Exp. [32]**	**Num.**	**Exp. [32]**	**Num.**	
	57.0	54.9	72.3	69.5	78.2	74.5	0.95
CFRP-strengthening system	**$FR_{time,CFRP}$ at 5 mm displacement (min)**		**$FR_{time,CFRP}$ at 8 mm displacement (min)**		**$FR_{time,CFRP}$ at CFRP failure instant (min)**		**$FR_{time,CFRP}$ ratio at failure instant of the CFRP system**
	Exp. [32]	Num.	Exp. [32]	Num.	Exp. [32]	Num.	
	12.2	11.8	23.0	20.1	30.5	27.7	0.91

Notwithstanding the slight differences above mentioned, the models presented general good agreement and accuracy between the experimental and numerical results of the RC beam and CFRP-strengthening system. All these results indicate that the estimated data is generally on the safe side but not too conservative, though. The satisfactory agreement and accuracy between the experimental and numerical results confirm the validity of the developed FE models and attest to their ability to simulate the mechanical response of simply supported RC and CFRP-strengthened beams under fire conditions.

5.3 Failure mode analysis

The numerical failure modes of the tested specimens under four-point bending configuration and at ambient temperature conditions obtained from the FEA are illustrated in Figure 11a to Figure 15a and they are compared to the experimental failure modes as shown in Figure 11b and Figure 15b.

The bending failure mode characterized by excessive deflections and flexural cracks at mid-span, without lateral displacements, due to tensile rupture and excessive elongation of the bottom rebars that were responsible for the collapse of the experimentally tested unstrengthened RC beams were also clearly identified in the predicted failure modes. Figure 11 shows a view of (a) numerical and (b) experimental deformed shape of the RC beam at the failure instant. Moreover, the cracking along the cross-section of the beam was also registered and a good similarity was achieved between the numerical and experimental models, as shown in Figure 12a and Figure 12b, respectively.

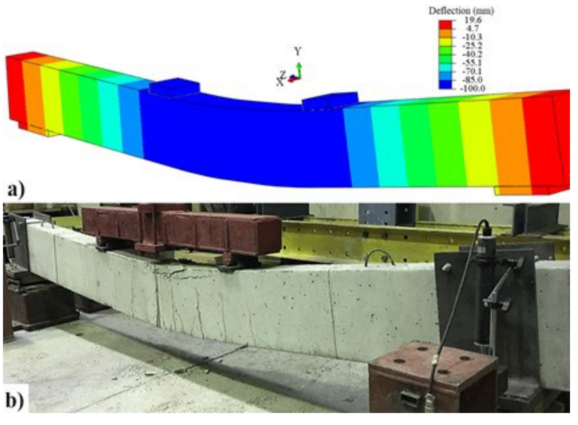

Figure 11. (a) Numerical (b) and experimental deformed shape for the unstrengthened RC beam (specimen RC_AT) at the failure instant: view 1

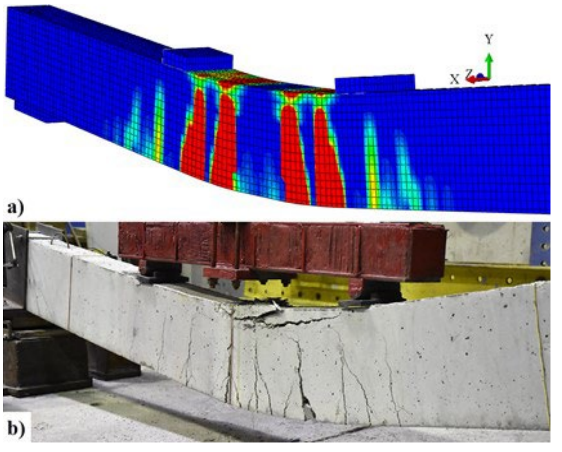

Figure 12. (a) Numerical (b) and experimental cracking along the cross-section of the unstrengthened RC beam (specimen RC_AT) at the failure instant: perspective view

Regarding the failure modes of the CFRP-strengthened beam at ambient temperature, that was characterized by the debonding of strengthening system in the CFRP-concrete bond region, a good agreement between the numerical and the experimental failure modes was noticed, as shown in Figure 13a and Figure 13b, respectively.

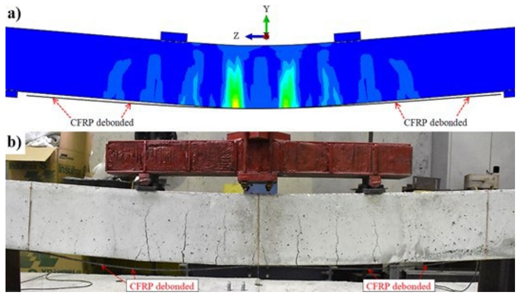

Figure 13. (a) Numerical (b) and experimental failure modes for the CFRP-strengthened RC beam (specimen CFRP_AT) after the laminate collapse

The debonding of the CFRP system was assumed when a displacement peak was observed in the strengthened beam while an excessive and abrupt unloading of the system occurred.

Furthermore, the deformed shape of the strengthened beam at the CFRP failure instant was precisely predicted by the FE model, as noticed in Figure 14. Similarities regarding the cracking along the cross-section of the strengthened specimen were also numerically estimated successfully as shown in Figure 15.

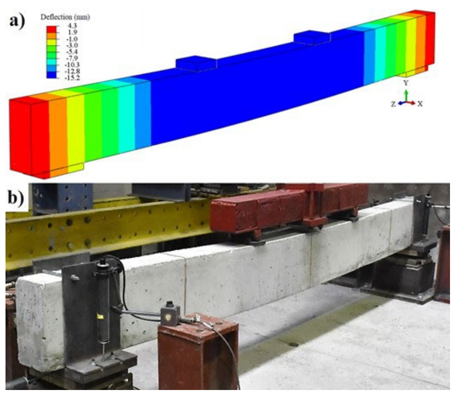

Figure 14. (a) Numerical (b) and experimental deformed shape for the CFRP-strengthened beam (specimen CFRP_AT)) at the CFRP failure instant

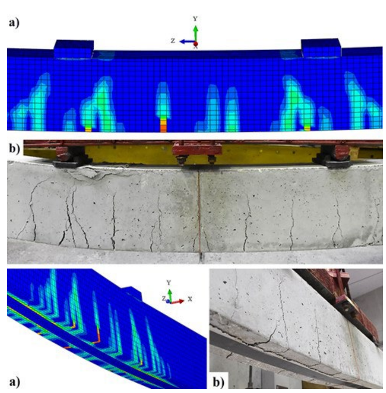

Figure 15. (a) Numerical (b) and experimental cracking along the cross-section of the CFRP-strengthened beam at the CFRP failure instant

The results above confirm that the finite element models predicted the failure modes of unstrengthened and CFRP-strengthened beams with good precision, attesting their consistency to simulate the mechanical response of this type of structures at ambient temperature. Furthermore, the mechanical validation of the model at ambient temperature allowed the FE model to assess mechanical analyses under fire conditions (Section 5.2).

5.4 Heat transfer analysis

The suitability of 2D thermal models developed using the heat transfer option available in Abaqus was assessed in this section. The purpose of this numerical approach was to determine the appropriate modelling parameters especially the input thermal boundary conditions and material thermal properties, so that standard fire resistances tests of unstrengthened and CFRP-strengthened RC beams can be simulated. It should be also noted that a uniform temperature along the entire longitudinal length of the beam was intended for the validation study, in contrast to the recorded at the mid-spam cross-section of beams tested in Laboratory [32]. Moreover, to calibrate the FE model for fire simulation of CFRP-strengthened RC beams, the furnace fire curve data registered from the fire resistance tests [32] were used. Note that the emissivity, the heat transfers, and the thermal contact conductance coefficients were constant with temperature evolution. The radiative heat flux was calculated as 0.49 using an emissivity of 0.7 for fire and 0.7 for the concrete surface. The Stefan-Boltzmann constant was defined as $5.67x10^{-8}$ W/m^{2}K^4. Figure 16b, Figure 16c and Figure 16d shows respectively the comparison between experimental (Exp.) [32] and predicted (Num.) temperatures as a function of fire exposure time for the different thermocouples at mid-span of the CFRP-strengthened beams fire-protected. The CFRP-strengthened RC beams were protected by three types of fire protection systems composed by VP, EC, and OP cement-based mortars. Moreover, a 35 mm thickness on the fire protection system was adopted. The specimens were referred to as EC-35, OP-35 and VP-35 for VP, EC and OP mortars fire protected with 35 mm thick, respectively.

The temperature vs. fire exposure time evolution for the different thermocouples of the unstrengthened and unprotected RC beam (referred as RC) is shown in Figure 16a. It is worthwhile mentioning that the temperature evolution in the CFRP-strengthened RC beams was presented in Figure 16bcd only until the collapse instant of the respective fire protection material reported in the experimental data [32], since the results after that time are negligible for the purpose of this numerical study. Regarding the RC beam, the results were plotted in Figure 16a until the collapse of the beam.

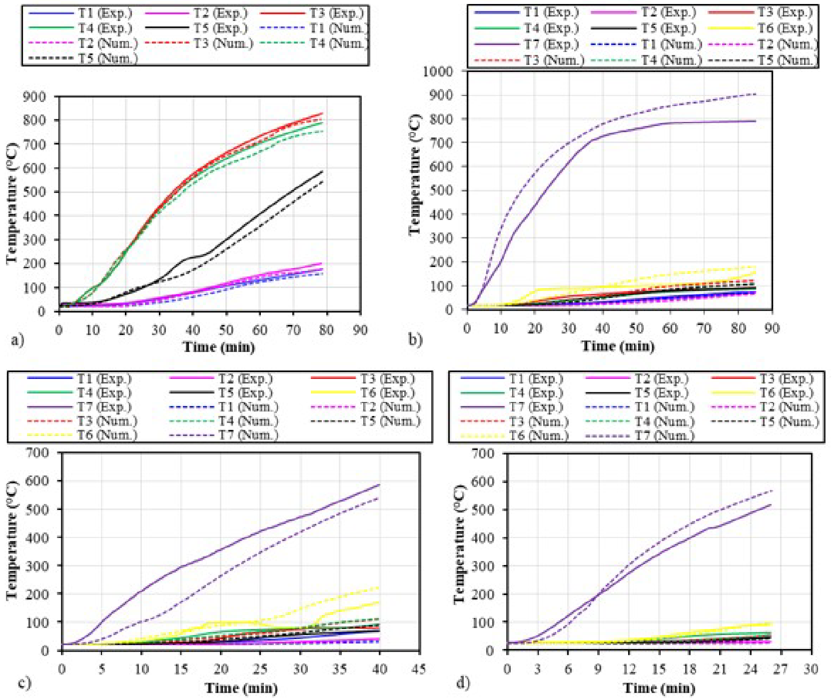

Figure 16. Experimental (Exp.) [32] and predicted (Num.) temperatures vs. fire exposure time curves at different points of the mid-span cross-section for the beams: a) RC, b) VP-35, c) OP-35 and d) EC-35

Overall, all FE models provided a good agreement with the experimental results in terms of temperature evolution, as noticed in the Figure 16a-d. With exception of thermocouples T6 and T7 (positioned on the bottom surfaces of the laminate and the fire protection material, respectively) for the strengthened beams protected by OP and VP mortar, all other temperature distributions at different points of the cross-section were accurately predicted by the models. Small deviations between Exp. and Num. temperatures in T6 and T7 of the VP-35 and OP-35 beams were observed, as depicted in Figure 16b and Figure 16c, respectively. Despite that, the FE models were still able to simulate the thermal behavior tendency with a relative consistency in the above-mentioned thermocouples. Concerning the strengthened EC-35 and RC beams (Figure 16a and Figure 16d, respectively), the numerical results by the heat transfer analysis presented an excellent convergence with the experimental measurements for all thermocouples. To sum up, the tools of Abaqus program for the application of thermal actions allowed simulating the phenomenon of heat transfer between hot air and composite structural elements with satisfactory results. Despite the above-mentioned deviations, all models overall provided a good estimate between the experimental and numerical results, confirming the ability of the FE models to accurately simulate the thermal response of unstrengthened and EBR-CFRP-strengthened RC beams subjected to fire, even when using complex and different fire protection materials.

6 CONCLUSIONS

The structural behavior of RC beams flexurally strengthened with CFRP laminates bonded according to the EBR technique and unstrengthened RC beams was numerically investigated in this paper. Finite element models capable of simulating the mechanical and thermal response of simply supported unstrengthened and CFRP-strengthened RC beams both under ambient and fire conditions were developed and described in the current research. Numerical simulations using the finite element software Abaqus has been performed. The results obtained from the numerical study presented herein allow to draw the following conclusions:

- The thermal response of the fire-protected CFRP-strengthened RC beams subjected to high temperatures was accurately predicted by the FE models, similarly to the heat transfer analysis of the unprotected and unstrengthened RC beam. Moreover, the modelling of the surrounding building slab allowed it to represent the thermal interactions and influence between the elements as faithful as possible, providing a better predicting of the experimental results and, consequently, more realistic.
- Concerning the prediction of the mechanical response at ambient temperature, the 3D models presented a satisfactory accuracy for both unstrengthened and CFRP-strengthened RC beams, especially for estimating the ultimate load capacity.
- The developed finite element models also estimate with precision the mechanical response of unstrengthened and CFRP-strengthened RC beams simultaneously subjected to a flexural load and high temperatures. An accuracy of about 91% and 95% was respectively achieved by the numerical models that represent the RC and CFRP-strengthened RC beams, compared to the experimental results in terms of failure instant.
- The failure modes of the beams and the aspects after the test were also estimated with accuracy by the finite element models. The predictions of deformed shape, failure and cracking aspects, stresses on the steel reinforcements and, especially, the CFRP failure aspect in the strengthened beams, were very similar to the ones observed in the reference experimental models tested.
- Finally, the presented results confirmed the validity of the developed FE models and strongly guaranteed an accurate prediction of the mechanical response of both strengthened and unstrengthened RC beams at ambient and high temperatures. Furthermore, it is still possible to stated that this developed FE models can be used as a valuable auxiliary tool for the design of fire protection systems for CFRP-strengthened RC structural members or in parametric studies outside the bounds of experimental field, as well as provide safe and economical structural solutions for these type of structures in fire situations.

ACKNOWLEDGEMENTS

The authors gratefully acknowledge CNPq (National Council of Scientific and Technological Development, Brazil) for the post-doctorate scholarship and financial support provided.

REFERENCES

[1] M. Mohammadi, M. Barghian, D. Mostofinejad, and A. Rafieyan, "Alkali and temperature long-term effect on the bond strength of fiber reinforced polymer-to-concrete interface," *J. Compos. Mater.*, vol. 52, no. 15, pp. 2103–2114, Jun. 2018, http://dx.doi.org/10.1177/0021998317740201.

[2] N. Dodds, A. G. Gibson, D. Dewhurst, and J. M. Davies, "Fire behaviour of composite laminates," *Compos., Part A Appl. Sci. Manuf.*, vol. 31, no. 7, pp. 689–702, Jul. 2000, http://dx.doi.org/10.1016/S1359-835X(00)00015-4.

[3] A. P. Mouritz and A. G. Gibson, *Fire Properties of Polymer Composite Materials.* Dordrecht: Springer, 2006.

[4] A. J. B. Tadeu and F. J. F. G. Branco, "Shear tests of steel plates epoxy-bonded to concrete under temperature," *J. Mater. Civ. Eng.*, vol. 12, no. 1, pp. 74–80, Feb. 2000, http://dx.doi.org/10.1061/(ASCE)0899-1561(2000)12:1(74).

[5] American Concrete Institute, *Guide for the Design and Construction of Externally Bonded FRP Systems for Strengthening Existing Structures*, ACI 440.2R-17, 2017.

[6] R. A. Hawileh, M. Naser, W. Zaidan, and H. A. Rasheed, "Modeling of insulated CFRP-strengthened reinforced concrete T-beam exposed to fire," *Eng. Struct.*, vol. 31, no. 12, pp. 3072–3079, 2009, http://dx.doi.org/10.1016/j.engstruct.2009.08.008.

[7] A. Ahmed and V. K. R. Kodur, "Effect of bond degradation on fire resistance of FRP-strengthened reinforced concrete beams," *Compos., Part B Eng.*, vol. 42, no. 2, pp. 226–237, Mar. 2011, http://dx.doi.org/10.1016/j.compositesb.2010.11.004.

[8] J. G. Dai, W. Y. Gao, and J. G. Teng, "Finite element modeling of insulated FRP-strengthened RC beams exposed to fire," *J. Compos. Constr.*, vol. 19, no. 2, 2010, http://dx.doi.org/10.1061/(ASCE)CC.1943-5614.0000509.

[9] J. P. Firmo, M. R. T. Arruda, and J. R. Correia, "Numerical simulation of the fire behaviour of thermally insulated reinforced concrete beams strengthened with EBR-CFRP strips," *Compos. Struct.*, vol. 126, pp. 360–370, 2015, http://dx.doi.org/10.1016/j.compstruct.2015.02.084.

[10] J. P. Firmo, M. R. T. Arruda, J. R. Correia, and I. C. Rosa, "Three-dimensional finite element modelling of the fire behaviour of insulated RC beams strengthened with EBR and NSM CFRP strips," *Compos. Struct.*, vol. 183, no. 1, pp. 124–136, 2018, http://dx.doi.org/10.1016/j.compstruct.2017.01.082.

[11] B. Williams, V. Kodur, M. F. Green, and L. Bisby, "Fire endurance of fiber-reinforced polymer strengthened concrete T-Beams," *ACI Struct. J.*, vol. 105, no. 1, pp. 60–67, 2008.

[12] ANSYS, *Finite Element Computer Code, Version 11.* Canonsburg, USA: ANSYS Inc., 2007.

[13] American Society for Testing and Materials, *Standard Test Methods for Fire Tests of Building Construction and Materials*, ASTM E119, 2002.

[14] V. K. R. Kodur and A. Ahmed, "Numerical model for tracing the response of FRP-strengthened RC beams exposed to fire," *J. Compos. Constr.*, vol. 14, no. 6, pp. 730–742, Dec. 2010, http://dx.doi.org/10.1061/(ASCE)CC.1943-5614.0000129.

[15] H. Blontrock, L. Taerwe, and P. Vandevelde, “Fire tests on concrete beams strengthened with fibre composite laminates,” in *Proceedings of the third Ph.D. symposium,* K. Bergmeister, Eds. Vienna*,* 2000, pp. 151–161. Accessed: Mar. 29, 2022. [Online]. Available: http://hdl.handle.net/1854/LU-130382

[16] A. Ahmed and V. Kodur, "The experimental behavior of FRP-strengthened RC beams subjected to design fire exposure," *Eng. Struct.*, vol. 33, no. 7, pp. 2201–2211, 2011, http://dx.doi.org/10.1016/j.engstruct.2011.03.010.

[17] H. V. S. GangaRao, N. Taly, and P. V. Vijay, *Reinforced concrete design with FRP composites.* Boca Raton, USA: CRC Press, 2007.

[18] ABAQUS, *Analisys Standard User’s Manual, Version 6.8.* Rhode Island, USA: Dassault Systèmes, 2008.

[19] International Federation for Structural Concrete, *The FIB Model Code for Concrete Structures: Model Code.* Lausanne: FIB, 1990.

[20] J. P. Firmo and J. R. Correia, "Fire behaviour of thermally insulated RC beams strengthened with EBR-CFRP strips: Experimental study," *Compos. Struct.*, vol. 122, pp. 144–154, Apr. 2015, http://dx.doi.org/10.1016/j.compstruct.2014.11.063.

[21] J. P. Firmo, M. R. T. Arruda, and J. R. Correia, "Contribution to the understanding of the mechanical behaviour of CFRP-strengthened RC beams subjected to fire: Experimental and numerical assessment," *Compos., Part B Eng.*, vol. 66, pp. 15–24, 2014, http://dx.doi.org/10.1016/j.compositesb.2014.04.007.

[22] ABAQUS, *Analisys Standard User’s Manual, Version 6.11*. Rhode Island, USA: Dassault systèmes, 2011.

[23] E. Klamer, “Influence of temperature on concrete beams strengthened in flexure with CFRP,” Ph.D. dissertation, Eindhoven University of Technology, Eindhoven, 2009. [Online]. Available: http://dx.doi.org/10.6100/IR656177.

[24] J. Dai, W. Y. Gao, and J. G. Teng, "Bond-slip model for FRP laminates externally bonded to concrete at elevated temperature," *J. Compos. Constr.*, vol. 17, no. 2, pp. 217–228, Apr. 2013, http://dx.doi.org/10.1061/(ASCE)CC.1943-5614.0000337.

[25] J. Dai, T. Ueda, and Y. Sato, "Development of the nonlinear bond stress–slip model of fiber reinforced plastics sheet–concrete interfaces with a simple method," *J. Compos. Constr.*, vol. 9, no. 1, pp. 52–62, 2005, http://dx.doi.org/10.1061/(ASCE)1090-0268(2005)9:1(52).

[26] W. Y. Gao, J. G. Teng, and J. Dai, "Effect of temperature variation on the full-range behavior of FRP-to-concrete bonded joints," *J. Compos. Constr.*, vol. 16, no. 6, pp. 671–683, Dec. 2012, http://dx.doi.org/10.1061/(ASCE)CC.1943-5614.0000296.

[27] J. C. P. H. Gamage, R. Al-Mahaidi, and M. B. Wong, "Bond characteristics of CFRP plated concrete members under elevated temperatures," *Compos. Struct.*, vol. 75, no. 1–4, pp. 199–205, 2006, http://dx.doi.org/10.1016/j.compstruct.2006.04.068.

[28] M. R. T. Arruda, J. P. Firmo, J. R. Correia, and C. Tiago, "Numerical Modelling of the bond between concrete and CFRP laminates at elevaded temperatures," *Eng. Struct.*, vol. 110, pp. 233–243, Mar. 2016, http://dx.doi.org/10.1016/j.engstruct.2015.11.036.

[29] European Committee for Standardization, *Eurocode 2: Design of Concrete Structures - Part 1-1 : General Rules and Rules for Buildings*, EN 1992-1-1, 2004.

[30] European Committee for Standardization, *Eurocode 2: Design of Concrete Structures - Part 1-2: General rules - Structural Fire Design*, EN 1992-1-2, 2004.

[31] International Federation for Structural Concrete, *FIB Bulletin 14: Externally Bonded FRP Reinforcement for RC Structures.* Lausanne: FIB, 2001.

[32] T. B. Carlos, J. P. C. Rodrigues, R. C. A. Lima, and D. Dhima, "Experimental analysis on flexural behaviour of RC beams strengthened with CFRP laminates and under fire conditions," *Composite Structures*, vol. 189, no. 2017, pp. 516–528, 2018, http://dx.doi.org/10.1016/j.compstruct.2018.01.094.

[33] T. B. Carlos and J. P. C. Rodrigues, "Experimental bond behaviour of a CFRP strengthening system for concrete elements at elevated temperatures," *Constr. Build. Mater.*, vol. 193, pp. 395–404, Dec. 2018, http://dx.doi.org/10.1016/j.conbuildmat.2018.10.184.

[34] ABAQUS CAE, *Abaqus Analisys User's Guide, Version 6.14*. Rhode Island, USA: Dassault systèmes, 2015.

[35] L. Laím, J. Paulo, C. Rodrigues, and L. Simões, "Experimental and numerical analysis on the structural behaviour of cold-formed steel beams," Ph.D. dissertation, University of Coimbra, Coimbra, Portugal, 2013.

[36] ABAQUS CAE, *Abaqus Theory Guide, Version 6.14*. Rhode Island, USA: Dassault Systèmes, 2015.

[37] Association Française de Normalisation, *Eurocode 2: Calcul des Structures en Béton - Partie 1-2: Règles Générales - Calcul du Comportement au Feu*, NF EN 1992-1-2 (Annexe Nationale), 2007.

[38] European Committee for Standardization, *Eurocode 4: Design of Composite Steel and Concrete Structures - Part 1-2: General Rules - Structural Fire Design,* EN 1994-1-2, 2005.

[39] C. A. Griffis, R. A. Masumura, and C. I. Chang, "Thermal response of graphite epoxy composite subjected to rapid heating," *J. Compos. Mater.*, vol. 15, no. 5, pp. 427–442, Sep. 1981., http://dx.doi.org/10.1177/002199838101500503.

[40] J. P. Firmo, J. R. Correia, and P. França, "Fire behaviour of reinforced concrete beams strengthened with CFRP laminates: Protection systems with insulation of the anchorage zones," *Compos., Part B Eng.*, vol. 43, no. 3, pp. 1545–1556, 2012, http://dx.doi.org/10.1016/j.compositesb.2011.09.002.

[41] Simpson Strong-Tie Company, "S&P C-Laminate: Carbon fiber polymer plates for structural reinforcement: product technical specifications." S&P. http://www.sp-reinforcement.eu/sites/default/files/field_product_col_doc_file/suiss_c-laminates_e_ver022018_co-branded_0.pdf (accessed Mar. 29, 2018).

[42] Perlita y Vermiculita, *Biofire: Product Technical Specifications*. Barcelona: Perlita y Vermiculita, 2008.

[43] Secil Martingança, *RHP Manual Interior: Product Technical Specifications*. Leiria: Secil Martingança, 2013.

[44] S. A. Argex, *ARGEX® 0-2: Product Technical Information*. Aveiro: Argex, 2008.

[45] K. Wang, B. Young, and S. T. Smith, "Mechanical properties of pultruded carbon fibre-reinforced polymer (CFRP) plates at elevated temperatures," *Eng. Struct.*, vol. 33, no. 7, pp. 2154–2161, 2011, http://dx.doi.org/10.1016/j.engstruct.2011.03.006.

[46] L. A. Bisby, *Fire Behaviour of FRP Reinforced or Confined Concrete.* Kingston: Queen's University, 2003.

[47] Ø. T. Moltubakk, "Nonlinear analysis of fibre reinforced concrete beams: Influence of fibre orientation and density," M.S. thesis. Norwegian University of Science and Technology, Trondheim, 2014. [Online]. Available: https://docplayer.net/62653923-Nonlinear-analysis-of-fibre-reinforced-concrete-beams.html

[48] J. A. O. Barros, *Modelos de Fendilhação para o Betão*. Porto: Universidade do Minho, 1996.

Author contributions: TBC: conceptualization, development, methodology, modeling, data analysis, writing, bibliographic research; VPS: conceptualization, methodological analysis, supervision, drafting and formal analysis.

Editors: Samir Maghous, Guilherme Aris Parsekian.

IBRACON Structures and Materials Journal
Revista IBRACON de Estruturas e Materiais
ISSN 1983-4195 ismj.org

ORIGINAL ARTICLE

Multi-objective optimization of outriggers in high-rise buildings subjected to wind loads

Otimização multiobjetivo de outriggers em edifícios altos submetidos a cargas de vento

Felipe Morrone Barbat Parfitt[a]
Inácio Benvegnu Morsch[a]
Herbert Martins Gomes[a,b]

[a]Universidade Federal do Rio Grande do Sul – UFRGS, Graduate Program in Civil Engineering, Porto Alegre, RS, Brasil
[b]Universidade Federal do Rio Grande do Sul – UFRGS, Graduate Program in Mechanical Engineering, Porto Alegre, RS, Brasil

Received 30 May 2022
Accepted 25 July 2022

Abstract: This paper aims to investigate a methodology for determining the optimum floor positioning of outriggers (ORs) and belt-trusses (BTs) over tall buildings height. The primary goal is to reduce the maximum lateral drift (MLD) and the core base moment (CBM), individually and concurrently. Furthermore, the influence of these elements on other criteria such as maximum acceleration and natural frequencies are analyzed. Throughout the work, the behavior of the structure is verified when the stiffness ratio of the main elements used in the bracing system (core, perimeter columns, OR, and BT) are varied. Therefore, a three-dimensional model of a tall building under lateral wind load is analyzed, using the finite element method with ANSYS software. The mono and multi-objective optimizations were solved, respectively, by the Nelder-Mead method with the author's modifications to deal with integer variables and by a utility function. Based on the results, it is concluded that by specifically adding ORs/ORs-BTs in tall buildings the influence on the reduction of the mentioned objectives is extremely relevant, reaching up to 68% for the CBM and 71% for the MLD, depending on the amounts employed.

Keywords: outrigger, tall buildings, structural optimization, integer programming, lateral load.

Resumo: Neste trabalho os autores têm por objetivo investigar uma metodologia para determinação dos pavimentos ótimos ao implementar outriggers (ORs) e belt-trusses (BTs) ao longo da altura de um edifício alto para reduzir tanto o máximo deslocamento lateral (MDL), quanto o momento na base do núcleo (MBN), de forma separada e concorrente. Além disso, analisa-se a influência destes elementos sobre outros critérios como a máxima aceleração e as frequências naturais. Ao longo do trabalho verifica-se o comportamento da estrutura quando a relação de rigidez dos principais elementos do sistema de contraventamento (núcleo, colunas perimetrais, OR e BT) são variados. Sendo assim, um modelo tridimensional de um edifício alto sob ação lateral de vento é analisado, empregando o método dos elementos finitos usando o software ANSYS. As otimizações mono e multiobjetivo foram resolvidas, respectivamente, pelo método Nelder-Mead modificado para variáveis inteiras pelos autores e pela função de utilidade. Diante dos resultados, conclui-se que ao introduzir de forma específica os ORs/ORs-BTs em edifícios altos a influência na redução dos objetivos mencionados é extremamente relevante, podendo chegar a 68% para o MBN e 71% para o MDL, dependendo de suas quantidades empregadas.

Palavras-chave: outrigger, edifícios altos, otimização estrutural, programação inteira, carga lateral.

How to cite: F. M. B. Parfitt, I. B. Morsch, and H. M. Gomes, "Multi-objective optimization of outriggers in high-rise buildings subjected to wind loads," *Rev. IBRACON Estrut. Mater.*, vol. 16, no. 2, e16203, 2023, https://doi.org/10.1590/S1983-41952023000200003

Corresponding author: Felipe Morrone Barbat Parfitt. E-mail: felipeparfitt@gmail.com
Financial support: The authors would like to acknowledge the financial support of CAPES and CNPq.
Conflict of interest: Nothing to declare.
Data Availability: The data that support the findings of this study are available from the corresponding author, Parfitt, F.M., upon reasonable request.

1 INTRODUCTION

Tall building constructions have been a global phenomenon in recent decades, as explained by their growing number, mainly, in the Asian continent [1]. Scarcity of land in large urban centers combined with the growing pace of urbanization in this period are factors that contributed to this fact. Hence, vertical solutions are considered the main and recognized options for accommodating the high population density, with a low impact on the environment [2].

However, skyscrapers are an engineering challenge, especially concerning structural design because they are highly sensitive to natural loads, such as lateral loads from wind and earthquakes. The intensity of these loads is directly proportional to the structure's height, i.e., as the buildings grow towards the sky, the control of structural behavior becomes more and more challenging. In this sense, the stability and stiffness criteria become more relevant than the strength criteria and thus control the design. Therefore, choosing the best structural system is a determining factor for reducing the amount of materials, as well as satisfying safety conditions related to normative criteria or even to fit architectural aesthetics [3].

Conventional structural systems - such as framed, composed of rigid cores, or a combination of both - are no longer an economical solution to mitigate lateral loads when the number of floors increases. Among the many possible solutions, the outrigger system is one of the most widely employed options in the last decades, due to its compatibility with contemporary high-rise buildings. The most important one is associated with the architectural issue due to the flexibility of the facades. Furthermore, for being employed on specific floors, they are already opportune to be combined with other projects (mechanical floors).

The outrigger system is composed of an internal system (rigid core) and an external system (perimeter columns), connected by a rigid element, known as outrigger (OR). Eventually, belts are added around the perimeter to provide connectivity between the external columns, known in the literature as belt-truss (BT). ORs and BTs, in principle, can be placed on any floor over the building's height. However, there are specific floors where their contribution is greater to ensure the control of certain objectives. The maximum lateral drift (MLD), as well as the core base moment (CBM), are both important objectives to be reduced to achieve an optimized design. Therefore, knowing their optimum floors is extremely relevant for designers.

This paper aims to investigate a methodology for determining the optimum floors when employing outriggers ORs/ORs-BTs over the tall building height to reduce both the maximum lateral drift and the core base moment, individually and concurrently. Furthermore, the influence of these elements on other criteria such as maximum acceleration and natural frequencies are analyzed.

1.1 Bibliographical review

Some of the ORs analysis and design literature includes an optimization task, in which objective functions are always linked to important design code criteria or economic aspects. Maximum lateral displacement, inter-story drift, core base bending moment, differential axial shortening between the core and the outer columns, and OR system volume are some of the factors that have been sought to be reduced, as shown in [4]–[8].

In a 400 m high reinforced concrete building, Park et al. [4] evaluated the optimal design of OR's structural system elements, namely the core, external columns, and the OR itself. They also included the best number of ORs and their placement. The solutions were found using a genetic algorithm, to minimize the volume of the structural system, which includes displacement constraints at the top of the building and bending stress at the core's base.

Moon [1] examined the OR system's structural performance in tall buildings with complex shapes, i.e., twisted, tilted, and tapered. For each shape, the impact of both the angle of variation of the façade and the total height of the structure was verified. The analysis was performed using commercial software (SAP 2000). They demonstrate that: lateral stiffness decreases with increasing torsion rate, and as height increases, the stiffness reduction is more pronounced; it is more appropriate to employ columns away from the perimeter, reducing the thickness of the building, rather than twisted columns; in the case where the shape of the structure is tilted, when the tilted angle increases in a range from 0 to 13°, lateral wind strength increases and, on the other hand, lateral displacements due to gravity loads are intensified; structures that shorten along the height are more efficient under wind loads when the shortening angle or height increases.

Chen and Zhang [5] investigated a multi-objective genetic algorithm for ORs based on a reduced mathematical formulation. For 1 to 10 ORs, Pareto optimum solutions were found, i.e., many optimal positions based on the number of ORs. The top displacement and core base bending moment were the analysis' objectives.

Kim et al. [6] conducted a study using three tall structures, each having 80 floors (280 m) and vertical elements of various shapes, to determine the ideal position of the truss OR over the height that minimizes the maximum lateral drift.

In the optimization process, the gradient-descent approach was used, along with linear and quadratic interpolations. In addition, they verified the impact of the wind loading shape and the ideal position of the OR on the minimal bending moment at the core's base.

Kim et al. [7], considering the same model as [6], carried out a multi-objective optimization study trying to simultaneously reduce the maximum lateral displacement and the differential axial shortening, where the floors were the design variables. In order to solve the single and multi-objective optimization problem, they used the steepest descent method and the weighted-sum method, respectively. For the tall building model where the vertical elements stiffness changes over the height, they obtained the following results: the best floor to position one OR to minimize the maximum lateral displacement is at 47th, and for two, 27th and 57th floors; to minimize the differential axial shortening the best floor ORs are for one, 60th and, for two, 47th and 68th floor.

Xing et al. [8] conducted a study based on a seismic spectral analysis of a simplified model using buckling restrained braces (BRBs) OR system which is considered a damped OR. The authors themselves proposed and validated the model using the ANSYS program. To reach their goal, i.e., to obtain the optimal position of the damped OR and the corresponding structure top displacement, several structural parameters were varied. In this way, they concluded that: by increasing the OR stiffness, both objectives gradually decrease; by increasing the stiffness of the core of the columns, the OR's optimal position rises and the displacement decreases; when increasing the distance between the core and the columns, the OR's optimal position increases, and the displacement, at first, decreases quickly and, then, increases slowly; when increasing the BRB's yielding force, both objectives initially decrease and, then, remain unchanged. When comparing the results with those of the conventional OR, under the same conditions, they obtained both optimal location and the top displacement smaller.

The papers [5] and [6] perform a similar study attempting to obtain the set of optimal floors to minimize the same objective function (maximum lateral displacement). For [5] when there is only one OR its position should be 0.45 of the total height of the building (H), while for [6] this position should be $0.59H$. When there are 2 ORs throughout the height [5] defines that their positions should be $0.31H$ and $0.68H$, while for [6] they should be $0.35H$ and $0.71H$. Although both studies use a high-rise building with almost the same height and apply a similar wind profile, other different aspects can justify the disagreement between the results. Such differences are the simplified model analysis and the stiffness of the OR system elements, which interfere with the OR optimum positioning.

2 THEORETICAL BASIS

2.1 Tall building model

The tall building model used in the analyses of this study is based on Kim et al. [6], which is illustrated in Figure 1. It has 80 floors with a distance between floors of $3.5\ m$, which results in a total height of $280\ m$. Its floor plan format is regular and contains dimensions of $43 \times 43\ m$. The distribution of the elements of the building structure is a central core, columns distributed around the perimeter, and beams and slabs between the inner and outer portions.

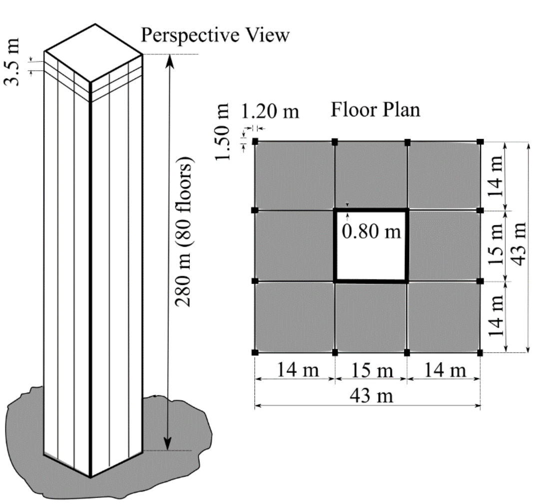

Figure 1. Tall building model

2.2 Dynamic effects of wind turbulence

The lateral wind loading was applied according to the methodology described in NBR 6123 [9]. For the development of the wind flow to excite a structure, the design speed $\overline{\mathrm{V}}_{\mathrm{P}}$, is calculated over a time period equal to 10 minutes, and it is given by

$$\overline{\mathrm{V}}_{\mathrm{P}} = 0.69\mathrm{V}_0\mathrm{S}_1\mathrm{S}_3, \tag{1}$$

where V_0 is the basic wind speed and the parameters S_1 and S_3 are the topographic and probabilistic factors, respectively. Since for each vibration mode j the total wind force at coordinate i can be calculated by the superposition of the mean force $\overline{\mathrm{X}}_{\mathrm{i}}$, and turbulence force $\hat{X}_i$, it results in

$$\tilde{X}_i = \overline{\mathrm{X}}_{\mathrm{i}} + \hat{X}_i. \tag{2}$$

The mean and turbulence forces are, respectively, given by

$$\overline{\mathrm{X}}_{\mathrm{i}} = \bar{\mathrm{q}}_0\mathrm{b}^2\mathrm{C}_{\mathrm{ai}}\mathrm{A}_{\mathrm{i}}\left(\frac{\mathrm{z}_{\mathrm{i}}}{\mathrm{z}_{\mathrm{r}}}\right)^{2\mathrm{p}} \tag{3}$$

and

$$\hat{X}_i = F_H\Psi_i x_i \tag{4}$$

where $\bar{\mathrm{q}}_0 = 0.613\overline{\mathrm{V}}_{\mathrm{P}}^2$ is the reference height pressure, b and p are correction parameters according to the roughness category, z_r is the reference height (10 meters), F_H is the force referring to the turbulence plot -, C_{ai}, A_i, z_i, $\Psi_i = m_0/m_i$ and x_i are, respectively, the drag coefficient, wind force area, height, and ratio between the discrete mass (m_i) and the arbitrary reference mass (m_0), and the vibration mode - each one at the i coordinate.
The force referring to the turbulence component can be calculated according to

$$\mathrm{F}_{\mathrm{H}} = \bar{\mathrm{q}}_0\mathrm{b}^2\mathrm{A}_0\frac{\sum_{\mathrm{i}=1}^{\mathrm{n}}\hat{\mathrm{a}}_{\mathrm{i}}\mathrm{x}_{\mathrm{i}}}{\sum_{\mathrm{i}=1}^{\mathrm{n}}\Psi_i x_i^2}\hat{\imath} \tag{5}$$

where A_0 is the reference area, $\hat{\imath}$ is the dynamic amplification coefficient, n is the number of degrees of freedom considered in the discretization, and the parameter $\hat{\mathrm{a}}_{\mathrm{i}}$ is given by

$$\hat{\mathrm{a}}_{\mathrm{i}} = C_{ai}\frac{A_i}{A_0}\left(\frac{z_i}{z_r}\right)^p. \tag{6}$$

When more than one vibration mode is used in the solution, the result of the r modes can be combined by

$$\widehat{\mathrm{Q}} = \left[\sum_{\mathrm{j}=1}^{\mathrm{r}}\widehat{\mathrm{Q}}_{\mathrm{j}}^2\right]^{1/2} \tag{7}$$

where $\widehat{\mathrm{Q}}_{\mathrm{j}}$ can be any static or geometric variable (force, stress, strain).
The acceleration in mode j, induced by the turbulence forces, can be estimated by the following equation

$$a_j = 4\pi^2 f_j^2\hat{u}_j \tag{8}$$

where f_j and $\hat{u}_j$ are, respectively, the frequency and the displacement due to the turbulence part at level z, both in mode j.

Since the tall building model is localized in the center of Porto Alegre (Category V), the basic speed is equal to $V_0 = 46\ m/s$. For being considered in a flat area and high occupancy factor, both correction factors, S_1 and S_3, were considered to be unitary. Considering that the model fits in category V, from Table 20 of NBR 6123 [9] the exponent $p = 0.31$ and the parameter $q = 0.5$ are assumed. From the model dimensions, the values $l_1/l_2 = 1$ and $H/l_1 = 6.5$ are obtained, which for a high turbulence wind provides a drag coefficient $Ca = 1.1$.

Taking into account that at each iteration of the optimization, the structure changes its configuration, the vibration mode x_i and the fundamental frequency f_j are constantly updated in APDL (Ansys Parametric Design Language) code. The vibration mode employed is calculated by the average of the displacements per floor, obtained through modal analysis. Furthermore, since the dynamic amplification coefficient ξ depends on the model's frequency, equations generated from Figure 18 of NBR 6123 [9] are generated by a degree-2 polynomial trend line when the damping ratio is equal to 2%.

2.3 Structural optimization

2.3.1 Problem formulation

The objective functions to be optimized in this work are: (a) the maximum lateral drift and (b) the core base bending moment. For such purposes, a set number of floors with ORs/ORs-BTs are introduced to each optimization, and then the result is obtained individually for each objective. The amount of design variables depends on the number of ORs that will be placed throughout the height of the tall building. The formulation of the first and second problems is given by:

Minimize:

$$f_1(\boldsymbol{x}) = \Delta_{top} \tag{9}$$

and

$$f_2(\boldsymbol{x}) = M_{core} \tag{10}$$

subject to

$$\boldsymbol{x} \in \mathbb{Z}^n,$$

$$x_{i,min} \le x_i \le x_{i,max}\ i = 1, \dots, n, \tag{11}$$

$$|x_i - x_{i+1}| \le h_{or}\ i = 1, \dots, n-1;$$

where x are the design variables (floors with ORs/ORs-BTs), Δ_{top} is the normalized MLD, h_{or} is the OR height, $\mathbb{Z}^n$ is the set of integer variables, n is the number of design variables, $x_{i,min}$ and $x_{i,max}$ represent the lower and upper limits, respectively, and M_{core} is the normalized CBM, which is calculated by the resultant of the sum of bending moments around the axes forming the plane of the core's base.

The minimization of each of these problems is performed by using the Nelder-Mead algorithm modified in this paper for integer variables, which is presented in subsection 2.3.2. The constraints are handled through the penalty method. It is noteworthy that the bounds are defined according to the number of floors and also by the number of floors that a single OR/OR-BT comprises. In this case, as presented in Chapter 3, the lateral bounds are from the 4th to the 80th floor, and to avoid overlapping of ORs/ORs-BTs, the height difference between ORs/ORs-BTs must always be larger than 4 floors.

2.3.2 Nelder-Mead algorithm modified for integer design variables

Introduced by Nelder and Mead [10], Nelder-Mead is a numerical method that aims to minimize or maximize mathematical functions. According to Arora [11], it is a direct search method that does not use gradients in its solution procedure and can solve optimization problems with nonlinear functions. Its approach is based on the comparison of the values of the objective function of $n+1$ vertices of a geometric configuration known as Simplex, where n is the number of design variables. In the case of a function with only two variables, the problem is considered two-dimensional, with the Simplex being a triangle formed by three vertices.

At each iteration of the Nelder-Mead algorithm, one seeks to improve the worst vertex of the Simplex through some operations - reflection, expansion, or contraction. The worst result function perturbation is always in the mean direction of the remaining points. If none of the operations results in an acceptable point, all vertices are approached in the direction of the best particle [12]. However, it was verified through benchmark functions that this procedure is very susceptible to being stuck in local minima and, therefore, the global minimum is not obtained. For this reason, algorithm modifications will be proposed here to avoid undesirable situations in the optimization process.

The modified Nelder-Mead algorithm shown below follows the same step-by-step as described by the original version, as referred at [12]. However, in this case, it will be introduced: (a) randomizations in each of the operations mentioned above; (b) a new operation when all particles are identical. Only particles with integer variables are aimed at dealing with integer programming problems. Always at the beginning of each iteration, all particles are arranged in ascending order so that

$$f(\boldsymbol{x_1}) \leq f(\boldsymbol{x_2}) \leq \cdots \leq f(\boldsymbol{x_{n+1}}) \tag{12}$$

and therefore, the centroid can be calculated according to:

$$\overline{\boldsymbol{x}} = \frac{1}{n}\sum_{i=1}^{n} x_i. \tag{13}$$

The first operation to be carried out is always the reflection and, depending on its result, other operations are performed. The mathematical expression that defines all operations mentioned is modified and takes the following form:

$$\boldsymbol{x} = round[\overline{\boldsymbol{x}}(1 + c_n \boldsymbol{R_{normal}}) + coef(\overline{\boldsymbol{x}} - \boldsymbol{x_{n+1}})], \tag{14}$$

where $round$ represents the rounding operation to the nearest integer number, $c_n = 0.1$ is the reducing coefficient, $\boldsymbol{R_{normal}}$ is a vector containing samples of a standard normal distribution (with mean 0 and standard deviation 1) and $coef$ varies according to the type of operation: in reflection $coef = 1$; in expansion $coef = 2$; in the external contraction $coef = 0.5$; in the internal contraction $coef = -0.5$.
If none of the operations improves the result of the objective function, retraction is applied, in which all particles approach the one with the best result. This can be calculated according to

$$\boldsymbol{x_i} = round\left[\boldsymbol{x_1} + \left(\frac{1}{2} + c_n \boldsymbol{R_{normal}}\right)(\boldsymbol{x_1} - \boldsymbol{x_i})\right] \; (i = 2, 3, \ldots, n+1). \tag{15}$$

Furthermore, before applying the contraction, it is always checked if all vertices are identical, i.e.,($\boldsymbol{x_1} = \boldsymbol{x_2} = \cdots = \boldsymbol{x_{n+1}}$). In case this condition is true, $\boldsymbol{x_1}$ is stored and then a random dilation is applied to $\boldsymbol{x_1}$, given by the expression:

$$\boldsymbol{x_i} = round(\boldsymbol{x_1} + c_d \boldsymbol{R_{normal}}) \; (i = 2, 3, \ldots, n+1) \tag{16}$$

where $c_d = 0.5$ is the dilatation coefficient.

As previously stated, all the coefficients used in the operations are the same as those proposed by Nelder and Mead [10] in the original method. The ones included in the new programming, c_n and c_d, were chosen according to the best results obtained through tests on eight benchmark functions for integer variables.

Python programming language was used to connect the optimization code and the structural analysis performed by ANSYS APDL. Every time the objective function is evaluated, a computational cost of a few seconds is spent. Thus, to speed up this process, a database was created. This procedure allows that a value already in the database does not need to be evaluated twice in the optimization process, since the analysis for those design variables has already been performed previously. This was only possible due to the integer feature of the problem being optimized.

Finally, to validate the modified Nelder-Mead algorithm, the authors tested 8 benchmark functions for integer variables presented in [13]. In fact, the modifications developed in this paper were fundamental for the success of the algorithm, considering that seven out of the eight benchmark functions reached global minima in each campaign of independent runs, which would not have happened without those modifications. More details about the algorithm can be found in [14].

2.3.3 Utility function method

As previously defined, both objective functions, f_1 and f_2, participate in multi-objective optimization. The utility function method was chosen in this study because it allows the use of the previously designed mono-objective optimization algorithm for integer variables. This method assigns weights to each objective function, where the sum of the weights must be one. Therefore, it is possible to prioritize one of the objectives by increasing its weight in the optimization. Although according to Arora [11], this approach is the most common among the multi-objective optimization methods, as seen later, it converges to a defined number of optimum values as the weight step decreases.

So, the problem containing both objectives can be now defined as:

Minimize:

$$f_1(\boldsymbol{x}) = \omega f_1(x) + (1-\omega) f_2(x), \tag{17}$$

subject to

$$\boldsymbol{x} \in \mathbb{Z}^n,$$

$$x_{i,min} \leq x_i \leq x_{i,max} \; i = 1, \dots, n, \tag{18}$$
$$|x_i - x_{i+1}| \leq h_{or} \; i = 1, \dots, n-1;$$

where ω is the weight factor that ranges from 0 to 1.

According to Equation 17, it is possible to prove that by combining both objective functions, the problem becomes simpler and can be solved by a single-objective optimization algorithm. On the other hand, the convergence of this method depends on the weight discretization ($\Delta\omega$) assumed, which defines a distance between the set of weights in the search of several prioritizing assumptions for each objective. This will result in the so-called "Pareto Frontier", a set of all possible solutions, assuming diverse prioritizing weights. The number of weight factors employed in the equation can be calculated by $Np = 1/\Delta\omega + 1$, then the distribution will be $\Omega = \{0, \Delta\omega, 2\Delta\omega, \dots, 1\}$. It is worth noting at the moment when ω is equal to 0 or 1, it means that one of the objectives does not have any influence on the optimization. In this case, the problem behaves as a single-objective optimization, with its results being the extremes of the Pareto solutions. Since the frontier is made up of a fixed number, there will be a discretization limit for ω, which will imply not finding new solutions.

3 TALL BUILDING MODEL AND ANALYSIS

3.1 Tall building numerical model

The representation of a part of the numerical model in finite elements is shown in Figure 2. Note that to improve the visualization, the elements are represented with thickness, being: a concrete core with elasticity modulus $E = 3.96 \times 10^4\ MPa$, Poisson's ratio $\nu = 0.2$ and thickness of $t = 0.8\ m$; ORs and BTs of steel trusses with elasticity modulus $E = 210 \times 10^3\ MPa$, Poisson's ratio $\nu = 0.3$ and area ratio between the chord and web bars of $A_{web} = A_{chord}\sqrt{2}$, being their values defined later through a study; perimeter columns with elasticity modulus $E = 3.96 \times 10^4\ MPa$, Poisson's ratio $\nu = 0.2$ and cross section of $1.5 \times 1.2\ m$ (see Figure 2b for the spatial orientations); and steel beams with elasticity modulus $E = 210 \times 10^3\ MPa$, Poisson's ratio $\nu = 0.3$ and area of $A_v = 0.08\ m^2$. The total model mass is $7.71 \times 10^7\ kg$. An important aspect that can be observed from Figure 2a is that the OR and the BT cross 3 floors, and their positions correspond to the highest floor they are located on.

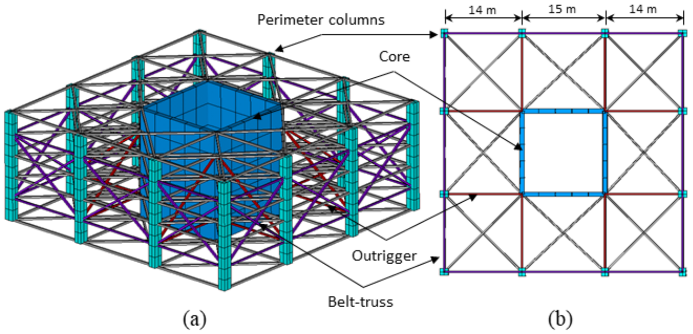

Figure 2. Numerical model in (a) perspective (b) plan.

The shell finite element (SHELL181) was used in the core, the truss element (LINK180) in the ORs, BTs, and floor beams, and the beam element (BEAM188) in the columns. According to a mesh study, the columns were discretized by two elements on each floor with a quadratic function and the core by twenty elements per floor. The building's base is fully fixed. It is worth noting that the truss elements placed on the floor simulate the rigid diaphragm promoted by the floor slabs, the same principle applied in other works, such as Lee and Tovar [15].

3.2 Tall building without outrigger/belt-truss analysis

3.2.1 Modal analysis

Modal analysis was used to determine the vibration modes and natural frequencies of the structure. Using the subspace iteration method, the first ten vibration modes or those that fit in a range of 0 to 2 Hz were extracted. Figure 3 illustrates the first six vibration modes of the structure.

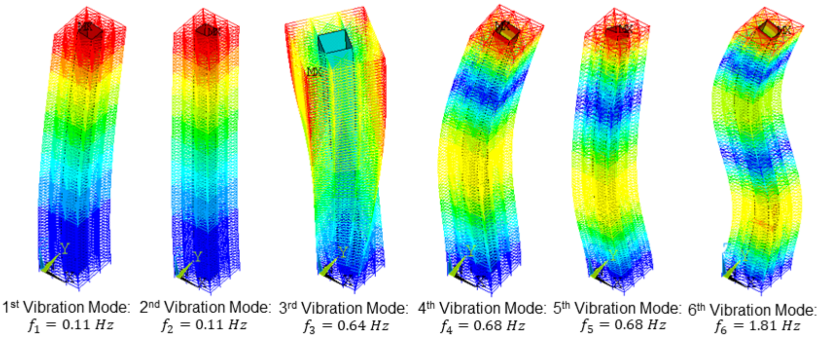

Figure 3. 1st to 6th tall building vibration mode without ORs-BTs.

As can be seen in Figure 3, for the first two modes, bending predominates, with the same frequency's values and perpendicular directions to each other, since the structure is symmetric. The 3rd mode is torsional, and the 4th presents bending characteristics with one node. Finally, the 5th mode is similar to the 4th, and the 6th mode, showing a bending mode with two nodes.

3.2.2 Static analysis

To obtain the maximum lateral drift and the core base bending moment of the structure when subjected to lateral wind loading applied according to section 2.2, a static analysis is performed. Additionally, maximum acceleration is determined.

3.2.2.1 Maximum lateral drift

The largest lateral drift is at the top and has a value of $0.7318\ m$. A result that compared to the overall building deflection limit of $H/500 = 0.56\ m$, is 30.7% higher and therefore must be controlled by a structural solution.

3.2.2.2 Core base bending moment

The core base bending moment, as already mentioned, is calculated by the resultant from the binaries and moments around the x and y axes, according to

$$M_{core} = \sqrt{\left(\sum M_x + \sum F_z d_y\right)^2 + \left(\sum M_y + \sum F_z d_x\right)^2} \tag{19}$$

where M_x and M_y are, respectively, the bending moments around x and y, d_x and d_y are, respectively, the variable distances in x and y from the point force F_z to its axis.

Based on the direction of all reactions at the core of the tall building model without ORs/BTs it is possible to calculate the resulting bending moment about the central point of the core, which is equal to $M_{core} = 2.3944 \times 10^3\ MN.m$, with more than 99% corresponding to the portion of the sum of $F_z dx$.

3.2.2.3 Maximum acceleration

The maximum acceleration, according to Equation 8, occurs on the floor with the largest lateral drift. Therefore, knowing that the maximum lateral drift for the first vibration mode due to the floating fraction is $0.2244\ m$, it follows that $a = 0.114\ m/s^2$. If compared to the human comfort criterion, such as the one for residential buildings of 1.5 to 2% of the gravity acceleration, which corresponds to $0.147\ m/s^2$, the acceleration obtained is lower and is also within this limit.

3.4 Tall building with outrigger/belt-truss analysis

In this section, the analyses of the numerical model using the outrigger system are presented. To evaluate the performance of the structure, the results of the objectives/criteria are verified as a couple of interest parameters are modified. In all cases, it is desired to minimize maximum lateral drift and the core base moment – and, concerning this criterion, to minimize maximum acceleration and maximize the natural frequencies.

3.4.1 Outrigger stiffness analysis

By increasing the OR stiffness, it is expected that the analyzed objectives follow an inversely proportional path, except in the case of the fundamental frequency, which must continue increasing. To verify the influence of the cross-sectional area of the OR in relation to the objectives, the horizontal member areas of the OR varied from 0 to $0.14\ m^2$. Figure 4 shows the best results found for each value of the adopted area, i.e., the OR is in the different optimum floors for each case of area.

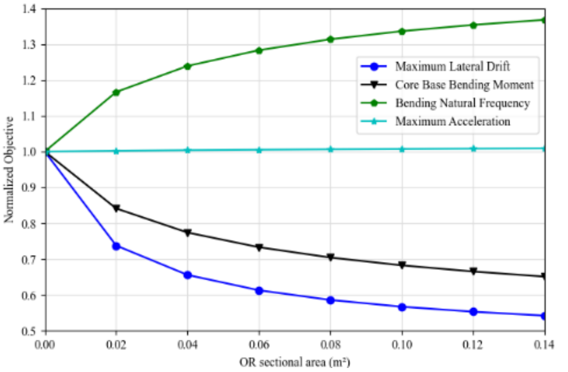

Figure 4. Influence of the OR area regarding the objectives/criteria analyzed.

Figure 4 shows that: (a) the influence of OR stiffness on the variation rate of the analyzed objectives, in absolute values, follows a decreasing trajectory; (b) there is a qualitatively constant relationship between the MLD and CBM; (c) after exceeding the OR cross-sectional area of $0.06\ m^2$ the objectives have a little change, with the largest variation of approximately 3%, which is possibly not justifiable in economic ways; and (d) the maximum acceleration shows an indifferent behavior with the OR area. Moreover, using an area of $0.06\ m^2$ for the horizontal bars of the OR, significant reductions of 39% for the MLD and 27% for the CBM are reached. For the bending natural frequency, there is an increase of 28%.

On the other hand, from Figure 5 it is worth emphasizing that the optimum OR positioning (given by the floor with the lowest value of the objective function) over the height of the model is variable according to the objective analyzed and also by the OR cross-section area. In general, the maximum lateral drift, the natural frequency, and the maximum acceleration have optimum floors close to each other, being located in the upper half of the building. Regarding the core base moment, the optimum floors are always located in the lower half. It is worth mentioning that by increasing the OR stiffness, the optimum floor decreases its location in all cases, i.e., it gets closer to the base. Another important point observed is the increasing OR capacity to redistribute the forces from the core to the perimeter columns as the OR stiffness increases, a fact verified by the CBM's curvature increment.

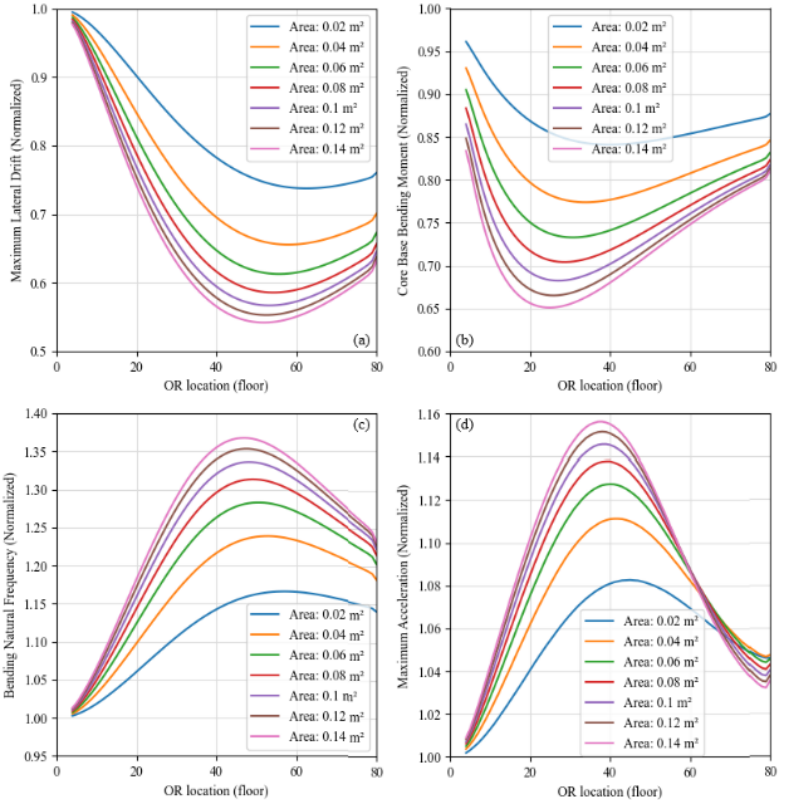

Figure 5. Influence of the OR area in relation to the optimum floor to (a) MLD (b) CBM (c) Bending nat. freq. (d) Max. accel.

3.4.2 Belt-truss stiffness analysis

An option to improve even more the tall building stiffness performance and also to take advantage of the available space of the mechanical floors is to implement a belt-truss around the perimeter of the floor where the OR is located. By joining the outer columns through the BT, not only those columns that are directly connected to the OR are going to support the intense lateral loads, but also all the others. Therefore, by adding this element to the lateral system, all the objectives analyzed should be modified, in order to improve the behavior of the building. The torsional stiffness of the building, which had not been checked in the previous analysis with ORs only, in principle, should also be benefited.

As in the case of subsection 3.4.1, at first the study is carried out by modifying the BT cross-section area from 0 to $0.14\ m^2$, to evaluate its influence on the structural behavior. The cross-section area ratio between the web and the chords is $\sqrt{2}$. Figure 6 shows the optimum results obtained for each value of BT area and analyzed objective function when there is only one OR.

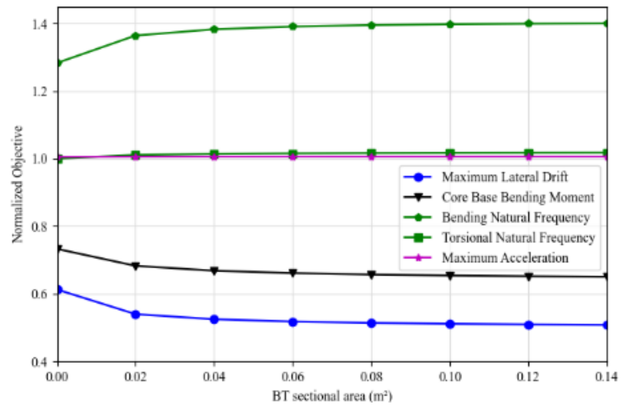

Figure 6. Influence of the BT area in relation to the objectives/criteria analyzed.

Figure 6 illustrates that by adding the BT together with OR, the analyzed objectives are smoothly improved, except for the torsional natural frequency and maximum acceleration, which remain almost constant. However, it is noticeable that the interference of the BT stiffness is almost imperceptible regarding any of the objectives. Another important point that should be highlighted is the null contribution of the BT on torsional stiffness, a parameter according to the studies that should be improved. Such a fact can be justified by the floor system used to simulate the rigid diaphragm of the slabs since the connection between the core and the outer columns through the truss elements does not allow the relative torsional strain between the outer and inner portions. Since the increase in the area of the BT does not reasonably affect the building's behavior, and for convenience, the same area ratio of the ORs is used, $A_{BT} = 0.06\ m^2$. Figure 7 illustrates for each objective the influence of the OR-BT concerning its location over height as well as the BT stiffness.

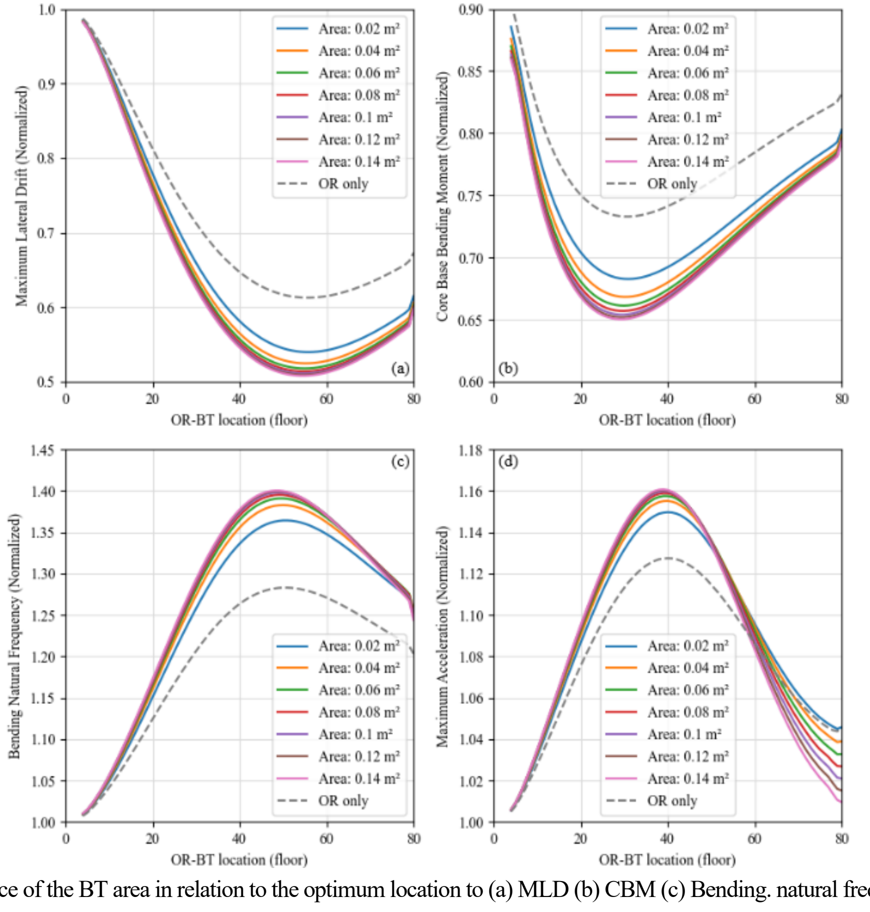

Figure 7. Influence of the BT area in relation to the optimum location to (a) MLD (b) CBM (c) Bending. natural freq. (d) Max. accel.

Observing Figure 7 it can be concluded that the BT area does not significantly affect the OR-BT optimum positioning. In fact, what happens is just a translation of the curve when there is only the OR.

3.4.3 Columns-core stiffness ratio analysis

Taking into consideration that the core and the outer columns are both components of the OR-BT lateral system and work together, possibly the stiffness ratio between these elements should affect the analyzed objectives. Thereby, to verify if this relationship is actually relevant to the study, the building response was calculated for several stiffness ratios (R_{rig}), whereas the equation for a single case is given by

$$R_{rig} = \frac{I_{cols}}{I_{core}} \quad (20)$$

where I_{core} and I_{cols} are, respectively, the area moment of inertia about the geometric center of the model for the core and the set of columns. Another important point is that in order to not prioritize any of the two elements, the standard model is used as a reference, i.e., the core or columns area value is modified in such a way that the sum of the areas remains always the same, regardless of the stiffness ratio. Additionally, to simplify the understanding, the stiffness ratio has been normalized from the standard model, which has $R_{rig} = 7.84$. Figure 8 shows the optimum results obtained for each stiffness ratio value and analyzed objective function when there is only one OR-BT.

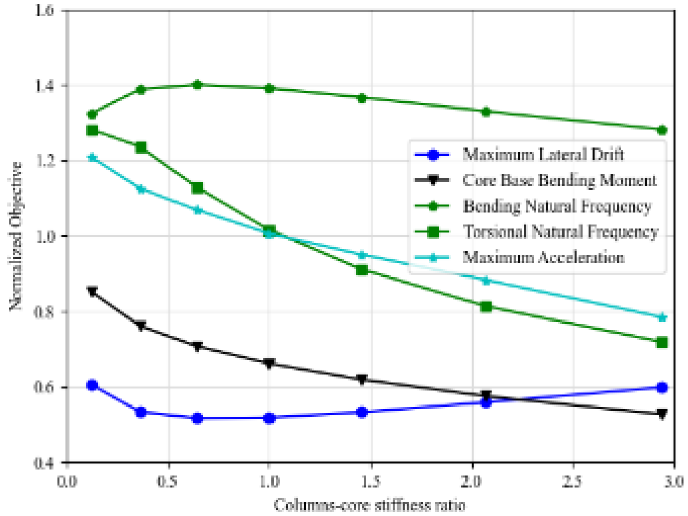

Figure 8. Influence of the column-core stiffness ratio on the objectives/criteria analyzed.

Based on Figure 8 it is proven that the stiffness ratio directly interferes with the model response. The maximum lateral drift and natural bending frequency curves show the existence of an optimum stiffness ratio ($0.36 < R_{rig} < 1$), which has a larger core area and, consequently, a smaller column area, when compared to the reference model. Regarding the core base moment, the lowest value is reached by increasing R_{rig}, so the outer columns are able to carry more axial load. The same behavior happens for the maximum acceleration. Meanwhile, for the torsional natural frequency the opposite happens, since the higher its value, the better the building response will be.

Figure 9 illustrates for each objective the influence of the OR-BT positioning as well as the stiffness ratio between the columns and the core.

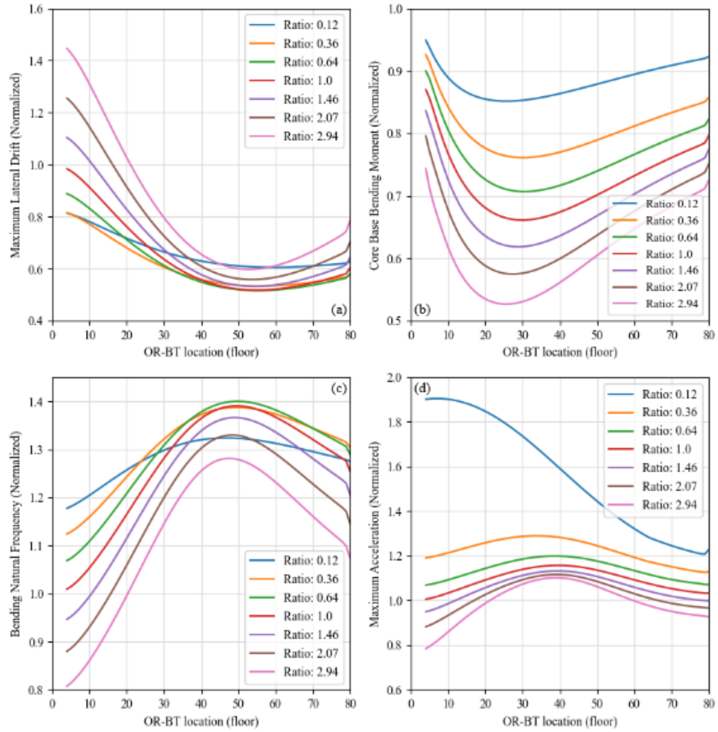

Figure 9. Influence of the column-core stiffness ratio on the optimum location to (a) MLD (b) CBM (c) Bending nat. freq. (d) Max. accel.

Analyzing Figure 9, at first, it is visible that when the stiffness ratio is low, the OR-BT becomes less effective, due to the small variation of the objectives by changing the position of the OR-BT. A different behavior occurs for the maximum acceleration when $R_{rig} = 0.12$, that from the 4th to 80th floors its value always decreases. As already highlighted for the MLD and natural bending frequency there is an optimum ratio that, for the cases studied, is $R_{rig} = 0.64$. Regarding the optimum floors, it should be noted the different stiffness ratio does not significantly change them, except for the CBM case.

4 STRUCTURAL OPTIMIZATION

4.1 Code validation

To prove that the modified Nelder-Mead algorithm is actually obtaining a global minimum, exhaustive searches were performed for three different cases: (i) a single-objective optimization considering 2 ORs being the objective of the CDM, as shown in Figure 10; (ii) a multi-objective optimization considering 2 ORs, as shown in Figure 11 (a); and (iii) a multi-objective optimization considering 2 ORs-BTs, as shown in Figure 11 (b). It is noteworthy that the graph in Figure 10 is symmetrical because there is no difference in the value of the objective function when the OR positioning is changed within the design variable. The presence of a continuous diagonal is merely illustrative, as both ORs cannot be present in the same position.

In the first exhaustive search illustrated in Figure 10, it is observed that the ideal floors to position the ORs are the 39th and 62nd. with a normalized result of 0.515, i.e., exactly the same values observed in the single-objective optimization. To obtain the optimal value when there are two ORs, regardless of the objective, using the modified Nelder-Mead it takes, on average, 30 iterations, against 2701 calls to the ANSYS program from the exhaustive search. This demonstrates, once again, the efficiency of the algorithm. Concerning the other two exhaustive searches carried out, it is concluded that both Pareto frontiers obtained through multi-objective optimization are correctly positioned, having, therefore, only non-dominated Pareto points to the others.

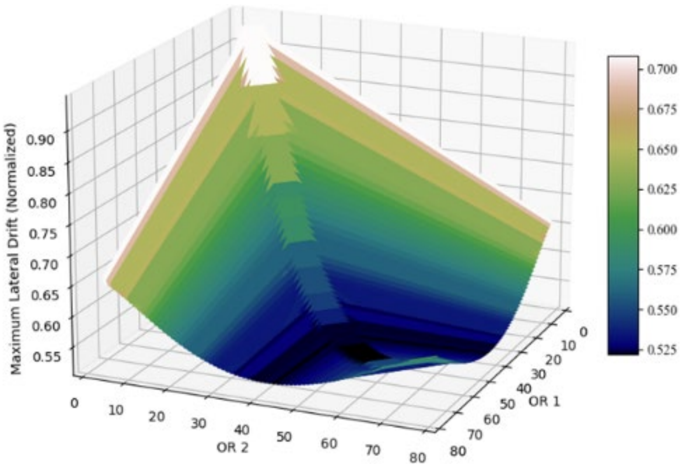

Figure 10. Exhaustive search with 2 ORs (Objective: MLD)

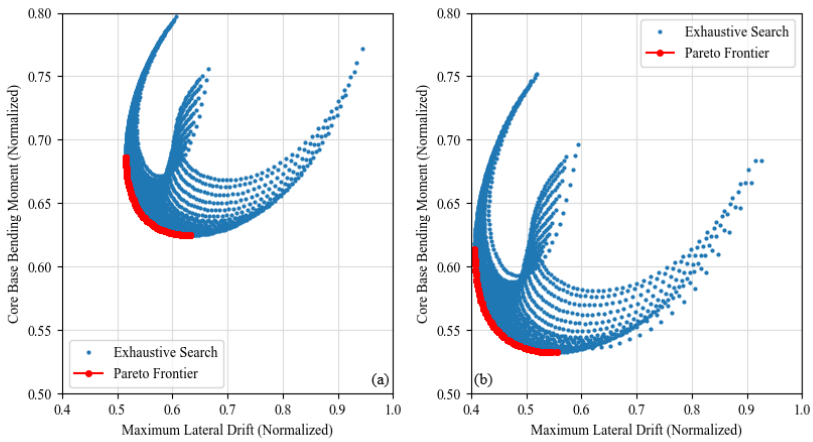

Figure 11. Exhaustive search with (a) 2 ORs (b) 2 ORs-BTs (compared to Pareto frontier obtained in this paper)

4.2 Single-objective optimization

The result of the single-objective optimization is obtained using the modified Nelder-Mead algorithm, adopting the same parameters as in subsection 2.3.2.

4.2.1 Maximum lateral drift

Table 1 and Table 2 show the optimum positions obtained to minimize the maximum lateral drift of the model presented in Chapter 3, with their respective results normalized by the values without ORs-BTs, which are: MLD of $0.732\ m$, CBM of $2.3944 \times 10^3\ MN.m$, fundamental frequency of $0.11\ Hz$, and maximum acceleration of $0.114\ m/s^2$. Table 1 presents the results of the optimizations with ORs only, and Table 2 with ORs and BTs.

Table 1. Results of single-objective optimizations for MLD (OR)

Number of ORs	Optimum floor	MLD	CBM	Fundamental freq.	Max. accel.
		norm.	norm.	norm.	norm.
1	56	0.613	0.775	1.279	1.098
2	39, 62	0.515	0.686	1.398	1.13
3	32, 47, 66	0.469	0.637	1.468	1.144
4	27, 39, 52, 68	0.442	0.601	1.515	1.155
5	24, 34, 44, 56, 70	0.423	0.576	1.549	1.161
6	21, 29, 38, 47, 58, 71	0.41	0.551	1.576	1.168

Table 2. Results of single-objective optimizations for MLD (OR-BT)

Number of ORs-BTs	Optimum floor	MLD norm.	CBM norm.	Fundamental freq. norm.	Max. accel. norm.
1	55	0.518	0.717	1.384	1.115
2	39, 62	0.406	0.614	1.562	1.157
3	31, 47, 66	0.355	0.553	1.672	1.185
4	30, 34, 51, 68	0.325	0.512	1.754	1.213
5	26, 30, 47, 51, 69	0.304	0.481	1.815	1.234
6	23, 27, 40, 44, 57, 70	0.289	0.454	1.862	1.249

It can be noted that by introducing at least one OR, the reduction of lateral displacement is already extremely relevant, with approximately a 39% reduction. As the amount of ORs increases, the displacement reduction also continues to increase, but at a lower rate. When there are six ORs, the reduction percentage reaches 59%. By adding the BT to the model, the reduction in MLD is even greater, from 48% for one OR-BT and 71% for six OR-BT. For the two models analyzed, with OR and OR-BT, both the CBM and the bending natural frequency improve with the addition of new ORs/ORs-BT and, on the other hand, the maximum acceleration worsens. It is also noteworthy that the optimum floors for both cases are very similar.

4.2.2 Core base bending moment

Table 3 and Table 4 show the optimum positions obtained to minimize the core base moment in the tall building model, with their respective results normalized by the values without ORs-BTs. Like the MLD, the CBM follows the same pattern, always improving the objectives by increasing the amount of ORs or ORs-BTs, except in the case of maximum acceleration. In the first case, with ORs only, by introducing one OR in the model, a 27% reduction in CBM is achieved, and when there are six ORs, 55%. In the second case, with ORs and BTs, with one OR-BT the reduction is 34% and with six ORs-BTs, 68%.

Table 3. Results of single-objective optimizations for CBM (OR)

Number of ORs	Optimum floor	CBM norm.	MLD norm.	Fundamental freq. norm.	Max. accel. norm.
1	31	0.733	0.704	1.214	1.116
2	17, 34	0.625	0.632	1.287	1.143
3	11, 19, 35	0.56	0.603	1.32	1.154
4	8, 12, 20, 36	0.514	0.585	1.341	1.161
5	4, 9, 13, 21, 36	0.476	0.577	1.352	1.164
6	4, 8, 12, 26, 23, 37	0.446	0.554	1.382	1.174

Table 4. Results of single-objective optimizations for CBM (OR-BT)

Number of ORs-BTs	Optimum floor	CBM norm.	MLD norm.	Fundamental freq. norm.	Max. accel. norm.
1	30	0.661	0.637	1.281	1.139
2	16, 33	0.534	0.555	1.379	1.172
3	12, 16, 34	0.452	0.524	1.422	1.184
4	4, 8, 18, 34	0.404	0.523	1.424	1.184
5	4, 8, 12, 16, 35	0.348	0.504	1.451	1.191
6	4, 8, 12, 16, 20, 36	0.316	0.465	1.515	1.212

Initially, the reduction in the MLD objective is more pronounced than the CBM. However, as the number of ORs increases, a smoothing happens in both curves, which converges to close results, as can be seen in Figure 12. Between the two objectives, the MLD has a greater reduction, with a tendency that if more than six ORs are used, the CBM will be lower. Comparing the optimum positions for both objectives, it can be said that the CBM always results in positions at floor levels below, regardless of the number of ORs.

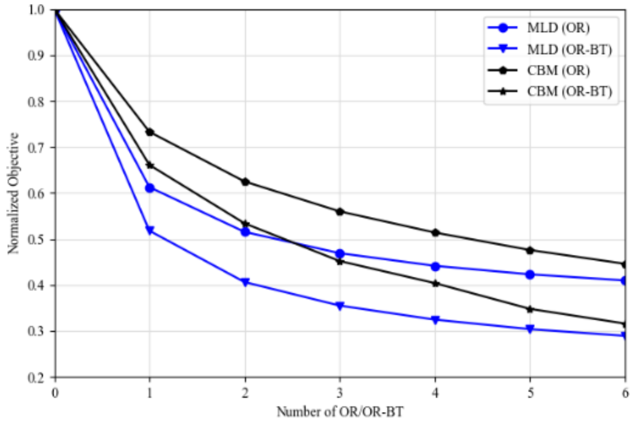

Figure 12. Result of each objective according to the number of OR/OR-BT

As already mentioned, adding the BT to the model helps to improve even more the main objectives. In this sense, it should be noted that it is possible to add fewer ORs over the building's height if there is a BT in the solution, as can be seen in the two cases presented in Figure 12. Given the MLD curves, it is possible to state that the solution with one OR-BT is equivalent to two ORs and the solution with two ORs-BTs is equivalent to six ORs. A similar situation happens with the CBM where, for example, three ORs-BTs are equivalent to six ORs. Moreover, adding ORs/ORs-BTs to the design of high-rise buildings implies an increase in execution time as well as in the project's final cost. Although such elements can be combined with mechanical floors, it must be carefully evaluated if this solution allows constructive and economical viability.

4.3 Multi-objective optimization

Each weight applied in Equation 17 provides only one optimum point on the Pareto frontier. Thus, it is necessary to discretize the weight in a small enough interval to obtain convergence in the results, that is, all Pareto solutions. Table 5 and Table 6 show the number of optimum positions according to the weight discretization ($\Delta\omega$) when the model has ORs and ORs-BTs, respectively. When the algorithm obtains the same number of solutions on the Pareto frontier in two consecutives $\Delta\omega$, the stopping criterion is reached.

Table 5. Number of optimal positions according to the weight discretization (ORs)

Number of ORs	$\Delta\omega$						
	0.1	0.05	0.025	0.0125	0.00625	0.004	0.002
1	11	19	26	26	-	-	-
2	11	21	32	39	41	42	42

Table 6. Number of optimal positions according to the weight discretization (ORs-BTs)

Number of ORs-BTs	$\Delta\omega$							
	0.1	0.05	0.025	0.0125	0.00625	0.004	0.002	0.001
1	11	19	26	26	-	-	-	-
2	11	21	32	37	39	41	42	42

As can be seen in Table 5, the minimum weight discretization, $\Delta\omega$, to reach all points of the frontier for one and two ORs are, respectively, 0.025 and 0.004. When the BT is added to the model, according to Table 6, the discretization for one OR-BT remains the same, and when there are two OR-BTs, $\Delta\omega$ decreases to 0.002. The extreme points of the Pareto frontier are the results of single-objective optimization. In the case of the optimization with one OR, the extreme positions are floors 31 and 56, resulting in exactly 26 points found. Therefore, even if $\Delta\omega$ was decreased, the number of positions would be the same. A similar behavior happens in the other cases.

Figure 13 illustrates all Pareto frontier points for both one and two ORs, as well as one and two ORs-BTs. It can be seen that the range of results for the MLD is more noticeable than for the CBM. In other words, CBM has a smaller variance compared to CBM. As already shown, the introduction of the BT causes an even greater reduction in the objectives. Another important point observed is the proximity of the frontier of two ORs and one OR-BT, which proves the efficiency of the BT and possibly exposes a feasible solution.

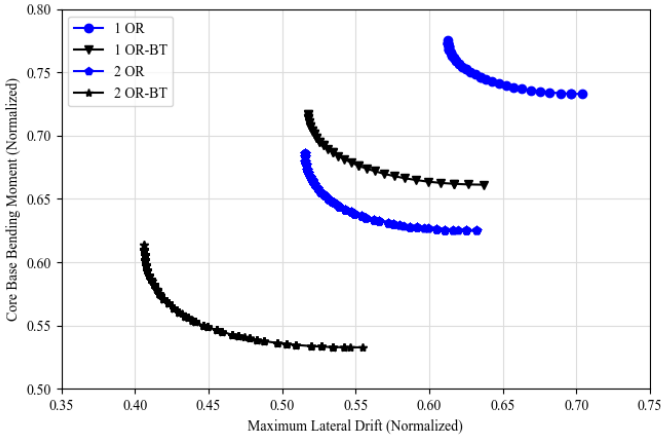

Figure 13. Pareto frontier for 1 and 2 ORs/ORs-BTs

All the optimum positions obtained through the optimizations can be seen in Table 7.

Table 7. Optimum positions resulting from multi-objective optimization

Number of ORs-BTs	Optimum positions
1 OR	all floors from the 31st to the 56th;
2 ORs	(17, 34); (17, 35); (17, 36); (18, 36); (18, 37); (18, 38); (18, 39); (19, 39); (19, 40); (19, 41); (19, 42); (20, 42); (20, 43); (20, 44); (21, 45); (21, 46); (22, 47); (22, 48); (23, 49); (23, 50); (24, 51); (25, 52); (25, 53); (26, 53); (26, 54); (27, 54); (27, 55); (28, 55); (28, 56); (29, 56); (29, 57); (30, 57); (31, 58); (32, 58); (32, 59); (33, 59); (34, 60); (35, 60); (36, 61); (37, 61); (38, 62); (39, 62);
1 OR-BT	all floors from the 30th to the 55th;
2 ORs-BTs	(16, 33); (16, 34); (17, 34); (17, 35); (17, 36); (17, 37); (18, 38); (18, 39); (18, 40); (19, 41); (19, 42); (19, 43); (20, 43); (20, 44); (20, 45); (21, 46); (21, 47); (22, 48); (22, 49); (23, 50); (23, 51); (24, 51); (24, 52); (25, 52); (25, 53); (26, 54); (27, 55); (28, 56); (29, 56); (29, 57); (30, 57); (30, 58); (31, 58); (32, 58); (32, 59); (33, 59); (34, 60); (35, 60); (36, 61); (37, 61); (38, 62); (39, 62);

All of the optimum floors presented above can be chosen to reduce the MLD and the CBM. However, if the designer wants to minimize one of the objectives more than the other, the choice must be made by observing the positions of the ORs/ORs-BTs along the height of the building. When the objective to be prioritized is the MLD, among all the options the best combination is the one with the floors positioned close to the top and, when it is the CBM, at the bottom. For example, for a tall building with two ORs-BTs and the priority is to reduce the CBM, the ORs positions should be as close as possible to the 16th and 33rd floors.

5 CONCLUSIONS

In view of the results and optimizations performed, this work proposed an algorithm and methodology to indicate the outriggers (ORs) or outriggers-belt-trusses (ORs-BTs) optimum positioning to minimize the maximum lateral drift (MLD) and the core base bending moment (CBM) in tall buildings under the action of lateral wind loads, as well as the influence of the implementation of these elements on maximum acceleration and natural frequencies. To this end, a tall building was modeled using the finite element method by the ANSYS program, and, using the Nelder-Mead algorithm, modified by the authors, the optimum positions were determined.

The comparison between the analysis results for the building with and without ORs/ORs-BTs proves that this bracing system is very efficient, considering the design criteria reductions. It is noticed that the optimal floors are different for each objective. In the MLD case, these floors are located more at the top. When there is only one OR/OR-BT, it is close to $0.7H$ and, when new elements are added, they are distributed along the height. In the CBM case, the floors are located at the bottom, regardless of the number of ORs/ORs-BTs. When there is one OR/OR-BT, it is at $0.37H$, and when new elements are added, they are distributed along the bottom in a range of $0.05-0.46H$. Kim et al. [6], considering a similar simplified model and adopting the building top drift as the objective function, obtain the optimal floor for one OR of $0.59H$. Difference of 16% in relation to that obtained in the present study, which can be justified by the presence of different stiffness in the elements of the OR system and wind loading profile.

It is noteworthy that for the tall building model used in the analyses, the solution with one OR would already be sufficient to be within the overall building deflection criterion since the element allows a reduction of about 39%. If necessary, it would be possible to reduce up to 60% of the lateral drift if six ORs were added in their optimal positions. On the other hand, if CBM were more important, introducing one OR could reduce it by 27%, or 55% with six ORs.

The advantage of including BT into the system is to reduce even more both main objectives by using fewer floors along the height. This solution allows the MLD to be reduced by 48% with one OR-BT, the same value obtained with two ORs. If two ORs-BTs were added the reduction would be 60%, which is equivalent to six ORs. A similar situation occurs with CBM, where three ORs-BTs are equivalent to six ORs.

The study carried out by varying the stiffness ratio between the external columns and the rigid core proves that there is a certain optimal ratio depending on the objective of interest. To obtain an optimal arrangement concerning the MLD, and based on the tall building model, it would be necessary to increase the core stiffness and decrease the stiffness of the column. The opposite is valid when the objective is the CBM. In this second case, in fact, it would be necessary to implement a constraint, because by increasing the ratio, the objective always continues to decrease.

The multi-objective optimization result provides engineers with several options to position ORs/ORs-BTs according to their interests. Such that choosing the best floor combination, fitting certain design considerations and specific objectives, is not conditioned to the extremes of the Pareto frontier (result considering only one objective), but close to it, with little interference in its optimal value.

ACKNOWLEDGEMENTS

The authors thank CNPq (National Council for Scientific and Technological Development) and CAPES (Coordination for the Improvement of Higher Education Personnel) for their support to this research.

REFERENCES

[1] K. S. Moon, "Outrigger systems for structural design of complex-shaped tall buildings," *Int. J. High-Rise Buildings*, vol. 5, no. 1, pp. 13–20, Mar 2016, http://dx.doi.org/10.21022/IJHRB.2016.5.1.13.

[2] K. S. Moon, "Why tall buildings? The potential of sustainable technologies in tall buildings," *Int. J. High-Rise Buildings*, vol. 1, no. 2, pp. 117–123, Jun 2012, http://dx.doi.org/10.21022/IJHRB.2012.1.2.117.

[3] M. H. Gunel and H. E. Ilgin, "A proposal for the classification of structural systems of tall buildings," *Build. Environ.*, vol. 42, no. 7, pp. 2667–2675, Jul 2007, http://dx.doi.org/10.1016/j.buildenv.2006.07.007.

[4] H. S. Park, E. Lee, S. W. Choi, B. K. Oh, T. Cho, and Y. Kim, "Genetic-algorithm-based minimum weight design of an outrigger system for high-rise buildings," *Eng. Struct.*, vol. 117, pp. 496–505, Jun 2016, http://dx.doi.org/10.1016/j.engstruct.2016.02.027.

[5] Y. Chen and Z. Zhang, "Analysis of outrigger numbers and locations in outrigger braced structures using a multiobjective genetic algorithm," *Struct. Des. Tall Spec. Build.*, vol. 27, no. 1, e1408, Aug 2018, http://dx.doi.org/10.1002/tal.1408.

[6] H.-S. Kim, Y.-J. Lim, and H.-L. Lee, "Optimum location of outrigger in tall buildings using finite element analysis and gradient-based optimization method," *J. Build. Eng.*, vol. 31, pp. 101379, Sep 2020, http://dx.doi.org/10.1016/j.jobe.2020.101379.

[7] H. S. Kim, H. L. Lee, and Y. J. Lim, "Multi-objective optimization of dual-purpose outriggers in tall buildings to reduce lateral displacement and differential axial shortening," *Eng. Struct.*, vol. 189, pp. 296–308, Jun 2019, http://dx.doi.org/10.1016/j.engstruct.2019.03.098.

[8] L. Xing, Y. Zhou, and W. Huang, "Seismic optimization analysis of high-rise buildings with a buckling-restrained brace outrigger system," *Eng. Struct.*, vol. 220, pp. 110959, Oct 2020, http://dx.doi.org/10.1016/j.engstruct.2020.110959.

[9] Associação Brasileira de Normas Técnicas, *Wind Loads on Buildings*, ABNT NBR 6123, 1988. (in Portuguese).

[10] J. A. Nelder and R. Mead, "A Simplex method for function minimization," *Comput. J.*, vol. 7, no. 4, pp. 308–313, Jan 1965., http://dx.doi.org/10.1093/comjnl/7.4.308.

[11] J. S. Arora, *Introduction to Optimum Design*, 4th ed. London, UK: Elsevier, 2017.

[12] J. Nocedal and S. Wright, *Numerical Optimization*, 2nd ed. New York, NY, USA: Springer Sci. Bus Media, 2006.

[13] F. Luchi and R. A. Krohling, "Differential evolution and nelder-mead for constrained non-linear integer optimization problems," *Procedia Comput. Sci.*, vol. 55, pp. 668–677, Jul 2015, http://dx.doi.org/10.1016/j.procs.2015.07.071.

[14] F. M. B. Parfitt, "Otimização multiobjetivo de outriggers em edifícios altos submetidos a cargas de vento," M.S. thesis, Dept. Civ. Eng., Univ. Fed. Rio Grande do Sul, Porto Alegre, 2022.

[15] S. Lee and A. Tovar, "Outrigger placement in tall buildings using topology optimization," *Eng. Struct.*, vol. 74, pp. 122–129, Jun 2014, http://dx.doi.org/10.1016/j.engstruct.2014.05.019.

Author contributions: FMP: conceptualization, writing, data curation; HMG: data curation, conceptualization, supervision, revision; IBM: supervision, methodology, conceptualization, formal analysis, revision.

Editors: Bernardo Horowitz, Guilherme Aris Parsekian.

Rev. IBRACON Estrut. Mater., vol. 16, no. 2, e16204, 2023

IBRACON Structures and Materials Journal
Revista IBRACON de Estruturas e Materiais
ISSN 1983-4195 ismj.org

ORIGINAL ARTICLE

Probabilistic models for live loads in buildings: critical review, comparison to Brazilian design standards and calibration of partial safety factors

Modelos probabilísticos para a ação de utilização em edifícios: análise crítica, comparação com normas brasileiras de projeto, e calibração dos fatores parciais de segurança

Luis Gustavo Lopes Costa[a]
Wagner Carvalho Santiago[b]
André Teófilo Beck[a]

[a]Universidade de São Paulo – USP, Escola de Engenharia de São Carlos, Departamento de Engenharia de Estruturas, São Carlos, SP, Brasil
[b]Universidade Federal do Vale do São Francisco – UNIVASF, Colegiado de Engenharia Civil, Juazeiro, BA, Brasil

Received 04 April 2022
Accepted 31 July 2022

Abstract: Nowadays, structural "limit state" design is made using characteristic or nominal values of actions, partial safety factors and load combination factors. The actual loading that a structure will be subjected to throughout its life is not known at the design phase. Yet, probabilistic models of such loadings are useful for the rational determination of partial safety factors and load combination factors. The probabilistic model leading to nominal live loads of NBR 6120:2019 (Design Loads for Structures) has never been openly discussed. Herein a simple probabilistic model describing spatial and temporal variabilities of live loads in buildings is presented and discussed. The model is built as a sum of two stochastic processes representing the sustained and intermittent parts of the live load. Model parameters are the ones recommended by the Joint Committee on Structural Safety (JCSS), based on extensive surveys done in several countries. By way of Monte Carlo simulations, sample values of live load actions are obtained for buildings of different occupancy types. These values are compared with those recommended by international standards, and those recommended in NBR 6120:2019 and NBR 8681:2003 (Actions and Safety of Structures). The corresponding statistics for the fifty-year extreme and arbitrary point-in-time distributions of live loads are presented; these statistics are very relevant for reliability analyses and for reliability-based code calibration. The stochastic live load model is also employed in a reliability-based calibration to obtain partial safety factors and load combination factors to be used in Brazilian design codes, for ultimate and serviceability limit state verifications.

Keywords: live load model, probabilistic model, structural reliability, partial safety factor, load combination factor, NBR 8681, NBR 6120.

Resumo: Hoje em dia, o projeto estrutural baseado em estados limites é feito utilizando valores característicos ou nominais das ações, fatores parciais de segurança e fatores de combinação de ações variáveis. As ações às quais uma estrutura estará sujeita durante sua vida não são conhecidas com exatidão na fase de projeto. Neste contexto, modelos estocásticos das ações são úteis para a determinação racional dos fatores parciais de segurança, e dos coeficientes de combinação de ações. O modelo probabilístico que levou aos valores nominais das ações de utilização da NBR 6120: 2019 (Ações para o Cálculo de Estruturas de Edificações) nunca foi discutido abertamente. Neste artigo, apresenta-se uma revisão crítica de um modelo estocástico simples que descreve as flutuações espaciais e temporais da ação variável de utilização em prédios. O modelo

Corresponding author: André Teófilo Beck. E-mail: atbeck@sc.usp.br
Financial support: CAPES; CNPq (grant n. 309107/2020-2); FAPESP (grant n. 2019/13080-9).
Conflict of interest: Nothing to declare.
Data Availability: The full dataset which supports the findings of this study are available in the first authors Master's Dissertation: L. G. L. Costa. Complementary results and discussion are available at https://doi.org/10.48331/scielodata.YU8FLN.

é construído como uma soma de dois processos estocásticos, representando as parcelas sustentada e intermitente da ação de utilização. Parâmetros para este modelo são recomendados pelo *Joint Committee on Structural Safety* (JCSS), com base em *surveys* realizados em diversos países. Utilizando simulações de Monte Carlo, amostras de ações de utilização são obtidas para edifícios com diferentes tipos de ocupação. Estes valores são comparados com aqueles recomendados em diferentes normas técnicas internacionais, bem como com valores preconizados nas normas brasileiras NBR 6120:2019 e NBR 8681:2003 (Ações e Segurança nas Estruturas). As estatísticas obtidas para as distribuições de probabilidade das ações "extrema de cinquenta anos" e de "ponto arbitrário no tempo" são apresentadas; estas distribuições são extremamente importantes em análises de confiabilidade. O modelo estocástico também é empregado em uma calibração baseada em confiabilidade dos coeficientes parciais de segurança e fatores de combinação de ações variáveis das principais normas de projeto brasileiras.

Palavras-chave: ação de utilização, modelo estocástico, confiabilidade estrutural, coeficiente parcial de segurança, fator de combinação de ações, NBR 8681, NBR 6120.

How to cite: L. G. L. Costa, W. C. Santiago, and A. T. Beck, "Probabilistic models for live loads in buildings: critical review, comparison to Brazilian design standards and calibration of partial safety factors," *Rev. IBRACON Estrut. Mater.*, vol. 16, no. 2, e16204, 2023, https://doi.org/10.1590/S1983-41952023000200004

1 INTRODUCTION

1.1 Background

In order to achieve consistent safety levels in the design of structures, while also meeting economical, functionality and robustness criteria, the engineer must have proper knowledge of the strength properties of materials and structural elements, but also of the loads to which a structure is expected to be subjected throughout its lifetime.

Among these loads, one of the most fundamental when designing buildings is the live load (sometimes also referred to as imposed load), generally specified in design codes as a uniformly distributed load depending on floor occupancy type. In Brazil, design live loads are prescribed by design code NBR 6120:2019 [1].

The nominal values of live loads given by most major foreign design codes are generally based on probabilistic models built from data measured in live load surveys. Extensive reviews of survey results are reported by Sentler [2] and Chalk and Corotis [3], covering investigations conducted between years 1893 and 1976 and covering many occupancy types in six different countries: Australia [4], United States [5]–[13], Finland [14], United Kingdom [15]– [18], Hungary [19] and Sweden [20], [21].

To the authors best knowledge, there are no records of any similar live load surveys carried out in Brazilian buildings, nor of the existence of stochastic models that may have been used to derive the nominal values for live loads presented in NBR 6120:2019. Instead, those values were established by consensus of the technical community, based upon comparisons with foreign design codes, such as the American ASCE/SEI 7-16 [22], the European EN 1991-1-1:2002 [23], and ISO 2103:1986 [24].

1.2 Representative values of variable actions

When designing a structure using a semi-probabilistic approach, such as the limit states format employed by most design codes, representative values of the loads are considered. These can be characteristic or nominal values, design values, or combination values used in ultimate or serviceability limit states. The definitions of these values are given in the Brazilian design code for Actions and Safety of Structures, NBR 8681:2003 [25].

Particularly for the live load, the recently superseded version of the design loads code, NBR 6120:1980 [26], did not mention the return period corresponding to the nominal values proposed. The current version, which came into effect late 2019, repeats the definition found in NBR 8681:2003: "the characteristic values of variable actions, established by consensus, correspond to values that have between 25 to 35% probability of being exceeded, in the unfavorable sense, in a period of 50 years". Furthermore, NBR 6120:2019 adds to this definition, stating that these probabilities correspond to an average return period between 174 and 117 years, respectively.

The definition used in this study is that the characteristic value L_k of the live load corresponds to the 70th percentile (i.e., the value that has 30% exceedance probability) of the fifty-year extreme live load, denoted L_{50} in this paper. This would be equivalent to saying that the mean return period of L_k is around 140 years. Consequently, L_k is equal to the mode of the 140-year extreme distribution (L_{140}) and can also be obtained as the $1 - 1/140 \approx 99{,}3\%$ fractile of the 1-year extreme distribution (L_1), provided that the annual maxima are independent. This hypothesis of independence in challenged in the sequence.

In the limit state design format, employed in Brazilian structural design codes, the required safety margin is achieved by introducing partial safety factors γ_m that reduce the characteristic value of material strength and γ_f that increase the nominal values of actions (or their effects), resulting in design values.

The safety factor for actions is expressed as the product of three other partial factors, $\gamma_f = \gamma_{f1}\gamma_{f2}\gamma_{f3}$. The first of these, γ_{f1}, takes into consideration possible unfavorable deviations from the representative values due to the inherently variable nature of loads. The second, γ_{f2}, is a load combination factor that takes into account the reduced probability that all actions happen simultaneously with their representative values. Lastly, γ_{f3} accounts for the inaccuracies in the assessment of action effects, whether due to constructive deviations or to shortcomings arising from simplifications assumed in modelling.

Particularly for live loads, the safety factor given by $\gamma_{f1}\gamma_{f3}$, denoted γ_L in this paper, is usually equal to 1.4 when considered grouped with other variable actions, or 1.5 when considered separately, as indicated in NBR 8681:2003. The γ_{f2} factor can be equal to ψ_0, ψ_1 or ψ_2, depending on what limit state is being verified.

The combination factor $\psi_0 \leq 1$, used in verification of ultimate limit states (ULS), takes into account that it is highly unlikely that two (or more) independent variable actions simultaneously present their maximum values of over a reference period. It is calculated so that the probability of the combined effect – due to multiple variable actions – being exceeded during the reference period is somewhat equivalent to the exceedance probability when only a single variable action is considered with its characteristic value.

The frequent and quasi-permanent values, used in verification of serviceability limit states (SLS), are obtained by multiplying the characteristic values by reduction factors $\psi_1 \leq 1$ and $\psi_2 \leq 1$. The frequent value ψ_1 can be defined in two different ways: based on the frequency with which the variable action exceeds this value or based on a small fraction of the total lifetime of the structure in which it is surpassed. NBR 8681:2003 states that the frequent value is that which is exceeded about 10^5 times in a period of 50 years, or during 5% of the structure lifetime. In the present study, the second definition was considered, since it is easier to use. Similarly, the quasi-permanent value ψ_2 is defined so that its total time of application is a considerable portion (around half) of the structure´s lifetime.

2 METHODOLOGY

2.1 Probabilistic model for live loads

Live loads in buildings depends on its corresponding occupancy type, and are intrinsically stochastic in nature, varying in space and time. In general, live loads can be decomposed in two parts with different behavior regarding its temporal variability: a sustained load and an extraordinary load (sometimes also referred to as intermittent or transient load).

The sustained load includes weight of all furniture, equipment, stored objects and personnel that are regularly present in the analyzed area. This load is the one effectively measured in load surveys.

The extraordinary load is associated with exceptional events that may lead to short duration high-intensity loading, such as temporary crowding due to a party or special event; or caused by a large number of people trying to evacuate the building in an emergency situation; or even the relocation and concentration of furniture in a room while the adjacent premises are undergoing renovations. Due to the exceptional and transient nature of extraordinary loads, it is very unlikely that these events can be reliably measured in load surveys.

The model analyzed in this study is the hierarchical model presented in Part 2 of the JCSS Probabilistic Model Code [27], which is based on a formulation initially proposed by Peir [28] and Peir and Cornell [29]. This model has been used with great success by several authors since then, among which McGuire and Cornell [30]; Ellingwood and Culver [31]; and Chalk and Corotis [3]. These were the studies that served as a basis for obtaining the live load statistics used in the calibration of the partial safety factors of North-American design codes in the eighties [32].

The central idea of the model is to represent the sustained load $Q(t)$ by a rectangular-wave process with random intensities and durations (Figure 1a), and the extraordinary load $P(t)$ by a spike process with random intensities and time between pulses (Figure 1b). The total live load is given by the sum of these processes, $L(t) = Q(t) + P(t)$ (Figure 1c). As shown in Figure 1, finding the maximum of the combined process is not a trivial task, since this value may not coincide with any of the individual maxima for each process.

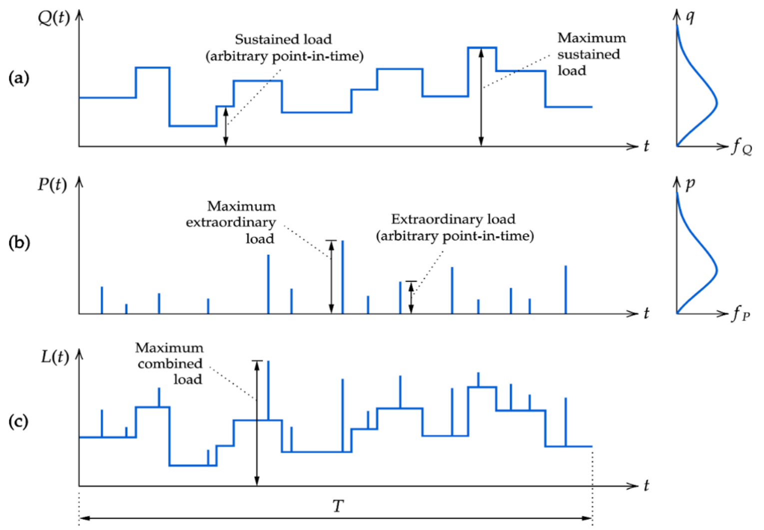

Figure 1. Time histories of live loads: (a) sustained load; (b) extraordinary load; (c) total live load.

2.1.1 Sustained load

As presented in JCSS [27], the sustained load intensity acting on an infinitesimal area δA at a location (x, y) of a given floor of a given building at an arbitrary point-in-time can be represented as a stochastic field $W(x, y)$ expressed by:

$$W(x, y) = m + V + U(x, y) \tag{1}$$

where m is a "grand mean" of the load intensity over all buildings under the same occupancy type; V is a zero-mean normally distributed random variable; and $U(x, y)$ is a zero-mean random field.

The random variable V can be thought as the sum of two other zero-mean independent and normally distributed random variables B and F, where B describes the deviation of the average for the whole building from the grand mean m; and F describes the deviation of the floor average with respect to $m + B$. The random field $U(x, y)$ represents the spatial variability of the load intensity within that particular floor and shows a characteristic skewness to the right [27].

This model, while very simple, allows for the calculation of load effects caused by the real loading up to a sufficient degree of accuracy for all practical purposes. Assuming linear elastic behavior, where the superposition principle is valid, the resulting effect S can be obtained by:

$$S = \iint_A W(x, y) I(x, y)\, dx\, dy \tag{2}$$

where $W(x, y)$ is the load intensity; $I(x, y)$ is the surface influence for the desired effect; and A is the influence area. For non-linear structural response, the load effect can be approximated by an incremental analysis assuming stepwise linearity, replacing W and S in Equation 2 for steps ΔW and ΔS of load magnitude and effect, and the surface influence $I(x, y)$ for some equivalent function that takes into account the total load history.

In design codes, live load values are generally specified as uniform loads. Thus, it is of practical interest to define an equivalent uniformly distributed load (EUDL), i.e., the uniform load that produces the same effect S as the actual load field $W(x, y)$. Denoting the sustained load EUDL by Q, it follows that:

$$Q = \frac{\iint_A W(x,y) I(x,y)\, dx\, dy}{\iint_A I(x,y)\, dx\, dy} \tag{3}$$

Its mean and variance are given by:

$$\mathrm{E}[Q] = \frac{\iint_A E[W(x,y)] I(x,y)\, dx\, dy}{\iint_A I(x,y)\, dx\, dy} = m \tag{4}$$

$$\mathrm{Var}[Q] = \frac{\iint_A \iint_A I(x_1,y_1) I(x_2,y_2)\, \mathrm{Cov}[W(x_1,y_1) W(x_2,y_2)]\, dx_1\, dy_1\, dx_2\, dy_2}{\left[\iint_A I(x,y)\, dx\, dy\right]^2} \tag{5}$$

In general, if the load intensity at a particular location (x_1, y_1) is greater than the floor average, it is likely that the load intensity at a nearby point (x_2, y_2) is also high. In other words, there is a generally positive correlation to the field $U(x, y)$ that tends to decay as the distance separating the points increases.

Hauser [33] proposed three different empirical expressions for the correlation of the random field U. The following one is widely used, due to its convenience for integration:

$$\mathrm{Cov}[U(x_1, y_1), U(x_2, y_2)] = \sigma_U^2 \exp\left(-\frac{r^2}{d^2}\right) \tag{6}$$

In the above expression, σ_U^2 is the variance of U; $r = \sqrt{(x_1 - x_2)^2 + (y_1 - y_2)^2}$ is the horizontal distance separating the points (x_1, y_1) and (x_2, y_2); and d is a constant to be determined that dictates how fast the correlation decays over distance (usually between 1 to 2 m).

Mitchell and Woodgate [16] studied what they called the "stacking effect", i.e., the tendency for tenants to load different floors in a similar way vertically. This effect can be accounted for by introducing a vertical correlation parameter ρ_c in Equation 6, as shown in [29]. This parameter was estimated by Peir and Cornell [29] to be approximately equal $\rho_c = 0.7$ for office buildings.

In this study, the random field $U(x, y)$ was regarded as a "white-noise" process, which means that load intensities in two points are uncorrelated if there is any separation between them. This frequently employed assumption is quite reasonable, as long as the area A is not too small [31]. Choi [34] investigated both hypotheses and concluded that, in general, the assumption that load intensity is spatially correlated is marginally better than the white-noise approximation. However, this uncorrelated assumption is sufficiently accurate for practical applications, and has the advantage of considerably simplifying the quadruple integral in Equation 5, allowing for a conservative upper bound to be established for $\mathrm{Var}[Q]$:

$$\mathrm{Var}[Q] \leq \sigma_V^2 + \sigma_U^2 \frac{A_0}{A} \kappa \tag{7}$$

where σ_V^2 is the variance of the random variable V; σ_U^2 is the variance of the random field U; A_0 is the smallest area for which a distributed load is of interest; and κ is a shape factor (sometimes also referred to as a peak factor) depending on the influence surface, given by:

$$\kappa = A \frac{\iint_A [I(x,y)]^2\, dx\, dy}{\left[\iint_A I(x,y)\, dx\, dy\right]^2} \tag{8}$$

Equation 7 is valid only for $A \geq A_0$. For $A < A_0$, one should take $A_0/A = 1$.

Usually, it is more convenient to normalize the double integrals in Equation 8. For example, for a rectangular area with sides a and b, one can define normalized coordinates (ξ, η) ranging from 0 to 1 so that $x = \xi a$ and $y = \eta b$. Then, the expression for κ becomes:

$$\kappa = \frac{\int_0^1 \int_0^1 [I(\xi,\eta)]^2\, d\xi\, d\eta}{\left[\int_0^1 \int_0^1 I(\xi,\eta)\, d\xi\, d\eta\right]^2} \tag{9}$$

Naturally, κ depends on the shape of the influence surface, which in turn depends on the considered load effect (Figure 1 of the Data Availability Material), usually assuming values between 2 and 3 [54]. JCSS [27] presents some examples of influence surfaces with $\kappa = 2.0$ and $\kappa = 2.4$, but does not clarify to which effect each of these corresponds. McGuire and Cornell [30] report the following values for κ: 2.76 for midspan moment in beams, 2.04 for end moment in beams, and 2.20 for column loads. Tran et al. [35] present κ values for flat slabs, ranging from 1.2 to 1.9.

The calculated EUDL is generally observed to be relatively insensitive to the action being considered, provided that the influence area and the shapes of their influence surfaces are reasonably similar. The exception to this rule would be midspan shear in beams, which becomes comparable to other effects when considering only half the influence area, since the influence surface for this effect has regions with negative values [30]. In this study, $\kappa = 2.0$ was adopted as a general value representing no particular effect for the sake of simplicity.

At this point, it is important to emphasize the distinction between influence area and tributary area, made very clear in the ASCE/SEI 7-16 [22]. The area A in Equations 7 and 8 is the influence area, i.e, the area over which the influence surface for a structural effect is significantly different from zero. This definition does not correspond to the usual notion of tributary area – often mistakenly called influence area – which is thought of as the area that contributes to the loading on a particular element, delimited by the panel centerlines in a slab. The influence area is usually equal to twice the tributary area for beams and four times the tributary area for columns (Figure 2).

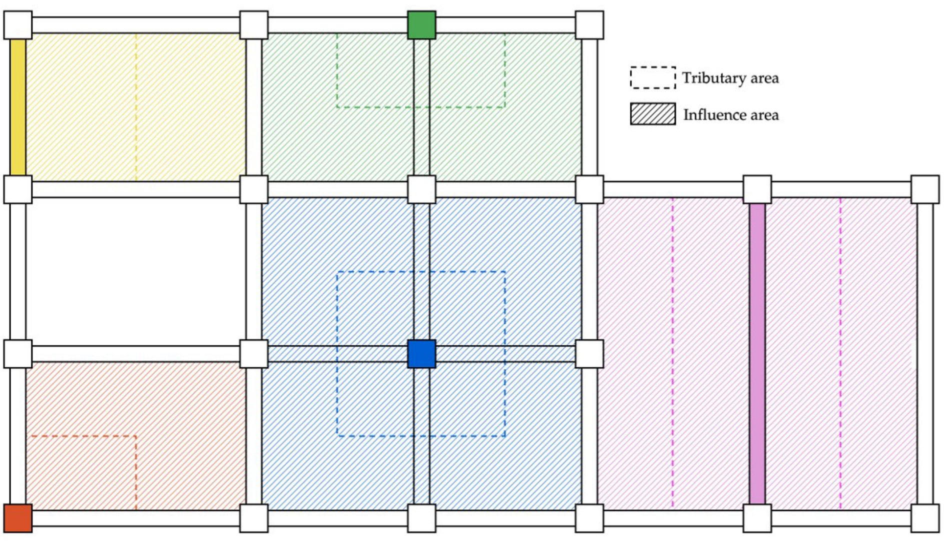

Figure 2. Tributary and influence areas for typical structural members.

Data from load surveys show a distinct skewness where most of the observed values sit left of the mean and exhibit very good agreement with a gamma distribution [29], [36]. Since the arbitrary point-in-time load intensity and the EUDL differ from each other only by the weighting function $I(x, y)$, it is reasonable to extend this hypothesis to Q and assume that it will also be gamma distributed, with mean and variance given by Equations 4 and 7, respectively.

In addition to spatial variability, live load is also variable over time. The EUDL is, therefore, a function of time. In general, the sustained load remains relatively constant for long periods of time, showing only insignificant fluctuations around a mean value that changes from time to time due to a tenancy or occupancy change.

Typically, it is assumed that the EUDL for sustained load is constant between occupancy changes[1], and that the number of occupancy changes follow a Poisson distribution with mean rate λ_q (Figure 1a). Consequently, the time between occupancy changes (or the duration of a tenancy) follows an exponential distribution, and the mean number of occupancy changes in a reference period T is equal to $\lambda_q T$.

Under these assumptions, the extreme value distribution for the maximum sustained load $Q_{\max}$ over a reference period T can be obtained from the arbitrary point-in-time distribution using the following expression [29]:

[1]This might not be the case for storage areas, where it may be necessary to take into account a gradual increase of the sustained load over time between occupancy changes.

$$F_{Q_{\max}}(x) = F_Q(x) \exp\left[-\lambda_q T F_Q(x)\left(1 - F_Q(x)\right)\right] \tag{10}$$

For values of x in the upper tail region, which are the loads of practical interest, $F_Q(x)$ tends to 1, and Equation 10 can be simplified to:

$$F_{Q_{\max}}(x) \approx \exp\left[-\lambda_q T\left(1 - F_Q(x)\right)\right] \tag{11}$$

2.1.2 Extraordinary load

The extraordinary load is associated with unusual gatherings of people, furniture or equipment in an area for a short period of time. Due to its extraordinary and transient nature, it is quite difficult to accurately measure data related to this type of loading during load surveys. Most of the available data on extraordinary load has been gathered through questionnaires submitted to the surveyed building occupants and is, therefore, liable to a considerable amount of uncertainty and subjectivity.

A model for extraordinary loads was initially proposed by Peir [28], which divides the area of interest into a number of randomly distributed load cells and represents the extraordinary event as a cluster of concentrated loads (such as the weight of people) acting on these cells, both the number and intensities of these loads being random variables. A similar model was used by McGuire and Cornell [30] and Ellingwood and Culver [31]. Harris et al. [37] proposed a more general extension of this model, where three different extraordinary load processes are considered, each modeled by a group of loads with their own parameters. The combination of these loads is accomplished using an expression proposed by Wen [38].

The JCSS Probabilistic Model Code [27] states that, for design purposes, the same approach as for the sustained load can be used. Thus, the EUDL for extraordinary load (denoted P in this paper) has mean and variance given by:

$$\mathrm{E}[P] = m_p \tag{12}$$

$$\mathrm{Var}[P] = \sigma_{U,p}^2 \frac{A_0}{A} \kappa \tag{13}$$

where the subscript p is used to differentiate extraordinary load parameters from sustained load ones (which are denoted by subscript q).

Similarly to the sustained load, it is assumed that the arbitrary point-in-time extraordinary load is adequately described by a gamma distribution, although there is not enough data to substantiate this assumption.

While it gives different values for m_p and $\sigma_{U,p}$, JCSS [27] also states that the standard deviation usually results in the same magnitude as the mean value, and that the extraordinary load is, therefore, assumed to be exponentially distributed. This assumption, however, is in clear contradiction with the previous statement: adopting the same formulation employed for sustained load would necessarily imply in a constant mean value for a given occupancy type and a standard deviation that decays with the increase in area, whereas an exponential distribution should always have equal mean and standard deviation regardless of the area A.

This inconsistency seems to have been clarified in a current draft for the "Technical Report for Reliability Background of Eurocodes"[2], that prescribes a single parameter m_p and states that $P \sim \mathrm{Exponential}(\mu_p = \sigma_p = m_p)$. However, the authors personally believe that the choice for an exponential distribution to represent extraordinary load is inadequate. This is due to the fact that, since its variance is area-independent, it tends to quickly dominate the behavior of the total load $L = Q + P$ as the area increases and $\mathrm{Var}[Q]$ gets smaller, leading to excessively conservative results for large areas when compared to the live load reduction allowed for in major design codes around the world.

Based on data from 1989 extraordinary events recorded in a load survey carried out in Sydney [39] in the seventies, Choi [40] found out that in reality both the mean and the standard deviation of the extraordinary load are area dependent. However, the variation for the mean value is much smaller, and it seems reasonable that it could be disregarded.

In this study, the intermittent part of the live load is represented by a Gamma distribution, following many other studies. Moments of the distribution are obtained from Equations 12 and 13.

[2] Unpublished, still being worked on at the time this paper was written.

As for temporal variability, the extraordinary load is represented by a Poisson-arriving spike process with mean rate λ_p (Figure 1b). Accordingly, time between pulse arrivals follows an exponential distribution. The duration d_p of each pulse is considered deterministic.

The extreme value distribution $P_{\max}$ of a Poisson-distributed number of extraordinary events happening over a reference period T is obtained from the arbitrary point-in-time distribution P using the same approach as for the sustained load (Equation 11).

2.1.3 Model parameters

Ideally, model parameters should be estimated from statistical analysis and fitting to the results of load survey data. Since there are no specific survey data on Brazilian live loads, the values for the model parameters used in this study were taken from JCSS [27] and Honfi [41], as shown in Table 1.

Table 1. Live load parameters for some major occupancies.

Occupancy type	A_0 (m^2)	Sustained load				Extraordinary load				Reference
		m_q *(kPa)*	$\sigma_{V,q}$ *(kPa)*	$\sigma_{U,q}$ *(kPa)*	$1/\lambda_q$ *(years)*	m_p *(kPa)*	$\sigma_{U,p}$ *(kPa)*	$1/\lambda_p$ *(years)*	d_p *(days)*	
Office	20	0.50	0.30	0.60	5	0.20	0.40	0.3	1–3	JCSS [27]
Residence	20	0.30	0.15	0.30	7	0.20	0.30	1.0	1–3	JCSS [27]
Hotel room	20	0.30	0.05	0.10	10	0.20	0.40	0.1	1–3	JCSS [27]
Patient room	20	0.40	0.30	0.60	5–10	0.20	0.40	1.0	1–3	JCSS [27]
Classroom	100	0.60	0.15	0.40	10	0.20	0.40	0.3	1–5	Honfi [41]
Retail	100	0.90	0.60	0.60	1–5	0.40	0.60	1.0	1–14	Costa [42]

The JCSS [27] also proposes parameters for classroom and retail areas. However, investigations by Costa [42] and Honfi [41] show that these parameters are too conservative, when compared to actual values employed in major international codes. For that reason, the values suggested by Honfi [41] and Costa [42] for these occupancies are adopted in this study.

2.1.4 Total live load

In order to obtain the total live load, one must consider the combined effects of the stochastic processes for the sustained and extraordinary loads over time, i.e., $L(t) = Q(t) + P(t)$ (Figure 1c). The statistical combination of extreme loads is not a trivial task.

An approximate theoretical model for the maximum total load $L_{\max}$ over a given reference period T is presented in Chalk and Corotis [3]. This simplified model, however, is limited as it assumes several simplifications that, while reasonable for values in the upper tail region of the distribution, makes this formulation more suitable for obtaining estimates for nominal values of loads (corresponding to the upper fractiles) rather than describing the complete distribution of $L_{\max}$.

In the present study, the total live load statistics for the extreme value and arbitrary point-in-time distributions are derived through Monte Carlo simulations. Daily realizations of both sustained and extraordinary loads are generated according to the known distributions of the model previously described, over reference periods T equal to 1, 50 and 140 years. An example of a realization of the sustained and extraordinary loads in an office floor with $A = 500$ m^2 over 50 years is shown in Figure 3.

This process is repeated 10^4 times for each considered influence area (ranging from $A = 10$ to 500 m^2), reference period and occupancy type. The obtained data is then plotted and fitted to candidate distributions. The quality of the distribution fit to the histogram is assessed through goodness-of-fit tests such as the Pearson's chi-squared, Kolmogorov-Smirnov or Anderson-Darling tests. A pseudocode detailing the simulation procedure employed herein is presented in Figure 4.

Figure 5 shows the obtained PDF and CDF histograms for 10^4 samples of the fifty-year extreme live load (L_{50}) in an office floor with influence area $A = 100$ m^2. Superimposed to the histograms, the fitted distribution is also shown in blue, which in this case is a Type I Extreme Value distribution, also known as Gumbel distribution. The quality of this fit is also graphically visualized through P-P (probability-probability) and Q-Q (quantile-quantile) probability plots, presented in Figure 6. The obtained p-values for the goodness-of-fit tests are shown in Table 2. At a significance level of $\alpha = 0.05$, the null hypothesis that L_{50} follows a Gumbel distribution is accepted considering all performed tests.

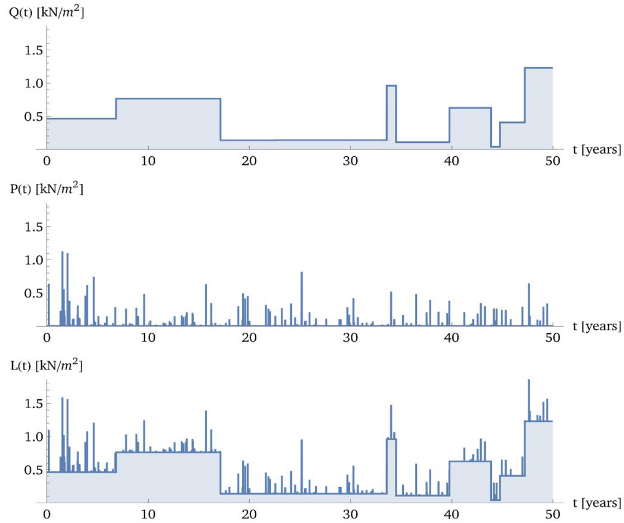

Figure 3. Time histories of one sample of sustained, extraordinary and total live load for an office floor with $A = 500\ \mathrm{m}^2$.

Algorithm: Monte Carlo simulation of live load in buildings

---

for each occupancy type **do** // office, residential, hotel, patient room, classroom, retail
  define A_0 from Table 1 // from Table 1
  define sustained load parameters (m_q, $\sigma_{V,q}$, $\sigma_{U,q}$ and λ_q) // from Table 1
  define extraordinary load parameters (m_p, $\sigma_{U,p}$, λ_p and d_p) // from Table 1
  for each influence area A **do** // A = 10 m² to 500 m² in steps of 10 m²
    calculate mean and variance of sustained load EUDL // Equations 6 and 7
    calculate mean and variance of extraordinary load EUDL // Equations 12 and 13
    calculate distribution parameters from moments // assuming Gamma distribution
    for each reference period T **do** // T = 1 year, 50 years or 140 years
      k = 0
      while k < nsamples **do** // nsamples = 10000 samples
        $\sum t_i = 0$
        while $\sum t_i \leq T$ **do**
          generate samples of time intervals t_i between tenancy changes following an exponential distribution with parameter λ_q
          generate samples of sustained load intensity corresponding to each time interval t_i following a Gamma distribution
        end while
        $\sum t_j = 0$
        while $\sum t_i \leq T$ **do**
          generate samples of arrival times t_j of each extraordinary load following an exponential distribution with parameter λ_p
          generate samples of extraordinary load intensity corresponding to each arrival time t_j following a Gamma distribution
        end while
        for each time discretization t in T **do** // discretization step = 1 day
          total live load at time t = (sust. live load at time t) + (extr. live load at time t)
        end for
        evaluate maximum live load L_T in reference period T for sample k
        k++
      end while
      calculate mean and standard deviation of L_T from all samples
      calculate distribution parameters of L_T // assuming Gumbel distribution
      perform goodness-of-fit tests // Pearson χ^2, Kolmogorov-Smirnov, Anderson-Darling
      calculate characteristic value from fitted distribution
    end for
  end for
end for

Figure 4. Pseudocode of Monte Carlo simulations of live loads in buildings

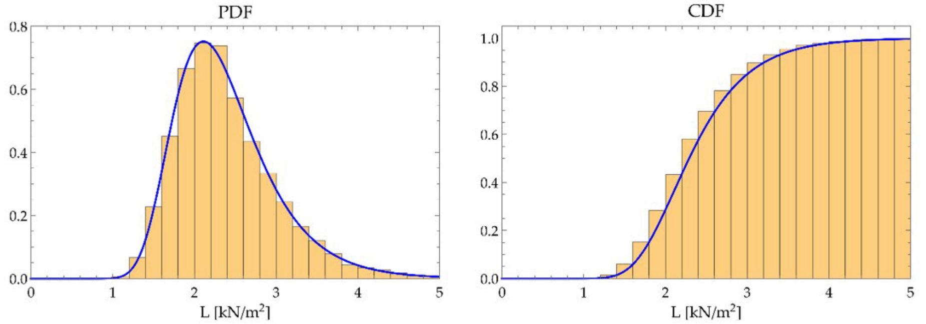

Figure 5. Probability density and cumulative distribution histograms vs. fitted Gumbel distribution for L_{50} in an office floor with $A = 100 \text{ m}^2$.

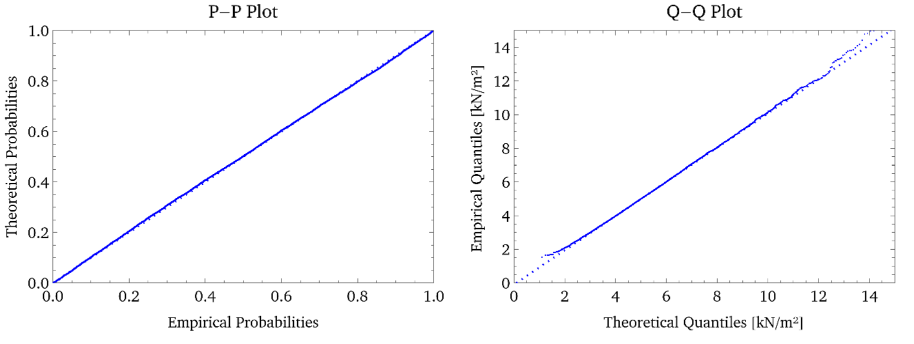

Figure 6. P-P and Q-Q probability plots showing the deviation of L_{50} from the fitted Gumbel distribution in an office floor with $A = 100 \text{ m}^2$.

Table 2. Goodness-of-fit tests for L_{50} in an office floor with $A = 100 \text{ m}^2$.

Test	Statistic	P-value
Anderson-Darling	0.2482592	0.9713050
Kolgomorov-Smirnov	0.0056237	0.9098539
Pearson χ^2	70.272	0.7479799

2.2 Partial safety factor for ULS verification

In this study, the partial safety factor $\gamma_F = \gamma_{f1}\gamma_{f3}$ for live loads is estimated using the Design Value Method, as presented in the Annex C of EN 1990:2002 [43], [44]. The partial safety factor γ_S for the effect of a generic variable action can be determined from its design value S_d and characteristic value S_k by:

$$\gamma_S = \frac{S_d}{S_k} \tag{14}$$

Characteristic values obtained with the stochastic model presented herein are shown in Section 3 (Results). The design value S_d, in turn, can be calculated as a function of the known probability distribution of S. For a Gumbel distributed variable, S_d is given by:

$$S_d = u - \frac{1}{a}\ln\left(-\ln\left(\Phi(-\alpha_S\beta_T)\right)\right) \tag{15}$$

where $\Phi(\cdot)$ is the cumulative distribution function of the standard normal distribution; α_S is the FORM sensitivity factor for the action effects, and β_T is the target reliability index. In Section 3.6, the reliability-based calibration of partial safety factors employed in Brazilian design codes for steel [45] and concrete [46] structures – originally performed by Santiago et al. [47] – is re-processed using the live load statistics developed herein, and the mean reliability index using current NBRs 8681, 8800 and 6118 factors is found to be equal to 3.17 for a period of 50 years. Hence, a target reliability index of $\beta_T = 3.17$ is considered herein. Also, the sensitivity factor was taken as $\alpha_S = -0.66$, which is the average value found in the re-calibration.

In Equation 15, u and a are the location and scale parameters of the Gumbel distribution, respectively, calculated from its mean μ and standard deviation σ as:

$$u = \mu - \frac{\gamma}{a} \tag{16}$$

$$a = \frac{\pi}{\sigma\sqrt{6}} \tag{17}$$

where $\gamma = 0.577216$ is the Euler-Mascheroni constant. Alternatively, Equation 15 can be reasonably approximated by [44]:

$$S_d \approx \mu - \sigma\left(0.45 + 0.78\ln\left(-\ln\left(\Phi(-\alpha_S\beta_T)\right)\right)\right) \tag{18}$$

2.3 Combination value

Similarly, the combination factor ψ_0 was also estimated using the same approach described in Annex C of EN 1990:2002 [43], [44]. This method is based on representing the effects of two independent generic variable actions to be combined, S_1 and S_2, by a Ferry-Borges-Castanheta model, that is, by a rectangular-wave process with fixed durations T_1 and T_2 (with $T_1 > T_2$) smaller than the reference period T. The magnitude of the effect in each basic interval is assumed constant, uncorrelated, and equal to the maximum value within this period (Figure 2 of the Data Availability Material). It is also assumed that S_1 and S_2 are stationary and ergodic, so that a particular realization over a sufficiently long interval may be used, instead of an envelope of samples.

The basic period for live loads is taken as the mean time between tenancy changes, $T = 1/\lambda_Q$, which usually ranges from 5 to 10 years for the major occupancy types. Live load effects are usually to be combined with environmental loads such as wind, whose basic period is generally taken as $T_2 = 1$ year.

Under these assumptions, the combination factor can be calculated as:

$$\psi_0 = \frac{F_S^{-1}(\Phi(0.4\beta_C)^r)}{F_S^{-1}(\Phi(\beta_C)^r)} \tag{19}$$

where $F_S^{-1}(\cdot)$ is the inverse cumulative distribution function of the extreme value of the accompanying action in the reference period T; $\Phi(\cdot)$ is the standard normal cumulative distribution function; r is the ratio T/T_1 rounded to the nearest integer; and β_c is the equivalent reliability index for the interval T_1, given by:

$$\beta_c = -\Phi^{-1}(\Phi(\alpha_S\beta_T)/r) \tag{20}$$

In the above expression, α_S and β_T are the same as described in Equation 15.

Alternatively, the combination factor can be derived according to Turkstra's Rule, leading to the following expression for a Gumbel distributed variable:

$$\psi_0 = \frac{1-0.78V\left[0.577+\ln\left(-\ln\left(\Phi(-0.4\alpha_S\beta_T)\right)\right)+\ln(r)\right]}{1-0.78V\left[0.577+\ln\left(-\ln\left(\Phi(-\alpha_S\beta_T)\right)\right)\right]} \tag{21}$$

where $V = \sigma/\mu$ is the coefficient of variation of the accompanying action for the reference period T. A more detailed derivation of these formulas can be found in ISO 2394:1998 [48].

2.4 Frequent and quasi-permanent values

Figure 3 of the Data Availability Material shows the temporal variability of a certain effect of a generic variable action S over a reference period T. For a given level S^*, the relative duration η that the process $S(t)$ spends above that level S^* given by the sum of the time periods $t_1, t_2, \dots, t_n$ divided by T.

For an ergodic process, the relative duration η can be computed as:

$$\eta = pq = q\left(1 - F_{S_{\text{apt}}}(S^*)\right) \tag{22}$$

where $F_{S_{\text{apt}}}$ is the cumulative distribution function of the average point-in-time value of action S; and q is the probability of S having a non-zero value. It is important to note that the distribution S_{apt} refers only to the cases where S has a non-zero value. Thus, the level S^* corresponding to a given relative duration η can be obtained by:

$$S^*(\eta) = F_{S_{\text{apt}}}^{-1}\left(1 - \frac{\eta}{q}\right) \tag{23}$$

The distinction for the case where S can assume values equal to zero may be relevant for a generic stochastic process $S(t)$. For live loads, however, the sustained load $Q(t)$ – and therefore the total load $L(t)$ – is always "on", i.e., $q = 1$ in Equation 23.

Following the definitions stated in Section 1.2, the frequent and quasi-permanent factors ψ_1 and ψ_2 can be calculated as:

$$\psi_1 = \frac{L_1}{L_k} = \frac{F_{L_{\text{apt}}}^{-1}(1-0.05)}{L_k} \text{ and } \psi_2 = \frac{L_2}{L_k} = \frac{F_{L_{\text{apt}}}^{-1}(1-0.50)}{L_k} \tag{24}$$

where L_k is the characteristic value calculated according to the definition given in NBR 8681:2003 [25] and NBR 6120:2019 [1]

It should be noted that, in order to determine ψ_1 and ψ_2 using Equation 24, one must know the arbitrary point-in-time distribution of the total live load (L_{apt}), which is obtained through Monte Carlo simulation. These simulations, however, can be very time and memory consuming. Alternatively, an approximate theoretical model can be employed that allows one to calculate the relative duration η that $L(t)$ spends above a given load level from the arbitrary point-in-time distributions for the sustained and extraordinary load. Both follow a gamma distribution whose moments are easily determined from the model parameters in Table 1. A more detailed derivation of this analytical model is provided in Corotis and Tsay [49]. Herein, the simulation approach is adopted, since many realizations of the load processes were already carried out in order to derive the 1, 50 and 140-year extreme distributions.

3 RESULTS AND DISCUSSIONS

3.1 Characteristic values of live loads

The characteristic values of live loads for the occupancy types indicated in Table 1 were obtained through Monte Carlo simulation for increasing values of influence area, up to $A = 500\ \text{m}^2$. The obtained results for office and residential buildings are shown in Figures 7 and 8, respectively.

Figure 7a shows the characteristic values as calculated by three approaches: a) as the 70th fractile (30% exceedance probability) of L_{50}; b) as the mode of L_{140}; and c) from the annual maxima L_1 as the value corresponding to the 140-year return period. Those values are compared to the nominal values from different international design codes [22], [23], [24], including the live load reduction prescribed by these codes. The nominal values from NBR 6120:2019 [1] are not indicated, since the Brazilian code does not allow area-based live load reduction; instead, it allows only story-based reduction for columns and foundations. A comparison with NBR 6120:2019 live-load reduction factor is presented in Section 3.2.

In general, the results obtained using the JCSS model seem to be slightly higher than those indicated in the considered design codes. However, a direct comparison is inappropriate, given that the definitions of characteristic value adopted by these codes differ from that of NBR 8681:2003. Furthermore, the curves for the 70th percentile of

L_{50} and the mode of L_{140} are practically coincident, but the results calculated from L_1 are somewhat higher. This occurs because the annual maxima are not fully independent, since the tenancy duration for the sustained load is usually longer than 1 year.

Figure 7b represents, in red, the nominal value ($L_n = 2.5\ \mathrm{kN/m^2}$) given in NBR 6120:2019 for office buildings, and the simulation results for exceedance probabilities of 25% and 35% in 50 years. The blue region between the curves correspond to the values that are in agreement with the definition of characteristic value from NBR 8681:2003. For influence areas around 100 to 120 m^2, the results obtained from the stochastic model are consistent within the 25% to 35% range definition. For the design of an internal beam, an influence area between 100 and 120 m^2 corresponds to a floor plan with a regular span between 7.1 and 7.7 m. For an internal column and considering a single-story load, this interval represents spans between 5.0 and 5.5 m.

Figure 7c shows the frequency with which the maximum total load L_{50} is caused by the combinations denoted by the authors as Cases I to IV, as explained in Table 3. For office buildings, the relative importance of the sustained load in the combination tends to increase while, on the other hand, the extraordinary load becomes less relevant for larger areas.

Table 3. Combinations of sustained and extraordinary loads leading to the maximum total load L_{50}.

Case	Description
I	Lifetime maximum sustained load + maximum extraordinary load during that tenancy
II	Lifetime maximum extraordinary load + corresponding instantaneous sustained load
III	Simultaneous occurrence of lifetime maxima for both sustained and extraordinary loads
IV	Combination where the neither the sustained nor the extraordinary loads are at their maximum values

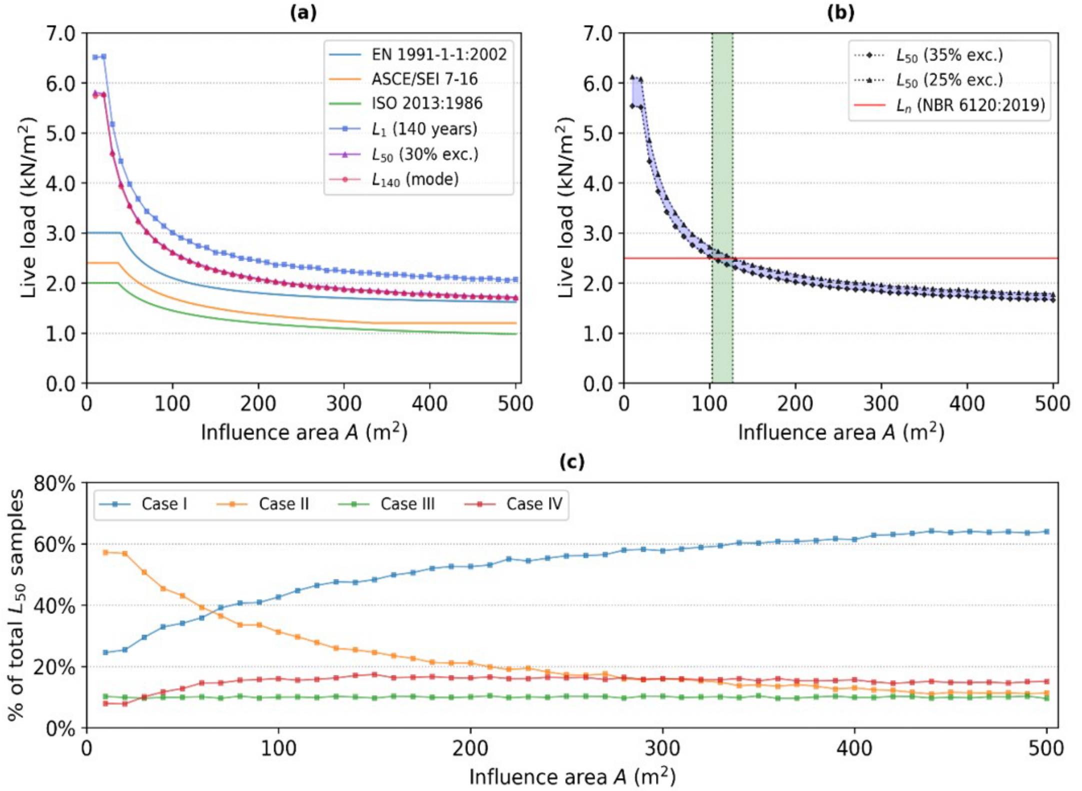

Figure 7. Simulated total live load for office buildings

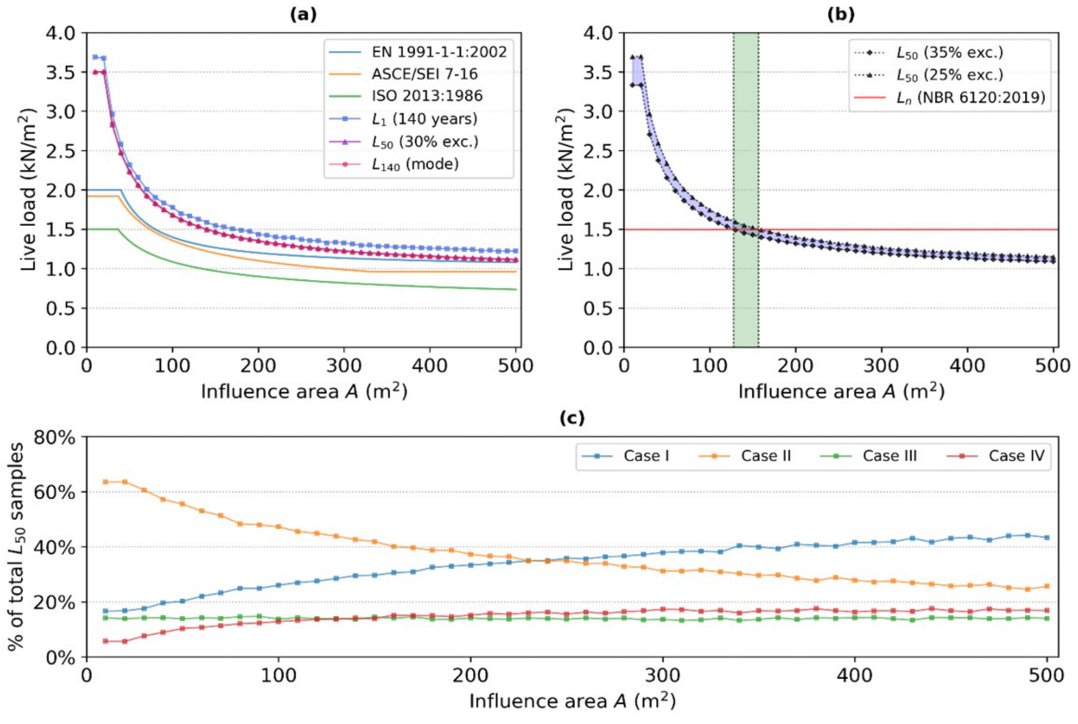

Figure 8. Simulated total live load for residential buildings.

Similar to office buildings, the simulated loads for residential buildings (Figure 8) seem to reasonably agree with the design codes – especially for higher influence areas –, resulting in marginally higher values. This is probably because office and residential buildings are by far the occupancy types with the most amount of available survey data, and therefore have more reliable model parameters. However, for influence areas smaller than 100 m^2, the stochastic model produces loads greater than the normative nominal values; this should be considered with caution when designing elements with small influence area. Figure 8 also shows the same tradeoff between sustained and extraordinary load as the influence area increases.

Similar results for the other occupancy types in Table 1 are shown and discussed in [42] and in the dataset related to this paper (Data Availability Material). The simulation results for classrooms and retail areas using JCSS [27] parameters, not shown here, led to results much higher than the representative values given in design codes [42]. A comparison with parameters used in similar studies [3], [37] shows that the values recommended by the JCSS are unreasonably high and should be revised, especially for the extraordinary load.

The same shortcoming of the JCSS [27] model was also observed by Honfi [41]. In an attempt to bring the results more in line with those of other occupancy types, the author proposed a set of modified parameters for these occupancy types (presented in Table 1), which are used in this study. The suggested parameters are more consistent with the JCSS [27] statement that the standard deviation and mean value of the extraordinary load are usually of the same magnitude. It should be mentioned that, for patient rooms and retail areas, the largest mean duration of the sustained load was adopted ($1/\lambda_Q = 10$ years and $1/\lambda_Q = 5$ years, respectively).

3.2 Live load reduction factor

As shown in the previous results, the characteristic value for live loads is primarily dependent on the influence area A. For larger areas, the equivalent uniformly distributed load tends to decrease, as it becomes more and more unlikely that the load magnitude would be very high over the entire loaded area. To account for this behavior, design codes usually allow some form of live load reduction to be applied.

The ASCE code [22] presents an expression for live load reduction based on the square root of the influence area, allowing for a reduction of up to 50%. Similar expressions can be found in EN 1991-1-1:2002 [23] and ISO 2103:1986 [24]. While the latter unambiguously states that the area to be considered is the tributary area, Eurocode 1 refers only to a “loaded area”, not making clear whether or not the area intended to be used in the formula corresponds to the customary definition of tributary area.

The Brazilian NBR 6120:2019 allows the design loads to be reduced only for columns and foundations. The reduction factor is specified as a function of the number of floors for which live load reduction is permitted. In addition to area-based reduction, Eurocode 1 [23] also allows story-based reduction for columns.

A column typically will have an influence area spanning over multiple floors, each floor owned by a different tenant. However, tenancy changes are not likely to occur over all floors simultaneously. Hence, there is some correlation between two successive values of the sustained load when designing a column, since a tenancy change in one floor only affects part of the area contributing to that effect. McGuire and Cornell [30] studied the influence of tenant arrangement and independence and floor-to-floor-correlation and concluded that the organization of tenants in a building does not significatively affect the upper fractiles of the maximum total load. Therefore, it is reasonable to conservatively assume that one tenant occupies the entirety of the influence area for a column. In this study, the same white-noise model employed in the previous section is also employed for multi-story column design.

In order to compare the stochastic model results with provisions of the Brazilian code, it is necessary to first assume a regular column spacing so that the total influence area of a column can be computed from the number of floors. Two situations were considered: an interior column and an edge column of a multi-story building with regular column spacing of 5 m, which is a usual span for concrete beams. The influence area contributing to the column load is, therefore, $A = 4A_{\text{trib}} = 4 \cdot 5 \cdot 5 = 100\ \text{m}^2$ per supported floor for the interior column, and half that area for the edge column. The adopted peak factor was $\kappa = 2.2$, as indicated by McGuire and Cornell [30] for column loads.

Simulations were performed only for office and residential buildings, since those are the most common reducible occupancy types and the model results have been shown to agree well with the nominal loads specified in NBR 6120:2019. The results are shown in Figure 9. Since each floor would have its own reduction factor, results from the simulations were compared to the average reduction factor over all floors. The story-based live load reduction formula given in Eurocode 1 [23] is also presented, for comparison purposes.

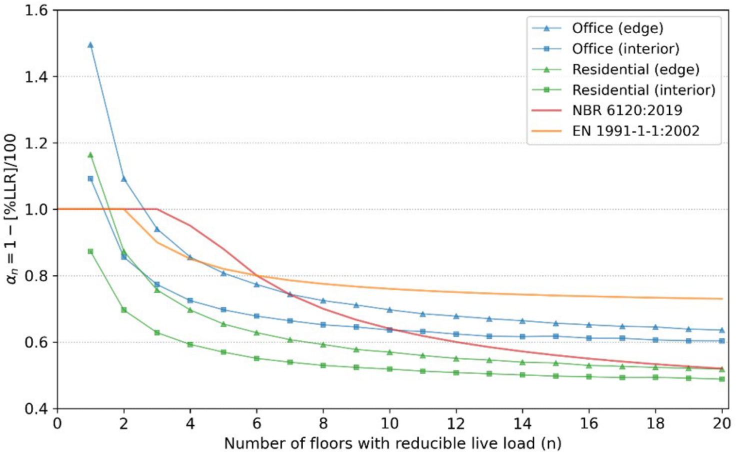

Figure 9. Comparison of the stochastic model results with the live load reduction factor allowed in the Brazilian design code for office and residential buildings.

As can be seen in Figure 9, the live load reduction allowed in NBR 6120:2019 is conservative until around 6 to 10 floors, but then becomes non-conservative, since α_n tends to 0.4 (i.e., an allowed reduction of 60%) when the number of floors increases, but the simulation results caps around 60% of the nominal load for offices and 50% for residential buildings when the area goes to infinity. The story-based reduction formula, on the other hand, seems to be overly conservative, allowing for a maximum reduction of 30%.

Because it is more consistent with the stochastic model, the influence-area based approach employed in ASCE/SEI 7-16 [22] seems to be better suited for determining live load reduction. Similar expressions are proposed for office and residential buildings by fitting simulation data to a power law of the form $\alpha_A = a + bA^{-0.5}$, where A is the influence area:

$$\text{Office} \Longrightarrow \alpha_A = 0.4 + \frac{6.25}{\sqrt{A}} \leq 1.0 \qquad (25)$$

$$\text{Residential} \Longrightarrow \alpha_A = 0.3 + \frac{5.45}{\sqrt{A}} \leq 1.0 \tag{26}$$

Figure 10 compares these two formulas to the simulation values obtained herein for office and residential occupancies: a very good match can be observed. Naturally, for practical applications, it is desirable to have a single formula that is valid for all occupancy types for which reduction is allowed. The objective of this example is only to show that the model presented herein can be used to derive a reasonably simple formula that is both easy to use and provides a good and consistent fit with the mathematical formulation.

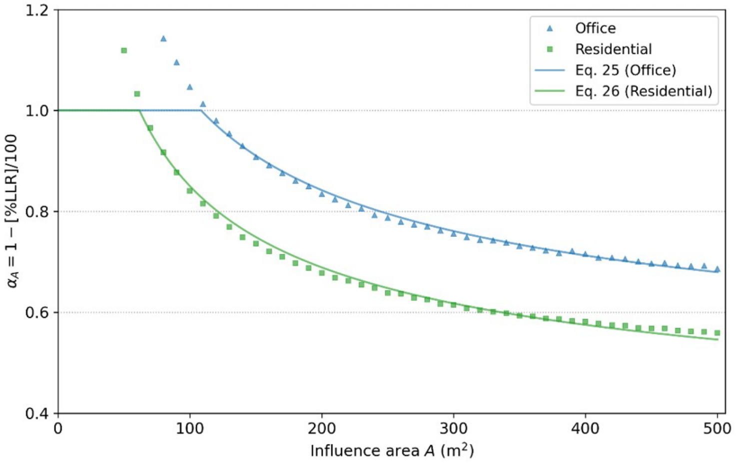

Figure 10. Example of proposed expressions for live load reduction based on influence area.

3.3 Partial safety factor for ULS verification

Figure 11 shows the variation of the partial safety factor γ_L for live loads, estimated using Equation 18, valid for a Gumbel distributed variable. Results for classrooms and retail premises are based upon the modified set of model parameters proposed by Honfi [41] and Costa [42].

It is clear that γ_L varies over a wide range of values for the different occupancy types considered, but tends to decay as the area increases, as a result of the decrease in the coefficient of variation of L_{50}. Table 4 shows the values of γ_L calculated for specific reference areas chosen so that the characteristic value from the simulations is equal to the representative value in NBR 6120:2019. For these areas, the coefficient γ_L seems to lie between 1.50 and 1.60 for most occupancy types. This result is more in line with the values $\gamma_L = 1.60$ prescribed by ASCE/SEI 7-16 [22] and $\gamma_L = 1.50$ found in EN 1991-1-1:2002 [23], This also indicates that the value $\gamma_L = 1.40$ adopted in Brazilian codes is too low and doesn't properly reflect the variability of live loads.

For comparison, Santiago et al. [47] found $\gamma_L = 1.68$ (rounded to 1.70) as result of a reliability-based calibration exercise. Yet, the authors of [47] acknowledged that the live load statistics they employed were leading to unusually low reliability indexes for many of the considered structural configurations, when compared to similar studies. This was the main motivations to develop the study presented herein. Section 3.6 presents the fresh results obtained in a re-evaluation of the reliability-based calibration, which reflect the new live load statistics in Table 4.

As for the 50-year extreme live load (L_{50}) statistics themselves, the results found in this study seem to indicate that the coefficient of variation adopted by Santiago et al. [47] was too high. The statistics indicated in Table 4 are more in line with those presented by Ellingwood et al. [32] and Szerszen and Nowak [50]. The reason why the L_{50} statistics reported by Holický and Sýkora [51] are so unlike the others is because the authors relate the characteristic value to a 5% exceedance probability in a reference period of 50 years, according to the definition found in background documents to the Eurocode 0 pre-standard ENV 1991-1:1994 [52]. In addition to that, Holický and Sýkora [51] only considered the sustained load part.

The average point-in time live load (L_{apt}) statistics obtained in this study have a coefficient of variation somewhat higher than those reported by Ellingwod et al. [32], but a smaller bias factor.

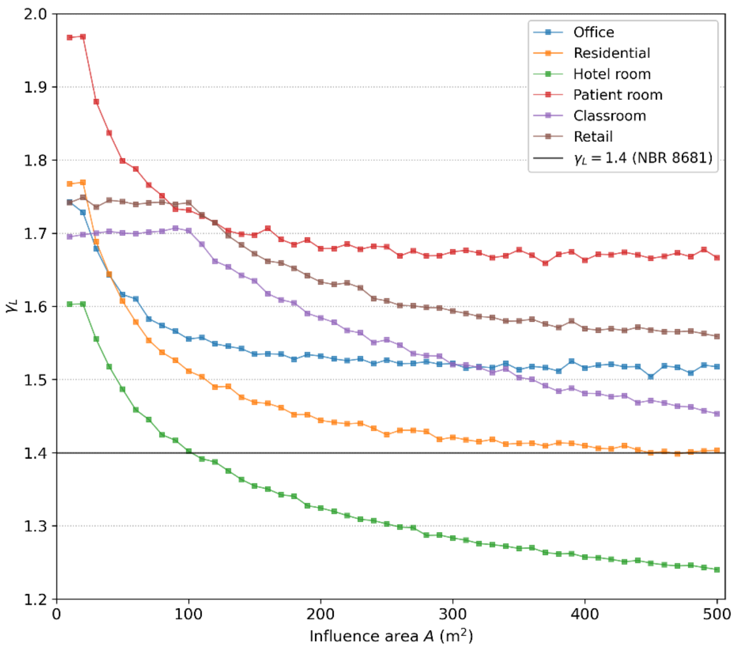

Figure 11. Partial safety factor γ_L with increasing influence area A.

Table 4. Live load statistics and corresponding estimated partial safety factor γ_L for specific reference areas A_{ref} and comparison with statistics from the literature.

Occupancy type	L_n* (kN/m^2)	A_{ref} (m^2)	L_{apt} (Gamma)		L_{50} (Gumbel)		L_{140} (Gumbel)		γ_L	ψ_0
			μ	c.o.v.	μ	c.o.v.	μ	c.o.v.		
Office	2.5	110	0.20 L_n	0.94	0.93 L_n	0.26	1.11 L_n	0.21	1.56	0.42
Residence	1.5	140	0.20 L_n	0.75	0.93 L_n	0.22	1.09 L_n	0.18	1.48	0.52
Hotel room	1.5	220	0.20 L_n	0.24	0.95 L_n	0.14	1.05 L_n	0.13	1.31	0.67
Patient room	2.0	110	0.20 L_n	1.16	0.89 L_n	0.35	1.13 L_n	0.28	1.72	0.42
Classroom	3.0	300	0.20 L_n	0.61	0.92 L_n	0.24	1.09 L_n	0.20	1.52	0.53
Retail	4.0	310	0.22 L_n	0.86	0.92 L_n	0.28	1.11 L_n	0.22	1.59	0.40
Average			**0.21 L_n**	**0.76**	**0.92 L_n**	**0.25**	–	–	**1.53**	**0.49**
Santiago et al. [47]			0.25 L_n	0.55	1.00 L_n	0.40	–	–		
Ellingwood et al. [32]			0.25 L_n	0.55	1.00 L_n	0.25	–	–		
Szerszen and Nowak [50]			–	–	0.93 L_n	0.18	–	–		
Holický and Sýkora [51]			–	–	0.60 L_n	0.35	–	–		

* The reference value L_n for each occupancy type is the nominal value given in NBR 6120:2019 [1].

3.4 Combination factor ψ_0, frequent and quasi-permanent values ψ_1 and ψ_2

Due to space constraints, combination values, frequent and quasi-permanent values are presented and discussed in the dataset related to this manuscript (Data Availability Material).

3.5 Updated reliability-based calibration of NBRs 8681, 6118 and 8800

The live load statistics L_{50} and L_{apt} presented in Table 4, direct result of this study, were used to reprocess the reliability-based calibration of partial load factors and load combination factors of NBRs 8681, 6118 and 8800. Due to space constraints, only the main results are presented here. For more information on the implementation of the calibration procedure, the reader is referred to Santiago et al. [47], where it is described in detail.

Using the new live load statistics, the mean reliability index obtained using current NBR 6118:2014 partial safety factors is equal to 3.17 and using NBR 8800:2008 factors is 3.28. The target reliability index $\beta_T = 3.17$ was considered herein in the calibration.

Table 5. Updated partial safety factors, following the procedure of [47] with new live load statistics.

Coefficient	Before calibration NBR 8800:2008 [45]	Before calibration NBR 6118:2014 [46]	Original calibration [47] $\beta_T = 3.0$	New calibration† $\beta_T = 3.17$
γ_C	–	1.40	1.40	1.40
γ_S	–	1.15	1.15	1.15
γ_{a1}	1.10	–	1.10	1.10
γ_{a2}	1.35	–	1.30	1.40
γ_D	1.25	1.40	1.25	1.20♑
γ_L	1.50	1.40	1.70	1.50
γ_W	1.40	1.40	1.65	1.50
ψ_L	0.50 / 0.70 / 0.80	0.50 / 0.70 / 0.80	0.35	0.45
ψ_W	0.60	0.60	0.30	0.35
$\gamma_L \cdot \psi_L$*	0.75 / 1.05 / 1.20	0.70 / 0.98 / 1.12	0.60	0.68
$\gamma_W \cdot \psi_W$*	0.84	0.84	0.50	0.53

* Effective combination value for secondary action. † Rounded values, to make NBR 6118 compatible with NBR 8800. ♑ This coefficient is suggested to remain 1.4 when live and wind loads are zero.

Results for the re-calibration are presented in Table 5. The main effect observed in [47] is also observed here: more uniform reliability indexes, for the different structures designed using the codes, are obtained by increasing the main variable load and reducing the secondary load in the combinations. The recommended values for live load ($\gamma_L = 1.5$) and for wind load ($\gamma_W = 1.5$) are very close to the values recommended in Eurocodes. The values $\gamma_L = 1.5$ and $\psi_L = 0.45$ obtained in the reliability-based calibration are very close to the $\gamma_L = 1.52$ and $\psi_0 = \psi_L = 0.51$ obtained herein as the mean for different occupancy types (see Table 4). The partial safety factors in Table 5 are recommended to be adopted in future revisions of NBRs 8681, 6118 and 8800.

4 CONCLUDING REMARKS

In this paper, the temporal and spatial variability of the live load in buildings is addressed, using a stochastic model that is well documented in the literature. Due to the lack of survey data for Brazilian buildings, the model parameters suggested by JCSS [27] and Honfi [41] were adopted. Monte Carlo simulations were performed for office buildings, residential buildings, hotel rooms, patient rooms, classrooms, and retail areas. From the results, the following conclusions can be drawn:

a) The parameters μ_Q and $\sigma_{U,Q}$ for sustained load suggested by JCSS seem to be largely based on the summary of survey data presented by Chalk and Corotis [3]. The $\sigma_{V,Q}$ parameter seems to be slightly larger than the findings of those authors, but not unreasonably so.

b) There is some contradiction in the JCSS Probabilistic Model Code over whether the extraordinary load should be modeled as a gamma or an exponential distribution. It is the authors' personal belief that the gamma distribution is more adequate, which is backed by most of the studies employing similar models found in the literature.

c) The parameters for the extraordinary load are mostly empirical, since there are very few survey data regarding this kind of load. For classrooms and retail premises, the JCSS suggested parameters are unreasonably high when compared to similar studies.

d) Brazilian code NBR 6120:2019 presents two definitions for the characteristic value of live loads: exceedance probabilities between 25 to 35%, and mean return periods between 174 and 117 years. The second definition would only be true if the annual maxima for live loads were independent, which is not the case, given that the mean time between occupancy changes is greater than one year for most uses. Hence, NBR 6120:2019 should follow NBR 8681:2003 and limit itself to the first definition.

e) Employing the model described herein, live load statistics that are consistent with the definitions given by Brazilian design codes were derived to be used in reliability analyses. The obtained fifty-year extreme live load (L_{50}) has a bias factor of 0.92 and coefficient of variation of 25%. For the arbitrary point-in-time distribution (L_{apt}), those values are equal to 0.21 and 76%, respectively. The obtained statistic for L_{50} has a smaller coefficient of variation than the one employed by Santiago [53] and is more in line with most of the statistics reported by other authors in the literature. The arbitrary point-in-time distribution (L_{apt}) obtained herein is also significantly different than that of [53].

f) The reference areas shown in Table 4 for which the nominal load values given in NBR 6120:2019 are reproduced by the stochastic model depend on occupancy type. These areas are somewhat greater than those considered in similar studies, such as Chalk and Corotis [3] – which employs a different model for the extraordinary load with both the mean and standard deviation decaying with the increase in area – further corroborating that the JCSS parameters might be overly conservative. Investigations by Costa [42] show that, while the reference areas that lead to Brazilian nominal loads obtained using other models for intermittent loads are smaller, their corresponding bias factors and coefficients of variation do not change appreciably with respect to the values reported in Table 4 for the JCSS model. Hence, it is the authors understanding that the L_{50} and L_{apt} statistics presented herein are adequate for use in reliability problems.

g) Currently, NBR 6120:2019 allows live load reductions only for columns and foundations, and the reduction factor is given as a function of the number of supported floors. However, an approach similar to ASCE/SEI 7-16 [22] is more consistent with the stochastic model, i.e., allowing live loads to be reduced for floor beams and slabs as well (although to a smaller extent), and based on the influence area.

h) The obtained results show that the partial safety factor for live loads currently employed in Brazilian codes ($\gamma_L = 1.40$ for grouped variable actions) is too low and should be revised. Using the live load statistics obtained herein, the reliability-based calibration of partial safety factors of NBRs 8681, 6118 and 8800 was re-processed, following Santiago et al. [47]. Using the target reliability index $\beta_T = 3.17$, $\gamma_L = \gamma_W = 1.5$ were found, which are recommended for adoption in future revision of the above codes. Suggested combination values are $\psi_L = 0.45$ and $\psi_W = 0.35$.

i) The results presented in the complementary dataset (Data Availability Material) related to this study also showed that, in general, the combination factor ψ_0 and the frequent value reduction factor ψ_1 should probably be higher for Category A buildings (residential and other private access buildings). On the other hand, a quasi-permanent reduction factor of $\psi_2 = 0.3$ seems to be sufficient for all occupancy types considered in this study, whereas a value of $\psi_2 = 0.4$ is currently prescribed for Category B buildings (office and other public access buildings). It should be noted that these results are very sensitive to the model parameters, which – as previously stated – need further investigation, and should therefore be considered with caution.

The probabilistic model employed in this study was shown to be appropriate to represent live load variability. Most of the obtained results show good agreement with the nominal loads found in Brazilian and foreign design codes, especially for office and residential buildings, since those are the occupancies most extensively surveyed. However, the majority of load survey data that backs up the model parameters was gathered decades ago. Ideally, new surveys should be carried out using modern technologies in order to validate and further support the stochastic model parameters.

ACKNOWLEDGEMENTS

Funding of this research project by Brazilian agencies CNPq (Brazilian National Council for Research, grant n. 309107/2020-2) and joint FAPESP-ANID (São Paulo State Foundation for Research – Chilean National Agency for Research and Development, grant n. 2019/13080-9 are cheerfully acknowledged. Valuable comments by the anonymous reviewers are also cheerfully acknowledged.

REFERENCES

[1] Associação Brasileira de Normas Técnicas, *Design Loads for Structures*, ABNT NBR 6120, 2019, 61 p.

[2] L. Sentler, *Live Load Surveys, a Review with Discussions* (Rep. 78). Lund, Sweden: Div. Build. Technol., Lund Inst. Technol., 1976.

[3] P. L. Chalk and R. B. Corotis, "Probability model for design live loads," *J. Struct. Div.*, vol. 106, no. 10, pp. 2017–2033, 1980, http://dx.doi.org/10.1061/JSDEAG.0005542.

[4] R. J. Dayeh, *Live Loads in Office Buildings – A Pilot Survey.* Sydney, Australia: Exp. Build. Station, Dept. Housing and Constr., N.W.S., 1974.

[5] C. H. Blackall, *Am. Architect. Build. News*, vol. XLI, no. 922, pp. 129–131, Aug 1893.

[6] C. H. Blackall, *Am. Architect. Archit. Rev.*, pp. 6–8, Jan. 1923.

[7] C. T. Coley, "A study of office building live loads," *ENR*, vol. 90, no. 13, pp. 584–586, Mar 1923.

[8] I. H. Woolson, *Recommended Minimum Requirements for Small Dwelling Construction* (Rep. Build. Code Comm.). Washington, DC, USA: US Dept. Commer., Nat. Bur. Stand., Jul. 1922.

[9] I. H. Woolson, *Minimum Live Loads Allowable for use in Design of Buildings* (Rep. Build. Code Comm.). Washington, DC, USA: US Dept. Commer., Nat. Bur. Stand., Nov. 1925.

[10] J. W. Dunham, "Design live loads in buildings," *Trans. Am. Soc. Civ. Eng.*, vol. 112, no. 1, pp. 725–739, 1947., http://dx.doi.org/10.1061/TACEAT.0006009.

[11] J. W. Dunham, C. N. Brekke, and G. N. Thompson, *Live Loads on Floors in Buildings* (Build. Mat. Struct. Rep. 133). Washington, DC, USA: US Dept. Commer., Nat. Bur. Stand., Dec. 1952.

[12] J. O. Bryson and D. Gross, *Techniques for the Survey and Evaluation of Live Floor Loads and Fire Loads in Modern Office Buildings* (Build. Sci. Ser. 16). Washington, DC, USA: US Dept. Commer., Nat. Bur. Stand., Dec 1968.

[13] C. G. Culver, *Survey Results for Fire Loads and Live Loads in Office Buildings* (Build. Sci. Ser. 85). Washington, DC, USA: US Dept. Commer., Nat. Bur. Stand., May 1976.

[14] E. Paloheimo and M. Ollila, *Research in the Live Loads in Persons*. Helsinki, Finland: Minist. Domest. Aff., 1973.

[15] C. M. White, *Survey of Live Loads in Offices* (First Interim Rep. Steel Struct. Res. Comm.). London, UK: His/Her Majesty's Stationery Office, 1931, pp. 45–65.

[16] G. R. Mitchell and R. W. Woodgate, *Floor Loadings in Office Buildings: Results of a Survey* (CP 3/71). Garston, UK: Build. Res. Station, Dept. Environ., Jan. 1971.

[17] G. R. Mitchell and R. W. Woodgate, *Floor Loading in Retail Premises: Results of a Survey* (CP 25/71). Garston, UK: Build. Res. Station, Dept. Environ., Sept. 1971.

[18] G. R. Mitchell and R. W. Woodgate, *Floor Loadings in Domestic Buildings: Results of a Survey* (CP 2/77). Garston, UK: Build. Res. Station, Dept. Environ., Jan. 1977.

[19] T. Karman, *Statistical Investigations on Live Loads on Floors* (Stud. Doc. CIB W23). Madrid, Spain: Int. Counc. Build. Res., Nov. 1969.

[20] L. Sentler, *A Live Load Survey in Domestic Houses* (Rep. 47). Lund, Sweden: Div. Build. Technol., Lund Inst. Technol., 1974.

[21] L. Sentler, *A Live Load Survey in Office Buildings and Hotels* (Rep. 47). Lund, Sweden: Div. Build. Technol., Lund Inst. Technol., 1974.

[22] American Society of Civil Engineers, *Minimum Design Loads and Associated Criteria for Buildings and Other Structures*, ASCE/SEI 7-16, 2016, 822 p.

[23] European Committee for Standardization, *Eurocode 1: Actions on Structures – Part 1-1: General Actions – Densities, Self-Weight, Imposed Loads for Buildings*, EN 1991-1-1, 2002, 44 p.

[24] International Organization for Standardization, *Loads Due to Use and Occupancy in Residential and Public Buildings*, ISO 2103, 1986, 3 p.

[25] Associação Brasileira de Normas Técnicas, *Actions and Safety of Structures – Procedure*, ABNT NBR 8681, 2003, 18 p.

[26] Associação Brasileira de Normas Técnicas, *Design Loads for Structures*, ABNT NBR 6120, 1980, 5 p.

[27] Joint Committee on Structural Safety, *Probabilistic Model Code – Part 2: Load Models.* 2001. [Online]. Available: https://www.jcss-lc.org/jcss-probabilistic-model-code/

[28] J.-C. Peir, *A Stochastic Live Load Model for Buildings* (Res. Rep. R71-35). Cambridge, MA, USA: Massachusetts Inst. Technol., Dept. Civ. Eng., Sept. 1971.

[29] J.-C. Peir and C. A. Cornell, "Spatial and temporal variability of live loads," *J. Struct. Div.*, vol. 99, no. 5, pp. 903–922, 1973, http://dx.doi.org/10.1061/JSDEAG.0003512.

[30] R. K. McGuire and C. A. Cornell, "Live load effects in office buildings," *J. Struct. Div.*, vol. 100, no. 7, pp. 1351–1366, 1974, http://dx.doi.org/10.1061/JSDEAG.0003816.

[31] B. Ellingwood and C. Culver, "Analysis of live loads in office buildings," *J. Struct. Div.*, vol. 103, no. 8, pp. 1551–1560, 1977, http://dx.doi.org/10.1061/JSDEAG.0004693.

[32] B. Ellingwood, T. V Galambos, J. G. MacGregor, and C. A. Cornell, *Development of a Probability Based Load Criterion for American National Standard A58* (Spec. Publ. 577). Washington, DC, USA: US Dept. Commer., Nat. Bur. Stand., Jun. 1980.

[33] R. Hauser, "Load correlation models in structural reliability," M.S. thesis, Massachusetts Inst. Technol., Dept. Civ. Eng., Cambridge, MA, USA, 1970.

[34] E. C. C. Choi, "Live load for office buildings: effect of occupancy and code comparison," *J. Struct. Eng.*, vol. 116, no. 11, pp. 3162–3174, 1990, http://dx.doi.org/10.1061/(ASCE)0733-9445(1990)116:11(3162).

[35] N. L. Tran, D. Müller, and C. Graubner, "Floor live loads of building structures," in *Proc. 14th Int. Probab. Workshop*, Cham: Springer, 2017, pp. 471–484, https://doi.org/10.1007/978-3-319-47886-9_32.

[36] R. B. Corotis and V. A. Doshi, "Probability models for live-load survey results," *J. Struct. Div.*, vol. 103, no. 6, pp. 1257–1274, 1977, http://dx.doi.org/10.1061/JSDEAG.0004651.

[37] M. E. Harris, R. B. Corotis, and C. J. Bova, "Area-dependent processes for structural live loads," *J. Struct. Div.*, vol. 107, no. 5, pp. 857–872, 1981, http://dx.doi.org/10.1061/JSDEAG.0005709.

[38] Y. K. Wen, "Statistical combination of extreme loads," *J. Struct. Div.*, vol. 103, no. 5, pp. 1079–1093, 1977., http://dx.doi.org/10.1061/JSDEAG.0004630.

[39] E. C. C. Choi, *Data structure and Data Processing Procedures for Live Loads and Fire Loads in Office Buildings* (Tech. Rec. 524). Sydney, Australia: Nat. Bdg. Technol. Ctr.,, 1988.

[40] E. C. C. Choi, "Extraordinary live load in office buildings," *J. Struct. Eng.*, vol. 117, no. 11, pp. 3216–3227, 1991., http://dx.doi.org/10.1061/(ASCE)0733-9445(1991)117:11(3216).

[41] D. Honfi, "Serviceability floor loads," *Struct. Saf.*, vol. 50, pp. 27–38, 2014., http://dx.doi.org/10.1016/j.strusafe.2014.03.004.

[42] L. G. L. Costa, "Modelos probabilísticos para ações variáveis brasileiras," M.S. thesis, São Carlos Sch. Eng., Univ. São Paulo, São Carlos, 2023 [in preparation].

[43] European Committee for Standardization, *Eurocode: Basis of Structural Design*, EN 1990, 2002, 116 p.

[44] H. Gulvanessian, J.-A. Calgaro, and M. Holický, *Designers' Guide to EN 1990 Eurocode: Basis of Structural Design.* London: Thomas Telford Publ., 2002, https://doi.org/10.1680/dgte.30114.

[45] Associação Brasileira de Normas Técnicas, *Design of Steel and Composite Structures for Buildings*, ABNT NBR 8800, 2008, 237 p.

[46] Associação Brasileira de Normas Técnicas, *Design of Concrete Structures – Procedure*, ABNT NBR 6118, 2014, 238 p.

[47] W. C. Santiago, H. M. Kroetz, S. H. C. Santos, F. R. Stucchi, and A. T. Beck, "Reliability-based calibration of main brazilian structural design codes," *Lat. Am. J. Solids Struct.*, vol. 17, no. 1, e245, 2020.

[48] International Organization for Standardization, *General Principles on Reliability for Structures*, ISO 2394, 1998, 73 p.

[49] R. B. Corotis and W. Tsay, "Probabilistic load duration model for live loads," *J. Struct. Eng.*, vol. 109, no. 4, pp. 859, 1983, http://dx.doi.org/10.1061/(ASCE)0733-9445(1983)109:4(859).

[50] M. M. Szerszen and A. S. Nowak, "Calibration of design code for buildings (ACI 318): Part 2 – reliability analysis and resistance factors," *ACI Struct. J.*, vol. 100, no. 3, pp. 383–391, 2003, http://dx.doi.org/10.14359/12614.

[51] M. Holický and M. Sýkora, "Conventional probabilistic models for calibration of codes," in *Proc. 11th Int. Conf. Appl. Statist. Probab. Civ. Eng.*, M. H. Faber, J. Köhler and K. Nishijima, Eds. Zurich, Switzerland: CRC Press, 2011, pp. 969–976.

[52] European Committee for Standardization, *Eurocode 1: Basis of Design and Actions on Structures – Part 1: Basis of Design*, ENV 1991-1, 1994.

[53] W. C. Santiago, "Calibração baseada em confiabilidade dos coeficientes parciais de segurança das principais normas brasileiras de projeto estrutural," Ph.D. dissertation, São Carlos Sch. Eng., Univ. São Paulo, São Carlos, 2019.

[54] Conseil International du Bâtiment pour la Recherche, l'Etude et la Documentation, *Actions on Structures – Live Loads in Buildings* (CIB Report 116). Rotterdam, Netherlands, Jun. 1989, 48 p.

Author contributions: LGLC: conceptualization, computer programming, data manipulation, formal analysis, methodology, writing; WCS: data manipulation, formal analysis, proofreading; ATB: formal analysis, writing review, proofreading, supervision.

Editors: Luis Oliveira Santos, Guilherme Aris Parsekian.

IBRACON Structures and Materials Journal
Revista IBRACON de Estruturas e Materiais
ISSN 1983-4195 ismj.org

ORIGINAL ARTICLE

Sonicating polycarboxylate-based superplasticizer for application in cementitious matrix

Sonicação de superplastificante à base de policarboxilato para aplicação em matrizes cimentícias

Laura Silvestro[a,b]
Artur Spat Ruviaro[a]
Geannina Terezinha dos Santos Lima[a]
Paulo Ricardo de Matos[c]
Erich Rodríguez[d]
Philippe Jean Paul Gleize[a]

[a]Universidade Federal de Santa Catarina, Department of Civil Engineering, Florianópolis, SC, Brasil
[b]Universidade Federal Tecnológica do Paraná, Guarapuava, PR, Brasil.
[c]Universidade Federal de Santa Maria, Coordenadoria Acadêmica, Campus Cachoeira do Sul, Cachoeira do Sul, RS, Brasil
[d]Universidade Federal de Santa Maria, Department of Structures and Civil Construction, Santa Maria, RS, Brasil

Received 15 April 2022
Accepted 11 August 2022

Abstract: Sonication is widely used for nanomaterials dispersion in cementitious matrices. Polycarboxylate-based superplasticizer (SP) admixtures are usually incorporated in the aqueous nanomaterials suspension before sonication to improve the dispersion of these materials. Nevertheless, the effect of sonicating SP on its molecular structure or dispersing performance has not been fully investigated. This work assessed the effect of sonicating a commercial SP at 20 kHz, 750 W power, 50 or 80% amplitude, during 15 and 30 min. Initially, the sonication effect was evaluated in aqueous suspension by determining the SP size distribution (through dynamic light scattering – DLS) and zeta potential. Subsequently, the aqueous SP suspensions were used for Portland cement paste production. Rheological tests up to 120 minutes and compressive strength at 14 and 28 days were conducted. DLS and zeta potential results suggested that sonication reduce the size of SP chains. As a result, SP sonication increased the initial dynamic yield stress, viscosity, and hysteresis area of cement pastes. In contrast, SP sonication improved its time-dependent dispersing performance, resulting in pastes with reduced viscosity from 80 minutes onwards. Finally, SP sonication did not affect the compressive strength of cement pastes at 14 and 28 days of hydration. Overall, when SP is sonicated together with nanoparticles for application in cementitious matrices, the effect of sonicating the chemical admixture must be considered when the fresh-state properties of the composite are evaluated.

Keywords: superplasticizer, sonication, cement paste, rheology.

Resumo: A sonicação é amplamente utilizada para dispersão de nanomateriais em matrizes cimentícias. Aditivos superplastificantes à base de policarboxilato (SP) são geralmente incorporados na suspensão aquosa de nanomateriais antes da sonicação para melhorar a dispersão desses materiais. No entanto, o efeito da sonicação na estrutura molecular e no desempenho de dispersão do SP não foi totalmente investigado. Este trabalho avaliou o efeito da sonicação de um SP comercial a 20 kHz, potência de 750 W, amplitude de 50 e 80%, durante 15 e 30 min. Inicialmente, o efeito de sonicação foi avaliado em suspensão aquosa, determinando a distribuição de tamanho do SP (através de espalhamento dinâmico de luz – DLS) e potencial zeta. Posteriormente, as suspensões aquosas de SP foram utilizadas para a produção de pastas de cimento Portland. Foram realizados ensaios reológicos durante os primeiros 120 minutos de hidratação e a resistência à compressão foi avaliada aos 14 e 28 dias. Os resultados do potencial zeta e DLS sugeriram que a sonicação reduz o tamanho das cadeias de SP. Como resultado, a sonicação do SP aumentou a tensão de escoamento dinâmica inicial, a viscosidade e a área de histerese das pastas de cimento. Em contraste, a sonicação SP melhorou seu desempenho de dispersão ao longo do tempo, resultando em pastas com viscosidade reduzida a partir de 80 minutos. Finalmente, a sonicação SP não afetou a resistência à compressão das pastas de cimento aos 14 e 28 dias de hidratação. Em geral,

Corresponding author: Laura Silvestro. E-mail: laurasilvestro1@gmail.com
Financial support: CAPES, CNPq, FAPESC from Brazil provided financial support for the study.
Conflict of interest: Nothing to declare.
Data Availability: The data that support the findings of this study are available from the corresponding author, LS, upon reasonable request.

quando o SP é disperso via sonicação juntamente com nanopartículas para aplicação em matrizes cimentícias, o efeito de sonicação do aditivo químico deve ser levado em consideração quando as propriedades de estado fresco do compósito são avaliadas.

Palavras-chave: superplastificante, sonicação, pastas de cimento, reologia.

How to cite: L. Silvestro, A. S. Ruviaro, G. T. S. Lima, P. R. Matos, E. Rodríguez, and P. J. P. Gleize, "Sonicating polycarboxylate-based superplasticizer for application in cementitious matrix" *Rev. IBRACON Estrut. Mater.*, vol. 16, no. 2, e16205, 2023, https://doi.org/10.1590/S1983-41952023000200005

1 INTRODUCTION

Sonication is widely used for nanomaterials dispersion for application in cementitious matrices, such as carbon nanotubes [1]–[5], nanosilica [6]–[10], silicon carbide nanowhiskers [11]–[13], nano-clay [14], [15], silica fume [16], among others. The high performance of nanoparticles used in cementitious materials is mainly due to their high specific surface area, which – in most cases – is reduced by its susceptibility to agglomeration. This effect reduces the mechanical strength of these cementitious nanocomposites. Thus, sonication is commonly used for enhancing the nanomaterials' dispersion. In this dispersion process, a cavitation field produces microbubbles that promote the nanomaterial agglomerates exfoliation [17], as well as (in some cases) the sonication promotes the formation of charged holes (h^+) on the nanoparticles' surface [18]. The nanomaterials' dispersion degree via sonication is a function of several aspects such as duration, intensity, output frequency, energy applied, sonicator type (bath or tip) and transducer oscillator, temperature, content, as well as characteristics of the nanomaterial dispersed [19], [20]. Tip sonicators provide denser energy compared to bath sonicators, where the ultrasounds are irradiated from the edge of the metallic tip to a smaller area around it. This concentrates the cavitational activity area, and a stronger spray is formed, which also produces an aggressive agitation of the solution [17]. Thus, the dispersion through tip sonicators usually requires a shorter duration than bath sonicators [20].

According to the literature, most of the studies with carbon nanotube addition in cement-based materials used sonication treatment to improve the nanomaterial dispersion, combined with the incorporation of dispersants (e.g., polycarboxylate-based superplasticizers – SP) [21]. The use of SP for nanomaterial's dispersion is attractive due to the compatibility of these admixtures with cement particles. Furthermore, this approach avoids using other types of dispersants (e.g., surfactants), reducing the possibility of incompatibility between matrix components and cement particles [22]. In this context, Sindu and Sasmal [23] reported that the use of surfactants like Sodium dodecyl benzene sulphonate (SDB), sodium lauryl sulphate (SLSD), and Triton X-100 (TX) for CNTs dispersion generally reduced the 28-day compressive and tensile strengths of cementitious composites compared to plain cement paste. This behavior was attributed to the surfactants that may have hindered the Portland cement hydration and increased the content of air trapped into the matrix, as evidenced by the density of the composites [23].

Concerning the duration of the sonication process for nanomaterials dispersion, long periods are usually used. For instance, Ma et al. [24] dispersed CNTs in mixing water with a polycarboxylate-based SP through sonication in a high-intensity sonicator (500 W) for 1 hour at 40% amplitude. Mohsen et al. [25] sonicated an aqueous CNTs suspensions with polycarboxylate-based SP for 30 minutes at 20% amplitude. Similarly, Sedaghatdoost and Behfarnia [26] dispersed CNTs and polycarboxylate-based SP by sonication for 30 minutes. According to Assi et al. [20], CNTs' dispersion via sonication is usually conducted during a period from 20 to 45 minutes. In this context, the SP usually is added to aqueous suspensions of nanomaterials before the sonication process, i.e., it is dispersed together with the nanomaterial. Several studies have reported that excessive sonication energy can damage the CNTs and, therefore, compromise the ability to enhance the mechanical properties of composites with the incorporation of these nanomaterials [27]–[29]. However, the effect of the sonication process on the molecules of SP admixtures used in cementitious composites has not yet been reported.

In other research fields, previous studies have reported that sonication is used for the degradation of surfactants. For instance, Dehghani et al. [30] used an ultrasonic bath to evaluate the degradation of an anionic surfactant. The results reported by the authors indicated that the duration of sonication plays an important role in the integrity of the surfactant. The surfactant degradation rate gradually increases with the process duration. In turn, an opposite trend was observed regarding the surfactant concentration: there was a decrease in the surfactant degradation rate with the increase of its concentration. Campbell and Hoffmann [31] also assessed surfactants degradation via sonication. The results showed that the degradation rate increased with the increase in power density applied. Similarly, Bhandari et al. [32] investigated the use of ultrasonic for degradation of sodium dodecyl sulfate surfactant in order to reduce water resources contamination.

Considering that sonication can cause the degradation of surfactants, it is expected to influence admixtures developed for application in cementitious matrices. Nevertheless, the effect of sonication on admixtures for cement-based materials has not been fully investigated. One of the only works on this topic is from Poinot et al. [33]. The authors observed that sonication of commercial water retention admixtures (hydroxypropyl methyl cellulose and hydroxypropyl guar) promoted an expressive molecular weight reduction of the molecules evaluated.

Although sonication is widely used for the dispersion of nanomaterials aiming for application in cementitious matrices, the effect of this dispersion process on the polycarboxylate-based superplasticizer admixtures has not been fully assessed. Thus, this work aimed to evaluate the effect of this dispersion process on the size distribution and zeta potential when a commercial polycarboxylate SP was sonicated. Furthermore, the effect of sonication of SP admixture on the rheology and compressive strength of Portland cement pastes was also evaluated.

2 MATERIALS AND METHODS

2.1 Materials

Portland cement (PC) was used for paste production. Table 1 details its chemical composition determined by X-ray fluorescence (XRF) using an EDX-7000 (Shimadzu, Tokyo, Japan) equipment, in addition to its physical properties. The size distribution of PC was evaluated through laser diffraction in air dispersion using a Particle Size Analyzer S3500 (Microtrac, Pennsylvania, USA) equipment. The specific surface area (SSA) of the PC was determined through the Brunauer–Emmett–Teller (BET) method (Autosorb Quantachrome Instruments, Florida, USA) with nitrogen adsorption. The sample was pre-heated at 40 ^{0}C during 12 h. The mineralogical composition of PC presented in Table 2 was obtained by X-ray diffraction (XRD) and Rietveld analysis. The analysis was conducted using an X'Pert Pro (PANalytical, Almelo, The Netherlands) diffractometer operating at 45 kV and 40 mA with CuK$\alpha_{1,2}$ radiation (λ = 1.5418 Å), scanning range of 7–70^0 2θ, and step size of 0.0167° 2θ. Rietveld quantitative phase analysis (QPA) was conducted using TOPAS v5 (Bruker) software and ICSD database (also detailed in Table 2).

Table 1. Chemical composition determined by XRF and physical properties of the cement used.

Property	Value
Al_2O_3 (wt.%)	4.40
SiO_2 (wt.%)	18.62
Fe_2O_3 (wt.%)	3.00
CaO (wt.%)	62.75
MgO (wt.%)	3.80
SO_3 (wt.%)	3.08
Loss on ignition at 950 ^{0}C (wt.%)	3.41
Insoluble residue	0.94
D_{10} (µm)	2.91
D_{50} (µm)	11.1
D_{90} (µm)	29.1
Mean diameter (µm)	13.1
Density (kg/m^3)	3,100
BET specific surface area (m^2/g)	2.22

Table 2. Mineralogical composition of the cement used obtained by XRD-Rietveld QPA.

Phase	ICSD code	PC (wt. %)
C_3S M1	*	44.11
C_3S M3	94742	17.36
C_2S á	81097	0.75
C_2S â	79550	10.33
C_3A cub	1841	2.70
C_4AF	9197	8.02
Goergeyite	30790	2.57
Syngenite	157072	2.42
Periclase	9863	1.12
Bassanite	69060	0.81
Gypsum	151692	3.43
Calcite	73446	5.93
Quartz	174	0.45
R_{wp} (%)		5.11

* Not in ICSD; crystal structure from Noirfontaine et al. [34].

A commercial polycarboxylate-based superplasticizer (SP) was evaluated in this study. The SP had a solid content of 42.0 wt.%, density of 1,120 kg/m^3, and pH of 6.15 at 23°C. For SP characterization, Fourier transform infrared spectroscopy (FTIR) was conducted in a liquid sample. The test was carried out in a Cary 600 Series FTIR Spectrometer using the following parameters: analysis range from 500 to 4000 cm^{-1}, resolution of 2 cm^{-1}, and 32 accumulations. Figure 1 shows the FTIR spectrum of the SP. The absorption peaks around 3300-3400 and 1639 cm^{-1} are attributed to O–H bond of water [35]. The absorption peaks at 2924 and 2875 cm^{-1} can be assigned to the stretching vibration of C–H bond from aliphatic groups [36]. The peaks at 1455, 1349, 1247, 1087, and 950 cm^{-1} belong to CH_2, CH_3, C–O, C–O–C, and C–C bonds, respectively [35], [37]. These peaks are characteristic of aliphatic, carbonyl, and ether groups present in SP [38].

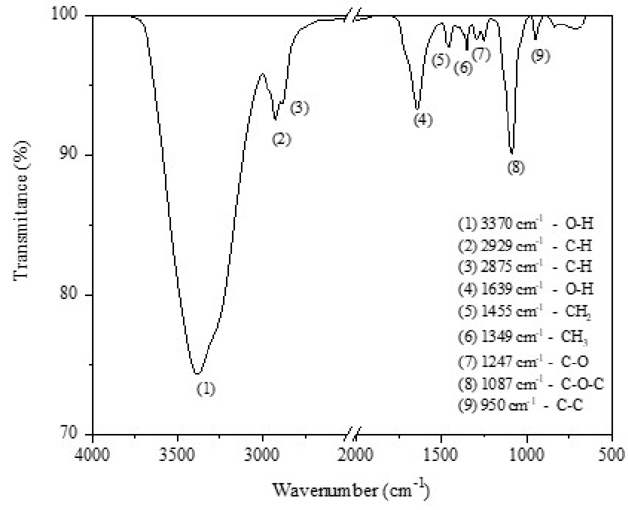

Figure 1. FTIR spectrum of the polycarboxylate-based SP.

2.2 Sample preparation

The SP aqueous dispersions evaluated are detailed in Table 3. The proportions of water and SP were defined to obtain cement pastes with a water-to-cement ratio of 0.4 and a SP content of 0.2 wt.% by weight of cement. Initially, fixed amounts of deionized water (48.0 g) and SP (0.24 g) were mixed and sonicated using a 13-mm ultrasonic probe VCX Serie Vibra-Cell, characterized by a maximum power of 750 W and frequency output of 20 kHz (Sonics & Materials Inc., Newtown, CT, USA). The solution was sonicated in a glass beaker of 50 ml, where the transductor probe was immersed at approximately 10 mm of the bottom, as illustrated in Figure 2. To prevent the samples from overheating, pulses of 20 seconds and resting of 20 seconds were alternated during the sonication process. Besides, the samples were sonicated in an ice bath for the same purpose. Two amplitudes (50 and 80%) and two duration times (15 and 30 minutes) of sonication were evaluated. Furthermore, a control sample (i.e., with superplasticizer not subjected to sonication) was also evaluated for comparison. After that, the SP aqueous dispersions were added to 120.0 g of cement and mixed for 2 minutes in a high-shear mixer at 10,000 rpm.

Table 3. SP aqueous dispersions evaluated.

Sample	Water (g)	SP (g)	Sonication parameters				
			Amplitude (%)	Duration (min)	Energy (J)	Energy (J/g of SP)	Temperature (^{0}C)
SP	48.00	0.24	-	-	-	-	-
SP-A50%-15 min	48.00	0.24	50	15	28,035.0	116,812.5	25
SP-A50%-30 min	48.00	0.24	50	30	56,146.0	233,941.7	25
SP-A80%-15 min	48.00	0.24	80	15	62,512.0	260,466.7	32
SP-A80%-30 min	48.00	0.24	80	30	125,537.0	523,070.8	32

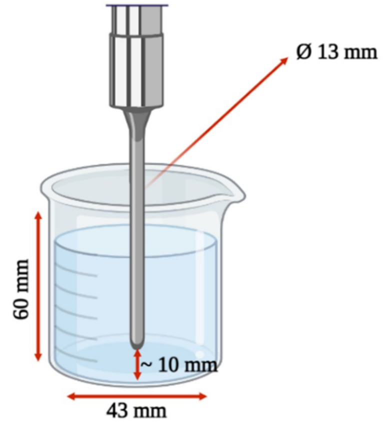

Figure 2. Schematic representation of the position of the ultrasonic probe in the glass beaker containing the aqueous SP solution.

2.3 Testing methods

2.3.1 Tests conducted in aqueous solution

For the SP aqueous solution characterization, zeta potential and size distribution measured by dynamic light scattering (DLS) were performed. The tests were carried out in a Zetasizer Nano (Malvern, UK). The analyses were conducted at 23 ^{0}C with a range from 3.8 nm to 100 µm. Before performing the analyses, the SP aqueous suspensions were vacuum filtered in a filter with a retention capacity of 7 µm to remove possible contaminants from the samples. A similar approach has been reported in previous studies [39]–[41].

2.3.2 Tests conducted in Portland cement pastes

Rheological tests were conducted in cement pastes using a Haake MARS III (Thermo Fisher Scientific, Waltham, MA, USA) rheometer at 23.0 °C. A hatched parallel-plate geometry with a diameter of 35.00 mm (Figure 3) and an axial gap of 1.000 mm were used. The test started 10 minutes after the contact of PC with water. Initially, a pre-shear at 100 s^{-1} was applied for 60 seconds to ensure the same analysis condition for all samples. Subsequently, the ascending flow curve was obtained by increasing the shear rate from 0.1 to 100 s^{-1} in 10 steps. Finally, the descending flow curve was determined by decreasing the shear rate from 100 to 0.1 s^{-1} in the same steps. In each step, the shear rate was kept for 10 seconds (previously defined as adequate for shear stress stabilization), and the last 3 seconds of each step were recorded. The data of the descending flow curve fitted using the Herschel-Bulkley (H-B) model, described in Equation 1. The equivalent plastic viscosity of cement pastes was calculated through Equation 2 [42]. The hysteresis area between the increasing and decreasing portions – associated with thixotropy – was also determined. The fluidity of the pastes was also elevated through the mini-slump test [43].

$$\tau = \tau_0 + K . \dot{\gamma}^n \tag{1}$$

$$\mu_{eq} = \frac{3K}{n+2} \cdot (\dot{\gamma}_{max})^{n-1} \tag{2}$$

where τ is the shear stress (Pa), τ_0 is the dynamic yield stress (Pa), $\dot{\gamma}$ is the shear rate (s^{-1}), K and n are respectively the consistency and the pseudoplastic parameters of the H-B model, and $\dot{\gamma}_{max}$ is the maximum shear rate applied.

To evaluate the variability of the rheological tests, two independent fresh pastes were tested for the following pastes: SP, SP-A80%-15 min, and SP-A80%-30 min. The mean values were adopted for the rheological parameters. The results exhibited good repeatability, where standard deviation values below 5.2% and 8.5% were observed respectively for the dynamic yield stress and the equivalent viscosity.

In addition, the samples SP, SP–A80%–15 min, and SP–A80%–30 min were selected for time-resolved rheological analyses to evaluate the influence of SP sonication condition on the rheology of pastes during the first 120 minutes hydration. These analyses were conducted with the same conditions previously described, performed each 10 min for 2 hours, resulting in 12 measurements over this time range. An insulation chamber was used to prevent mixing water evaporation (Figure 3).

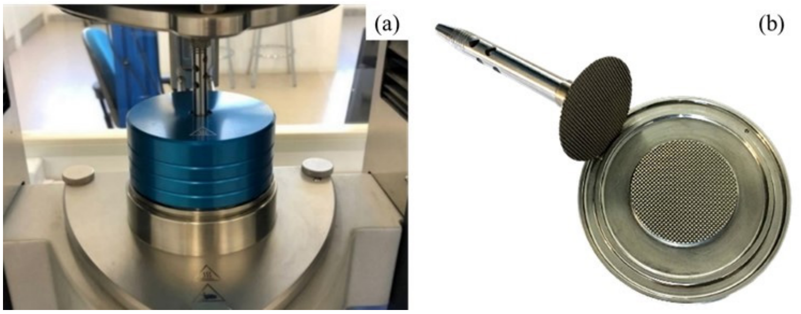

Figure 3. Rheological tests setup used. (a) Rheological tests setup with insulation chamber used to prevent the mixing water evaporation; (b) parallel-plate geometry with hatched surface.

Finally, the compressive strength of cement pastes was determined after 14 and 28 days of hydration. The test was performed following ASTM C1231 [44]. The mean compressive strength of each composition was calculated based on the results of 5 cylindric specimens with diameter of 20 mm and height of 26 mm. Analysis of Variance (ANOVA) was conducted on OriginPro software (OriginLab, Massachusetts, USA), considering a significance level of 0.05.

3 RESULTS AND DISCUSSIONS

3.1. Superplasticizer aqueous suspensions characterization

Figure 4 shows the size distribution of SP as received and after the sonication with an amplitude of 80% for 15 and 30 min. The results indicated that the SP had an average diameter of around 190 nm. Besides, the SP exhibited a polydispersity index (PDI) of 0.2, which indicated a monodisperse distribution [45]. The SP size diameter agrees with the hydrodynamic radius of a few tens of nanometers of usual polymers used in cement-based materials [39]. Note that this diameter is higher than those reported for polycarboxylate SP by some authors [40], [41]. Nevertheless, it should be considered that in the studies previously mentioned, the SP molecules were synthesized under controlled conditions. In contrast, the SP used in this research is a commercial organic admixture. Thus, the composition and all constituents of this admixture are not fully disclosed by the manufacturer due to confidentiality reasons. This may help to explain the higher average diameter of the SP used in this study compared to other reported in the literature. The DLS results showed that the sonication of SP promoted changes in the size distribution of the admixture. Overall, the sonication slightly shifted the size distribution to smaller values. Thus, SP aqueous dispersions sonication for 15 and 30 minutes increased the PDI by 170.0% (SP – A80% - 15 min) and 100.0% (SP – A80% - 30 min), respectively, compared to SP. These results indicated that sonication increased the heterogeneity of the SP aqueous dispersions. This suggests that sonication may reduce the length of SP chain, as further discussed in the rheological test results. This trend is in line with the results reported by Poinot et al. [33], where the authors observed reductions in the molecular weight of commercial water retention admixtures submitted to sonication.

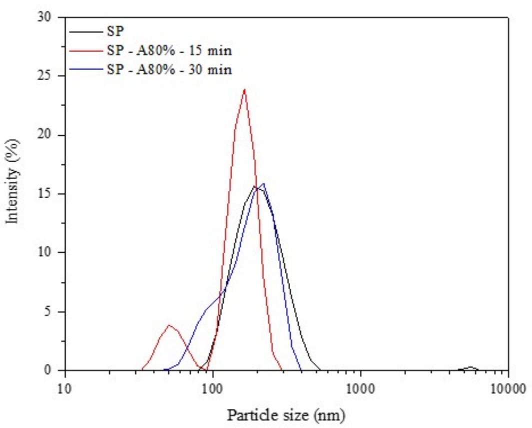

Figure 4. Size distribution of SP, SP - A80% - 15 min, and SP - A80% - 30 min aqueous dispersions, determined by DLS.

Figure 5 shows the zeta potential of SP, SP – A80% – 15 min, and SP – A80% – 30 min aqueous dispersions. All dispersions evaluated exhibited negative potential zeta values, which is attributed to the negative charge provided by the carboxylic groups (–COO–) present in the molecular structure of SP admixtures [46]. Furthermore, it was observed that increasing the sonication time increased the absolute value of zeta potential. This behavior may be related to the decrease in the chain length of SP with sonication (suggested by our size distribution results), which increases the amount of free carboxylic groups [47]. This trend is consistent with the previous studies that reported that SP molecules with shorter side chain lengths resulted in high absolute zeta potential values [48], [49]. Moreover, although these results indicated that sonication slightly improved the colloidal stability of SP, it should be noted that the particle dispersion (e.g., cement and/or nanomaterials) promoted by polycarboxylate SP comes mainly from steric hindrance [46], [50]. Feng et al. [51] reported that the side chain length possibly has a higher effect on the steric hindrance compared to the electrostatic repulsion of the functional groups. Thus, this increase in the absolute zeta potential values may not be associated with a greater dispersion capacity, as further discussed in the rheological test results.

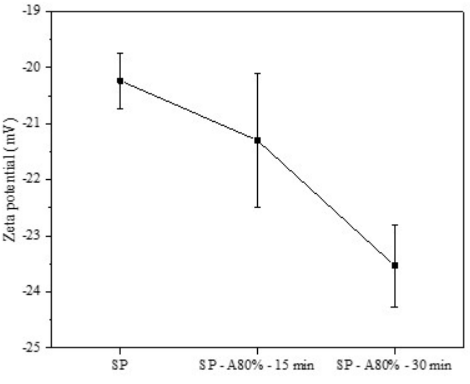

Figure 5. Zeta potential of SP, SP – A80% - 15 min, and SP – A80% - 30 min aqueous dispersions.

3.2. Paste rheological tests

Figure 6 exhibits the shear stress and viscosity curves of the cement pastes as a function of the shear rate, and Figure 7 summarizes the rheological test results. SP sonication slightly reduced the mini-slump values of the cement pastes compared to the reference sample with non-sonicated SP. Besides, it increased the dynamic yield stress, equivalent viscosity, and hysteresis area of cement pastes. For instance, increases of up to 13.4%, 16.7%, and 16.8% were observed for dynamic yield stress, viscosity, and hysteresis area, respectively, when SP was sonicated. However, no clear relationship between SP sonication amplitude and duration with the increase in the rheological properties was observed. Increasing the sonication time for a given amplitude apparently increased the viscosity and thixotropy (associated with the hysteresis area) of paste, but these differences may fall within the measurement error (see error bars in Figure 7). Besides, this trend did not occur for the yield stress and mini slump. This behavior is in line with the results reported by Malhotra [52]. The author also observed that in systems composed of hydroxypropyl cellulose and water, the cavitation intensity did not show a linear increase with the ultrasound intensity.

Overall, the rheological test results indicate that SP sonication reduced its dispersion capacity, supporting the hypothesis that sonication affected its molecular structure as suggested by our DLS and zeta potential results. According to Winnefeld et al. [47], the adsorption of polycarboxylate SP onto cement particles is affected by its molecular weight. Erzengin et al. [53] identified that the higher the density and length of side chains and the molecular weight of polycarboxylate SP, the higher the adsorption onto cement surface. In this context, Magarotto et al. [54] observed that the increase in molecular weight of polycarboxylate-based SP enhances the polymer adsorption and, therefore, the dispersing performance of the admixture. Peng et al. [55] also reported that polycarboxylate-based SP with a high molecular weight exhibited a more pronounced initial dispersing ability, resulting in lower yield stress than SP with a low molecular weight. A similar trend was identified in the study conducted by Palacios et al. [56]. The authors found that the polycarboxylate-based SP admixture with the highest molecular weight resulted in the lower yield stress value of slag-blended cement pastes, which was attributed to a higher steric repulsion effect. This trend is in line with previous studies regarding the adsorption of other types of polymers. Considering the adsorption equilibrium of polymers at interfaces, those with high molecular weight tend to preferentially adsorb [54]. By contrast, considering that sonication may have reduced the chain length of the SP molecules (see Section 3.1), it reduced the molecular weight for a given polymer concentration, reducing the particle dispersion ability.

Another aspect that should be stressed is that water sonication can produce hydrogen peroxide (H_2O_2) [57], [58]. Nevertheless, its effect on the fresh-state properties of cement pastes was not yet investigated. Thus, future studies should assess whether the formation of hydrogen peroxide occurs and how this can affect the rheological properties of cement-based materials.

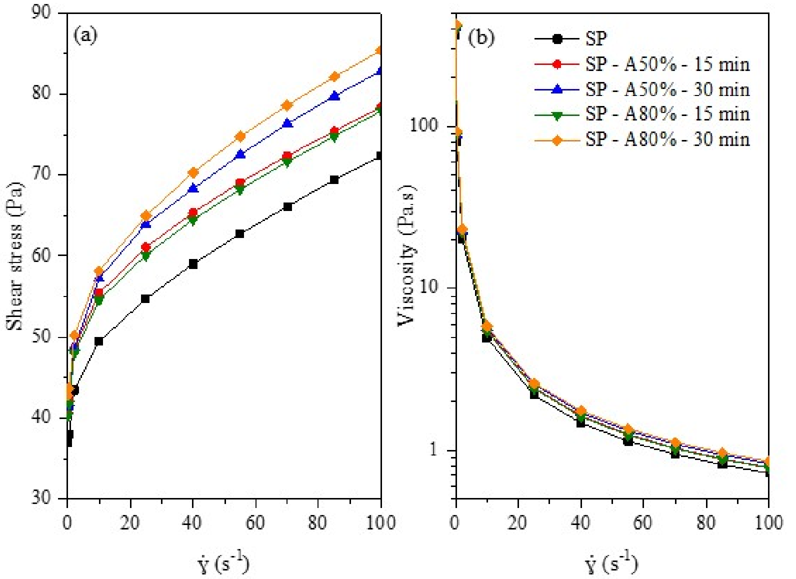

Figure 6. Flow curves (a) and viscosity vs. shear rate curves (b) of cement pastes evaluated after 10 min of hydration.

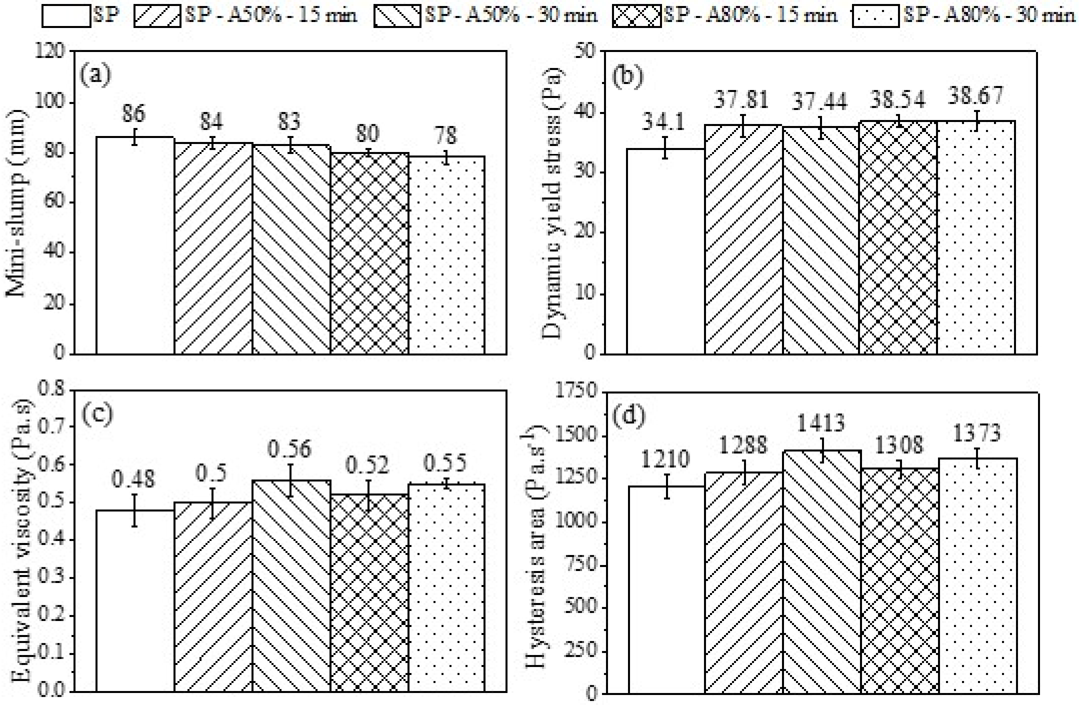

Figure 7. Fresh-state properties of the pastes at 10 minutes of hydration: mini-slump (a); dynamic yield stress (b); equivalent viscosity (c); and hysteresis area (d). Note: error bars in (a) correspond to ±1 standard deviation, while in (b)-(d) were estimated based on complementary tests.

Regarding the dispersing ability of SP over time, Figure 8 exemplifies the shear stress and viscosity curves as a function of the shear rate for the time-resolved tests. Figure 9 shows the dynamic yield stress and equivalent viscosity of SP, SP–A80%-15 min, and SP–A80%-30min pastes within the first 2 hours of hydration. As a general trend, the yield stress of the pastes was practically constant during the first 60 minutes of hydration, while a constant increase in viscosity was observed. However, from 60 minutes onwards, both yield stress and viscosity increased. A similar trend was observed in the study from Liu et al. [59], where the yield stress of a cement paste with polycarboxylate SP remained practically unchanged during the first 30 min, while between 30 and 180 min it showed a linear increase.

According to Rousel et al. [60], the yield stress of cement paste increases over time due to the combination of flocculation (already at a few seconds after stop shearing) and the progressive formation of C-S-H that form a rigid network. It is known that polycarboxylate-based SPs delay the hydration kinetics of Portland cement, either by Ca^{2+} ions complexation [61], the change in the morphology of hydrated phases [62], [63], or the hindered dissolution of cement particles caused by adsorbed SP molecules. Irrespective of the mechanism, the precipitation of C-S-H and the consequent formation of the rigid network proposed by Roussel et al. [60] are delayed in the presence of SP. In turn, viscosity is the macroscopic signature of the flow of water in the porosity of the granular system [64], so it depends primarily on the particle concentration of the suspension [65]. Ettringite precipitation consumes a great amount of water (chemical formula $Ca_6Al_2(SO_4)_3(OH)_{12}\cdot 26H_2O$) and starts in the very first minutes of hydration, even in the presence of SP. Jansen et al. [66] and Pott et al. [67] observed ettringite contents of 4-7 wt% in cement pastes with SP already at 10 minutes of hydration through *in-situ* XRD. This relation between the ettringite content and the viscosity of cement paste was confirmed by Jakob et al. [68] by coupling time-resolved rheological tests and *in-situ* XRD. These reports explain why the yield stress of the pastes with SP did not significantly change within the first 60 minutes, but the viscosity did.

When comparing the different sonication conditions, although SP sonication apparently increased the viscosity of paste at the first measurement (mentioned earlier), the viscosity increase over time was higher for the paste with non-sonicated SP than for those containing sonicated SP. In fact, significant differences (higher than the testing variability) can be observed from 90 min onward. In this regard, Kirby and Lewis [69] and Winnefeld et al. [47] evaluated the effect of the molecular architecture of different SPs on the rheology and hydration of cement pastes. The authors found that SPs with reduced chain length and molecular weight lead to higher delays in cement hydration. This would result in a slower formation of hydrated products (e.g., C-S-H and ettringite) responsible for the yield stress and viscosity increases over time discussed earlier. Thus, although SP sonication reduced its initial dispersing ability, sonication improved the time-dependent dispersing performance of the admixture. These results are in line with those from Peng et al. [55], which observed that SPs with high molecular weight had greater initial dispersing capacity but lower dispersion stabilization over time, i.e., dispersion ability after 60 minutes.

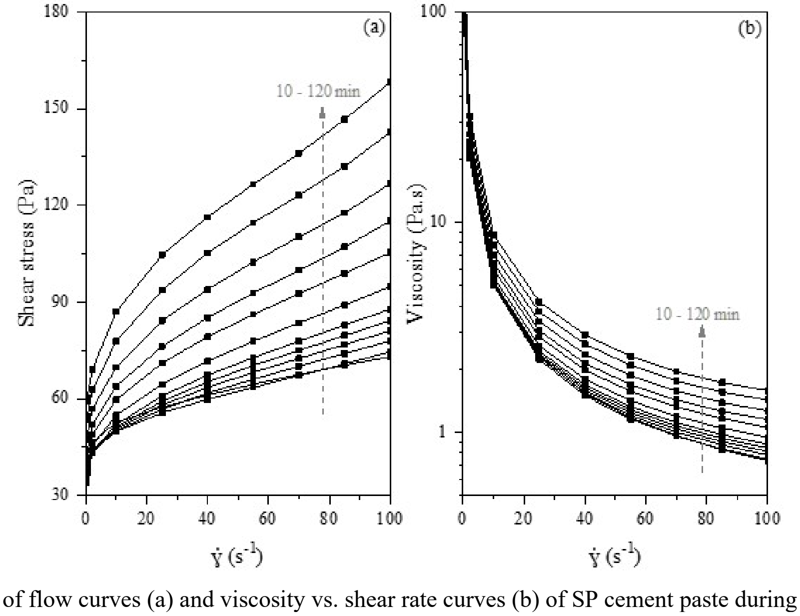

Figure 8. Example of flow curves (a) and viscosity vs. shear rate curves (b) of SP cement paste during the first 120 min of hydration.

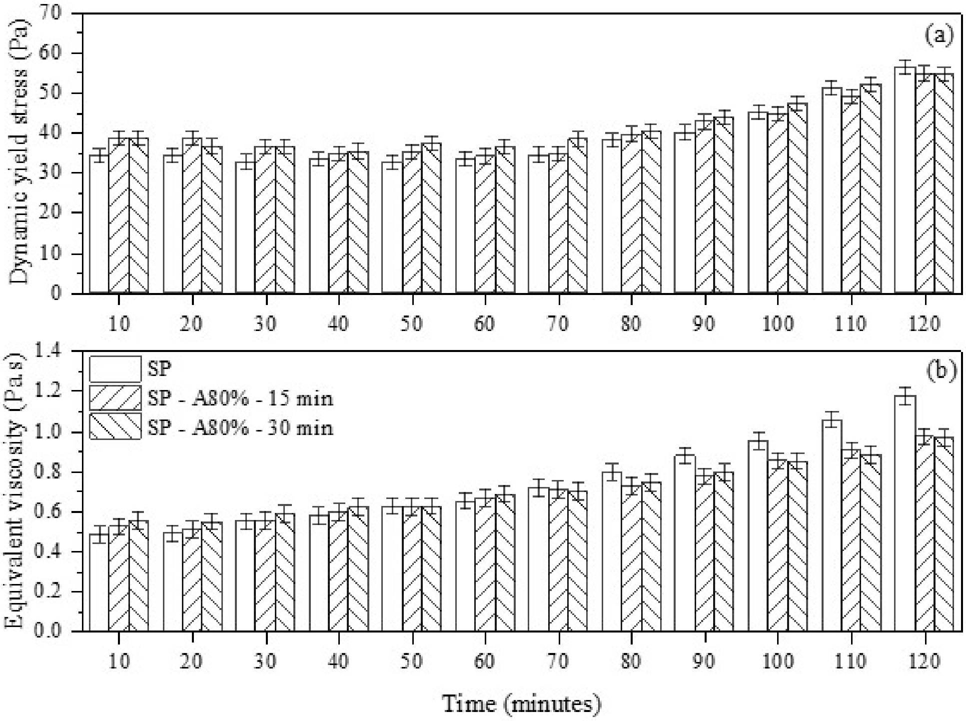

Figure 9. Dynamic yield stress (a) and equivalent viscosity (b) of the pastes over time.

3.3. Compressive strength

Figure 10 shows the compressive strength of the pastes at 14 and 28 days of hydration. Overall, the cement pastes evaluated showed compressive strength values around 65 MPa and 75 MPa at 14 and 28 days, respectively. Although the SP sonication affected the fresh properties of the cement pastes, it did not affect the compressive strength at the ages evaluated. ANOVA (summarized in Table 4) indicated that the amplitude and duration of sonication do not exert a significant influence on the compressive strength of paste. Moreover, no statistical differences were observed between the strength values of the cement pastes evaluated according to the Tukey test conducted.

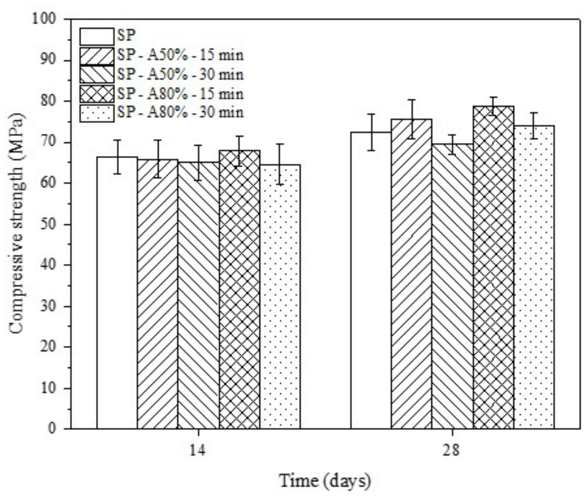

Figure 10. Compressive strength of the pastes.

Table 4. Two-way ANOVA of compressive strength results.

Factor	Sum of squares (SS)	Degrees of freedom (DF)	Mean square (MS)	P value	
Amplitude (A)	100.335	2	50.167	0.247	Not significant
Duration (B)	69.423	2	34.711	0.373	Not significant
A x B	98.068	4	24.517	0.582	Not significant
Error	776.245	23	33.749	-	-

4 CONCLUSIONS

This work assessed the effect of sonicating polycarboxylate-based SP used in cementitious composites. DLS and zeta potential results suggested that sonication reduced the length of SP chains. In cement pastes, sonication reduced the initial dispersion capacity of SP, resulting in samples with increased yield stress, viscosity, and hysteresis area values at the first measurement (10 minutes) compared to those from paste produced with non-sonicated SP. In contrast, SP sonication improved the particle dispersion improving the maintenance of dispersion over time, observed by the lower increases in viscosity for the sonicated SP samples up to 120 minutes. Finally, SP sonication did not significantly affect the compressive strength of the pastes at 14 and 28 days. Therefore, when SP is sonicated together with nanoparticles for application in cementitious matrices, the effect of sonicating the chemical admixture must be considered when the fresh-state properties of the composite are evaluated.

ACKNOWLEDGEMENTS

The governmental agencies CAPES, CNPq, FAPESC from Brazil provided financial support for the study. The Interdisciplinary Laboratory for the Development of Nanostructures (LINDEN – UFSC) is acknowledged for carrying out the DLS analysis. XRD analyses were conducted in the Laboratory of X-ray Diffraction (LDRX – UFSC) multiuser facility.

REFERENCES

[1] L. Silvestro et al., "Influence of ultrasonication of functionalized carbon nanotubes on the rheology, hydration, and compressive strength of portland cement pastes," *Materials*, vol. 14, no. 18, pp. 5248, Sep 2021, http://dx.doi.org/10.3390/ma14185248.

[2] M. S. Konsta-Gdoutos, P. A. Danoglidis, M. G. Falara, and S. F. Nitodas, "Fresh and mechanical properties, and strain sensing of nanomodified cement mortars: The effects of MWCNT aspect ratio, density and functionalization," *Cement Concr. Compos.*, vol. 82, pp. 137–151, 2017, http://dx.doi.org/10.1016/j.cemconcomp.2017.05.004.

[3] P. A. Danoglidis, M. S. Konsta-Gdoutos, and S. P. Shah, "Relationship between the carbon nanotube dispersion state, electrochemical impedance and capacitance and mechanical properties of percolative nanoreinforced OPC mortars," *Carbon N. Y.*, vol. 145, pp. 218–228, 2019, http://dx.doi.org/10.1016/j.carbon.2018.12.088.

[4] L. Silvestro, A. Spat Ruviaro, P. Ricardo de Matos, F. Pelisser, D. Zambelli Mezalira, and P. Jean Paul Gleize, "Functionalization of multi-walled carbon nanotubes with 3-aminopropyltriethoxysilane for application in cementitious matrix," *Constr. Build. Mater.*, vol. 311, pp. 125358, 2021, http://dx.doi.org/10.1016/j.conbuildmat.2021.125358.

[5] L. Silvestro, G. T. D. S. Lima, A. S. Ruviaro, and P. J. P. Gleize, "Stability of carboxyl-functionalized carbon nanotubes in simulated cement pore solution and its effect on the compressive strength and porosity of cement-based nanocomposites," *C - J Carbon Res*, vol. 8, no. 3, pp. 39, Jul 2022, http://dx.doi.org/10.3390/c8030039.

[6] Y. Sargam and K. Wang, "Influence of dispersants and dispersion on properties of nanosilica modified cement-based materials," *Cement Concr. Compos.*, vol. 118, pp. 103969, 2021, http://dx.doi.org/10.1016/j.cemconcomp.2021.103969.

[7] X. Liu, P. Hou, and H. Chen, "Effects of nanosilica on the hydration and hardening properties of slag cement," *Constr. Build. Mater.*, vol. 282, pp. 122705, 2021, http://dx.doi.org/10.1016/j.conbuildmat.2021.122705.

[8] Y. S. B. Fraga, J. H. S. Rêgo, V. M. S. Capuzzo, D. S. Andrade, and P. C. Morais, "Ultrasonication and synergistic effects of silica fume and colloidal nanosilica on the C–S–H microstructure," *J. Build. Eng.*, vol. 32, pp. 101702, 2020, http://dx.doi.org/10.1016/j.jobe.2020.101702.

[9] L. U. D. Tambara Jr. et al., "Effect of the nanosilica source on the rheology and early-age hydration of calcium sulfoaluminate cement pastes," *Constr. Build. Mater.*, vol. 327, pp. 126942, 2022, http://dx.doi.org/10.1016/j.conbuildmat.2022.126942.

[10] G. T. S. Lima, A. Zaleski, L. U. D. Tambara Jr., J. C. Rocha, F. Pelisser, and P. J. P. Gleize, "Evaluation of the effect of nanosilica and recycled fine aggregate in Portland cement rendering mortars," *Rev. IBRACON Estrut. Mater.*, vol. 15, no. 5, e15509, 2022, http://dx.doi.org/10.1590/s1983-41952022000500009.

[11] N. H. Azevedo, P. R. Matos, P. J. P. Gleize, and A. M. Betioli, "Effect of thermal treatment of SiC nanowhiskers on rheological, hydration, mechanical and microstructure properties of Portland cement pastes," *Cement Concr. Compos.*, vol. 117, pp. 103903, 2021., http://dx.doi.org/10.1016/j.cemconcomp.2020.103903.

[12] N. H. Azevedo and P. J. P. Gleize, "Effect of silicon carbide nanowhiskers on hydration and mechanical properties of a Portland cement paste," *Constr. Build. Mater.*, vol. 169, pp. 388–395, Apr 2018, http://dx.doi.org/10.1016/j.conbuildmat.2018.02.185.

[13] Y. Lan et al., "Preliminary investigation on silicon carbide whisker-modified cement-based composites," *Open Ceram.*, vol. 6, pp. 100107, 2021, http://dx.doi.org/10.1016/j.oceram.2021.100107.

[14] N. Hamed, M. S. El-Feky, M. Kohail, and E. S. A. R. Nasr, "Effect of nano-clay de-agglomeration on mechanical properties of concrete," *Constr. Build. Mater.*, vol. 205, pp. 245–256, 2019, http://dx.doi.org/10.1016/j.conbuildmat.2019.02.018.

[15] M. A. Mirgozar Langaroudi and Y. Mohammadi, "Effect of nano-clay on workability, mechanical, and durability properties of self-consolidating concrete containing mineral admixtures," *Constr. Build. Mater.*, vol. 191, pp. 619–634, 2018, http://dx.doi.org/10.1016/j.conbuildmat.2018.10.044.

[16] E. D. Rodríguez, S. A. Bernal, J. L. Provis, J. Payá, J. M. Monzó, and M. V. Borrachero, "Structure of Portland cement pastes blended with sonicated silica fume," *J. Mater. Civ. Eng.*, vol. 24, no. 10, pp. 1295–1304, 2012, http://dx.doi.org/10.1061/(ASCE)MT.1943-5533.0000502.

[17] K. M. Liew, M. F. Kai, and L. W. Zhang, "Carbon nanotube reinforced cementitious composites: an overview," *Compos., Part A Appl. Sci. Manuf.*, vol. 91, pp. 301–323, 2016, http://dx.doi.org/10.1016/j.compositesa.2016.10.020.

[18] T. Selvamani, S. Anandan, A. M. Asiri, P. Maruthamuthu, and M. Ashokkumar, "Preparation of $MgTi_2O_5$ nanoparticles for sonophotocatalytic degradation of triphenylmethane dyes," *Ultrason. Sonochem.*, vol. 75, pp. 105585, 2021, http://dx.doi.org/10.1016/j.ultsonch.2021.105585.

[19] T. Manzur and N. Yazdani, "Strength enhancement of cement mortar with carbon nanotubes: early results and potential," *Transp. Res. Rec.*, vol. 2142, no. 1, pp. 102–108, 2010, http://dx.doi.org/10.3141/2142-15.

[20] L. Assi et al., "Multiwall carbon nanotubes (MWCNTs) dispersion & mechanical effects in OPC mortar & paste: a review," *J. Build. Eng.*, vol. 43, pp. 102512, 2021, http://dx.doi.org/10.1016/j.jobe.2021.102512.

[21] L. Silvestro and P. Jean Paul Gleize, "Effect of carbon nanotubes on compressive, flexural and tensile strengths of Portland cement-based materials: a systematic literature review," *Constr. Build. Mater.*, vol. 264, pp. 120237, Dec 2020, http://dx.doi.org/10.1016/j.conbuildmat.2020.120237.

[22] M. Liebscher et al., "Impact of the molecular architecture of polycarboxylate superplasticizers on the dispersion of multi-walled carbon nanotubes in aqueous phase," *J. Mater. Sci.*, vol. 52, no. 4, pp. 2296–2307, 2017, http://dx.doi.org/10.1007/s10853-016-0522-3.

[23] B. S. Sindu and S. Sasmal, "Properties of carbon nanotube reinforced cement composite synthesized using different types of surfactants," *Constr. Build. Mater.*, vol. 155, pp. 389–399, 2017, http://dx.doi.org/10.1016/j.conbuildmat.2017.08.059.

[24] S. Ma, Y. Qian, and S. Kawashima, "Performance-based study on the rheological and hardened properties of blended cement mortars incorporating palygorskite clays and carbon nanotubes," *Constr. Build. Mater.*, vol. 171, pp. 663–671, 2018, http://dx.doi.org/10.1016/j.conbuildmat.2018.03.121.

[25] M. O. Mohsen, N. Al-Nuaimi, R. K. Abu Al-Rub, A. Senouci, and K. A. Bani-Hani, "Effect of mixing duration on flexural strength of multi walled carbon nanotubes cementitious composites," *Constr. Build. Mater.*, vol. 126, pp. 586–598, 2016, http://dx.doi.org/10.1016/j.conbuildmat.2016.09.073.

[26] A. Sedaghatdoost and K. Behfarnia, "Mechanical properties of Portland cement mortar containing multi-walled carbon nanotubes at elevated temperatures," *Constr. Build. Mater.*, vol. 176, pp. 482–489, 2018, http://dx.doi.org/10.1016/j.conbuildmat.2018.05.095.

[27] T. Jarolim, M. Labaj, R. Hela, and K. Michnova, "Carbon Nanotubes in Cementitious Composites: Dispersion, Implementation, and Influence on Mechanical Characteristics," *Adv. Mater. Sci. Eng.*, vol. 2016, pp. 1–6, 2016, http://dx.doi.org/10.1155/2016/7508904.

[28] P. C. Ma, N. A. Siddiqui, G. Marom, and J. K. Kim, "Dispersion and functionalization of carbon nanotubes for polymer-based nanocomposites: A review," *Compos., Part A Appl. Sci. Manuf.*, vol. 41, no. 10, pp. 1345–1367, 2010, http://dx.doi.org/10.1016/j.compositesa.2010.07.003.

[29] J. E. L. Siqueira and P. J. P. Gleize, "Effect of carbon nanotubes sonication on mechanical properties of cement pastes," *Rev. IBRACON Estrut. Mater.*, vol. 13, no. 2, pp. 455–463, 2020, http://dx.doi.org/10.1590/s1983-41952020000200013.

[30] M. H. Dehghani, A. Zarei, and M. Yousefi, "Efficiency of ultrasound for degradation of an anionic surfactant from water: Surfactant determination using methylene blue active substances method," *MethodsX*, vol. 6, pp. 805–814, 2019, http://dx.doi.org/10.1016/j.mex.2019.03.028.

[31] T. Campbell and M. R. Hoffmann, "Sonochemical degradation of perfluorinated surfactants: Power and multiple frequency effects," *Separ. Purif. Tech.*, vol. 156, pp. 1019–1027, 2015, http://dx.doi.org/10.1016/j.seppur.2015.09.053.

[32] P. S. Bhandari, B. P. Makwana, and P. R. Gogate, "Microwave and ultrasound assisted dual oxidant based degradation of sodium dodecyl sulfate: Efficacy of irradiation approaches and oxidants," *J. Water Process Eng.*, vol. 36, pp. 101316, 2020, http://dx.doi.org/10.1016/j.jwpe.2020.101316.

[33] T. Poinot, K. Benyahia, A. Govin, T. Jeanmaire, and P. Grosseau, "Use of ultrasonic degradation to study the molecular weight influence of polymeric admixtures for mortars," *Constr. Build. Mater.*, vol. 47, pp. 1046–1052, 2013, http://dx.doi.org/10.1016/j.conbuildmat.2013.06.007.

[34] M.-N. Noirfontaine, M. Courtial, F. Dunstetter, G. Gasecki, and M. Signes-Frehel, "Tricalcium silicate Ca_3SiO_5 superstructure analysis: a route towards the structure of the *M* $_1$ polymorph," *Z. Kristallogr.*, vol. 227, no. 2, pp. 102–112, 2012, http://dx.doi.org/10.1524/zkri.2012.1425.

[35] M. Palacios and F. Puertas, "Stability of superplasticizer and shrinkage-reducing admixtures in high basic media," *Mater. Constr.*, vol. 8, no. 4, pp. 683–691, 2018.

[36] S. Li, J. Zhang, Z. Li, Y. Gao, and C. Liu, "Feasibility study of red mud-blast furnace slag based geopolymeric grouting material : Effect of superplasticizers," *Constr. Build. Mater.*, vol. 267, pp. 120910, 2021, http://dx.doi.org/10.1016/j.conbuildmat.2020.120910.

[37] Y. Alrefaei, Y. S. Wang, and J. G. Dai, "The effectiveness of different superplasticizers in ambient cured one-part alkali activated pastes," *Cement Concr. Compos.*, vol. 97, pp. 166–174, 2019, http://dx.doi.org/10.1016/j.cemconcomp.2018.12.027.

[38] E. Janowska-Renkas, "The effect of superplasticizers' chemical structure on their efficiency in cement pastes," *Constr. Build. Mater.*, vol. 38, pp. 1204–1210, 2013, http://dx.doi.org/10.1016/j.conbuildmat.2012.09.032.

[39] H. Bessaies-Bey, R. Baumann, M. Schmitz, M. Radler, and N. Roussel, "Effect of polyacrylamide on rheology of fresh cement pastes," *Cement Concr. Res.*, vol. 76, pp. 98–106, 2015, http://dx.doi.org/10.1016/j.cemconres.2015.05.012.

[40] H. Bessaies-Bey, R. Baumann, M. Schmitz, M. Radler, and N. Roussel, "Organic admixtures and cement particles: Competitive adsorption and its macroscopic rheological consequences," *Cement Concr. Res.*, vol. 80, pp. 1–9, Feb 2016, http://dx.doi.org/10.1016/j.cemconres.2015.10.010.

[41] X. Wang, Y. Yang, X. Shu, Y. Wang, Q. Ran, and J. Liu, "Tailoring polycarboxylate architecture to improve the rheological properties of cement paste," *J. Dispers. Sci. Technol.*, vol. 40, no. 11, pp. 1567–1574, 2019, http://dx.doi.org/10.1080/01932691.2018.1485578.

[42] F. De Larrard, C. F. Ferraris, and T. Sedran, "Fresh concrete: a Herschel-Bulkley material," *Mater. Struct. Constr.*, vol. 31, no. 211, pp. 494–498, 1996, http://dx.doi.org/10.1007/bf02480474.

[43] P. A. Wedding and D. L. Kantro, "Influence of water-reducing admixtures on properties of cement paste: a miniature slump test," *Cem. Concr. Aggreg.*, vol. 2, no. 2, pp. 95, 1980, http://dx.doi.org/10.1520/CCA10190J.

[44] American Society for Testing and Materials, *Standard Practice for Use of Unbonded Caps in Determination of Compressive Strength of Hardened Cylindrical Concrete Specimens*, ASTM C1231/C1231M, 2015.

[45] P. Alafogianni, K. Dassios, S. Farmaki, S. K. Antiohos, T. E. Matikas, and N. M. Barkoula, "On the efficiency of UV-vis spectroscopy in assessing the dispersion quality in sonicated aqueous suspensions of carbon nanotubes," *Colloids Surf. A Physicochem. Eng. Asp.*, vol. 495, pp. 118–124, 2016, http://dx.doi.org/10.1016/j.colsurfa.2016.01.053.

[46] Y. Ma, J. Bai, C. Shi, S. Sha, and B. Zhou, "Effect of PCEs with different structures on hydration and properties of cementitious materials with low water-to-binder ratio," *Cement Concr. Res.*, vol. 142, pp. 106343, 2021, http://dx.doi.org/10.1016/j.cemconres.2020.106343.

[47] F. Winnefeld, S. Becker, J. Pakusch, and T. Götz, "Effects of the molecular architecture of comb-shaped superplasticizers on their performance in cementitious systems," *Cement Concr. Compos.*, vol. 29, no. 4, pp. 251–262, 2007, http://dx.doi.org/10.1016/j.cemconcomp.2006.12.006.

[48] M. Ezzat, X. Xu, K. El Cheikh, K. Lesage, R. Hoogenboom, and G. De Schutter, "Structure-property relationships for polycarboxylate ether superplasticizers by means of RAFT polymerization," *J. Colloid Interface Sci.*, vol. 553, pp. 788–797, 2019, http://dx.doi.org/10.1016/j.jcis.2019.06.088.

[49] X. Qiu, X. Peng, C. Yi, and Y. Deng, "Effect of side chains and sulfonic groups on the performance of polycarboxylate-type superplasticizers in concentrated cement suspensions," *J. Dispers. Sci. Technol.*, vol. 32, no. 2, pp. 203–212, 2011, http://dx.doi.org/10.1080/01932691003656888.

[50] N. Roussel, *Understanding the Rheology of Concrete.* Cambridge: Woodhead Publishing, 2011. http://dx.doi.org/10.1533/9780857095282.

[51] H. Feng, Z. Feng, W. Wang, Z. Deng, and B. Zheng, "Impact of polycarboxylate superplasticizers (PCEs) with novel molecular structures on fluidity, rheological behavior and adsorption properties of cement mortar," *Constr. Build. Mater.*, vol. 292, pp. 123285, 2021, http://dx.doi.org/10.1016/j.conbuildmat.2021.123285.

[52] S. L. Malhotra, "“Ultrasonic degradation of hydroxypropyl cellulose solutions in water, ethanol, and tetrahydrofuran," *J. Macromol. Sci. Part A Chem.*, vol. 17, no. 4, pp. 601–636, 1982, http://dx.doi.org/10.1080/00222338208062411.

[53] S. G. Erzengin, K. Kaya, S. Perçin Özkorucuklu, V. Özdemir, and G. Yıldırım, "The properties of cement systems superplasticized with methacrylic ester-based polycarboxylates," *Constr. Build. Mater.*, vol. 166, pp. 96–109, 2018, http://dx.doi.org/10.1016/j.conbuildmat.2018.01.088.

[54] R. Magarotto, I. Torresan, and N. Zeminian, “Influence of the molecular weight of polycarboxylate ether superplasticizers on the rheological properties of fresh cement pastes, mortar and concrete,” in *Proc. 11th Int. Congr. Chem. Cem.*, 2003, pp. 514–526.

[55] X. Peng, C. Yi, X. Qiu, and Y. Deng, "Effect of molecular weight of polycarboxylate-type superplasticizer on the rheological properties of cement pastes," *Polym. Polymer Compos.*, vol. 20, no. 8, pp. 725–736, 2012, http://dx.doi.org/10.1177/096739111202000808.

[56] M. Palacios, F. Puertas, P. Bowen, and Y. F. Houst, "Effect of PCs superplasticizers on the rheological properties and hydration process of slag-blended cement pastes," *J. Mater. Sci.*, vol. 44, no. 10, pp. 2714–2723, 2009, http://dx.doi.org/10.1007/s10853-009-3356-4.

[57] L. N. Assi, Y. A. J. Al-Hamadani, E. E. Deaver, V. Soltangharaei, P. Ziehl, and Y. Yoon, "Effect of sonicated deionized water on the early age behavior of portland cement-based concrete and paste," *Constr. Build. Mater.*, vol. 247, pp. 118571, 2020, http://dx.doi.org/10.1016/j.conbuildmat.2020.118571.

[58] S. Ziembowicz, M. Kida, and P. Koszelnik, "The impact of selected parameters on the formation of hydrogen peroxide by sonochemical process," *Separ. Purif. Tech.*, vol. 204, pp. 149–153, 2018, http://dx.doi.org/10.1016/j.seppur.2018.04.073.

[59] Y. Liu, Z. Zhang, R. Jing, and P. Yan, "The interaction of sodium citrate and polycarboxylate-based superplasticizer on the rheological properties and viscoelasticity of cement-based materials," *Constr. Build. Mater.*, vol. 293, pp. 123466, 2021, http://dx.doi.org/10.1016/j.conbuildmat.2021.123466.

[60] N. Roussel, G. Ovarlez, S. Garrault, and C. Brumaud, "The origins of thixotropy of fresh cement pastes," *Cement Concr. Res.*, vol. 42, no. 1, pp. 148–157, 2012, http://dx.doi.org/10.1016/j.cemconres.2011.09.004.

[61] M. Y. A. Mollah, W. J. Adams, R. Schennach, and D. L. Cocke, "Review of cement-superplasticizer interactions and their models," *Adv. Cement Res.*, vol. 12, no. 4, pp. 153–161, 2000, http://dx.doi.org/10.1680/adcr.2000.12.4.153.

[62] F. Ridi, L. Dei, E. Fratini, S. H. Chen, and P. Baglioni, "Hydration kinetics of tri-calcium silicate in the presence of superplasticizers," *J. Phys. Chem. B*, vol. 107, no. 4, pp. 1056–1061, 2003, http://dx.doi.org/10.1021/jp027346b.

[63] J. Rieger, J. Thieme, and C. Schmidt, "Study of precipitation reactions by X-ray microscopy: $CaCO_3$ precipitation and the effect of polycarboxylates," *Langmuir*, vol. 16, no. 22, pp. 8300–8305, 2000, http://dx.doi.org/10.1021/la0004193.

[64] F. De Larrard and T. Sedran, "Mixture-proportioning of high-performance concrete," *Cement Concr. Res.*, vol. 32, no. 11, pp. 1699–1704, 2002., http://dx.doi.org/10.1016/S0008-8846(02)00861-X.

[65] I. M. Krieger and T. J. Dougherty, "A mechanism for non-newtonian flow in suspensions of rigid spheres," *Trans. Soc. Rheol.*, vol. 3, no. 1, pp. 137–152, 1959, http://dx.doi.org/10.1122/1.548848.

[66] D. Jansen, J. Neubauer, F. Goetz-Neunhoeffer, R. Haerzschel, and W.-D. Hergeth, "Change in reaction kinetics of a Portland cement caused by a superplasticizer: calculation of heat flow curves from XRD data," *Cement Concr. Res.*, vol. 42, no. 2, pp. 327–332, Feb 2012, http://dx.doi.org/10.1016/j.cemconres.2011.10.005.

[67] U. Pott, C. Jakob, D. Jansen, J. Neubauer, and D. Stephan, "Investigation of the incompatibilities of cement and superplasticizers and their influence on the rheological behavior," *Materials*, vol. 13, no. 4, pp. 977, 2020, http://dx.doi.org/10.3390/ma13040977.

[68] C. Jakob et al., "Relating ettringite formation and rheological changes during the initial cement hydration: a comparative study applying XRD analysis, rheological measurements and modeling," *Materials*, vol. 12, no. 18, pp. 2957, 2019, http://dx.doi.org/10.3390/ma12182957.

[69] G. H. Kirby and J. A. Lewis, "Comb polymer architecture effects on the rheological property evolution of concentrated cement suspensions," *J. Am. Ceram. Soc.*, vol. 87, no. 9, pp. 1643–1652, Sep 2004, http://dx.doi.org/10.1111/j.1551-2916.2004.01643.x.

Author contributions: LS: Conceptualization, formal analysis, data curation; LS, GL, AR: methodology; LS, AR: investigation; PRM, ER, PG: resources; LS, GL, AR: writing—original draft preparation; LS, PRM, PG: writing—review and editing; PG: supervision; PRM, ER, PG: funding acquisition.

Editors: Bernardo Tutikian, Guilherme Aris Parsekian.

IBRACON Structures and Materials Journal
Revista IBRACON de Estruturas e Materiais
ISSN 1983-4195 ismj.org

ORIGINAL ARTICLE

RC beams with rectangular openings in case of fire

Vigas de concreto armado com aberturas retangulares em situação de incêndio

Fabrício Longhi Bolina[a]
Guilherme Fisch[a]
Valdir Pignatta e Silva[b]

[a]Universidade do Vale do Rio dos Sinos, Escola Politécnica da Unisinos, São Leopoldo, RS, Brasil
[b]Universidade de São Paulo, Escola Politécnica, Departamento de Engenharia de Estruturas e Geotécnica, São Paulo, SP, Brasil

Received 19 January 2022
Accepted 13 August 2022

Abstract: Openings in reinforced concrete (RC) beams may be required due to building installations (electrical, water, etc.). They weaken its cross-sectional area and, in case of fire, can increase the thermal field of the structure. NBR 15200 does not consider this. The paper evaluated the influence of rectangular openings on the Fire Resistance Rating (FRR) of RC beams by the Simplified Method of NBR 15200. This method combines a non-linear thermal analysis (isotherms) with the evaluation of the flexural strength of the beams using a manual design calculation method. The thermal field were obtained by a thermal model solved by finite element analysis (FEA) with Abaqus software. Thermal parameters of NBR 15200 were used. This FRR was compared with equivalent beams without openings solved by the Tabular Method of NBR 15200. Twelve 60 cm high beams with different widths and dimensions of openings were studied. Beams with openings had a FRR up to 60 min lower than the equivalent beam without openings. The larger the size of the rectangular opening, the greater the mechanical degradation of the beam in fire. NBR 15200 Tabular Method proved to be unsafe in this case. Prescriptions for beams with openings must be shown in NBR 15200.

Keywords: reinforced concrete, beams, fire, openings, NBR 15200.

Resumo: As aberturas e furos em vigas de concreto são corriqueiramente exigidas em virtude das instalações prediais (de água, elétrica, etc). Elas fragilizam a seção e, em situação de incêndio, podem amplificar o campo térmico do elemento estrutural. A NBR 15200 não faz menção à essa situação. Este estudo avaliou a influência de aberturas retangulares no Tempo de Resistência ao Fogo (TRF) de vigas de concreto pelo Método Simplificado da NBR 15200. O método combina a definição de uma análise térmica não linear (isotermas) com o cálculo manual da resistência a flexão destas vigas. As isotermas foram obtidas por um modelo térmico resolvido pela teoria dos elementos finitos com auxílio do software Abaqus. Os resultados foram comparados com o TRF obtido em vigas sem aberturas pelo Método Tabular normatizado. Doze vigas de 60 cm de altura e com diferentes larguras e dimensões de aberturas foram avaliadas. As vigas com aberturas tiveram um TRF até 60 min inferior às sem aberturas. Quanto maior a dimensão da abertura, tanto maior foi a degradação mecânica da viga ao incêndio. O Método Tabular se mostrou inseguro nessa circunstância. Prescrições a vigas com aberturas devem ser apresentadas na NBR 15200.

Palavras-chave: estruturas de concreto, vigas, incêndio, aberturas, NBR 15200.

How to cite: F. L. Bolina, G. Fisch, and V. P. Silva, "RC beams with rectangular openings in case of fire" *Rev. IBRACON Estrut. Mater.*, vol. 16, no. 2, e16206, 2023, https://doi.org/10.1590/S1983-41952023000200006

1. INTRODUCTION

In the design of reinforced concrete (RC) beams under normal temperature conditions, it may be required to incorporate openings for the passage of plumbing, electrical, telephone and/or internet installations. The openings can occur in the direction of the width or height of the beam and must be allowed in the structural design through specific standardized procedures.

Corresponding author: Fabrício Longhi Bolina. E-mail: fabriciobolina@gmail.com
Financial support: None.
Conflict of interest: Nothing to declare.
Data Availability: Data-sharing is not applicable to this article as no new data were created or analyzed in this study.

In Brazil, NBR 6118 [1] shows these beams structural integrity and safety requirements. Horizontal and vertical reinforcement adjacent to the opening can be used to compensate for the loss of its cross-section.

The subject has been studied for decades and still arouses interest among researchers.

Studies show alternatives to optimize the steel consumption of reinforcement in the opening region, mitigate the concrete stresses and cracks and propose more current calculation techniques than those already established by Leonhardt and Monnig [2] and Sussekind [3]. Research has been carried out, for example, by Shoeib and Sedawy [4], to understand the magnitude of mechanical damage in these beams; by El-Mar et al. [5], to analyze the region where concrete cracks begin; by Sayed [6], to investigate the shear stresses along the beam; by Mansour [7], to understand the use of steel fibers in crack mitigation and stress dissipation, among others.

Herrera et al. [8] and Elsanadedy [9] showed that failure of RC beams with openings under normal temperature conditions predominantly occurs under excessive shear stresses. In this sense, Campione and Minafò [10] evaluated beams with a low span-depth ratio to make these stresses critical. It was concluded that if the opening is placed in the region next to the columns, where the shear stresses are greater, reducing its structural capacity from 18 to 30%. Using vertical reinforcement increases the structural capacity in these regions by 15%. Similar research was presented by Mansour [7] and Ashour and Rishi [11], indicating that the RC beam mechanical capacity reduces as the openings approach the supports. Sayed [6] concluded that the opening size generates a more damaging structural consequence than the number of openings in the beams.

In this sense, Aykac et al. [12] experimentally evaluated the influence of multiple openings arranged in RC beams, both rectangular and circular. The authors show that the transverse reinforcements next to the supports prevent their premature failure by the Vierendeel action, which is only possible due to the longitudinal reinforcements surrounding the openings, in the flanges. The authors also concluded that circular openings are less harmful than rectangular ones, which was also showed by Tsavdaridis et al. [13] in the behavior of composite steel and concrete beams. Both researches [12], [13] were experimental. However, experimental procedures should be considered with caution to RC beams with openings. According to Shoeib and Sedawy [4], laboratory tests on RC beams with openings are influenced by load application points.

Research has focused on analyzing RC beams with openings under normal conditions (i.e., normal temperatures). A lack of studies has analyzed them in extreme conditions, such as in a fire. The subject is interesting because the opening can increase the thermal field of the cross-section, which accelerates the mechanical damage of the RC beam in case of fire.

It is known that in the fire design of a building, not all beams must meet the thermal insulation requirement. In these cases, the openings do not need passive protection (e.g., intumescent collars, fire stop, etc). In this case, pipes would be unprotected. Due to their constitutive characteristics, normally based on synthetic plastic polymers, they would disintegrate in a short period of fire, providing faster beam heating than those that do not have openings. The thermal field of beams with openings is probably higher.

A lack of research evaluated the influence of openings in RC beams in case of fire. This gap may even justify the negligence of standards such as NBR 15200 [14] and EN 1992.1-2 [15] regarding the fire design of RC beams with openings. According to Issa and Izadifard [16] and Kodur et al. [17], most current practices are more of a visual descriptive approach that is more concern with the adequate steel bar minimum cover and member size while ignoring a more meticulous approach of understanding the thermal and mechanical behavior and real building conditions of RC members exposed to fire.

This paper aims to fill this gap. Under normal temperature conditions, Sayed [6], Herrera et al. [8], Elsanadedy [9], Tsavdaridis et al. [13] showed that openings tend to cause beam failure by shear, which contradicts research on beams without openings in case of fire, as Li et al. [18], Gedam [19], Silva [20] and Xu et al. [21], showing that failure of RC beams does not occur due to shear stresses. Design standards cannot predict all situations. In this sense, performance-based fire safety design approach is becoming the method of choice, leading to numerical simulation of RC members at elevated temperatures, as can be seen in recent researches as Kumar and Kodur [22].

This research evaluates the influence of openings on the Fire Resistance Rate (FRR) of RC beams. First, the beams were designed at a normal temperature according to NBR 6118 [1]. Subsequently, for fire design requirements, they were evaluated by the Simplified Method of NBR 15200 [14], based on the thermal field obtained through a numerical model solved by FEA with the Abaqus software. The thermal field makes it possible to define the temperature at the cross-section of the beam with opening and later calculate the flexural strength of these beams using a manual design calculation method. These results were compared to the Tabular Method of NBR 15200 admitting equivalent beams without openings. Twelve cross-sections were evaluated. The research was motivated by the lack of standardized prescriptions and research on the fire performance of RC beams with openings.

2. ANALYTICAL AND NUMERICAL PROCEDURES

Two cases of RC beams were employed: one without openings and another with openings. First, the longitudinal and transverse reinforcement were calculated for normal temperature according to NBR 6118 [1]. Subsequently, they were verified in fire according to NBR 15200 [14], where its Fire Resistance Rate (FRR) was defined. In beams without openings, the FRR was obtained by the Tabular Method of NBR 15200 [14], which is the most conservative. In the beam with an opening, given the inapplicability of the Tabular Method, the verification was done by the Simplified Method of NBR 15200 [14].

The description of these procedures is detailed below.

2.1 Beams characteristics

In the beams without openings, 3 rectangular cross-sections with a height of 60 cm and breadth "b" of 15, 20 and 25 cm were used, as shown in Figure 1a. These beams were named Vb15, Vb20, Vb25, respectively.

The beams with openings were analyzed with the same height and breadth as the previous ones. Three rectangular openings were admitted. The opening length of the opening (parallel to the beam axis) was 30 cm, while the height "h" was 10, 15 or 20 cm, as shown in Figure 1b. The summary of beams with openings is shown in Table 1.

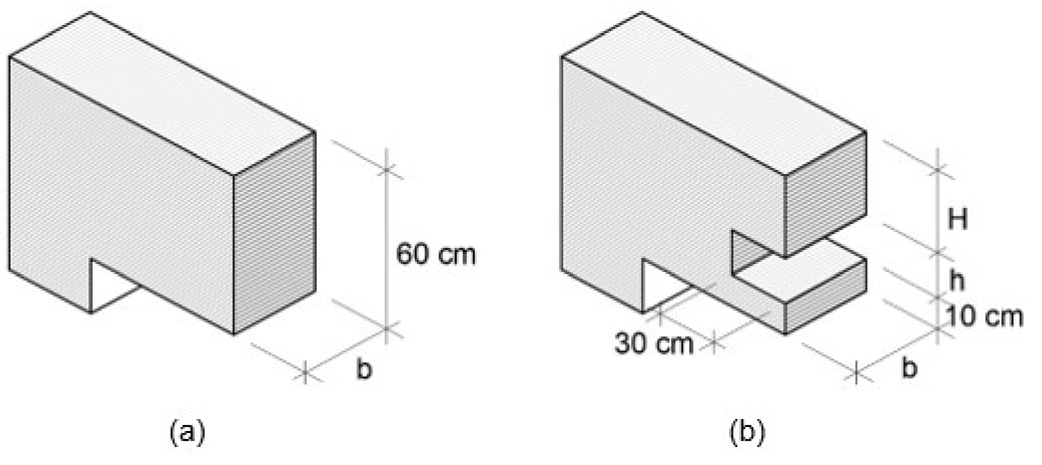

Figure 1 – Beams cross-section (a) without and (b) with openings

Table 1 – Beams with openings

Beam	b (cm)	h (cm)	H (cm)
Vb15h10	15	10	40
Vb15h15		15	35
Vb15h20		20	30
Vb20h10	20	10	40
Vb20h15		15	35
Vb20h20		20	30
Vb25h10	25	10	40
Vb25h15		15	35
Vb25h20		20	30

It is understood that the proposed values of b, h and H are the ones commonly found in Brazilian buildings, and represent the common geometry of reinforced concrete beams.

Twelve cross-sections were studied: 3 without openings and 9 with openings. In a fire situation, all were verified for 30, 60, 90 and 120 min of exposure to ISO 834 [23].

2.2 Criteria for analysis at normal temperature

The beams without openings were designed based on NBR 6118 [1] of Ultimate Limit State (ULS). The design was carried out per section 17.2.2 of the NBR 6118 criteria. The sagging moment was 10 tf·m in all cases. To define the cross-sectional area of the reinforcements, the theory of balance of internal forces and deformation (i.e., concrete and reinforcements) was used, with support from Carvalho and Figueiredo [24] and NBR 6118 [1] (flexural theory of RC beams). This procedure begins with defining the type of crack that the RC beam will present in the failure. Hence, it is necessary to use the relation between the depth of the neutral axis (x) and the useful height (d), since this parameter (x/d) determines if it will be a fragile or ductile failure. For RC elements with fck up to 50 MPa, NBR 6118 [1] limits this value to 0.45. Thus, the tensile stresses of the concrete and positive steel are calculated.

To comply the durability criteria of NBR 6118 [1] for CAA II (environmental aggressiveness class #2, in Portuguese), typical of urban environments, the reinforcement cover thickness was 30 mm and the concrete compressive strength was 30 MPa.

For the analysis of RC beams with opening, the requirements of section 13.2.5 of NBR 6118 [1] were used. It was assumed that the opening was positioned in the region of the maximum sagging moment – i.e., 10 tf·m – of the RC beam. The design of longitudinal and transverse rebars was based on the classical procedure of Leonhardt and Monnig [2], according to the Equation 1 to 6. The upper flange (cross-section above the opening) was designed by combined bending and axial compression (N_c and M_c) and shear force (V_c) while the lower one (cross-section below the opening) for flexo-traction (N_t and M_t) and shear force (V_t). The Leonhardt and Monnig theory was used due to its validation over time, in addition to allowing the adjustment of the equations for the application of the Simplified Method of NBR 15200.

$$N_c = \frac{M_{sd}}{z} \tag{1}$$

$$N_t = \frac{M_{sd}}{z} \tag{2}$$

$$V_c = 0{,}80 \cdot V_{Sd} \tag{3}$$

$$V_t = 0{,}20 \cdot V_{Sd} \tag{4}$$

$$M_c = \frac{V_c}{0{,}50 \cdot L_{opening}} \tag{5}$$

$$M_t = \frac{V_t}{0{,}50 \cdot L_{opening}} \tag{6}$$

2.3 Criteria for analysis in fire

The fire analysis was made according to NBR 15200 [14]. The FRR of the beam without opening was obtained by the Tabular Method, as it is the most used in commercial structural design software. In beams with opening, given the inexistence of any tabulated method in this case, the analysis was made by the Simplified Method of NBR 15200.

The Tabular Method application followed the definition of the minimum dimensions of each cross-section and the C_1 coefficient, which for these beams was 40 mm. The coefficient was defined by the reinforcement cover thickness (30 mm), stirrup diameter (hypothetically arbitrated in 5 mm) and half of the longitudinal reinforcement diameter (arbitrated in 10 mm).

The application of the Simplified Method used the thermal field of the cross-section of the beam and its respective mechanical damages to the materials (i.e., concrete and steel). The beam in case of fire was designed with the same theoretical basis to normal temperature, but with $\gamma_s = 1{,}0$ and $\gamma_c = 1{,}0$ and without the long-term coefficient α=0.85, given the exceptionality of this case. The bending moment applied was equal to 70% of that used in the design at normal temperature. This criterion is defined by the NBR 15200 [14].

2.4 FEA model

The thermal field in the beam cross-section was solved by FEA (Finite Element Analysis) with the Abaqus software. The FEA model was made assuming the thermal diffusivity parameters of the concrete and steel. Thermal conductivity and density were proposed at NBR 15200 [14]. The specific heat was also taken from NBR 15200 [14]. They are presented in Annex A, being the specific heat of the steel shown in Figure A1 and their thermal conductivity in Figure A2. The density of the steel was constant (7850 kg/m^3). For concrete, the specific heat is in Figure A3, the density in Figure A4 and the thermal conductivity in Figure A5.

Figure 2 shows the FEA thermal model. The cross-section was the one adjacent to the beam opening. The FEA model of the beam without opening was similar, but without the opening.

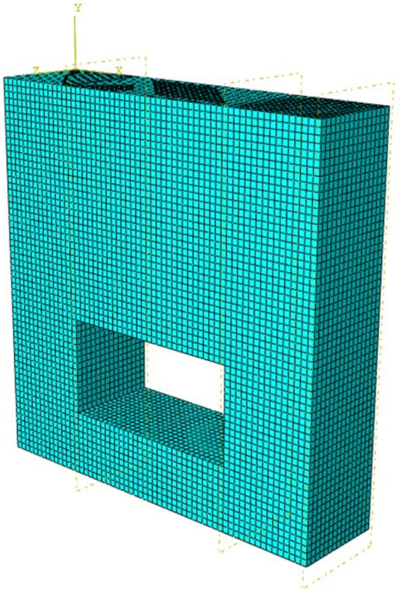

Figure 2 – Computational thermal model (beam with opening)

The concrete was modeled with a general 3D solid 8-node linear isoparametric (DC3D8) finite element from the Abaqus software library and the reinforcement with a truss of 2-node link (DCC1D2), as performed by Issa and Izadifard [16], Li et al. [18] and Xu et al. [21], and others. A mesh sensitive analysis was performed, and the size of the elements is approximately 0.5 x 0.5 x 0.5 mm for the DC3D8 and 0.5 mm for the DCC1D2. The total coupling of the rebars in the concrete was used, admitting a total interaction between them.

The FEA model was solved by Abaqus (non-linear model) by the Equation 7, which represents the thermal diffusivity that produces a thermal field in the cross-section of the beam. The analysis depends on the density ρ, thermal conductivity k and specific heat C_p of the materials (i.e., steel and concrete).

$$\alpha = \frac{k}{\rho . C_p} \tag{7}$$

On the bottom surface of the beam, the ISO 834 [23] fire curve was considered by thermal convection (with a heat transfer coefficient α=25 W/m^2.K) and radiation (with a thermal emissivity Ɛ=0,70 according to EN 1992.1-2). On the top surface of the beam, an ambient temperature of 25ºC was considered by convection (with α=9 W/m^2·K). The absolute zero of the model was -273,15 ºC and the Stefan-Boltzmann Constant (σ=5,67$\cdot 10^{-8}$ W/m$^2\cdot$ K^4).

The surfaces to which the heating was applied are shown in Figure 3. In Figure 3a, the cross- section without opening is shown, with the heating applied peripherally, excluding the beam's upper surface. Figure 3b details the cross-section with the opening. Heating is also done around the perimeter, including the opening region. The upper surface of the lower and upper flanges was not heated. The criterion was based on the principles of thermodynamics developed in an environment under fire.

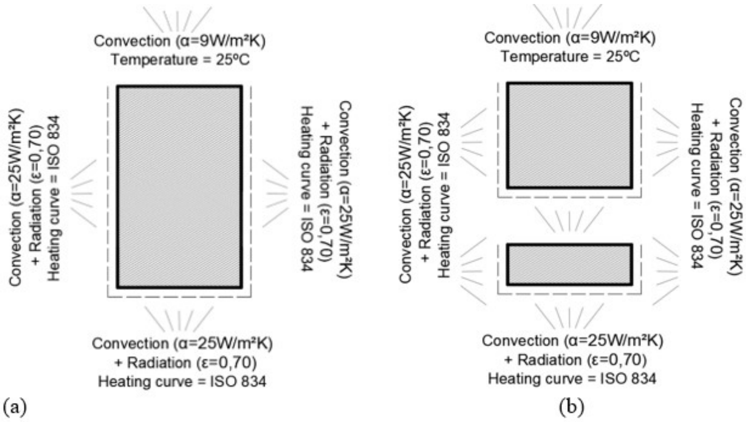

Figure 3 – Heating surfaces in the cross-section of the beams (a) without and (b) with opening

The temperature of the concrete cross-section was defined by the average between the reading points of Figure 4a and Figure 4b for the beam without and with opening, respectively. Since the concrete cross-section at the beam's load-bearing capacity is above the neutral axis, only reading points in this region were used for beam without opening. For beams with openings, reading points on both the lower and upper flanges were considered, since both participate in the beam's load-bearing capacity in this region, according to the classical theory of Leonhardt and Monnig [2]. Figure 4c shows the procedure for defining the temperatures in the reinforcements. Four rebars were chosen, numbered from 1 to 4, which were positioned at the region usually used in the structural design.

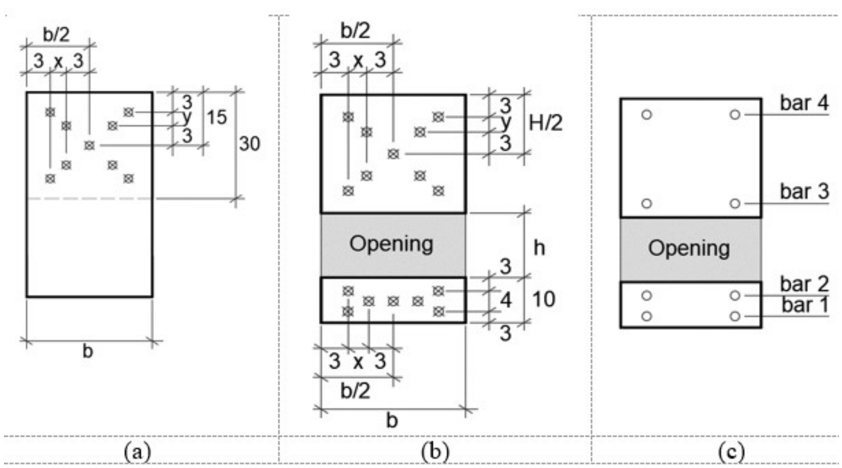

Figure 4 – Temperature reading points in the cross-section of the beams (a) without and (b) (c) with openings

3. RESULTS

3.1 Design at normal temperature

The reinforcement design of the beams with and without openings is presented.

a) Beams without openings

Table 2 shows the required reinforcement area for Vb15, Vb20 and Vb25. The longitudinal and transverse reinforcement area, the longitudinal reinforcement ratio, the elongation of the concrete and reinforcements, deformation domain, depth of the neutral axis and the ductility requirement according to NBR 6118 [1] are shown.

Table 2 – Structural design of beams without opening

Beam Name	$A_{s,min}$ (cm²)	A_s (cm²)	$A_{sw,min}$ (cm²)	A_{sw} (cm²)	$\frac{A_s}{A_c}$(%)	ε_s (%)	ε_c (%)	Domain number	X (cm)	$\frac{x}{d}$
Vb15	1,4	4,4	1,7	3,6	0,5	10	1,8	2	8,7	0,16
Vb20	1,8	4,3	2,3	2,1	0,4	10	1,3	2	6,4	0,11
Vb25	2,3	4,2	2,9	1,2	0,3	10	1,0	2	5,1	0,09

The longitudinal reinforcement area used in these beams was between 4.2 and 4.4 cm². As expected, increasing the RC beam width subtly reduces the reinforcement area required. However, it affects the total area of transverse reinforcement (stirrups), but they will not be analyzed because, according to [18]–[21], the beams do not fail by shear in a fire. The beams are in domain 2 of deformation (according to section 17.2.2 of the NBR 6118), meeting the requirements of these standard. The standardized ductility limit is also respected.

It can be concluded that the beams Vb15, Vb20 and Vb25 can be used because they respect the standardized requirements of structural design of RC.

b) Beams with openings

Table 3 shows the required longitudinal and transverse reinforcement area, both in the upper (compressed) and lower flange (tension) around the opening. The shear and suspension transverse reinforcements were also defined.

Table 3 – Structural design of beams with opening

Beam Name	$A_{st,min}$ (cm²)	A_{st} (cm²)	$A_{sc,min}$ (cm²)	A_{sc} (cm²)	$A_{swc,min}$ (cm²)	A_{swc} (cm²)	$A_{swt,min}$ (cm²)	A_{swt} (cm²)	A_{sws} (cm²)
Vb15h10	0,2	8,3	0,9	0,0	1,7	5,4	1,7	4,9	2,2
Vb15h15	0,2	8,3	0,8	0,0	1,7	6,9	1,7	4,9	2,2
Vb15h20	0,2	8,3	0,7	0,0	1,7	8,8	1,7	4,9	2,2
Vb20h10	0,3	8,2	1,2	0,0	2,3	4,4	2,3	3,8	1,1
Vb20h15	0,3	8,2	1,1	0,0	2,3	5,8	2,3	3,8	1,1
Vb20h20	0,3	8,2	0,9	0,0	2,3	7,6	2,3	3,8	1,1
Vb25h10	0,4	8,1	1,5	0,0	2,9	3,3	2,9	2,7	0,0
Vb25h15	0,4	8,1	1,3	0,0	2,9	4,7	2,9	2,7	0,0
Vb25h20	0,4	8,1	1,2	0,0	2,9	6,5	2,9	2,7	0,0

The longitudinal reinforcement area of the tensioned flange (lower) was between 8.1 and 8.3 cm², while in the compressed flange (upper) the use of reinforcement is unnecessary. In this case, the minimum reinforcement area practiced by NBR 6118 [1] was used, being between 0.7 and 1.5 cm². Comparing the beam above (section a, beam without opening), it is necessary to add longitudinal reinforcements in the opening region. Reinforcements used outside the cross-section around the opening (i.e., beam without opening according to Table 2) would not be sufficient. The transverse reinforcements (stirrups) were not analyzed due to the abovementioned circumstances [18]–[21].

3.2 Thermal field in cross-section

Figure 5 shows the average temperatures in the cross-section of the beams in case of fire.

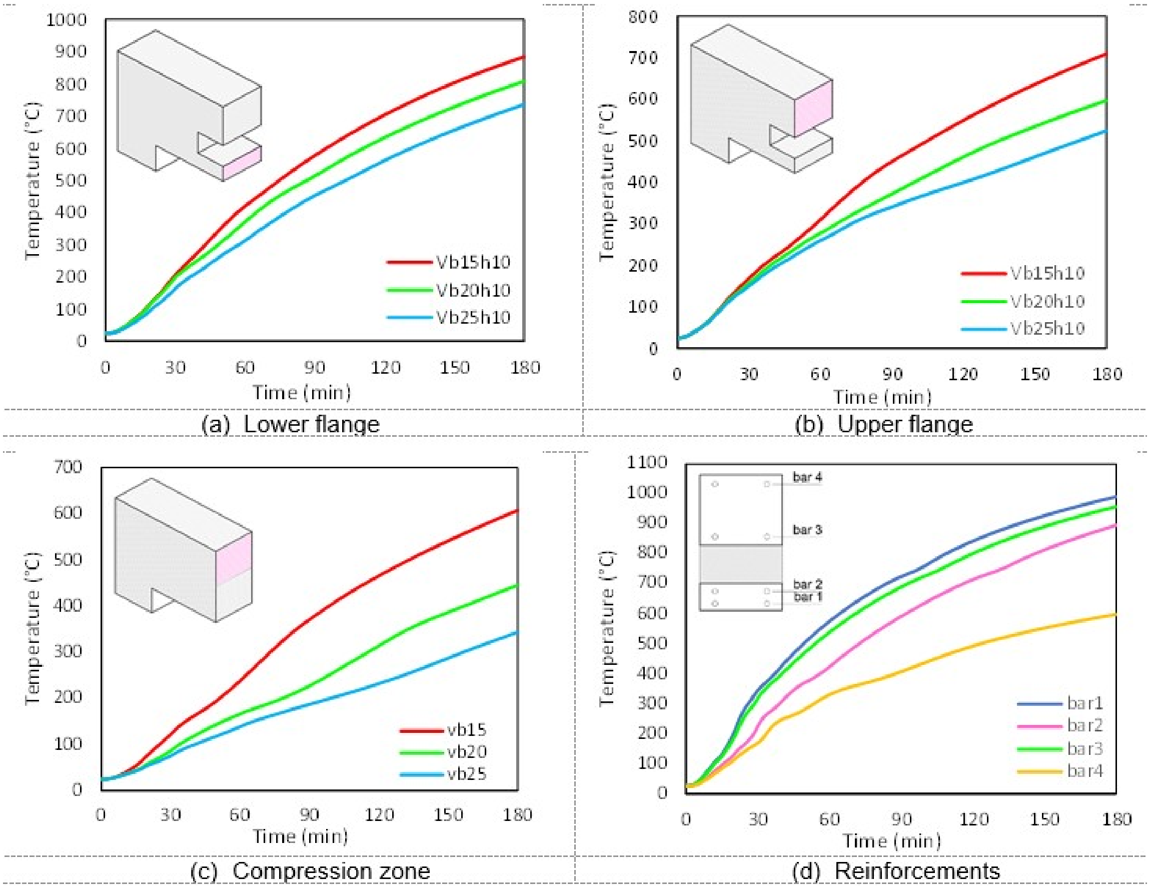

Figure 5 – Thermal field in (a) lower and (b) upper flange of the concrete (beam with opening), (c) in the compresses region of the concrete (beam without opening) and (d) in the reinforcements

Figure 5a shows beams with an opening of h=10 cm (see Figure 1 and Table 1), i.e., Vb15f10, Vb20f10 and Vb25f10. The size of the opening does not affect the cross-sectional area of the lower flange (see Figure 1b) and therefore its average temperature. On the other hand, Figure 5b shows the average temperatures of the upper flange, which change with the opening dimensions. For the other beams, the temperatures are in Table 4. The comparison between beam without and with opening is shown in Figure 6. Control points of Figure 4a and b were used. For the reinforcements in Figure 5d, the criterion shown in Figure 4c was used.

Table 4 – Average temperatures in the cross-section of beams with openings

Beam Name	Average temperature (°C)							
	Upper flange				Lower flange			
	Time (min)				Time (min)			
	30	60	90	120	30	60	90	120
Vb15h10	160	310	449	548	210	426	585	703
Vb15h15	163	314	452	552				
Vb15h20	175	323	462	562				
Vb20h10	155	278	374	467	200	374	517	636
Vb20h15	156	279	377	469				
Vb20h20	174	312	411	497				
Vb25h10	151	262	342	401	170	311	456	564
Vb25h15	153	263	345	405				
Vb25h20	154	264	347	410				

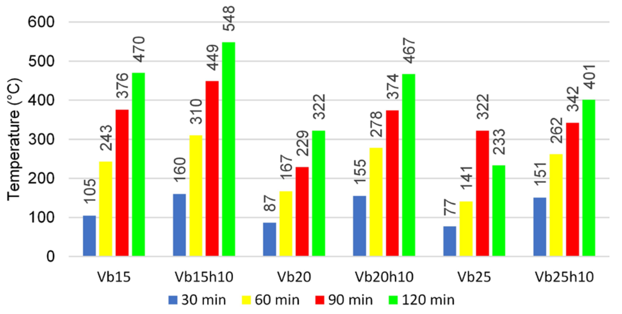

Figure 6 – Average temperature on the upper flange (beam with opening) and the compression zone (beam without opening)

The reduced cross-section of the lower flange and the heating by its surface justify the higher average temperature, as shown in Figure 5a and Table 4. This region is the most affected by temperatures, causing more severe damage to the mechanical parameters of the materials that constitute it. For every 5 cm increase in the breadth of the beam, their average temperatures decreased around 20, 55, 65 and 70 °C for, respectively, 30, 60, 90 and 120 min of exposure to high temperatures (ISO 834 heating curve).

Therefore, increasing the breadth of the beam decreases the average temperature of the lower flange. However, for design purposes, the magnitude of the temperature reduction contributes subtly to the maintenance of the mechanical properties of the materials at each analysis time.

In the upper flange, the opening dimension influences the concrete's thermal field, as shown in Figure 5b and Table 4. Increasing the opening reduces the total area of the upper flange cross-section, increasing its average temperature. The increase in the opening causes, in addition to the reduction of the load-bearing capacity of the beam (due to the reduction of its cross-section), promotes more accentuated damage to the mechanical properties of materials (steel and concrete) in a fire situation.

Comparing the temperature between the beam with (Figure 5b) and without opening (Figure 5c), it is noted that the average temperature is always higher in the first case. This comparison was shown in Figure 6. The largest temperature difference recorded was at 120 min, between Vb25 and Vb25h10, which was 178 °C. The smallest difference was at 30 min, noted between Vb15 and Vb15h10, which was 55 °C.

In the case of the beam with an opening, it is shown that the concrete above the neutral axis has a temperature that can be almost 200 °C higher about the beam without an opening.

Figure 5d shows that the critical region of the beam with an opening is the lower flange, where the reinforcements (bar 1 and bar 2) reached the limit temperature of 500 °C around 60 min. This is the critical temperature according to FIB Bulletin nº 46 [25], the temperature at which the mechanical strength of the steel is practically negligible. Failure of these reinforcements can trigger a structural collapse, which should be evaluated in future research.

Figure 7 and Figure 8 show, respectively, the thermal field of the RC beams with and without openings. The opening in the beam becomes a critical condition, providing a more aggressive temperature evolution along the cross-section.

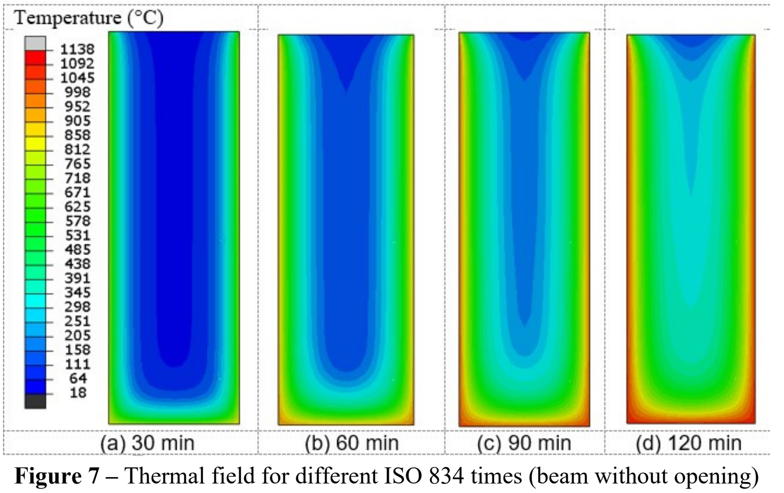

Figure 7 – Thermal field for different ISO 834 times (beam without opening)

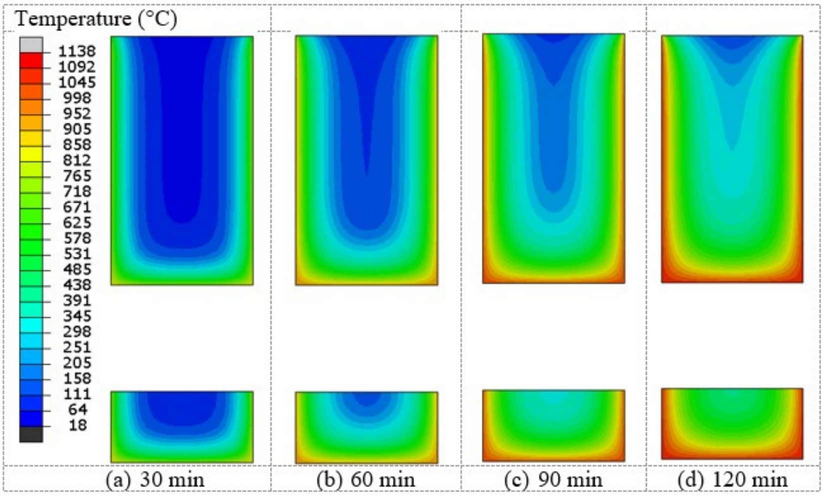

Figure 8 – Thermal field for different ISO 834 times (beam with opening)

Based on the reinforcement designed by NBR 6118 (section 3.1) and the thermal field already shown (section 3.2), the verification in fire according to NBR 15200 is carried out.

3.3 Fire design

The analysis in case of fire of the beams designed at normal temperature is shown.

a) Beams without openings

Based on the geometric characteristics of Vb15, Vb20 and Vb25 and applying the Tabular Method of NBR 15200 [14], it is concluded that the beams in question meet the FRR of, respectively, 60, 60 and 90 min if designed as simply supported at both ends, and 60, 90 and 120 min if fixed at both ends (structurally continuous). Each condition depends on the analytical design model, which this research will not analyze.

b) Beams with openings

Table 5 shows the required area of longitudinal reinforcement in the lower and upper flange for the 30, 60, 90 and 120 min of ISO 834 heating curve.

Table 5 – Required area of longitudinal reinforcement (beam with opening)

Viga	FRR (min)				FRR (min)			
	30	60	90	120	30	60	90	120
	$A_{st.fi}$ (cm^2)				$A_{sc,fi}$ (cm^2)			
Vb15h10	4,8	6,7	-	-	0,0	0,0	-	-
Vb15h15	5,1	6,8	-	-	0,0	0,0	-	-
Vb15h20	5,3	6,9	-	-	0,0	0,0	-	-
Vb20h10	4,5	6,5	14,8	-	0,0	0,0	0,0	-
Vb20h15	4,9	6,7	14,9	-	0,0	0,0	0,0	-
Vb20h20	4,9	6,9	15,1	-	0,0	0,0	0,0	-
Vb25h10	4,4	6,4	14,5	35,1	0,0	0,0	0,0	0,0
Vb25h15	4,9	6,8	15,0	35,7	0,0	0,0	0,0	0,0
Vb25h20	4,9	7,0	13,9	37,7	0,0	0,0	0,0	0,0

According to Table 5, in the case of the b=15 cm, the verification at 90 and 120 min cannot be done due to the excessive damage of the mechanical property of the concrete and steel in the lower flange, causing a mathematical inconsistency in the calculation. The same is valid for the beam with b=20 cm in the time of 120 min.

In the case of the beam without opening, the analysis made in Table 3 (show in section 3.1) has already indicates that the required steel reinforcement area on its lower face depends on the width of the beam, about 8.1 to 8.3 cm^2. Table 5 shows that the area of reinforcement required for the beam with openings in fire is always greater than 8.1 to 8.3 cm^2 after 90 min. In this case, the structural design in fire would prevail over the design at normal conditions (without fire). An addition of reinforcement should be made, except the beam with a b=15 cm, at 90 and 120 min; and b=20 cm, at 120 min; for the reasons mentioned in the previous paragraph. Although there is no mathematical inconsistency in the beam b=25 cm at 120 min, it is clear that the required reinforcement area is excessive, and complex to be carried out in structural design of beams with openings.

The upper flange is less mechanically damaged by fire and the existing concrete cross-section area is sufficient to balance of internal forces. It is not necessary to add reinforcements to the upper flange. The lower flange is the most fire damaged.

Table 5 (if analyzed together with Table 3) show that the FRR of the beam with the openings is 60 min, justified by the excessive heating of the lower flange. It is possible to increase the FRR with the increase of the reinforcement area, as shown in Table 5. However, the required reinforcement area is impractical.

3.4 Final remarks

Table 6 shows the comparison between RC beams without and with openings. The first (i.e., without opening) was verified by the tabular method of NBR 15200, admitting two cases: simply supported at both ends (SSBE) and fixed at both ends (FBE). The second (i.e.,with opening) was determined by applying the Simplified Method.

The RC beam with an opening shows a FRR lower than the beams without openings, especially those with greater widths. The tabular method proved unsafe to be applied to RC beams with openings, which presented the FRR twice as long as it had.

In the simply supported beams without opening with b = 25 cm, the FRR was 30 min longer than the equivalent beam (b = 25 cm) with an opening. On the other hand, in case of fixed beams with b = 20 cm and b = 25 cm, their FRR was 30 and 60 min higher than the equivalent beams with openings, respectively.

Table 6 – FRR of the RC beams used in the research

Without opening			With opening	
Beam number	**Tabular (SSBE)***	**Tabular (FBE)****	**Beam number**	**Simplified**
Vb15	60	60	Vb15h10	60
			Vb15h15	60
			Vb15h20	60
Vb20	60	90	Vb20h10	60
			Vb20h15	60
			Vb20h20	60
Vb25	90	120	Vb25h10	60
			Vb25h15	60
			Vb25h20	60

*SSBE: simply supported at both ends. **FBE: fixed at both ends

3.5 Future work

Others numerical and experimental researches should be done to increase the range of results. FE thermomechanical models should be made to better understand the fire performance of RC beams, especially the stress distribution along the opening. Analysis with more realistic fire curves, as proposed by Rein et al. [26], can produce new answers and conclusions and need to be developed.

4. CONCLUSIONS

This paper evaluated the influence of opening in RC beams in case of fire. The research was motivated by the lack of NBR 15200 prescriptions for these cases. The following conclusions of this research may be outlined:

• Preserving the same beam height, the increase in the opening dimension causes an increase in the thermal field in the beam cross-section;

- Increasing the size of a beam opening causes, in addition to the reduction of its load-bearing capacity caused by the opening, greater mechanical damage to materials due to increased thermal field developed in the cross-section in fire;
- In case of fire, beams with openings are more thermally affected than beams without openings, being more susceptible to collapse;
- The average temperature of the beam cross-section with an opening can be up to 178 °C higher than that of the beam without opening;
- The NBR 15200 tabular method is unsafe if applied to RC beams with openings, as it showed a longer FRR than they actually have. This difference was up to 60 min;
- The beams with openings showed a FRR up to 50% lower than the equivalent beams without openings;
- The NBR 15200 tabular method cannot be applied to RC beams with openings;
- It is recommended that RC beams with openings be fire designed by the simplified, advanced or experimental method of NBR 15200;
- It is suggested that NBR 15200 shows requirements for the evaluation of RC beams with openings in case of fire;
- The use of intumescent collars and thermal protection of passing pipes can mitigate the damage and the thermal field of these beams. However, their effectiveness must be evaluated experimentally, through laboratory tests within the scope of NBR 5628 [27] and equivalent standards;
- As a suggestion for future research, it is recommended to experimentally evaluate whether the failure of beams with openings – which occurs by shear stresses at normal temperature – can also occur in case of fire. A set of tests is recommended to evaluate different positions of openings in RC beams exposed to high temperatures.

REFERÊNCIAS BIBLIOGRÁFICAS

[1] Associação Brasileira de Normas Técnicas, *Projeto de Estruturas de Concreto – Procedimento*, ABNT NBR 6118, 2014. [in Portuguese].

[2] F. Leonhardt and E. Monnig, *Construction in Concrete, vol. 227.* Rio de Janeiro: Ed. Interciencia, 1978. [in Portuguese].

[3] J. C. Sussekind, *Reinforced Concrete Course*, vol. 2. Rio de Janeiro: Globo, 1984, 280 p. [in Portuguese].

[4] A. E. Shoeib and A. E. Sedawy, "Shear strength reduction due to introduced opening in loaded RC beams," *J. Build. Eng.*, vol. 13, pp. 28–40, 2017, http://dx.doi.org/10.1016/j.jobe.2017.04.004.

[5] H. S. S. El-Mar, A. S. Sherbini, and H. E. M. Sallam, "Locating the site of diagonal tension crack initiation and path in reinforced concrete beams," *Ain Shams Eng. J.*, vol. 6, pp. 15–24, 2015, http://dx.doi.org/10.1016/j.asej.2014.10.006.

[6] A. Sayed, "Numerical study using FE simulation on rectangular RC beams with vertical circular web openings in the shear zones," *Eng. Struct.*, vol. 198, pp. 1–15, 2019, http://dx.doi.org/10.1016/j.engstruct.2019.109471.

[7] W. Mansour, "Numerical analysis of the shear behavior of FRP-strengthened continuous RC beams having web openings," *Eng. Struct.*, vol. 227, pp. 1–17, 2021, http://dx.doi.org/10.1016/j.engstruct.2020.111451.

[8] L. Herrera, S. Anacleto-Lupianez, and A. Lemnitzer, "Experimental performance of RC moment frame beams with rectangular openings," *Eng. Struct.*, vol. 152, pp. 149–167, 2017, http://dx.doi.org/10.1016/j.engstruct.2017.08.043.

[9] H. M. Elsanadedy, Y. A. Al-Salloum, T. H. Almusallam, A. O. Alshenawy, and H. Abbas, "Experimental and numerical study on FRP-upgraded RC beams with large rectangular web openings in shear zones," *Constr. Build. Mater.*, vol. 194, pp. 322–343, 2019, http://dx.doi.org/10.1016/j.conbuildmat.2018.10.238.

[10] G. Campione and G. Minafò, "Behaviour of concrete deep beams with openings and low shear span-to-depth ratio," *Eng. Struct.*, vol. 41, pp. 294–306, 2012, http://dx.doi.org/10.1016/j.engstruct.2012.03.055.

[11] A. F. Ashour and G. Rishi, "Tests of reinforced concrete continuous deep beams with web openings," *ACI Struct. J.*, vol. 97, pp. 418–426, 2000, http://dx.doi.org/10.14359/4636.

[12] Aykac, I. Kalkan, S. Aykac, and Y. E. Egriboz, "Flexural behavior of RC beams with regular square or circular web openings," *Eng. Struct.*, vol. 53, pp. 2165–2174, 2013, http://dx.doi.org/10.1016/j.engstruct.2013.08.043.

[13] K. D. Tsavdaridis, C. D'Mello, and B. Y. Huo, "Experimental and computational study of the vertical shear behaviour of partially encased perforated steel beams," *Eng. Struct.*, vol. 56, pp. 805–822, 2013, http://dx.doi.org/10.1016/j.engstruct.2013.04.025.

[14] Associação Brasileira de Normas Técnicas, *Projeto de Estruturas de Concreto em Situação de Incêndio*, NBR 15200, 2012. [in Portuguese].

[15] European Committee for Standardization, *Design of Concrete Structures – Part 1.2 - Design Rules, Structural Fire Design*, EN 1992-1-2, 2010.

[16] C. A. Issa and R. A. Izadifard, "Numerical simulation of the experimental behavior of RC beams at elevated temperatures," *Adv. Model. Simul. Eng. Sci.*, vol. 12, no. 1, pp. 1–17, 2021, http://dx.doi.org/10.1186/s40323-021-00198-1.

[17] V. K. R. Kodur, M. S. Dwaikat, and M. B. Dwaikat, "Hight-temperature properties of concrete for fire resistance modelling of structures," *ACI Mater. J.*, vol. 105, pp. 517–527, 2008.

[18] Z. Li, F. Ding, and S. Cheng, "Numerical investigation on moment redistribution of continuous reinforced concrete beams under local fire conditions," *Adv. Struct. Eng.*, vol. 24, no. 15, pp. 3375–3388, 2021, http://dx.doi.org/10.1177/13694332211026226.

[19] B. A. Gedam, "Fire resistance design method for reinforced concrete beams to evaluate fire-resistance rating," *Structures*, vol. 33, pp. 855–877, 2021, http://dx.doi.org/10.1016/j.istruc.2021.04.046.

[20] V. P. Silva, *Projeto de Estruturas de Concreto em Situação de Incêndio, vol. 1*, 2a ed. São Paulo: Blucher, 2017, 238 p.

[21] Q. F. Xu, C. Han, Y. C. Wang, X. Li, L. Chen, and Q. Liu, "Experimental and numerical investigations of fire resistance of continuous high strength steel reinforced concrete T-beams," *Fire Saf. J.*, vol. 78, pp. 142–154, 2015, http://dx.doi.org/10.1016/j.firesaf.2015.09.001.

[22] P. Kumar and V. K. R. Kodur, "Response of prestressed concrete beams under combined effects of fire and structural loading," *Eng. Struct.*, vol. 246, pp. 1–17, 2021, http://dx.doi.org/10.1016/j.engstruct.2021.113025.

[23] International Organization for Standardization, *Fire Resistance Tests – Elements of Building Construction*, ISO 834-8, 1999.

[24] Carvalho RC, Figueiredo JR Fo., Calculation and Detailing of Usual Reinforced Concrete Structures According to NBR 6118: 2014. São Carlos: EdUFSCar, 2016. [in Portuguese].

[25] Fédération Internationale du Béton, *Fire Design of Concrete Structures – Structural Behaviour and Assessment. State-of-Art Report* (FIB Bulletin 46). Lausanne: FIB, 2008.

[26] G. Reins et al., "Multi-story fire analysis for high-rise buildings," in *Proc. 11th Int. Interflam Conf.*, London, 2007, pp. 605–616.

[27] Associação Brasileira de Normas Técnicas, *Structural Building Components – Determination of Fire Resistance*, ABNT NBR 5628, 1980. [in Portuguese].

Author contributions: FLB: conceptualization, methodology, validation, formal analysis, investigation, resources, writing original draft, visualization. GF: conceptualization, writing. VPS: conceptualization, validation, investigation, supervision, formal analysis.

Editors: Maurício de Pina Ferreira, Guilherme Aris Parsekian.

NOTATION:

$A_{s,min}$	Cross-sectional area (minimum) of longitudinal reinforcement (beam without opening)
A_s	Cross-sectional area of longitudinal reinforcement (beam without opening)
$A_{st,min}$	Cross-sectional area (minimum) of longitudinal reinforcement in tension flange (opening region)
A_{st}	Cross-sectional area of longitudinal reinforcement in tension flange (opening region)
$A_{st.fi}$	Cross-sectional area of longitudinal reinforcement in tension flange (opening region) in case of fire
$A_{sc,min}$	Cross-sectional area (minimum) of longitudinal reinforcement in the compression flange (opening region)
A_{sc}	Cross-sectional area of longitudinal reinforcement in compression flange (opening region)
$A_{sc,fi}$	Cross-sectional area of longitudinal reinforcement in compression flange (opening region) in case of fire
$A_{sw,min}$	Cross-sectional area (minimum) of transverse reinforcement (beam without opening)
A_{sw}	Cross-sectional area of transverse reinforcement (beam without opening)
$A_{swt,min}$	Cross-sectional area (minimum) of transverse reinforcement in tension flange (opening region)
A_{swt}	Cross-sectional area of transverse reinforcement in tension flange (opening region)
$A_{swc,min}$	Cross-sectional area (minimum) of transverse reinforcement in compression flange (opening region)
A_{swc}	Cross-sectional area of transverse reinforcement in the compression flange (opening region)
A_{sws}	Cross-sectional area of suspension transverse reinforcement (opening region)
A_s/A_c	Reinforcement ratio (area of steel reinforcement in the beam cross-section)
CAA	Class of environmental aggression of NBR 6118 standard
$L_{opening}$	Length of the opening in the beam
N_c	Compression force acting on the compressed (upper) flange of the opening
N_t	Tensile force acting on the tensioned (bottom) flange of the opening
M_{sd}	Bending moment acting on the beam in the opening region
M_c	Bending moment acting on the compressed (upper) flange of the opening
M_t	Bending moment acting on the tensioned (bottom) flange of the opening

V_{Sd}	Shear force action on the beam in the opening region
V_c	Shear force action on the compressed (upper) flange of the opening
V_t	Shear force action on the tensioned (bottom) flange of the opening
x	Neutral axis depth
x/d	Beam ductility according NBR 6118 requirements
z	distance between axes of the compressed and tensioned flange of the opening
ε_s	Theoretical steel reinforcement elongation
ε_c	Theoretical shortening of concrete
γ_c	Partial factor for concrete
γ_s	Partial factor for steel reinforcement

Annex A. Fea model: thermal properties of concrete and steel reinforcement.

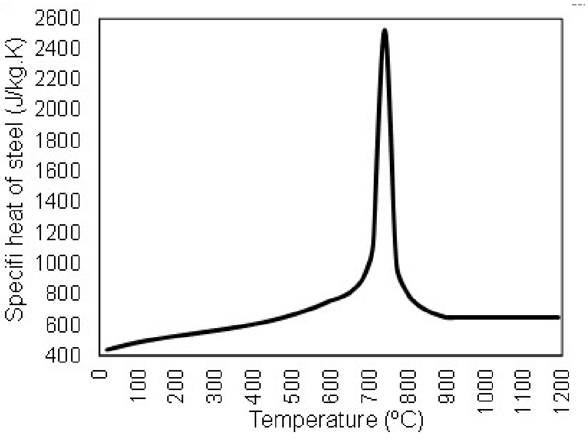

Figure A1 – Specific heat of steel

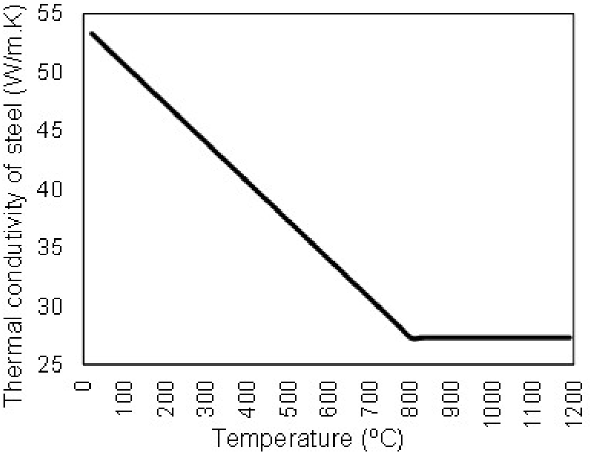

Figure A2 – Thermal conductivity of steel

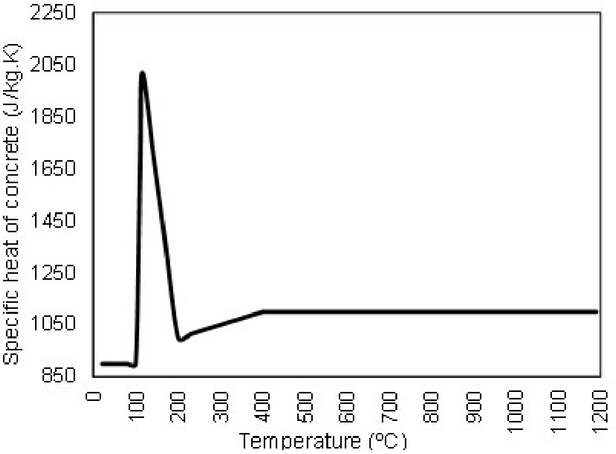

Figure A3 – Specific heat of concrete

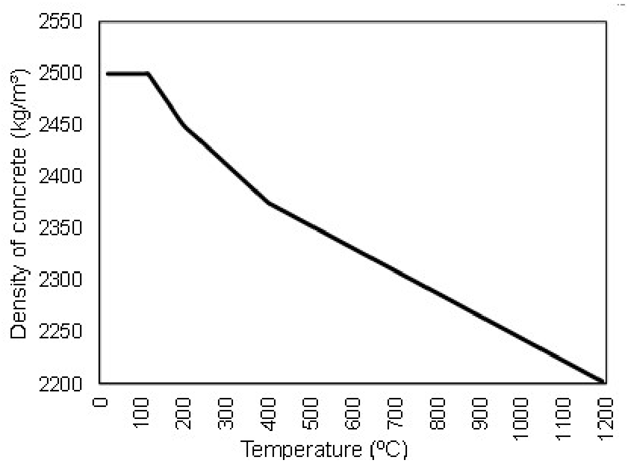

Figure A4 – Density of concrete

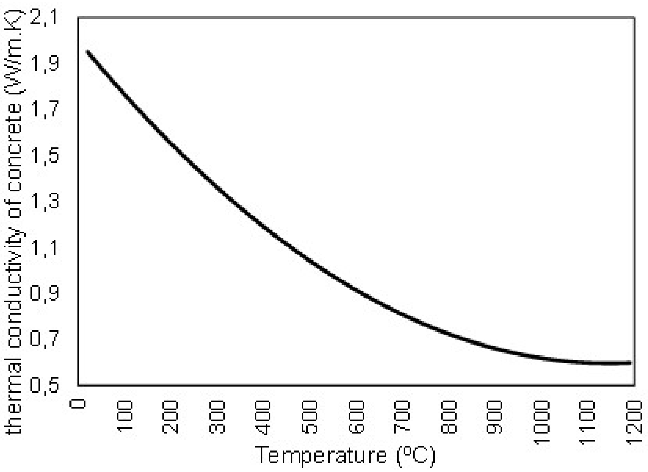

Figure A5 – Thermal conductivity of concrete

IBRACON Structures and Materials Journal
Revista IBRACON de Estruturas e Materiais
ISSN 1983-4195 ismj.org

ORIGINAL ARTICLE

Damage assessment & innovation of efficient retrofitting solution of RC slabs exposed to contact explosion

Avaliação de danos e inovação de solução eficiente de reabilitação de lajes de concreto armado expostas a explosão de contato

Ibrahim Mohamed Metwally[a]

[a]Housing & Building National Research Center, Concrete Structures Research Institute, Dokki, Giza, Egypt

Received 03 February 2022
Accepted 15 August 2022

Abstract: Under contact explosions, the reinforced concrete structures can behave in a brittle manner with highly localized damage like concrete cratering, spalling, and reinforcement rupturing. High-speed fragmentation resulting from concrete spall may cause severe casualties and injuries. It is therefore important to restrained concrete fragments and improve collapse resistance of the slab. A new retrofitting technique is proposed in this paper which completely prevents fragmentation. To mitigate blast effects on civil structures, a new kind of concrete material named Ultra-High-Performance-Concrete (UHPC) is now widely studied and applied. UHPC material is known for its high compressive and tensile strength, large energy absorption capacity as well as good workability and anti-abrasion ability compared to normal strength concrete(NRC). All of recent experimental published work concerning blast performance of UHPC slabs under far or near explosion effect, on the other side, the contact explosion tests are relatively limited experimentally and nearly impossible because of security restrictions and costly in terms of both preparation and measurements. So, the real and accurate finite element models are needed to address this gap and understanding the real contact-explosion behavior of both NRC and UHPC slabs. The numerical analyses allow gaining insight into the complex failure mechanisms occurring in the slab and not directly observable. In this study, coupled smoothed particle hydrodynamics (SPH) method and finite element method is utilized to simulate the contact blast tests. Numerical results are compared with the experimental observations, and the feasibility and accuracy of the numerical model are validated. The validated numerical model provided a useful tool for designing potential blast-retrofitting solutions which can prevent the local material damage and fragmentations in both NRC & UHPC slabs subjected to contact explosion. This study introduced adequate and very efficient protection solution for both NRC & UHPC slabs exposed to contact explosion (1 kg of TNT) by utilizing the composite action generated between slabs & bonded steel plates. The 2 mm and 1 mm bonded steel plates at both faces of the NRC and UHPC slabs respectively attained a superior resistance to contact explosion.

Keywords: UHPC, contact explosion, slabs, Ansys Workbench.

Resumo: Sob explosões de contato, as estruturas de concreto armado podem se comportar de forma frágil com danos altamente localizados, como crateras de concreto, "spalling" e ruptura de reforço. A fragmentação em alta velocidade resultante de "spalling" de concreto pode causar graves mortalidades e ferimentos. Por isso, é importante conter fragmentos de concreto e melhorar a resistência ao colapso da laje. Uma nova técnica de reabilitação é proposta neste artigo que impede completamente a fragmentação. Para mitigar os efeitos da explosão nas estruturas civis, um novo tipo de material concreto chamado Ultra-High-Performance-Concrete (UHPC) é agora amplamente estudado e aplicado. O material UHPC é conhecido por sua alta resistência à compressão e tração, grande capacidade de absorção de energia, bem como boa trabalhabilidade e resistência à abrasão em comparação com o concreto de resistência normal (NRC). Todos os trabalhos publicados experimentais recentes sobre o desempenho das lajes UHPC consideram o efeito de uma explosão longe ou muito perto, por outro lado, os testes de explosão de contato são relativamente limitados experimentalmente e quase impossíveis devido a restrições de segurança e dispendiosos em termos de preparação e medições. Assim, os modelos reais e precisos de elementos finitos são necessários para resolver essa lacuna e entender o comportamento real de explosão de contato das lajes NRC e UHPC. As análises numéricas permitem obter informações sobre os complexos mecanismos de falha que ocorrem na laje e não diretamente observáveis.

Corresponding author: Ibrahim Mohamed Metwally. E-mail: ibrahimhbrc@gmail.com
Financial support: None.
Conflict of interest: Nothing to declare.
Data Availability: The data that support the findings of this study are openly available in reference list at the end of this paper.

Neste estudo, o método de hidrodinâmica de partículas suavizadas (SPH) e o método de elemento finito são utilizados para simular os testes de explosão de contato. Os resultados numéricos são comparados com as observações experimentais, e a viabilidade e a precisão do modelo numérico são validadas. O modelo numérico validado forneceu uma ferramenta útil para projetar soluções potenciais de adaptação de explosão que podem evitar danos e fragmentações de materiais locais em ambas as lajes NRC e UHPC submetidas à explosão de contato. Este estudo introduziu uma solução de proteção adequada e muito eficiente para ambas as lajes NRC e UHPC expostas à explosão de contato (1 kg de TNT) utilizando a interação composta gerada entre lajes e placas de aço ligados. As chapas de aço coladas de 2 mm e 1 mm em ambas as faces das lajes NRC e UHPC, respectivamente, obtiveram uma resistência superior à explosão de contato.

Palavras-chave: UHPC, explosão de contato, lajes, Ansys Workbench.

How to cite: I. M. Metwally, "Damage assessment & innovation of efficient retrofitting solution of RC slabs exposed to contact explosion," *Rev. IBRACON Estrut. Mater.*, vol. 16, no. 2, e16207, 2023, https://doi.org/10.1590/S1983-41952023000200007

1 INTRODUCTION

Under explosive loading conditions, various failure modes can be observed on reinforced concrete structures, including bending failure, shear failure and concrete spalling failure. Flexural damage is the most ideal damage mechanism because it has the greatest ductility and can absorb energy to the greatest extent. In addition to bending and shearing damage, concrete spalling is another important damage mode, which mainly occurs at close range or in contact with explosion [1], [2].

When subjected to explosive loadings, the concrete structures may present local damage, including cratering, spalling and breaching damage. As shown in Figure 1, cratering damage occurs because of high compressive pressure in the contacted surface between the concrete and charges. Spalling damage appears in the free surface of the concrete structures when the tensile stress generated by the compressive waves in the free surface is larger than the spalling strength of the concrete. Breaching damage arises when the impulse generated by the explosion is large enough to overcome the resistant forces of structures [1].

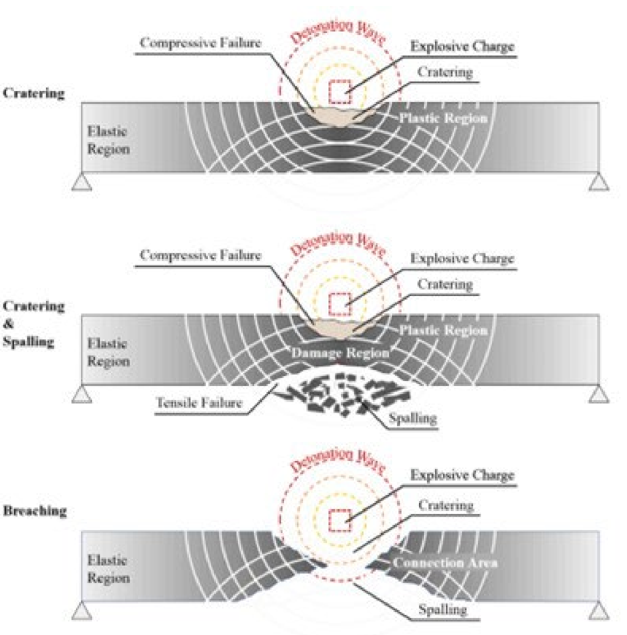

Figure 1- Cratering, spalling and breaching damage of concrete structures exposed to contact explosion [2].

In the blast event, the high-speed fragments produced by the spalling and breaching damage of structures could cause unexpected casualties and property loss [3]–[5]. Therefore, it is most significant to prevent and decrease the spalling and breaching damage of the structures under blast loadings. To solve this problem, Morishita et al. [6], as well as Tanaka and Tuji [7] attempted to increase the reinforcement ratio and compressive strength of concrete to obtain an outstanding blast resistance of concrete structures, but the results of the tests were not consistent with the desired effect.

In the protective structures against blast loadings, Nam et al. [8] found that the energy absorption capacity and the fracture energy of materials have an obvious influence on the blast resistance performance of structures. Ultra-high performance concrete (UHPC) has a compressive strength of 150–250 MPa and a flexural strength of 30–40 MPa. It has exceptionally high energy absorption capacity compared to NRC and has resistance to fragmentation, making it ideal for panels and components that need to perform under explosive, impact or shock loads. Besides, it also shows excellent fracture energy with 20,000–40,000 J/m^2, which is several orders of magnitude higher than that of normal concrete materials. Its flexural toughness is greater than 200 times that of conventional fiber reinforced concrete. That indicates UHPC can be employed to prevent and decrease spalling damage. Furthermore, UHPC presents better durability, fire performance, the excellent cyclic, fatigue and impact performance [9].

Because of previous advantages of UHPC, it could have great prospects in the engineering structures against blast loadings. It is regretted that only few researches were conducted on the spalling resistant performance of UHPC. The primary purpose of conducting the blast tests and numerical analysis of UHPC is to provide adequate structural protection against explosions.

The response of reinforced concrete (RC) members subjected to contact explosion effects is more severe than the response to non-contact explosions due to local material failure. The shock-wave reflection within the RC member causes severe local material damage. The resulting loss of concrete cross-section reduces the axial load and bending capacity of the RC member. Therefore, it is of great significance to study the local damage and fragments of RC members under contact explosions. The response of RC components to contact explosion effects is highly non-linear and is an ongoing field of study. Besides, mitigation of contact explosion effects is yet to be studied. Therefore, it is imperative to design strategically important structures envisaged as a potential target for terrorist attacks by incorporating mitigation strategies that limit the damage caused by contact explosions.

Based on the excellent energy absorption property and high fracture energy of UHPC, it is promising to prevent and decrease the spalling damage. Moreover, the test results conducted by Li et al. [10] can also provide data for calibrating and verifying the dynamic constitutive model of UHPC. In this study, two UHPC slabs and one NRC slab as a control one were prepared, by Li et al. [10]. 1 kg TNT explosives were employed to generate the contact-blast loadings. The primary objective of this research is to develop an accurate numerical model to simulate the real behavior, damage mechanism, & fragmentation of NRC & UHPC reinforced concrete slabs under contact explosion, and comparing the numerical results with those obtained by the tests of the slab specimens of the experiments conducted by Li et al. [10] for validation of the proposed model. Besides, promising retrofitting technique that have shown impressive results for fragmentations prevention.

2 DESCRİPTİON OF SLAB TESTS

For a more comprehensive description of the slab tests including slab specimens, materials properties, experimental procedure and test setup, instrumentation, as well as description of the test results including damage patterns, reinforcement strains & fragmentations can be found as detailed by the work of Li et al. [10]. In total, three slabs including one normal strength concrete (NRC-2) slab and two micro steel fiber reinforced ultra-high performance concrete (UHPC-4 & UHPC-7) slabs were tested [10]. The dimension of all slabs is: 2000 mm long, 800 mm wide and 120 mm thick. UHPC-4 slab was longitudinally reinforced by 9D12, while UHPC-7 slab was reinforced by less longitudinal reinforcement bars (5D12). This modification was made to investigate the influence of longitudinal reinforcement spacing on slab response. The shear reinforcement for all slab are constant equal 11D8. Both of these two reinforcements (D12 & D8) have 360 MPa yielding strength. Table 1 and Figure 2 show the slab concrete dimensions and reinforcement. The control NRC slabs were constructed by concrete with unconfined compressive strength of 40 MPa, while UHPC concrete made with micro steel fibers with a length of 15 mm and diameter of 0.12 mm were mixed at a volume dosage of 2.5%; the tensile strength of the micro steel fiber is 4295 MPa. Ultra-high performance fiber reinforced concrete with uniaxial compressive strength of 145 MPa and tensile strength of 22 MPa was used to build the UHPC slabs [10].

Table 1-Summary of slab specimens tested by Li et a [10]

Specimen	Slab thickness, mm	Compressive strength of concrete, MPa	Longitudinal reinforcement	Shear reinforcement	Observed damage mode
NRC-2	120	40	9D12	11D8	Perforation
HPC-4	120	145	9D12	11D8	Perforation
UHPC-7	120	145	5D12	11D8	Perforation

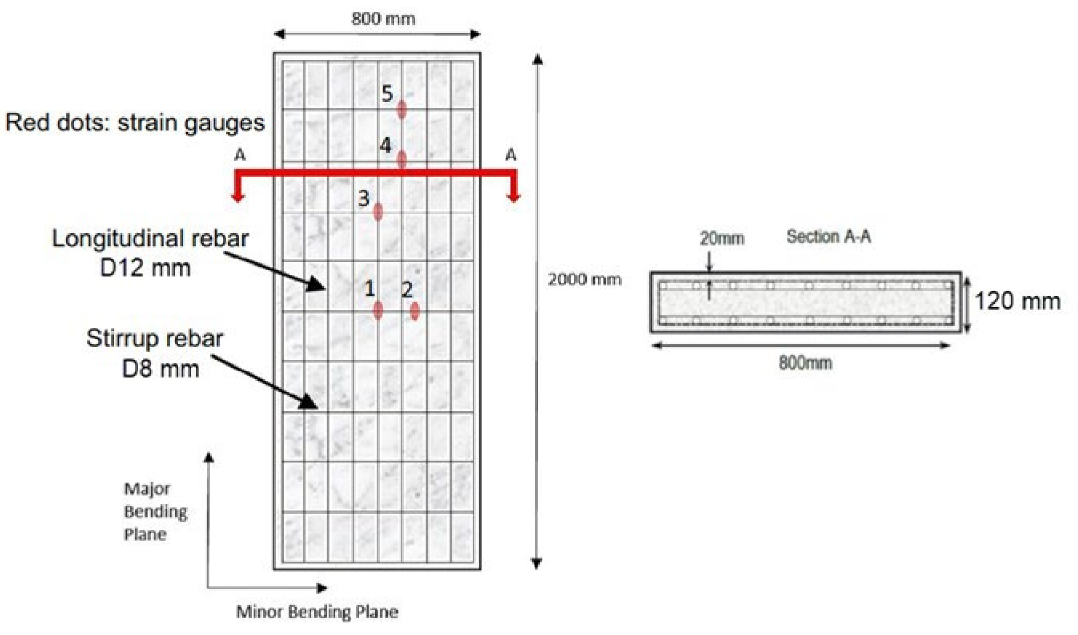

Figure 2 - Reinforcement layout of slab specimens tested by Li et al. [10]

3 EXPERIMENTAL SETUP

As depicted in Figure 3, the slab was firstly placed on the steel rig using a crane, then both ends of the slab were bolt fixed with the angle steel cleats. The slab was subjected to contact explosions of cylindrical explosives of and 1 kg of TNT. During the sample preparation, strain gauges were attached to the reinforcement bars at different locations of each slab as indicated by red dots in Figure 2. The positions where the strain gauges located were carefully grinded using electrical grinder, and later mopped using liquid acetone. These procedures were carried out to guarantee the contact between the strain gauge and reinforcing bar. Strain gauges were used to record the strain time history [10].

Figure 3 - Test setup of the slab specimens tested by Li et al. [10]

4 FİNİTE ELEMENT MODELİNG & ANALSİS

In this study, both NRC & UHPC slab specimens tested by Li et al. [10] under contact explosion are numerically modeled and analyzed using ANSYS Workbench Explicit Dynamic module [11]. A three-dimensional finite element model has been created for the slabs with the use of the Explicit Dynamics Lagrangian formulation. The detailed modeling steps are described in the following sections.

4.1 Geometry

The ANSYS Workbench Design Modeler, which provides analysis-specific geometry modeling tools, has been used to model the specimens. The concrete slabs with dimensions of 2000 × 800 × 120 mm and 1 kg TNT explosion material have been modeled using the hexahedron solid body. The shape of TNT charge in the experimental test was cylindrical shape (Figure 2), in the present study, a cubical shape was used in all FE models. This based on the findings of Zhao et al. [12] that is using the cubic charge instead of the cylinder charge is allowable and don't affect the damage mechanism and performance of RC slab exposed to contact explosion. The reinforcement bars have been modeled using discrete line body (Beam Elements) objects and were placed in exact coordinates matching their respective locations as of Figures 2 and 4. The created geometry model for the whole problem using ANSYS Design Modeler is illustrated in Figure 4. This model is then imported by the Explicit Dynamics system to continue with the modeling and analysis steps.

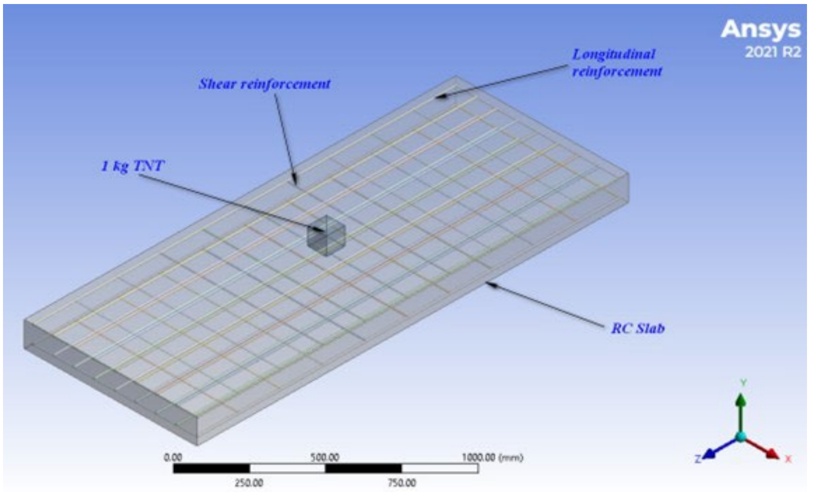

Figure 4- Geometry model of the reinforcement discrete line bodies(beam elements) embedded within the concrete slab solid body of the slab specimens under contact explosion tested by Li et al. [10]

4.2 Material Modeling

4.2.1 Constitutive model of concrete

ANSYS explicit materials library has two concrete materials named as CONC-35 and CONC-140 in addition to CONCRETE-L material model. These models have advanced plasticity options for brittle materials covered by the RHT concrete strength [13] which is expressed in terms of pressure dependent initial elastic yield surface, failure surface and residual friction surface in the stress space. The mathematical description of RHT model, descriptions of the parameters such as polynomial equation of state (EOS) parameters, damage parameters, and failure surface parameters and their default values corresponding to standard 35 MPa concrete can be found in Borrvall and Riede [14]. The RHT constitutive model is an advanced plasticity and shear damage model. Similar to other hydrodynamic codes, the study of the dynamic response of materials and structures involves the governing equations and in ANSYS Explicit Dynamics they are established through the principle of conservation of mass, momentum and energy. The finite element analysis itself is a study of continuum, therefore another two relationships describing the material behavior is required, namely the Equation of State (EOS) and a constitutive material model. RHT concrete model combines the strength model and failure model that form the constitutive material model in a single formulation [13], [14]:

$$F_{fail}\left(P,\sigma_{eq},\theta,\varepsilon_p,\dot{\varepsilon_p}\right)=\sigma_{eq}-\left[f_c\times Y^*\left(\varepsilon_p,P^*,\dot{\varepsilon_p}\right)\times F_{CAP}\left(P^*\right)\times R_3\left(\theta\right)\right]$$

$$Y^*\left(\varepsilon_p,P^*,\dot{\varepsilon_p}\right)=f_c\left[\varepsilon_p,Y^*_{TXC}\left(P^*,F_{RATE}\left(\dot{\varepsilon_p}\right)\right)\right]$$

where
σ_{eq} = equivalent stress,
f_c = uniaxial compressive strength,
$Y*(\varepsilon_p, P^*, \dot{\varepsilon}_p)$ = pre-peak yield surface on the compressive meridian,
P = pressure,
P^* = pressure normalized by the uniaxial compressive strength,
θ = Lode angle,
ε_p = plastic strain,
$\dot{\varepsilon}_p$ = plastic strain rate,
F_{CAP} = pressure dependent elastic cap function,
$R_3(\theta)$ = third invariant dependency,
$Y^*_{TXC}(P^*, F_{RATE}(\dot{\varepsilon}_p))$ =pressure and rate dependent peak surface on the compressive meridian and
$F_{RATE}(\dot{\varepsilon}_p)$ = strain rate dependency.

The strain rate independent compressive meridian in RHT formulation is developed through the following equations:

$$Y^*_{TXC}(P^*) = A(P^* - P_s^*)^n$$

$$P_s^* = \frac{1}{3} - \left(\frac{1}{A}\right)^{\frac{1}{n}}$$

Where:
A and n *are the failure surface parameters that define the shape of the failure surface as a function of pressure. On the other hand,* P_s^* *is the spall strength.*

Strain rate effects are incorporated into the equation through the increases in peak strength. Two different terms are used for compression and tension, defined as:

$$F_{RATE} = \begin{cases} \left(\frac{\dot{\varepsilon}}{\dot{\varepsilon}_o}\right)^{\delta} \\ \left(\frac{\dot{\varepsilon}}{\dot{\varepsilon}_o}\right)^{\alpha} \end{cases}$$

where
F_{RATE} = represents the dynamic increase factor (DIF) as the function of strain rate $\dot{\varepsilon}$,
α and δ = user defined parameters and
$\dot{\varepsilon}_0$ = reference strain rate (quasi-static).

The minimum value F_{RATE} is 1.0. This rate enhancement factor is applied to the peak strength surface using the equations:

$$Y^*_{TXC}\left(P^*, F_{RATE}(\dot{\varepsilon})\right) = A_{dyn}(P^* - P^*_{s,dyn})^n$$

$$A_{dyn} = AF_{RATE}^{1-n}$$

$$P^*_{s,dyn} = F_{RATE}\left(\frac{1}{3} - \frac{1^{\frac{1}{n}}}{A}\right)$$

Figure 5 shows a typical deviatoric section plane of a strength surface. In the case of concrete material, the deviatoric section changes from triangular shape at low pressure (brittle condition) to a circular shape at high pressure (ductile condition). In RHT concrete model, the transition is represented through the third invariant dependent term $R3(\theta)$ and evaluated by the following equations:

$$R_3\,(\theta) = \frac{2(1-\psi^2)cos\theta + (2\psi-1)(4(1-\psi^2)cos^2\theta + 5\psi^2 - 4\psi)^{\frac{1}{2}}}{4-(1-\psi^2)cos^2\theta + (1-2\psi)^2}$$

$$\psi = \psi_0 \times B_Q \times P^*$$

$$\cos(3\theta) = \frac{3(3)^{\frac{1}{2}} \times j_3}{(2)^{\frac{3}{2}} \times (j_2)^{\frac{1}{2}}}$$

where
ψ = ratio of a material tensile strength to compressive strength,
ψ_0 = tensile to compression meridian ratio at zero pressure,
B_Q = rate at which the fracture surface transits from a triangular to a circular form with increasing pressure and
J_2 & J_3 = second and third invariants of the deviatoric stress tensor

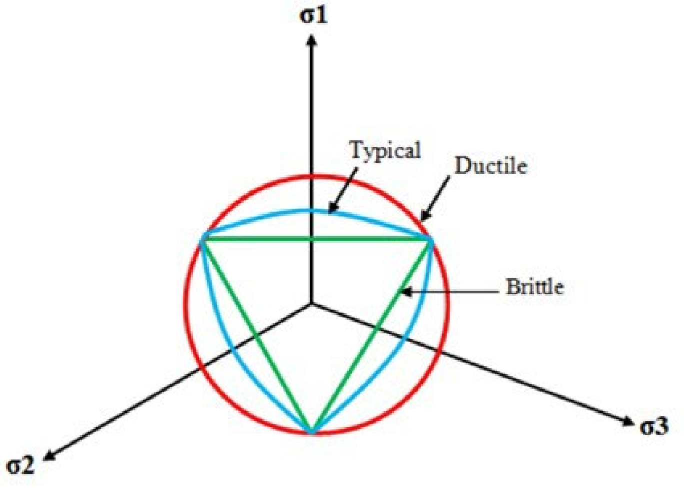

Figure 5- Deviatoric cross section of a strength surface

Figure 6 illustrates the concept of strain hardening based on a uniaxial compression curve. In order to allow for strain hardening behaviour, an elastic limit surface and a hardening slope is introduced. The elastic limit surface is scaled down from the peak surface by the normalized elastic strength parameters (user defined). The pre-peak yield surface is defined through the interpolation between the elastic and peak surfaces based on the ratio of elastic and plastic shear moduli using:

$$Y^* = \frac{\varepsilon_p}{\varepsilon_{p,pre}}(Y^*_{TXC} - Y^*_{el}$$

$$\varepsilon_{p,pre} = \frac{Y^*_{TXC}}{3G} \times \frac{G}{G-G_{pl}}$$

where
Y^*_{el} = initial elastic limit scaled down from peak surface,

ε_p = plastic strain, accumulated as soon as elastic surface is exceeded,
$\varepsilon_{p,pre}$ = pre-peak plastic strain,
G = shear modulus and
G_{pl} = plastic shear modulus.

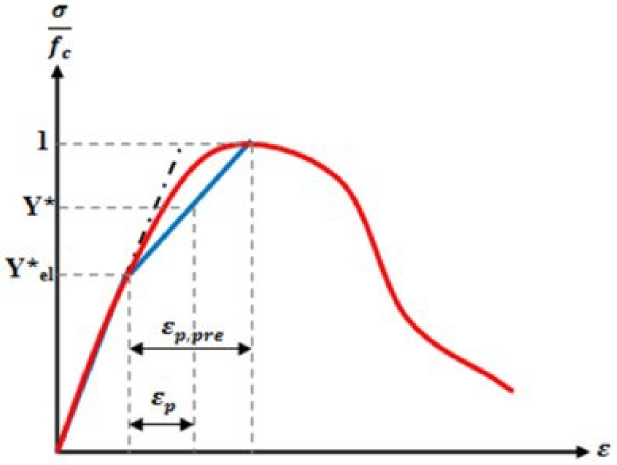

Figure 6- Concept of strain hardening in RHT concrete model

Damage is assumed to accumulate due to the shear induced cracking once the peak yield has been exceeded. A damage index D is used to determine the value of the current strength surface using the relationship:

$$D = \sum \frac{\Delta \varepsilon_p}{\varepsilon_p^{fail}}$$

$$\varepsilon_p^{fail} = MAX(D1(P^* - htl^*)^{D2}, \varepsilon_{p,min}^{fail}$$

$$htl^* = -\frac{f_t}{f_c} \times \frac{f_s}{f_c} \times \psi_0 \left(\frac{\frac{f_t}{f_c}}{3\left(\psi_0 \frac{f_s}{f_c} - \frac{f_t}{f_c}\right)} \right)$$

where
D = damage index (ranging from zero to unity),
$D1$ & $D2$ = damage constants,
ε_p^{fail} = pressure dependent plastic strain to failure,
$\varepsilon_{p,min}^{fail}$ = minimum strain to failure (complete damage at low pressure),
htl^* = normalized hydrodynamic tensile limit,
f_t / f_c = normalized tensile strength and
f_s / f_c = normalized shear strength.

The strength of the completely crushed material in the present model is defined through the reduction in strength (strain softening) using equation:

$$Y_{res} = (B \times (P^*)^m)$$

Where:
Y_{res} = residual strength surface and
B & m = residual strength parameters.

On the other hand, the current shear modulus of the crushed material $G_{fractured}$ is defined through:

$$G_{fractured} = (1 - D)G + DG_{residual}$$

where
$G_{residual}$ = residual shear modulus at fracture (post-damage shear).

In the present work, the strength of CONC-35 was set to 40 MPa for the normal strength concrete material for which the density value was set to 2350 kg/m3. The shear modulus of concrete was calculated as 11,976 MPa which is 40 percent of the concrete's modulus of elasticity which is 29,940 MPa. Initial compaction pressure was considered as 16.7 MPa. On the other side, the strength of CONC-140 was set to 145 MPa for UHPC and tensile strength equal 22 MPa (f_t / f_c = 0.15).

The RHT concrete model parameters for both NRC & UHPC used in the present numerical analysis are summarized in Table 2.

Table 2 - Material model properties for RHT concrete model [10], [14]

Name	Units	NRC	UHPC
Density	t/mm^3	2.5 e-09	2.7 e-09
Poisson's ratio	None	0.20	0.20
Compressive strength	MPa	40	145
Tensile to comp. strength (f_t/f_c)	None	0.08	0.15
Shear strength to compressive (f_s/f_c)	None	0.18	0.18
Intact failure surface constant A	None	1.6	1.6
Intact failure surface exponent N	None	0.61	0.61
Tens./Comp. Meridian ratio Q2.0	None	0.6805	0.6805
Brittle to Ductile Transition BQ	None	0.0105	0.0105
Hardening Slope	None	2	2
Elastic Strength/ft	None	0.7	0.7
Elastic Strength/fc	None	0.53	0.53
Residual Strength constant B	None	1.6	1.6
Residual Strength constant M	None	0.61	0.61
Compressive strain rate exponent, á	None	0.029	8.79e -03
Tensile strain rate exponent, ä	None	0.034	0.012
Maximum fracture strength ratio SFMAX	None	1E+20	1E+20
Use cap on elastic surface	None	Yes	Yes
Damage Constant D1	None	0.04	0.04
Damage Constant D2	None	1	1
Minimum strain to failure	None	0.01	0.01
Residual shear modulus fraction	None	0.13	0.13
Shear Modulus	MPa	11,976	22,802
Porous Sound speed	mm/s	2897E03	3242E03
Initial Compaction Pressure Pe	MPa	18.37	93.30
Solid Compaction Pressure Ps	MPa	6000	6000
Compaction Exponent n	None	3	3

4.2.2 Constitutive model of reinforcement

Steel bars reinforcement were simulated by Steel 4340 model which is implement in Ansys Workbench library. The behavior of Steel 4340 is defined by Johnson-Cook strength and failure model. Johnson-Cook model was used to define strength of the material Steel 4340. This constitutive model defines the strength behavior of materials subjected to large strains, high strain rates and high temperatures [15]

$$Y = \left[A + B\varepsilon_p^n\right]\left[1 + c\, log\varepsilon_p^n\right]\left[1 - T_H^m\right] \tag{1}$$

Where:
ε_p= effective plastic strain
ε_p*= normalized effective plastic strain rate
T_H = homologous temperature = $(T - T_{room})/ (T_{melt}- T_{room})$
The used parameters of Johnson - Cook damage model of steel reinforcement [15] is shown in Table 3.

Table 3- Johnson-Cook constitutive parameters for steel 4340 model [15]

Material	Density	õ	E	όy(A)	B	n	m	C	Tmelt	Troom
Steel 4340	7.8E-009 t/mm^3	0.3	200,000 MPa	360 MPa	1500 MPa	0.4	1.2	0.045	1800 K	293 K

Where:
A: Yield stress of the used steel bars is taken as 360MPa & Youngs modulus = 200,000MPa [10]
B, n, m and C are material constants

Constitutive Model of Explosive Material

TNT (Explosive). The TNT is defined using Jones-Wilkins-Lee (JWL) form of equation of state

$$P = A[1 - \omega/R_1V]e^{-R1V} + B[1 - \omega/R_2V]e^{-R2V} + \omega E/V \tag{2}$$

Where A, B, R1, R2, are empirically derived constants varies with each explosive, V is the relative volume of expansion of explosive product and E is the detonation energy per initial unit volume [16]. The material property of TNT and variable for JWL equations listed in Table 4.

Table 4- Jones-Wilkins-Lee (JWL) constitutive parameters for TNT

Variable	Value
Density, kgm^3	1.225
A	373.77
B	374.71
R1	4.15
R2	0.9
ù	0.35
C-J Detonation velocity (m/ms)	6.93
C-J Energy/unit volume (MJ/m^3)	6000
C-J Pressure (Mpa)	21000

4.3 Boundary Conditions

Boundary conditions of the finite element models were simulated accurately like experiential ones. Both ends of the slab were fixed. As reported by Li et al. [10] that contact explosion which induces highly localized response and damage does not depend on the boundary condition.

4.4 Steel-Concrete Bond

The bond between steel reinforcement and concrete in the FE models were simulated as full bonded. Because the govern failure and damage modes is sudden local material damage and fragmentations which will occurs before bond slippage.

4.5 Finite Element Analysis

The finite analysis was carried out using ANSYS Workbench Explicit Dynamic Version 2021R2 [11]. This widely and famous used software is capable of solving problems including impact, explosions, collusions and material failure using a Lagrange solver. Users can run the software as part of ANSYS workbench environment. For contact explosion test simulation, coupled finite element and smoothed particle hydrodynamics (SPH) method is adopted(FEM-SPH), coupled FEM-SPH algorithm is the most effective method to reproduce the damage progresses of the RC slab to contact explosion as investigated by Zhao et al. [12]. The SPH particles are used to simulate the high explosive and finite elements are used to simulate the reinforced concrete slab.

4.5.1 Mesh sensitivity

For studying the element mesh sizes whether it affects the analysis or not, the slabs have been modeled using three different mesh sizes of 10 mm, 20 mm, and 30 mm respectively. Table 5 shows the details of the mesh data for the current slab model. For each slab, refined element mesh sizes have been used to carry out the analysis and a comparison of experiential results with FE ones has been conducted to see the best size which gives more accurate results and damage shapes.

Table 5: Mesh size data for slab (NRC-2) model

	Mesh 1	Mesh 2	Mesh 3
Mesh Size	10 mm	20 mm	30 mm
Nodes	223093	34443	13144
Elements	197929	26725	9023

From the above trails, the slab specimens using the 20 mm mesh size can be used to show clearly the crack propagation of the slab system with more refined eroded particles than the coarser mesh(30mm). 20 mm mesh size will be used for all FE models; it gave more accurate results with reasonable computational time.

4.5.2 Analysis types

Dynamic explicit analysis is performed for all cases. Solutions are computed up to 500 µs, where no further permanent deformation is observed for all load values.

5 RESULTS AND DISCUSSIONS

5.1 Validation of the Proposed FE Models

One critical aspect of numerical simulations is validation with experimental results or physical phenomenon to ensure the accuracy of selected material models, boundary conditions, and contact algorithms adopted in the established FE model.

5.2 Normal Strength Concrete (NRC) Slab

Based on the experimental work of Li et al. [10], the normal strength concrete slab NRC-2 was subjected to 1 kg TNT contact explosion placing also at the center of slab surface. As can be noticed from Figures 7, and 8 severe blast load induced perforation or punching failure in the slab. It is also noted that significant concrete cracking occurred along the two free (unsupported) edges near the slab boundary. As no clear slab deformation was observed, these damages were believed also caused owing to the following reasons:

1- Stress wave propagation

2- Reflection

Stress wave of contact explosion caused cracks along the two unsupported edges because of the short propagation distance between the contact TNT explosive material and the free boundary edges, which produced high tensile stresses which is extremely bigger than the concrete tensile strength due to wave reflection and thus cracking of concrete.

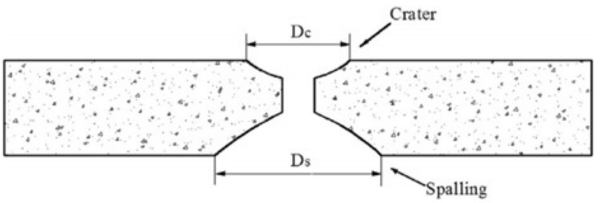

Figure 7-Measurement of the damaged areas

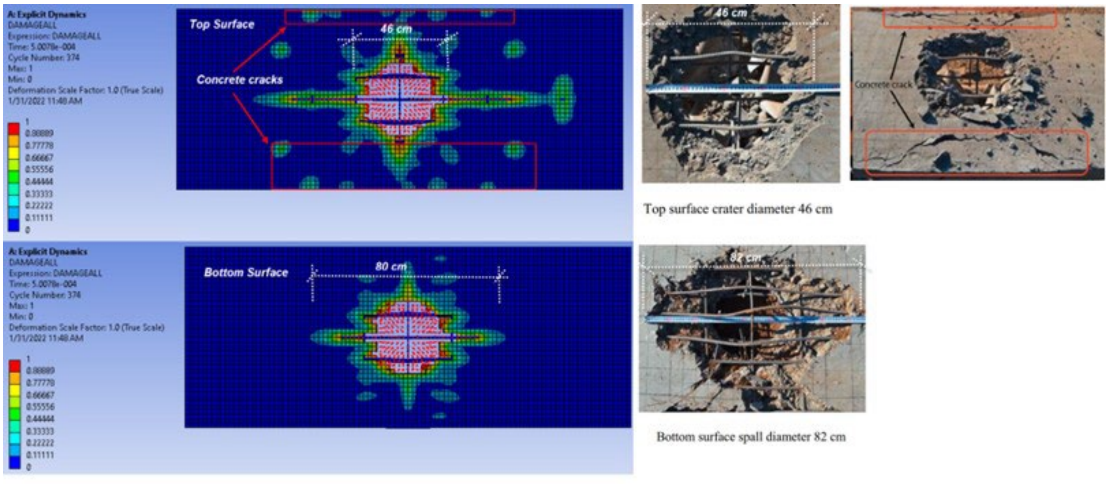

Figure 8 – Comparison between experimental damage & FE damage of NRC-2 Slab

5.3 Damage Pattern of RC Slab under Contact Explosion

Damage behavior of RC slabs under contact explosion refers to the dimensions of the crater and spalling of the NRC-2 slab. The level of damaged is estimated by the crater diameter (D_C) and spalling diameter (D_S). These values measured in both experiential work conducted by Li et al. [10] and the current FE models as illustrated in Table 6.

Table 6 - The diameters of the crater and spalling from the numerical simulations and experimental test

Slab	Damage Failure	Experimental Test [10]	FEM-SPH	EXP/FEM
NRC-2 Slab	Concrete Crater Top Surface	46	46	1
	Concrete Spalling Bottom Surface	82	80	1.025
UHPC-4 Slab	Concrete Crater Top Surface	23	24	0.96
	Concrete Spalling Bottom Surface	45	48	0.94
UHPC-7Slab	Concrete Crater Top Surface	25	26	0.96
	Concrete Spalling Bottom Surface	48	50	0.96

The damage diameters of the crater and spalling are found in Figures 7 and 8. The contour value between 0 and 1 indicates the concrete element damage [0: undamaged material & 1: fully damaged material]. As shown in Figure 8, the elements with damage values between 0.9 to 1.0 are not shown. The purpose of such processing is to better and clearly show the damage status of the RC slab. This is because when the damage values of the damage zone are between 0.9 and 1.0, the concrete material has been severely damaged. Lots of macroscopic cracks will appear in the damaged region of the RC slab, and the SPH particles have been flying. Under contact blast conditions, the blast pressure directly impacts the top surface and causes a crater failure which is approximately circular and localized at the middle of the slab.

The crater diameters for the FEM-SPH is about 46 cm. When the blast pressure impacts the top surface of the RC slab, it induces a punching failure. Meanwhile, the interaction between the incident stress and reflective stress causes a spalling failure on the bottom surface of the RC slab. The spalling failure diameters for the FEM-SPH is about 80 cm. Table 6 shows the diameters of the crater and spalling from the numerical simulations and experimental test, it appears that a good matching between both results was achieved.

It is noted in both test slabs and numerical results, that the dynamic response of the RC slab is highly localized in the contact explosion at the middle of the slab. The global flexural behavior of the slab has not been observed in the RC slab and is expected to be very small. Due to the lack of the deformation and strain data of the test slab, only the failure mode and failure dimension (D_C & D_S) are compared between the test slabs and numerical results. As can be clearly seen, the damage profiles from the numerical models all match reasonably with the experimental results of Li et al. [10] in terms of the diameters of the crater and spalling. Overall, it may be concluded that the FE models created by FEM-SPH method can effectively predict the damage processes of the RC slabs subjected to contact explosion.

Based on FEM-SPH method, the top crater, punching and bottom spalling of the RC slab are all well reproduced, and the deformation and failure modes of the reinforcement steel bars are also well predicted.

Figure 6 shows the comparison between experimental damage profile of the NRC-2 slab exposed to contact explosion obtained from the experimental test conducted by Li et al. [10] & FEM-SPH model, good matching is observed. Figure 9 shows comparison between experimental & FE results of the recorded strain time histories on reinforcement bars detected by strain gauge at the center (Point 1) of NRC-2 Slab. Very good accuracy was achieved in the current FE methodology, Exp./ FE results of long. steel bars at center =1.04.

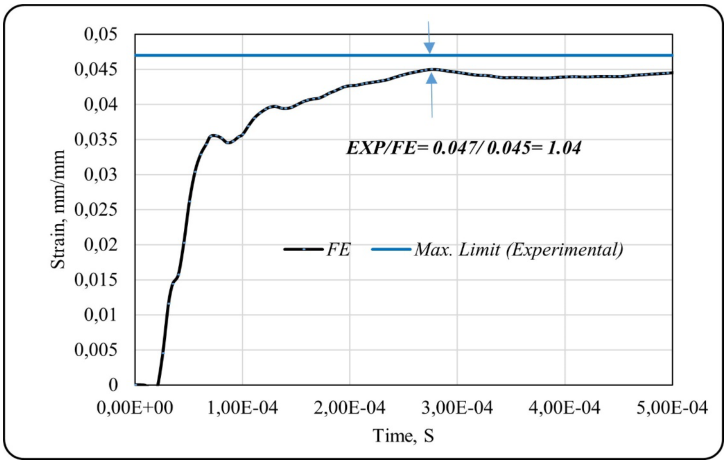

Figure 9 -Comparison between experimental & FE results of steel strain detected by strain gauge at the center (Point 1) of NRC-2 Slab

5.4 Ultra-High Performance Concrete Slab

The proposed finite element model showed the UHPC material's ability to effectively resist contact explosion. UHPC-4 slab was tested experimentally and modeled numerically with a 1 kg TNT detonated at its central surface. The damage behavior of UHPC-4 slab is similar as NRC-2, which is localized punching or perforation failure (crater and spalling). A very good matching of damage mode was attained between tested UHPC-4 slab and FE simulated one as shown in Figure 10. It was noted that UHPC-4 slab has better blast resistance capacity compared with NRC-2 slab under the same blast load condition. The top surface crater diameter and the bottom surface spall diameter were reduced from 46 cm and 82 cm to 23 cm and 45 cm (50% and 45%,) respectively. Accurate Predicted values of D_C & D_S are noticed in Table 6. Moreover, no side concrete cracking as in NRC-2 was observed, and no reinforcement fracture was observed either. These comparisons clearly demonstrate the better blast loading resistance capacity of UHPC than normal concrete. To show more accuracy of the model, Figure 11 shows comparison between experimental & FE results of the recorded strain time histories on reinforcement bars detected by fixed strain gauge in long. steel bars at center of slab (Point 1) of UHPC-4 Slab. Very good accuracy was achieved in the current FE methodology, Exp./ FE results =0.95

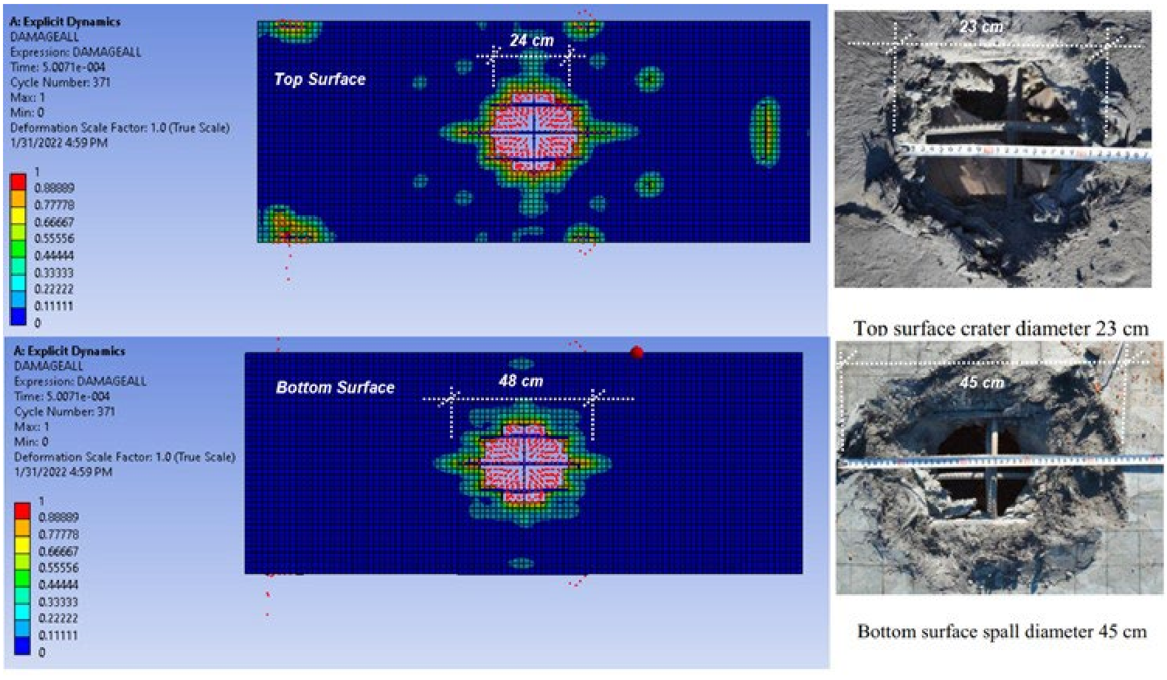

Figure 10– Comparison between experimental damage & FE damage of UHPC-4 Slab

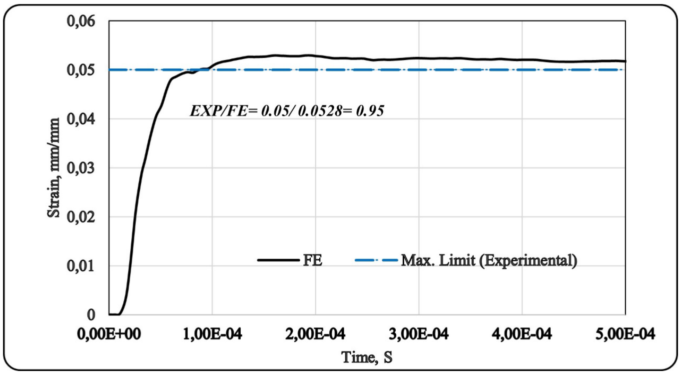

Figure 11 -Comparison between experimental & FE results of steel strain detected by strain gauge at the center (Point 1) of UHPC-4 Slab

To investigate the reinforcement mesh confinement effect on spalling damage, UHPC-7 slab was made the same as UHPC-4 but with less number of the longitudinal reinforcements in both the compressive and tensile face, i.e., the number of longitudinal reinforcement bars is reduced to 5 from 9. The slab was also tested experientially under 1.0 kg contact explosion and modeled numerically with the same FE approach used in the previous models. Comparison was made between UHPC-7 and UHPC-4 to investigate the influence of reinforcement mesh confinement effect on concrete crushing and spalling damages. A severe localized punching failure was observed. Comparing with UHPC-4, the top surface crater diameter and bottom surface spall diameter increased from 23 cm and 45 cm to 25 cm and 48 cm, respectively. As seen in Figure 12 and Table 6 that the used FE model accurately represent the real behavior and damage failure of tested UHPC-7 slab. Besides, the proposed FE model also shows good matching of deformation & buckling of longitudinal reinforcement at mid span with tested one as shown in Figure 13, which was not observed in UHPC-4. Generally speaking, the reinforcement mesh contributed to the resistance against the contact blast loads experimentally and numerically. Regarding measuring of steel strain with time, the strain detected by fixed strain gauge in long. steel bars at center of the slab (Point 1) of UHPC-7 Slab, current FE model matched well with tested one with ratio = 1.02 as shown in Figure 14.

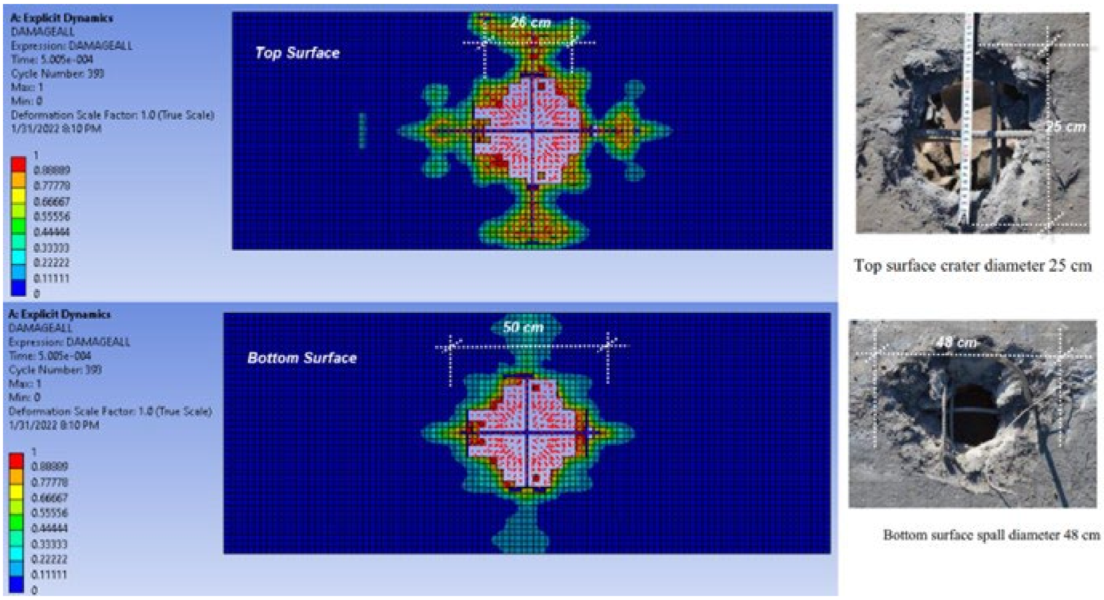

Figure 12 – Comparison between experimental damage & FE damage of UHPC-7 Slab

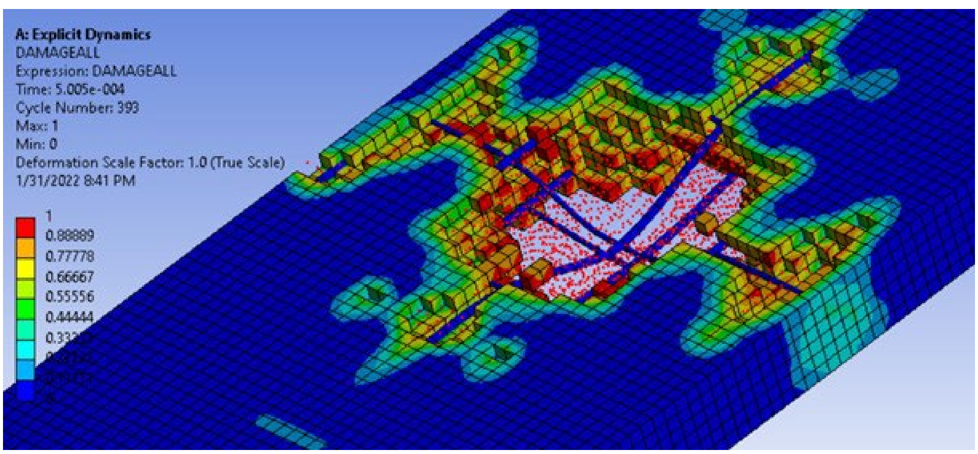

Figure 13 Deformation and steel buckling at mid of UHPC-7 Slab

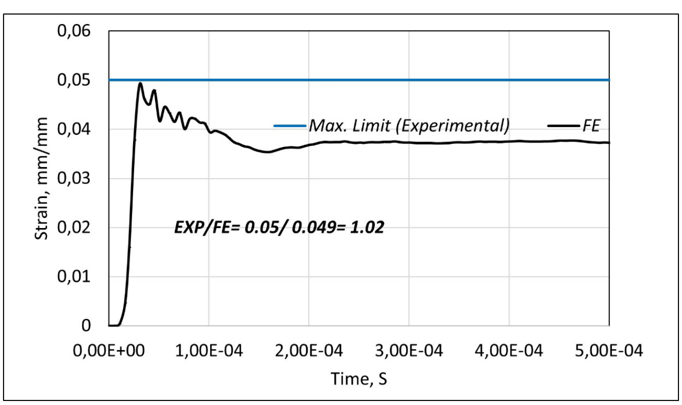

Figure 14-Comparison between experimental & FE results of steel strain detected by strain gauge at the center (Point 1) of UHPC-7 Slab

6 RETROFITTING PROPOSAL

6.1 Retrofitting of Normal Strength Concrete Slab by Bonded Steel Skin Layer

The above results and discussion indicate that the UHPC slab can resist the contact explosion with some permanent deformation and fragmentations better than NRC slab. To enhance the blast-resistance of both slabs, parametric studies are carried out to examine the retrofitting effect by bonded steel skin plates for top and bottom face of slabs upon the structural response under the contact blast scenario.

Two NRC slabs with steel skin thicknesses of 1 and 2 mm are compared in this section. The steel skin yield strength and the failure (erosion) strain of steel sheet were taken equal 330 MPa and 0.045 respectively as recommended in many papers [17]–[19].

The failure or damage occurs in slabs were monitoring by DAMAGEALL contour in Ansys Workbench Environment, which indicates to material damage: 0– intact material & 1- fully fractured. It is found that the NRC-2 slab retrofitted with 1 mm steel skin in both sides and exposed to 1 Kg TNT contact explosion experiences no perforation or punching failure and less central damage, compared to control one(experimental results of NRC-2 without retrofitting which damaged with perforation failure as shown in Figures 15 and 8).

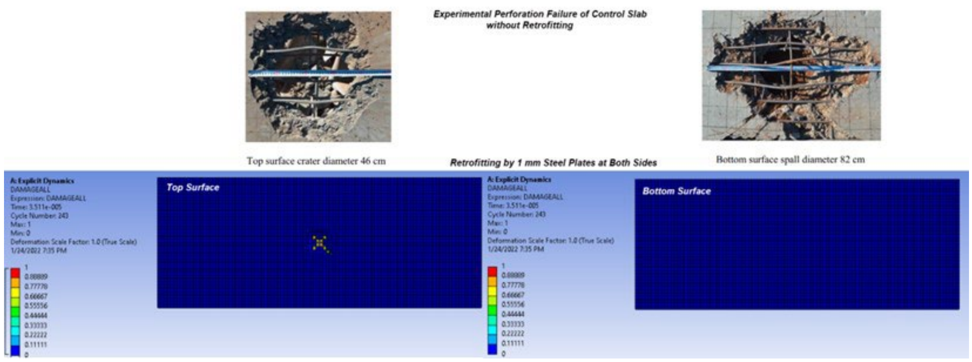

Figure 15 – Comparison between mode of failure of experimental non-retrofitted NRC-2 Slab and retrofitted NRC-2 by 1 mm steel skin plates at top & bottom surfaces

The increased thickness enhances the moment of inertia of steel skin. It can be concluded that increasing the skin thickness results in a significant improvement on the blast resistant performance. When the skin thickness increases from 1mm to 2 mm, the NRC-2 panel can attain the best performance against contact explosion. Retrofitting by 2 mm steel plate at both sides, leads to no damage, no punching failure, and no cracks were observed (Figure 16). Only central small deformation has been observed on the steel plate at top surface which adjacent to contact explosion.

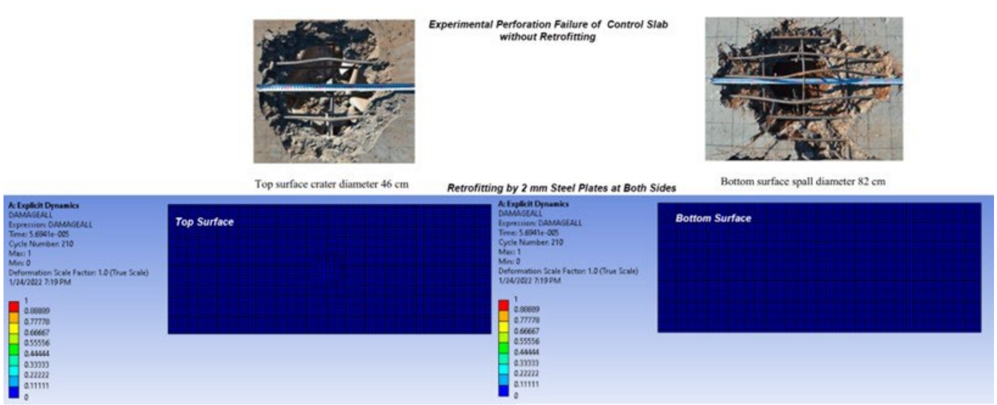

Figure 16– Comparison between mode of failure of experimental non-retrofitted NRC-2 Slab and retrofitted NRC-2 by 2 mm steel skin plates at top & bottom surfaces

6.2 Retrofitting of Ultra-High Performance Concrete Slab by Bonded Steel Skin Layer

Composite action generated from UHPC & 1mm bonded steel plates at both faces of the UHPC-4 slab has a superior resistance to contact blast. As clearly shown in Figure 17, a negligible damage in a few points at the top surface, and completely no damage occurs at bottom surface. Adequate protection is obviously shown compared with non-retrofitted one. By bonded steel plate retrofitting technique & UHPC material, no fragmentation is happened.

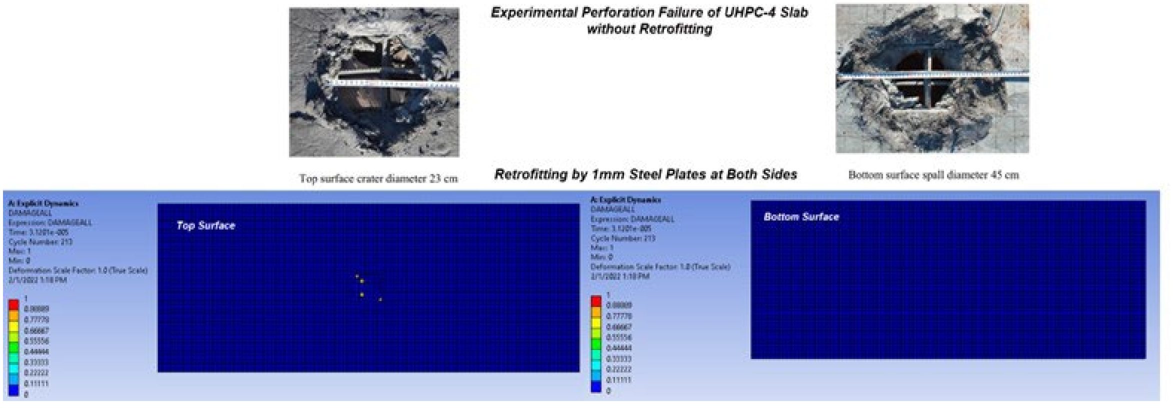

Figure 17 – Comparison between mode of failure of experimental non-retrofitted UHPC-4 Slab and retrofitted one by 1 mm steel skin plates at top & bottom surfaces

By analogy with the above, the use of 2mm bonded steel plate retrofitting will give more protection but, with more cost. For practical and economical use, 1 mm is enough to protect UHPC slab under 1 kg TNT contact explosion and adequate to prevent any fragmentation. To prove the previous phenomenon, Figure 16 shows bare concrete surfaces without covered plates. Regarding the upper surface of the concrete adjacent to the bottom of the covered plate, no punching damage is observed, just only small localized damage at slab center, which is negligible compared to UHPC-4 without retrofitting. The Figure 18 show also that 1 mm is very enough to completely protect the bottom surface without any damage, or not even any cracks.

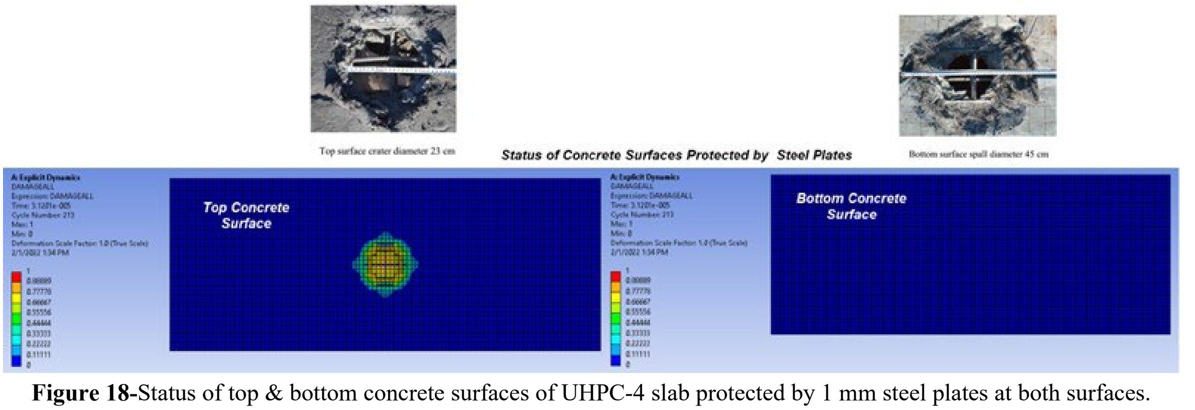

Figure 18-Status of top & bottom concrete surfaces of UHPC-4 slab protected by 1 mm steel plates at both surfaces.

7 CONCLUSIONS

The following are the main drawn concluding remarks:

1. In both test slabs and numerical results, the dynamic response of the both NRC & UHPC slabs is highly localized punching or perforation failure (crater and spalling) in the contact explosion at the middle of the slab.
2. The damage profiles from the numerical models all match reasonably with the experimental results of Li et al. [10] in terms of the diameters of the crater and spalling and steel strain. Overall, it may be concluded that the FE models created by FEM-SPH method can effectively predict the damage processes of the NRC and UHPC slabs subjected

to contact explosion. The suggested finite element model is valid to solve the reinforced concrete slab under contact-explosion problems. The top crater, punching and bottom spalling of the RC slab are all well reproduced, and the deformation and failure modes of the reinforcement steel bars are also well predicted.

3. ANSYS Workbench Explicit Dynamics and the RHT Concrete Damage model introduced powerful and reliable results to simulate the overall performance of NRC & UHPC slabs exposed to contact explosion.
4. UHPC slab has better blast resistance capacity compared with NRC slab under the same blast load condition. The top surface crater diameter and the bottom surface spall diameter were reduced by 50% and 45%, respectively. Moreover, no side concrete cracking like in NRC was observed, and no reinforcement fracture was observed either.
5. The influence of reinforcement mesh confinement effect upon concrete crushing and spalling damages is examined. With reducing the amount of reinforcement mesh confinement in compressive and tensile faces of the UHPC slab, a severe localized punching failure and buckling of longitudinal reinforcement at mid span were observed numerically and verified experimentally.
6. Steel skin plate retrofitting results in a significant improvement on the blast resistant performance. When the skin thickness increases from 1mm to 2 mm, the NRC panel can attain the best performance against contact explosion. Retrofitting of normal strength concrete slab by bonded 2mm steel skin plates of both sides significantly improved the blast resistance by preventing completely fragmentations and securing stability and proves to be an effective solution to eliminate contact- blast damage.
7. Composite action generated from UHPC & 1mm bonded steel plates at both faces of the UHPC slab has a superior resistance to contact explosion, it is very enough to completely protect against contact explosion with 1kg TNT, It has a superior resistance to contact blast, no perforation failure, and no cracks were observed.

ACKNOWLEDGEMENTS

The author wishes to thank the Ansys Co., for giving him Ansys Academic Version.

REFERENCES

[1] J. Li and H. Hao, "Numerical study of concrete spall damage to blast loads," *Int. J. Impact Eng.*, vol. 68, pp. 41–55, Jun 2014, http://dx.doi.org/10.1016/j.ijimpeng.2014.02.001.

[2] N. Gebbeken and M. Ruppert, "A new material model for concrete in high-dynamic hydro code simulations," *Arch. Appl. Mech.*, vol. 70, no. 7, pp. 463–478, 2000, http://dx.doi.org/10.1007/s004190000079.

[3] M. Mines, A. Thach, S. Mallonee, L. Hildebrand, and S. Shariat, "Ocular injuries sustained by survivors of the Oklahoma City bombing," *Ophthalmology*, vol. 107, no. 5, pp. 837–843, May 2000, PMid:10811071.

[4] S. Mallonee, S. Shariat, G. Stennies, R. Waxweiler, D. Hogan, and F. Jordan, "Physical injuriesand fatalities resulting from the Oklahoma City bombing," *JAMA*, vol. 276, no. 5, pp. 382–387, Aug 1996, http://dx.doi.org/10.1001/jama.1996.03540050042021.

[5] B. Brismar and L. Bergenwald, "The terrorist bomb explosion in Bologna, Italy, 1980: an analysis of the effects and injuries sustained," *J. Trauma Inj. Infect. Crit. Care*, vol. 22, no. 3, pp. 216–220, Mar 1982, http://dx.doi.org/10.1097/00005373-198203000-00007. PMid:7069805.

[6] M. Morishita, H. Tanaka, T. Ando, and H. Hagiya, "Effects of concrete strength and reinforcing clear distance on the damage of reinforced concrete slabs subjected to contact detonations," *Concr. Res. Technol.*, vol. 15, no. 2, pp. 89–98, Jan 2004, http://dx.doi.org/10.3151/crt1990.15.2_89.

[7] H. Tanaka and M. Tuji, "Effects of reinforcing on damage of reinforced concrete slabs subjected to explosive loading," *Concr. Res. Technol.*, vol. 14, no. 1, pp. 1–11, 2003, http://dx.doi.org/10.3151/crt1990.14.1_1.

[8] J. Nam, H. Kim, and G. Kim, "Experimental investigation on the blast resistance of fiber reinforced cementitious composite panels subjected to contact explosions," *Int. J. Concr. Struct. Mater.*, vol. 11, no. 1, pp. 29–43, Feb 2017, http://dx.doi.org/10.1007/s40069-016-0179-y.

[9] F. Toutlemonde and J. Resplendino, *Designing and Building with UHPFRC: State of the Art & Development.* Hoboken: John Wiley & Sons.

[10] J. Li, Ch. Wu, H. Hao, Zh. Wang, and Y. Su, "Experimental investigation of ultra-high performance concrete slabs under contact explosions," *Int. J. Impact Eng.*, vol. 93, pp. 62–75, Jul 2016, http://dx.doi.org/10.1016/j.ijimpeng.2016.02.007.

[11] ANSYS, *Finite Element Analysis Program, 2021R2 Release*. USA: SAS IP Inc., 2021.

[12] X. Zhao, G. Wang, W. Lu, P. Yan, M. Chen, and Ch. Zhou, "Damage features of RC slabs subjected to air & underwater contact explosions," *Ocean Eng.*, vol. 147, pp. 531–545, Jan 2018, http://dx.doi.org/10.1016/j.oceaneng.2017.11.007.

[13] W. Riedel, K. Thoma, S. Hiermaier, and E. Schmolinske, “Penetration of reinforced concrete by beta-b-500, numerical analysis using a new macroscopic concrete model for hydrocodes,” in *Proc. 9th Int. Symp. Interact. Eff. Mun. Struct.*, Strausberg, Berlin, 1999, pp. 315-322. CD-ROM.

[14] T. Borrvall and W. Riedel, “The RHT concrete model in LSdyna,” in *Proc. 8th Eur. LS-DYNA Users Conf.*, Strasbourg, France, 2011.

[15] G. R. Johnson and W. H. Cook, “A constitutive model and data for metals subjected to large strains, high strain rates and high temperatures,” in *Proc 7th Int. Symp. Ballis.*, The Netherlands, 1983.

[16] A. Hameed, “Numerical analysis of vehicle bottom structures subjected to anti-tank mine explosions,” Ph.D. dissertation, Canfield Univ., 2008.

[17] Y. Cui, M. Song, Z. Qu, S. Sun, and J. Zhao, "Research on damage assessment of concrete-filled steel tubular column subjected to near-field blast loading," *Shock Vib. J.*, vol. 2020, pp. 8883711, 2020, http://dx.doi.org/10.1155/2020/8883711.

[18] D. Thai, T. Pham, and D. Nguyen, "Damage assessment of reinforced concrete columns retrofitted by steel jacket under blast loading," *Struct. Des. Tall Spec. Build.*, vol. 29, no. 1, e1676, 2020, http://dx.doi.org/10.1002/tal.1676.

[19] H. Draganić, G. Gazić, and D. Varevac, "Experimental investigation of design and retrofit methods for blast load mitigation: a state-of-the-art review," *Eng. Struct.*, vol. 190, pp. 189–209, Jul 2019, http://dx.doi.org/10.1016/j.engstruct.2019.03.088.

Author contributions: IMM: conceptualization, formal analysis, writing.

Editors: Bruno Briseghella, Guilherme Aris Parsekian.

IBRACON Structures and Materials Journal
Revista IBRACON de Estruturas e Materiais
ISSN 1983-4195 ismj.org

ORIGINAL ARTICLE

Analysis of shear strength of complementary mechanisms trends in reinforced concrete beams

Análise das tendências nos mecanismos complementares de resistência ao cisalhamento de vigas de concreto armado

Igor José Santos Ribeiro[a]
José Renato de Castro Pessoa[b]
Túlio Nogueira Bittencourt[a]

[a]Universidade de São Paulo – USP, Programa de Pós-graduação em Engenharia Civil, São Paulo, SP, Brasil
[b]Universidade Estadual de Santa Cruz – UESC, Programa de Pós-graduação em Ciência, Inovação, e Modelagem de Materiais, Ilhéus, BA, Brasil

Received 31 July 2021
Accepted 16 August 2022

Abstract: The study of shear failure in concrete beams is one of the subjects growing in importance due to both the recent reformulations, and increasingly higher cross-section depths used. For instance, the recent updates in the ACI 318 (2019) shows the need to incorporate the size effect in the design of reinforced concrete elements. In this study, the same database adopted by the ACI-ASCE Committee DAfStb 445-D has been used to calculate shear strength, with and without the consideration of size effect, i.e., the design prescribed by ACI 318 (2014), ACI 318 (2019), Frosch et al. (2017), and the ABNT NBR 6118 (2014). Later these predictions are compared with test results. A dispersion analysis has outlined the trends regarding compressive strength, span to depth ratio, longitudinal reinforcement ratio and beam depth. Every variable was discussed per interval, delineating the causes related to the observable trends. Regarding the most prominent influences (effective depth and longitudinal reinforcement ratio), the approaches considering them directly through factors had provided results with no appreciable trends, with lower coefficients of variation (COV) and substantially more conservative for higher cross-section depths. As the Brazilian code does not consider both, a correction factors, determined by a two-step regression analysis on these parameters to adjust this design, are briefly introduced.

Keywords: fracture, size effect, concrete shear strength, reinforced concrete beams without stirrups, complementary mechanisms.

Resumo: O estudo da ruptura ao cisalhamento em vigas de concreto armado é uma dessas áreas que têm avultado em importância tanto devido às recentes reformulações efetuadas quanto as peças de seções cada vez maiores utilizadas. Por exemplo, as recentes atualizações no código ACI 318 (2019) apontam para a necessidade que tem sido demonstrada de incorporar o efeito escala no projeto de seções de concreto armado. Nesse estudo, o banco de dados adotado pelo Comitê ACI-ASCE DAfStb 445-D foi utilizado para cálculo da resistência ao cisalhamento, com e sem efeito escala, prescritas nas formulações ACI 318 (2014), ACI 318 (2019), Frosch et al. (2017), e ABNT NBR 6118 (2014). Em sequência, as predições foram comparadas com os resultados de ensaios. Uma análise da dispersão delineou as tendências concernentes à resistência à compressão, taxa vão-cisalhamento, taxa de reforço longitudinal e altura da viga. Cada uma das variáveis foi discutida por intervalo, discutindo as causas relacionadas às tendências observadas. No que tange as maiores influências (altura útil e taxa de reforço longitudinal), das abordagens que os consideram diretamente, resultaram em saídas sem tendências apreciáveis, com menores coeficientes de variação (COV) e satisfatoriamente mais conservadoras para seções com maiores alturas. Como o código brasileiro não considera esses fatores, fatores de correção obtidos mediante uma análise de regressão efetuada em duas etapas, são brevemente introduzidos.

Palavras-chave: fratura, efeito escala, resistência ao cisalhamento do concreto, vigas de concreto armado, mecanismos complementares.

Corresponding author: Igor José Santos Ribeiro. E-mail: ijoseribeiro@gmail.com
Financial support: Fundação de Amparo à Pesquisa do Estado da Bahia – FAPESB.
Conflict of interest: Nothing to declare.
Data Availability: The data that support the findings of this study are available from the corresponding author, Igor JS Ribeiro, upon reasonable request.

How to cite: I. J. S. Ribeiro, J. R. C. Pessoa, and T. N. Bittencourt, “Analysis of shear strength of complementary mechanisms trends in reinforced concrete beams,” *Rev. IBRACON Estrut. Mater.*, vol. 16, no. 2, e16208, 2023, https://doi.org/10.1590/S1983-41952023000200008

1 INTRODUCTION

The progression of acquisition and monitoring systems, in juxtaposition with theoretical development and new approaches, provide different perspectives to safely achieve the goal of design structures more economically. The study of concrete shear strength of complementary mechanisms is one of those areas that have attracted researchers due to recent reformulations of the codes, together with the more demanding designs.

First, Ritter approached the cracked behavior of concrete due to loads by a truss, with parallel chords, with compressed struts that were inclined with a fixed angle of 45°, later expanded for torsion applications by Mörsch. Because this approach had provided conservative results compared with available tests in the period, it was disseminated in the literature [1].

Several approaches and models followed, regarding the change of the diagonal crack angle, load transfer mechanisms considered, and tensile strength after cracking, juxtaposed with its prominence in the final shear strength. In the attempt to better describe the shear behavior, these complementary mechanisms were included in the design codes. Nevertheless, its calculation is still done in a multitude of approaches delineating the lack of scientific consensus, which tends to reflect in empirical expressions in various codes [2].

Illustrating, the long standing ACI 318 [3] expression for the shear strength of the cross-section mechanisms (V_c), was updated to consider both the size effect and the longitudinal reinforcement ratio (ρ_L) in the ACI 318 [4]. One of the proposals to the north American committee, the Unified Approach by Frosch et al. [5] although was not adopted, presents an approach based on the depth of the compression zone. The authors state that this means to consider the average shear stress over the uncracked cross-section instead of over the effective depth.

Despites the better fitting of the newest version of north American code, the results obtained through ACI-DAfStb 445-D Database [6]–[8], shows a wide range in the influencing parameters, whose tendencies could be even more clear with additional analysis [6]–[8].

Simultaneously, in Brazil, the calculation of shear strength for concrete beams is governed by ABNT NBR 6118 [9] prescribing simple design formulation for the complementary mechanisms, based on concrete tensile strength for both models. Therefore, the current code may be improved regarding the contribution of the aforementioned mechanisms.

Hence, the comparison between the results predicted by the ACI 318 [3], ACI 318 [4], The Unified Approach [5] and ABNT NBR 6118 [9], regarding the scatter though the intervals in relation to main design parameters may allow a broader comprehension of localized or overall trends, as well as possible optimization of the current design by inclusion of correction factors related to these trends.

2 SHEAR STRENGTH OF COMPLEMENARY MECHANISMS OF REINFORCED CONCRETE BEAMS

The first approach to the shear strength of concrete beam, was originally proposed by Ritter, and later generalized by Mörsch. Next, aiming for the simplicity of application for designs, some codes have incorporated other load transfer mechanisms to this model, as well as formulations with variable compression strut angle. The generalized truss, considering the contribution of shear transfer cross-section mechanisms, is present in the Brazilian code ABNT NBR 6118 [9].

2.1 Shear Transfer Mechanisms

After cracking, different mechanisms allow the transfer of shear stresses. The principals have been summarized into cantilever action, shear transfer at the interfaces, dowel action, residual concrete tensile strength, and arch effect [1], [3], [4], [10]:

- **Cantilever effect:** Cracked concrete may transfer shear stresses between two flexural cracks, a region designated as “tooth”, fixed in the compression zone [11]. The concept was brought up by Kani [12], who, considering bending cracks do not transmit shear stresses, states that the beam would resist this effort through a compressed region in the upper envelope of the cracks formed together with the bending of each of these regions.
- **Interface Friction:** The phenomenon of shear transfer through cracks is defined as interface shear transfer, or crack friction. However, this designation infers the dependence of the crack surface conditions, not being a property of the material. Sato et al. [13] affirmed that the relative slip between the interfaces and concomitantly this action, were higher for lower *a/d* rates. Fernández Ruiz et al. [14] corroborate this understanding and state that the load transfer capacity of this mechanism is limited by the surface roughness that is influenced by the aggregate size

(micro level), ripples and changes in the direction of the crack (meso level), and by relative displacement (macro level).

- **Dowel action:** This mechanism is defined by the capacity of the beam to transfer stresses through the concrete longitudinal reinforcement, which acts as a pin between the interfaces generated in the propagation of a diagonal crack.
- **Residual concrete tensile strength:** According to the ACI 445R [1], the basic explanation for this mechanism is because after cracking, a few portions of concrete bridge the cracks and continue to transmit stresses to small openings. In juxtaposition, concrete has a quasi-brittle fracture behavior, summarily characterized by the stress relaxation curve that occurs after the peak tensile load.
- **Arch effect:** The previously described mechanisms are modeled from the consideration of a constant lever arm between the compressed and tensioned fibers, which implies in the variation of the tensioned reinforcement stresses according to the loads for which the cross-section is submitted. These mechanisms are classified as shear transfer mechanisms. Alternatively, the forces on the stressed reinforcement may be fixed and the lever arm varies, which corresponds to a compression field of the plasticity theory with force transmission through a direct compressed strut. This mechanism develops through the failure of all the others and is associated with the longitudinal reinforcement loss of adhesion [14], [15].

2.2 Kani's Valley

The mechanisms have different relevance, varying with parameters such as the transverse reinforcement, height, shear span to effective depth ratio, or longitudinal reinforcement ratio. When studying how slenderness influenced the preponderance of shear transfer or the arch effect, Kani [12] exposed the Kani Valley, where four distinct regions may be seen on the response due to slenderness, as illustrated in Figure 1.

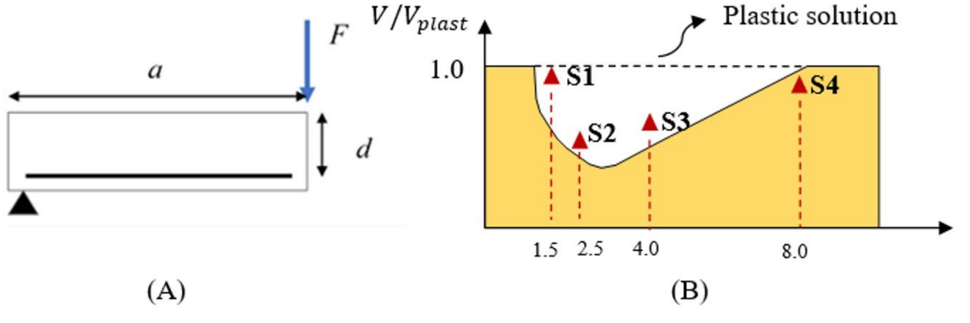

Figure 1 – (A) Shear span (*a*) to effective depth (*d*) to a point load (B) Kani's valley

Specimens S1, S2, S3, and S4 are beam tests with several slenderness available from Leonhardt and Walther [16]. The tests show for small *a/d* ratios, as S1, results closer to those predicted by the theory of elasticity, and the shear strength is governed by the ρ_L, calculated by Equation 1:

$$\rho_L = \frac{A_s}{b_w d} \quad (1)$$

where A_s is the area of the steel in the cross-section, b_w is the width of the beam and d is the effective depth, i.e., the distance from the centroid of tensile reinforcement to the most compressed fiber.

Then, even around the *a/d*=2.4 ratio, where S2 is located, the governing mechanism is the arch effect, in which bending cracks propagate in the stably compressed struts [15]. For slightly larger spans the cross-section transfer mechanisms predominate, where S3 is, until the longitudinal reinforcement begins to govern with the shear stress transfer mechanisms still developing.

3 SHEAR STRENGTH MECHANISMS EXPRESSIONS

Several concrete design codes had incorporated the concrete strength to adjust the results of an obtained dataset. The ACI 318 originally, came from the observation of several parameter in numerous tests where the longitudinal reinforcement rate (ρ_w), a/d ratio, and "concrete quality", which had per measure f_c' (MPa), were the most influent variables. After fitting two tendency lines to the dataset of that period, result in the long stand relation, which lasts until the new version, in S.I. units on Equation 2:

$$V_c = 0.166\lambda\sqrt{f_c'}b_w d \tag{2}$$

where b_w(mm) is the width of the cross-section, d(mm), λ is the aggregate factor, being $\lambda = 1.0$ for normal weight type. However, in the last version of the code [4], if the provided transversal reinforcement is less than the minimum, a new expression (3), most be used:

$$V_c = 0.644\lambda\lambda_s(\rho_L)^{1/3}\sqrt{f'_c}\,b_w d \tag{3}$$

where ρ_L (%) is the longitudinal reinforcement ratio and λ_s is a dimensionless size effect factor calculated by Equation 4:

$$\lambda_s = \sqrt{\frac{2}{1+\frac{d}{254}}} \tag{4}$$

Some other similar proposals were made by Frosch et al. [5]. The approach inferred that since reinforcement stiffness is a primary parameter in shear strength, an effective reinforcement ratio could be defined according to the Equation 5:

$$\rho_{eff} = \rho_L n \tag{5}$$

where n is calculated by Equation 6:

$$n = \frac{E_r}{E_c} \tag{6}$$

where E_r is the modulus of elasticity of the longitudinal reinforcement and E_c the modulus of elasticity of the concrete. Since the stiffness of the reinforcement also affects the location of the neutral axis, the author sought to develop a formulation considering the depth of the cracked cross-section of the concrete, through the Equation 7:

$$c = kd \tag{7}$$

where k is defined by Equation 8:

$$k = \sqrt{2\rho_L n + (\rho_L n)^2} - \rho_L n \tag{8}$$

The use of "c", instead of the usual approaches, allows the incorporation of other effects, as simplifying the design when multiple layers become necessary [5]. From these considerations, the authors fitted an expression to a dataset, with the Equation 9, in S.I. units:

$$V_c = \left(0.415\sqrt{f_c'}b_w c\right)\gamma_d \tag{9}$$

where γ_d is a size effect factor that must be taken as $\gamma_d = 1{,}00$ if the depth from the first layer of reinforcement (d_t) is less than 10 in (25.4 cm), or if d_t is simultaneously less than 100 in (254 cm), and the transverse reinforcement is higher than the minimum ratio. If these conditions are not fulfilled, the size effect should be calculated by Equation 10:

$$\gamma_d = \frac{1.4}{\sqrt{1+\frac{d_t}{d_0}}} \tag{10}$$

where $d_0 = 254$mm, if the transverse reinforcement is less than the minimum, or $d_0 = 2540mm$. The proximity to the Type II size effect law (SEL), proposed by Bažant, is observed. The author had performed an analysis in energy terms through an asymptotic approach describing the transitional behavior between the plasticity theory and Linear Elastic Fracture mechanics [17]

Finally, the current Brazilian code, the ABNT: NBR 6118 [9] does not consider the size effect and is solely based on concrete resistance to compression. On the model I, a fixed angle truss model, the shear strength of the complementary mechanisms is calculated by the expression 11 in S.I. units:

$$V_c = 0{,}6 f_{ctd} b_w d \tag{11}$$

where f_{ctd} is the concrete tensile design resistance, calculated by Equation 12:

$$f_{ctd} = \frac{0{,}7 f_{ctm}}{\gamma_c} = \frac{0.7 f_{ctm}}{1.4} = 0.5 f_{ctm} \tag{12}$$

Where γ_c is the concrete compressive strength safety factor and f_{ctm} is the concrete tensile average resistance, calculated by (13) if the concrete has $f_{ck} < 55MPa$ or else (14):

$$f_{ctm} = 0{,}3(f_{ck})^{\frac{2}{3}} \tag{13}$$

$$f_{ctm} = 2{,}11\ ln(1 + 0{,}11 f_{ck}) \tag{14}$$

where f_{ck} is in MPa. As the safety factor is included in this analysis is not desirable that this prediction returns shear strength smaller than tests results.

4 MATERIALS AND EXPERIMENTAL PROGRAM

The survey carried out included 1356 beam tests from the ACI-DAfStb database, from the American and German committees. These data were obtained from several authors and initially filtered using the criteria set out in Reineck et al. [6], removing specimens with lack of information. The primary outputs were two sets: 1008 slender beams and 348 non-slender beams. The filters also ensure that the failure under analysis was due to shear, that the beams have the same type of anchorage in the longitudinal reinforcement and with a width greater than 5 cm.

Another additional filter was applied so that only concrete for structural purposes, with 20 MPa < f_{ck}< 100MPa, would be part of the set. Nonetheless, the North American code adopts the control of 10% chance of failure for this parameter, being f_c' the resistance meeting this criterion. The European and Brazilian codes, on the other hand, adopt 5%, and the f_{ck} is the strength fulfilling these criteria. Therefore, the value of f_c' was set to f_{ck} for both the filter and for the calculation of the Brazilian code, for this database. The conversion was the same performed by Reineck et al. [6] to comparisons with codes using similar control, calculated by Equation 15:

$$f_{ck} = f_c' - 1{,}6 \tag{15}$$

This equation is obtained considering a scatter of $\Delta f = 4\ MPa$ [6] to the same database. For instance, considering the cylinder compressive strength of 24th reference of Annex A, the Table 1 is obtained:

Table 1- Expression of Reineck et al. [6] applied to two specimens

Author	Specimen	$f_c'\ (MPa)$	$f_{ck}(MPa)$
Drangsholt, G.; Thorenfeldt, E. (1992)	B11	51,60	$f_{ck} = 51{,}6 - 1{,}6 = 50{,}00$
	B21	75,38	$f_{ck} = 75{,}38 - 1{,}6 = 73{,}78$

Moreover, the samples were restricted to data with *a/d* > 2.4 and beams with point loads. After this process, a database with 617 slender beams without stirrups with point loads used was obtained from 88 studies collected in the literature, according to Annex A.

4.1 Design Models

Having filtered data as input, the model codes in ACI 318 [3], ACI 318 [3], the Unified Approach [5], and ABNT: NBR 6118 [9] were used to calculate the shear strength of the complementary mechanism. Each of the models generates a prediction of the shear strength of the complementary mechanisms ($R = V_c$), by using data such as b_w, d, compressive strength, and ρ_L for each of the beams. Furthermore, each of these beams were tested until failure, and the database contains the ultimate strength of the test ($S = V_{test}$).

A satisfactory approach would have no tendencies, be as close to one as possible and have a small coefficient of variation. Additionally, when partial safety factors are considered, they should have an S/R>1 for most of the database, as shown in Reineck et al. [6], who used the 95% percentile for analysis of the ACI 318 [3]. This condition implies that the model predicted a lower resistance than measured in the test; therefore, the design would be reliable. Concomitantly S/R should not be much higher than 1, for project optimization. Henceforth, two upper limits (UL), establishing the percentiles of 5 and 10 of the results were set to analysis, and will be represented by a light blue dashed line (UL 5%) and a dark blue dashed line (UL 10%). This limit allows to identify optimum responses, i.e., closer to 1. The Figure 2 illustrates these concepts.

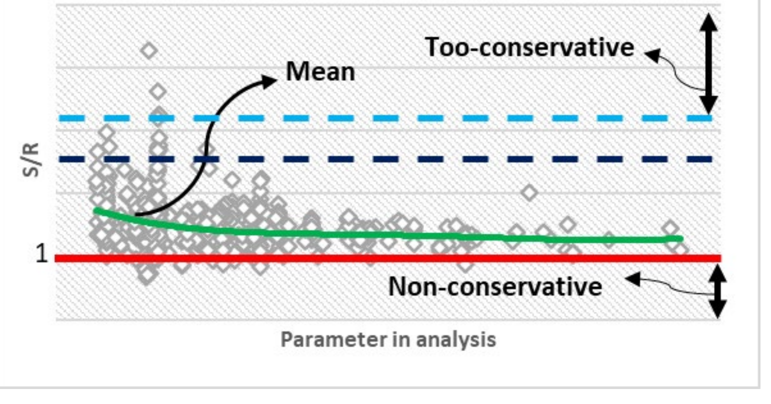

Figure 2- Dispersion points of analysis

5 RESULTS AND DISCUSSIONS

The distribution of the database through the analyzed parameter is in Figure 3, where the frequency per ranges of the parameters is exhibit:

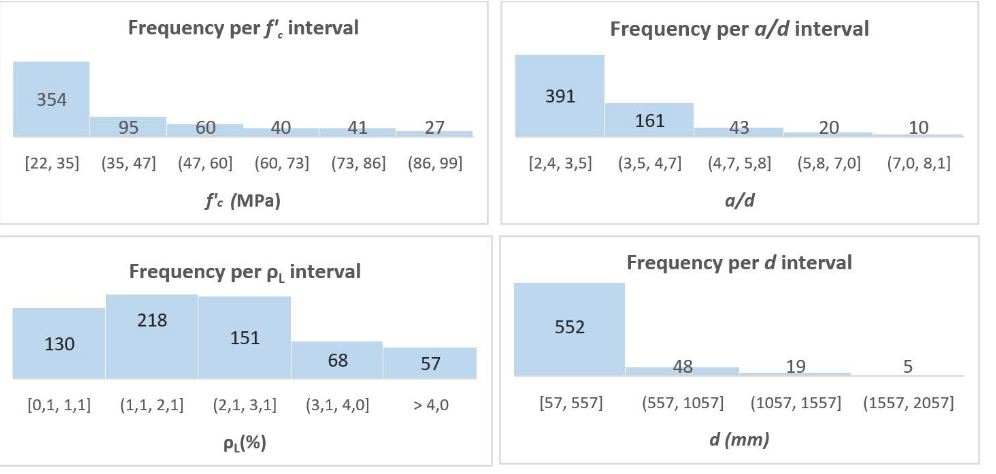

Figure 3- Distribution of the data

From the distribution, becomes clear the concentration of data in the first interval, except for ρ_L, associated with the technical difficulties with higher f_c', a/d, and d, hence, there is a need to expand the data to a better analysis. All the dispersion plots of S/R in relation to each of these parameters are in the following section. Additionally, in the Table 2 are shown the upper limits (UL) to both 5 and 10% limits, obtained by establishing limits to the dataset in such way that the UL fractile are reached.

Table 2- Upper Limits to 5 and 10%

Model	Upper Limit (5%)	Upper Limit (5%)
ACI 318-14	2,42	2,09
ACI 318-19	2,17	1,87
Frosch et al. [5]	2,37	1,97
NBR6118-14	2,61	2,20

The Unified Approach by Frosch et al. [5] and the Brazilian code present higher limits, which indicates more conservative results to the database. Furthermore, an expression related to mean and COV by the Equation 16 is proposed:

$$UL = \mu + kCOV \tag{16}$$

where μ is the mean and k is a factor related to the model sensitivity. The difference between UL and μ is the distance from the mean to the corresponding upper limit. Thus, k indicates a distance normalized by the COV. From Table 2 and Equation 16, considering the mean and COV obtained by the design codes model applied to the dataset (to be presented in sections 5.1 to 5.3), Table 3 is obtained:

Table 3- Upper Limits to 5 and 10%

Model	Upper Limit (5%)	Upper Limit (10%)
ACI 318-14	$UL = \bar{\mu} + 2.33COV$	$UL = \bar{\mu} + 1.50COV$
ACI 318-19	$UL = \bar{\mu} + 2.70COV$	$UL = \bar{\mu} + 1.50COV$
Frosch et al. [5]	$UL = \bar{\mu} + 3.14COV$	$UL = \bar{\mu} + 1.92COV$
NBR6118-14	$UL = \bar{\mu} + 2.51COV$	$UL = \bar{\mu} + 1.51COV$

The Table 3 shows the Frosh et al. [5] approach as the more conservative, followed by the ACI 318 [4], instead of ABNT NBR 6118 [9].

5.1 ACI 318

Initially the two models of the North American Code are considered. The mean of S/R of the ACI 318 [3] for the filtered database was 1.49 with COV=0.40. Also, 6.96% of the values that have S/R<0.75. In juxtaposition, the new code (ACI 318 [4]) had a mean of 1.48 with COV= 0.25 with 0.48% of the values, for which S/R<0.75. The values agree with Kuchma et al. [8] although he has applied different filters to the same set. Additionally, the Upper Limits to both 5 and 10 percentiles are smaller in the newest version; therefore, the model presents an optimized design. Accounting the multitude of studies accumulating data in each portion, the dispersion could be better evaluated per intervals.

5.1.1 Compressive Strength

Figure 4, exhibit ACI 318 [3] (yellow) and ACI 318 [4] (blue) regarding compressive strength. As shown in Figure 3, the interval from 20 to 40 MPa, comprehends most of the test results. Hence, is expected that standard deviation increases. However, is possible to see a strong trend of decreasing in S/R mean as compressive strength increases that is not related to this. The ranges concentrating most of the values against safety are 60-100 MPa, with higher COV and lower means. The standard under analysis stipulates, for the calculation of a maximum value for V_c of $f_c' = 82.76$MPa, which may help to reduce the variation associated with this parameter. Moreover UL_5 and UL_{10} delineates a more conservative model between 20 and 40 MPa. Although the newest code version has a smaller band of dispersion there are more results above UL_{10}.

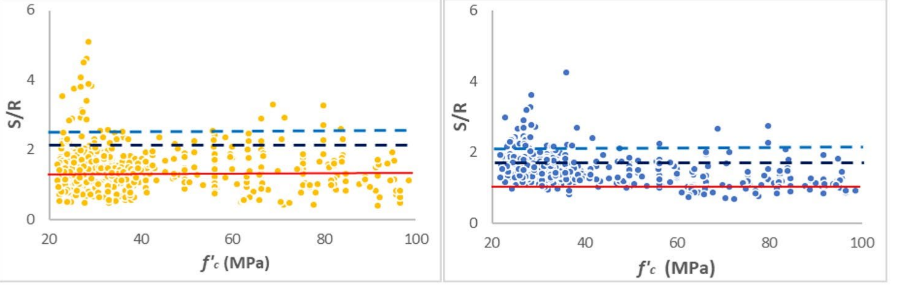

Figure 4- S/R in relation to f_c' to ACI 318 [3] (yellow) and ACI 318 [3] (blue)

The Table 4 expose in detail the tendencies of this dataset.

Table 4- ACI 318 [3] and ACI 318 [4] results

N	f_c' (MPa)	ACI 318 [3]			ACI 318 [4]		
		S/R<1 (%)	Mean	COV	*S/R*<1 (%)	Mean	COV
423	20-40	13.71	1.52	0.40	1.18	1.56	0.24
86	40-60	10.47	1.48	0.29	1.16	1.44	0.19
60	60-80	33.33	1.40	0.49	30,00	1.24	0.30
48	80-100	20.83	1.29	0.35	18.75	1.2	0.23

In the newest code version, a reduction in the S/R<1 values, is noted, with 33 tests for this formulation and only three, considering the factor φ=0.75 indicating both model guarantees the safety, and it can still be optimized. Lower COV's in all intervals, with an observed tendency to decrease with the increasing in compressive strength, is presented, even more accentuated than the previous formulation. Similar patterns are also observed in relation to the results with an S/R<1 in the intervals. Bažant et al. [18], observed the same trend, attesting the proportionality with $\sqrt{f_c}'$ as satisfactory, which Kuchma et al. [8] ratify, when analyzing this parameter in the new standard. Since both curves use this proportionality, the result reiterates this understanding.

5.1.2 Shear Span to Effective Depth Ratio

The Kani's Valley stats that when $a/d \geq 2.40$ the contributions of the shear transfer cross-section mechanisms are preponderant, linearly approaching itself to the prediction of the theory of plasticity as the ratio reaches values ranging from 6 to 8 [10], [12], [15], [16]. Hence, it is useful to group in intervals that may allow a better analysis among them. Figure 5 show the model error (S/R) in relation to span to depth ratio (*a/d*). This filtered dataset only has only beams with $a/d \geq 2.40$. There are no trends concerning the data in the ACI 318 [3]. In turn, the ACI 318 [4], presents a slight decrease trend. Finally, the UL_5 and UL_{10} demonstrates most of the highly conservative values located between $2.4 < a/d < 3$, where the shear transfer cross-sections mechanisms are preponderant, as stated in section 2.2. Notably, ACI 318 [4] is more conservative (more values above UL_{10}).

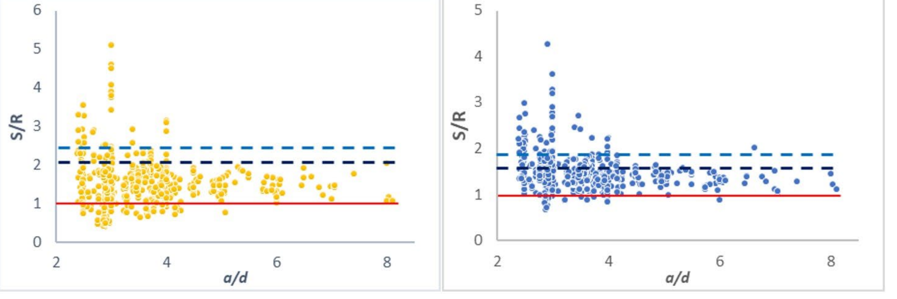

Figure 5 - S/R in relation to a/d to ACI 318 [3] (yellow) and ACI 318 [3] (blue)

The Table 5 shows the results obtained per interval in detail.

Table 5 – S/R x *a/d* results

N	a/d (-)	ACI 318 [3]			ACI 318 [4]		
		S/R<1 (%)	Mean	COV	*S/R*<1 (%)	Mean	COV
390	2.40 – 3.55	19.74	1.48	0.45	5.90	1.54	0.46
154	3.55 – 4.70	11.04	1.54	0.30	4.54	1.43	0.19
45	4.70 – 5.85	2.22	1.47	0.16	2.22	1.36	0.10
28	5.85 – 8.15	0.00	1.41	0.19	3.57	1.29	0.16

Two main trends appear from the analysis, i.e., the COV's are smaller for the ratios above 4.70 and most of results where S/R<1 is in the first intervals. Both have feasible explanations in the Kani's study. For higher values of *a/d*, the approximation of the current version leads to satisfactory results. Nonetheless, the first intervals, where the cross-section mechanisms govern the shear transfer, have the most significant fraction with S/R<1.

The simplified version approximates the *a/d* ratio through the Vd/M term, through the 0.166λ coefficient without significant changes. Additionally, the decreasing values of the mean in the new formulation, may be related to the consideration of longitudinal reinforcement by the term ρ_L, to be discussed in next section.

5.1.3 Longitudinal Reinforcement Ratio (ρ_L)

Figure 6 exhibit a clear tendency to increase in the S/R mean in the ACI 318 [3] that does not explicitly include the influence of this parameter on strength. To light reinforced beams parameters this design has most of the non-conservative values. Similarly, most of excessively conservative results lay on the beams with greater reinforcement ratios.

The ACI 318 [4] presents no notable trends regarding this parameter, indicating the introduction of ρ_L as an efficient way to correct this design. Furthermore, the upper limit to oldest version shows interval between 2 to 3%, holding most of the highest conservative values. However, there is a strong tendency which affect this analysis. The newest code is more conservative with no appreciable localized changes regarding UL_5 and UL_{10}. To analyze the changes in the database, it is useful to group through intervals, once more, obtaining the Table 6.

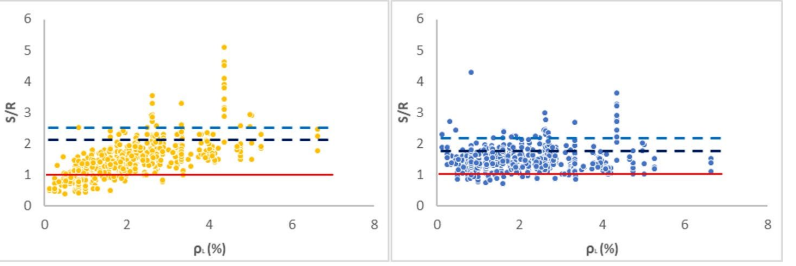

Figure 6- S/R in relation to ρ_L to ACI 318 [3] (yellow) and ACI 318 [3] (blue)

Table 6- S/R x ρ_L results

N	ρ_L (%)	ACI 318 [3]			ACI 318 [4]		
		S/R<1 (%)	Mean	COV	*S/R*<1 (%)	Mean	COV
168	0-1.30	50.00	1.00	0.30	10.71	1.41	0.20
232	1.30 – 2.60	4.74	1.47	0.23	4.74	1.47	0.21
154	2.60 – 3.90	1.32	1.75	0.26	2.63	1.50	0.24
68	3.90 – 6.70	0.00	2.29	0.39	0.00	1.62	0.39

The most of results against safety are found in lightly reinforced beams whereas higher COV's and predictions with higher means are observed for the experiments with higher ρ_w rates. When considering longitudinal reinforcement rate with the proportion $\sqrt[3]{\rho_L}$ directly, trends were not recognized. Lower COV's were obtained compared with the previous approach, although there is still a tendency for the S/R ratio to increase with the reinforcement ratio. In addition, lightly reinforced beams retain, proportionally, most of the designs against safety, and for higher reinforcement ratio, oversizing occurs, with higher COV’s.

This effect was studied by El-Ariss [19] who, when adjusting a numerical model, specifically for the contribution of the pin action of the longitudinal reinforcement, observed its contribution was essential to lightly reinforced beams, for a correct prediction, pointing the need to investigate how other parameters as compressive strength and bar diameter affected the contribution of this mechanism.

5.1.4 Effective Depth

The Figure 7 show a remarkable trend of mean decreasing as the effective depth increases to the ACI 318 [3]. In the turn, the new design code, significantly corrects the model error in first intervals, leading to smaller S/R, and increasing its value in the rest of dataset.

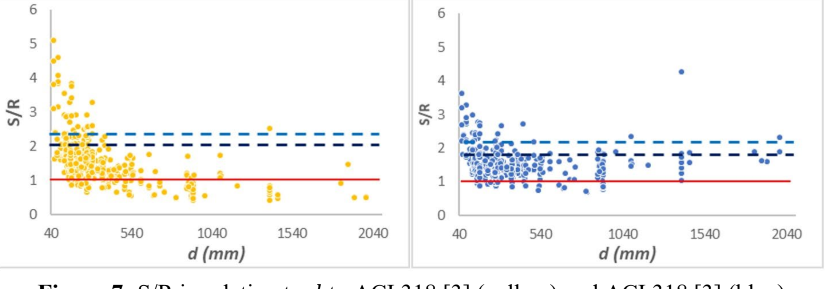

Figure 7- S/R in relation to d to ACI 318 [3] (yellow) and ACI 318 [3] (blue)

Table 7 exhibit in detail the trends regarding the beam depth. There is an increase in predictions against safety (S/R<1) with the increase in the height of the beams under analysis, which together with the COV’s in the settled intervals, attest the reliability of the trend. Regardless, in the ACI 318 [4] there is a significant reduction in data with inadequate design, with a lower mean of 1.31 in the intervals taken, with lower coefficients of variation, indicating a good fit through the adoption of the factor for the size effect. The proposed upper limits delineate the most conservative values in the smaller beam depth to both design code. Even though the ACI 318 [4] is more conservative there were small changes regarding the values above UL_5 and UL_{10}, but with less tendencies.

Table 7- S/R x d results to ACI 318

N	d (mm)	ACI 318 [3]			ACI 318 [4]		
		S/R<1 (%)	Mean	COV	S/R<1 (%)	Mean	COV
225	0-250	1.78	1.86	0.35	2.22	1.58	0.28
298	250-500	10.40	1.40	0.27	4.36	1.42	0.19
37	500-750	48.65	1.09	0.34	18.92	1.39	0.25
33	750-1000	81.82	0.78	0.37	27.27	1.31	0.28
24	1000-2000	75.00	0.78	0.39	4.17	1.61	0.18

Bažant's approach, which was adopted in the new version of the code, performs an asymptotic analysis of concrete, as a quasi-brittle material, between the constant resistance prescribed by the theory of plasticity, and the Linear Elastic Fracture Mechanics (LEFM), which claims the inelastic process zone as negligible compared to cross-section dimensions.

Since even for data with dimensions of the order of 2 m in height, good fits were obtained by applying the factor, the FPZ did not become negligible for the range adopted, with a transitional formulation between the LEFM and the plasticity theory being adequate.

5.2 Unified Approach

Using the proposed expression of Frosch et al. [5], the mean to the database was 1.59 with COV=0.27. Only eight results had S/R≤ 1 and one bellow 0.75. This proposal was calibrated to this database on Frosch et al. [5]. The model has the highest upper limit in the analysis with the more conservative design.

5.2.1 Compressive Strength (f'_c)

The Figure 8 show S/R in relation to f'_c to this approach. First, no trends are noted, and the approach is the more conservative. This is also corroborated by the upper limits, which shows more values above them across the intervals. However, the same interval (20-40 MPa), still has the most values above the proposed upper limits. A more detailed analysis is possible by filtering the data similarly to the last section, as show in Table 8.

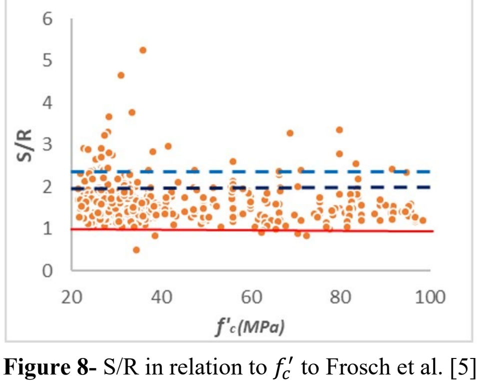

Figure 8- S/R in relation to f'_c to Frosch et al. [5]

Table 8- S/R x f'_c to the Unified Approach

N	f'_c (MPa)	S/R<1 (%)	Mean	COV
423	20-40	0.44	1.61	0.28
86	40-60	0.00	1.59	0.20
60	60-80	10.00	1.50	0.35
48	80-100	0.00	1.52	0.21

The COV's have more uniformity among the groups and the same decreasing trend whereas f_c' increases. The formulation remains satisfactorily in favor of safety along the compressive strengths. Since f_c' is considered with the same proportion of the previous code, considering the depth of the uncracked compressed zone and the scale effect may be one of the generators of the distinction among the analyzed data.

5.2.2 Shear Span to Effective Depth Ratio

Figure 9 shows S/R in relation to *a/d*. Once more, no strong trends are present. This is expected because this parameter is not directly considered. However, the dispersion band and S/R through the intervals are different. Thus, the Table 9 show the dataset information in detail. Once more the upper limits allow to demonstrate that the highest values are between 2.0 to 3.0 as explained in section 2.2.

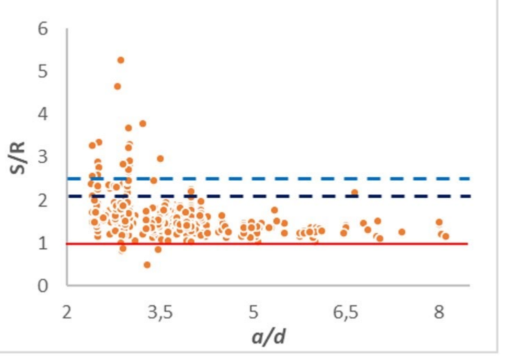

Figure 9- S/R in relation to a/d to Frosch et al. [5]

Table 9- S/R x *a/d* to the Unified Approach

N	*a/d* (-)	S/R<1 (%)	Mean	COV
392	2.40 – 3.55	0.26	1.84	0.25
154	3.55 – 4.70	0.00	1.51	0.16
47	4.70 – 5.85	0.00	1.43	0.12
25	5.85 – 8.15	0.00	1.45	0.20

In general, there is a reduction in COV's while *a/d* ratio approaches itself to the right level of the Kani valley. Muttoni and Ruiz Fernandez [10] obtained good adjustments for the ranges 2.47 to 3.0, extended in Ruiz Fernandez et al. [2] to 4.5, considering the contribution of the shear transfer mechanisms of the cross-sections.

In juxtaposition, the formulation by Frosch et al. [5] is close to these authors, considering the depth of the cracked compression zone, calculated to contemplate the higher rigidity of the reinforcement and consequent alteration of the compressed zone and obtained designs with satisfactory performance in all ranges.

5.2.3 Longitudinal Reinforcement Ratio (ρ_L)

Figure 10 shows the S/R in relation to ρ_L to this approach. Notably, no trends are present, and the results are dispersed in a more uniform manner in a smaller band, over all the dataset. The same interval (2 to 3%) has most of the values above the upper limits.

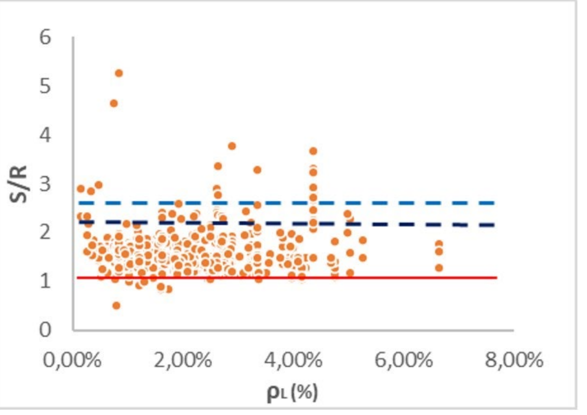

Figure 10- S/R in relation to ρ_L to Frosch et al. [5]

Dividing in intervals by the same criteria, Table 10 is obtained:

Table 10 – S/R x ρ_L to the Unified Approach

N	ρ_L (%)	S/R <1 (%)	Mean	COV
168	0-1.30	2.98	1.61	0.30
232	1.30 – 2.60	1.29	1.54	0.19
152	2.60 – 3.90	0.00	1.57	0.28
65	3.90 – 6.70	0.00	1.72	0.37

In the intervals taken there are no observable trends; therefore, there is a correct consideration of the term, although higher COVs are still observed for higher rates of longitudinal reinforcement. The dispersion band is the smallest among the considered design to this dataset, nevertheless, this approach also has the more conservative approach.

5.2.4 Effective Depth

Figure 11 shows S/R in relation to d to this approach. No trends until d is over 1000mm where an increasing trend occurs. This dispersion is like ACI 318 [4] but is more conservative, mainly to the smaller beam depths. Even after the size affect factor, the smallest beams depth concentrates most of the values above UL_5 and U_{10}. This may be related to correlation between longitudinal reinforcement and size effect, which was not considered on this approach. Utilizing the same intervals to this parameter to the previous code the Table 11, is obtained to analyze in detail.

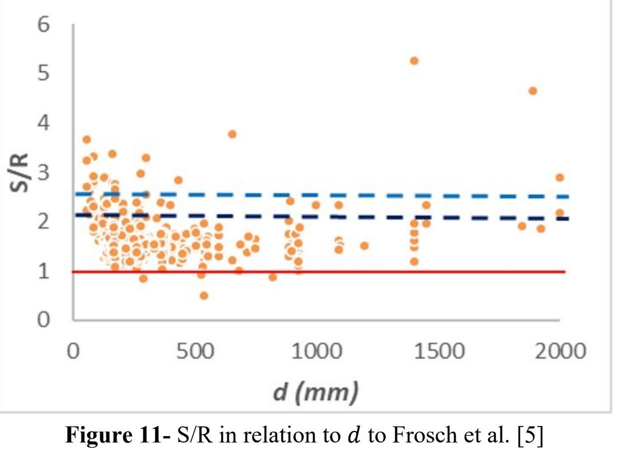

Figure 11- S/R in relation to d to Frosch et al. [5]

Table 11 – S/R x d to the Unified Approach

N	d (mm)	S/R <1 (%)	Mean	COV
225	0-250	0.00	1.70	0.25
298	250-500	0.34	1.48	0.20
37	500-750	10.81	1.49	0.32
33	750-1000	9.09	1.50	0.24
24	1000-2000	0.00	2.06	0.47

Good adequacy is denoted by the smaller dispersion band, by the mean of S/R demonstrating results closer to those tested and with less variation for the distinct ranges, with adequate values for practical purposes.

The size effect is also calculated with $\alpha \times\ d^{1/2}$, but there is a difference. The transitional dimension d_0 is a function of the ZPF, and it is sensitive to the inhomogeneities of the material [20]. In this model, even when a transversal reinforcement greater than the minimum is provided, a size effect could be applied if $d \geq 2{,}54m$, i.e., a suppression to size effect may occur, but it will not become negligible as the height increases. The adjusted value for the database under analysis provides more conservative results for the lower range, and the with adequate adjustment for higher beams.

5.3 ABNT: NBR 6118 [9]

The application of the Model I formulations of the Brazilian standard provides a mean of 1.58 with COV= 0.42 and 14.10% with S/R<1. Moreover, the upper limit to the fractile of 5 ($UL_5 = 2{,}61$), is the most conservative among all the analyzed approaches.

5.3.1 Compressive Strength (f_{ck})

It is important to comprehend that f_{ck} is different from f_c' (which is related to the 10%) control of acceptable results. The same trends concerning the highest conservative models are obtained to this model, i.e., on the range 20 to 40 MPa. The results obtained after the calculations are exposed in the Figure 12. The S/R in relation to f_c' have a similar trend to ACI 318 [3], i.e., there is a decrease trend over the dataset, slightly more prominent. The Table 12 shows the dataset results in detail.

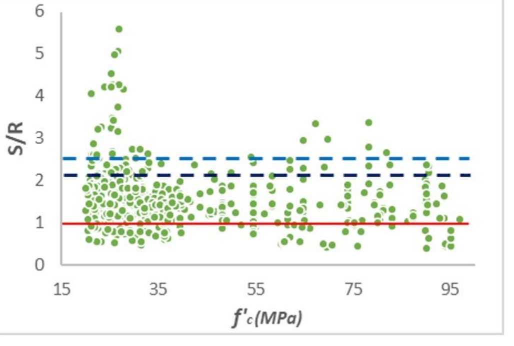

Figure 12- S/R in relation to f_c' to NBR 6118:2014

Table 12 – S/R x f_{ck} to NBR 6118: 2014

N	f_{ck} *(MPa)*	S/R <1 (%)	Mean S/R	COV
423	20-40	11.35%	1.65	0.41
86	40-60	11.63%	1.48	0.29
60	60-80	31.67%	1.43	0.32
48	80-100	22.92%	1.29	0.37

Eighty-seven of S/R results are below 1. As the NBR factor of 1.4 was considered, the ϕ=0.75 usual to American codes are not considered. In addition, there is a high dispersion, which is expected, based on what was previously discussed for the American code ACI 318 [3], i.e., the contribution of concrete calculated by Model I of the code does not consider the size effect, nor the change of the rate of longitudinal reinforcement. The proportionality to V_c with the compressive strength is calculated by $\sqrt[3]{f_{ck}^2}$ for values below 55 MPa and by a function of the natural logarithm for higher values, distinct from the previous codes.

In the initial ranges there are fewer predictions against safety, compared with the ACI code 318 [3], with non-negligible coefficients of variation. The trend with increasing resistance is also towards a reduction in the S/R factor, as shown by the increase in the S/R<1 column and decrease in the mean. When compared with both ACI 318 [4] and the Unified Approach, the trends regarding this parameter are similar.

5.3.2 Shear Span to Effective Depth Ratio (*a/d*)

The Figure 13 shows S/R in relation to *a*/d. First, no trends are presented in the dispersion, being the differences observed in the previous approaches in the COV`s observed, as well as the dispersion band of the dataset.

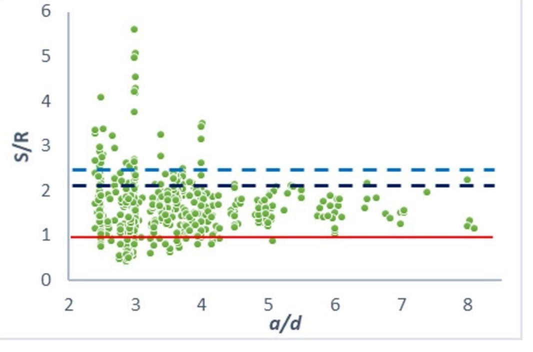

Figure 13- S/R in relation to a/d to NBR 6118:2014

Considering the explained intervals, the Table 13 is obtained. Where the Brazilian code shows the same behavior presented in the ACI 318 [3], i.e., no trends concerning the mean, most of the results with S/R<1 are located next to inflection point of Kani's valley and the lesser COV's are also in the higher *a/d* values. Hence, the influence of not considering *a/d* appears increasing the variance, and consequently the fraction to which S/R<1 near to a $a/d = 2.4$.

Table 13 - S/R x *a/d* to NBR 6118: 2014

N	a/d (-)	S/R <1 (%)	Mean	COV
392	2.40 – 3.55	17.44	1.58	0.48
154	3.55 – 4.70	10.39	1.61	0.31
47	4.70 – 5.85	2.22	1.61	0.17
25	5.85 – 8.15	0.00	1.55	0.20

5.3.3 Longitudinal Reinforcement Ratio (ρ_L)

The results of S/R in relation to ρ_L, to Brazilian code, are in the Figure 14. The current Brazilian design code has most of the values to which S/R<1 to light reinforced beams, with a strong increase trend. The same pattern was observed and analyzed in the ACI 318 [3], pointing some similar correction to this trend may be effective. Simultaneously, the range of 2 to 3% has most of the values above the proposed upper limits. Alternatively, the unified approach proposal [5], could be use. Nevertheless, this change implies in considering the depth of the compressed zone, a substantial transition from our current design.

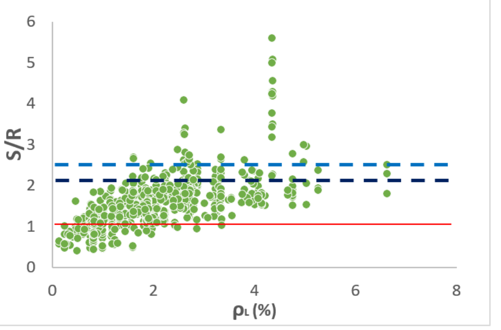

Figure 14- S/R in relation to ρ_L to NBR 6118:2014

The details of this dispersion are shown in the Table 14. Once more, the trends of this code are like ACI 318 [3], with the most results to which model error are below 1 regarding longitudinal reinforcement occurring for the light reinforced beams and the excessively safe outcomes in the higher ρ_L.

Table 14 - S/R x ρ_L to NBR 6118: 2014

N	ρ_L (%)	S/R <1 (%)	Mean	COV
168	0-1.30	44.05	1.05	0.32
232	1.30 – 2.60	5.17	1.54	0.25
152	2.60 – 3.90	1.32	1.87	0.27
65	3.90 – 6.70	0.00	2.42	0.42

Samora et al. [21] state that, from tests like those contained in this database, within the same range of compressive strength, for the lowest rates of longitudinal reinforcement, there was a greater contribution of the other complementary mechanisms, increasing with the increase in strength in compression and decreasing with the diameter of the bar.

An explanation is based on the study of Krefeld and Thurston [22], which is also used by Ruiz Fernandez et al. [2] in the model incorporated in the Swiss standard, Critical Shear Crack Theory (CSCT), which considers other parameters such as spacing between bars of reinforcement, diameter of bars, concrete tensile strength, and deformations in the reinforcement, obtaining adequate fits. Hence, the formulations under analysis presenting a direct proportionality only with the rate of reinforcement may underestimate the contribution of this mechanism, which would induce high *S/R* values.

5.3.4 Effective Depth

The Figure 15 exhibit S/R in relation to d for the Brazilian code. A strong decrease trends, like ACI 318 [3] occurs, i.e., excessively conservative design for shallow beams, decreasing until non conservative results to higher beam depth. The excessively conservative design occurs to smallest beams depth. Once more, as the trends are near the old north American code, the incorporation of a size effect factor could result in a more reliable design.

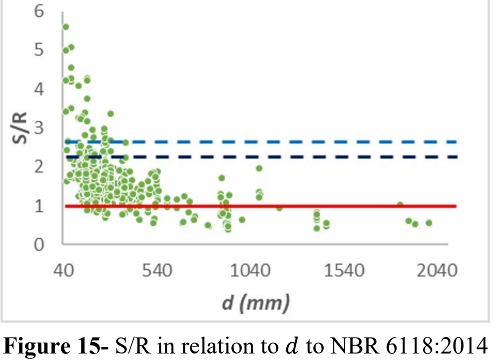

Figure 15- S/R in relation to d to NBR 6118:2014

Finally, disposing the results to analysis in the same intervals, Table 15 is obtained. There is a clear trend towards a reduction in the S/R mean with increasing height, with COV`s in the same range as those found in the ACI 318 [3]

There is a gradual increase in predictions against safety with the effective depth, juxtaposed with lower means, even below 1, for the last range. This parameter, together with the longitudinal reinforcement rate, are the strongest influences, which could provide optimized dimensions if adjusted to the Brazilian standard.

Table 15 - S/R x d to NBR 6118 [9]

N	d (mm)	S/R <1 (%)	Mean	COV
225	0-250	2.22	1.96	0.38
298	250-500	9.40	1.49	0.28
37	500-750	37.84	1.14	0.38
33	750-1000	75.76	0.80	0.39
24	1000-2000	70.83	0.85	0.42

Considering that increasing higher beams depths are being used in engineering practice there is a need to correct this trends that may lead to unsafe design conditions to higher beam depths. A correction may be realized in two steps:

1- A minimum square regression using a power law (like ACI 318 [4]) to a ρ_L factor;
2- A linear regression to dataset after (1), after applying a transformation in d using size effect law.

These steps result in:

$$V_c = 5.2\gamma_e f_{ctd} b_w d \rho_L^{0.44} \tag{17}$$

where γ_e is:

$$\gamma_e = \sqrt{\frac{1{,}53}{1+\frac{d}{254}}} \tag{18}$$

Leading to Figure 16, where S/R is represented as Model Error ***(ME)***. No notable trends are present, pointing to a better approach, which still must calibrate its partial safety factors. The purple line represents UL_{10} to this model in $UL_{10} = 1.60$. The fitting curve and the analysis of this model is still in study.

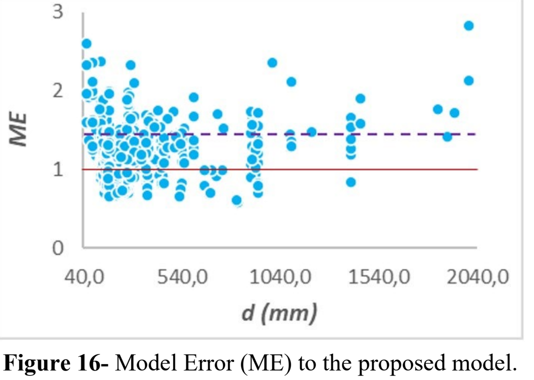

Figure 16- Model Error (ME) to the proposed model.

6 CONCLUSIONS

The analysis of the selected parameters has allowed to outline trends, as well as to analyze sources of dispersion of predictions not only in a global manner, but in localized phenomena, e.g., the a/d influence over the model error, and the tendencies regarding longitudinal reinforcement ratio. In Annex B there is a summary of the main conclusions obtained through this study

When comparing the ACI 318 [3] and ACI 318 [4], the non-consideration of the size effect and the longitudinal reinforcement ratio directly generates a larger dispersion band and non-conservative results for higher depths and lightly reinforced concrete beams, respectively. Therefore, the benefit of incorporating these parameters is notorious. The improved observed behavior with the proper consideration of these effects emerges even clearer when the Unified Approach by Frosh et al. [5] is introduced. In this model, the calculation considering the concrete and reinforcement stiffnesses, also the reinforcement ratio through the depth of compression zone, leads to the best results. However, it was also the more conservative model.

Finally, the ABNT: NBR 6118 has provided results like the North American previous code (ACI 318 [3]), which suggests the benefits of incorporating the size effect and the urgency to adapt to the Brazilian standard, considering the increasing dimensions of the structural elements used currently. The joint exposure of American codes (previous and current version) to the filtered database provides an overview of the changes generated by applying ρ_L and λ_s factor, which provide a basis for the analysis of the current Brazilian code. As a suggestion, two steps adjust is suggested considering the obtained results. The results briefly introduced exhibits the proposed model reduced tendencies and may be calibrated to the targeted safety, which is still in study.

REFERENCES

[1] American Concrete Institute, *Recent Approaches to the Shear Design of Structural Concrete*, ACI-ASCE Committee 445R, 1999, 55 p. (reapproved 2015).

[2] M. Fernández Ruiz, A. Muttoni, and J. Sagaseta, "Shear strength of concrete members without transverse reinforcement: a mechanical approach to consistently account for size and strain effects," *Eng. Struct.*, vol. 99, pp. 360–372, 2015.

[3] American Concrete Institute, *Building Code Requirements for Structural Concrete*, ACI Committee 318, 2014, 519 p.

[4] American Concrete Institute, *Building Code Requirements for Structural Concrete*, ACI Committee 318, 2019, 629 p.

[5] R. J. Frosch et al., "A unified approach to design," *Concr. Int.*, no. September, pp. 147–158, 2017.

[6] K. H. Reineck et al., "ACI-DAfStb database of shear tests on slender reinforced concrete beams without stirrups," *ACI Struct. J.*, vol. 110, no. 5, pp. 867–876, 2013.

[7] K. H. Reineck, E. Bentz, B. Fitik, D. A. Kuchma, and O. Bayrak, "ACI-DAfStb database of shear tests on slender reinforced concrete beams with stirrups," *ACI Struct. J.*, vol. 110, no. 5, pp. 1, 2014.

[8] D. A. Kuchma, S. Wei, D. H. Sanders, A. Belarbi, and L. C. Novak, "Development of the one-way shear design provisions of ACI 318-19 for reinforced concrete," *ACI Struct. J.*, vol. 116, no. 4, pp. 285–296, 2019.

[9] Associação Brasileira de Normas Técnicas, *Design of Concrete Structures: Procedures*, NBR 6118, 2014.

[10] A. Muttoni and M. Ruiz Fernandez, "Shear strength of members without transverse reinforcement as function of critical shear crack width," *ACI Struct. J.*, vol. 105, no. 2, pp. 163–172, 2008.

[11] F. Cavagnis, J. T. Simões, M. F. Ruiz, and A. Muttoni, "Shear strength of members without transverse reinforcement based on development of critical shear crack," *ACI Struct. J.*, vol. 117, no. 1, pp. 103–118, 2020.

[12] G. N. Kani, "The riddle of shear failure and its solution," *ACI J. Proc.*, vol. 61, no. 4, pp. 441–468, 1964.

[13] Y. Sato, T. Tadokoro, and T. Ueda, "Diagonal tensile failure mechanism of reinforced concrete beams," *J. Adv. Concr. Technol.*, vol. 2, no. 3, pp. 327–341, 2004.

[14] M. Fernández Ruiz, A. Muttoni, and J. Sagaseta, "Shear strength of concrete members without transverse reinforcement: a mechanical approach to consistently account for size and strain effects," *Eng. Struct.*, vol. 99, pp. 360–372, 2015.

[15] F. Cavagnis, “Shear in reinforced concrete without transverse reinforcement: from refined experimental measurements to mechanical models (8216),” M.S. thesis, Ec. Polytech. Fed. Lausanne, Suisse, 2017, 223 p.

[16] F. Leonhardt and R. Walther, "The Stuttgart shear tests" *Beton Stahlbetonbau*, vol. 56, no. 12, 1961.

[17] Q. Yu, J.-L. Le, M. H. Hubler, R. Wendner, G. Cusatis, and Z. P. Bažant, "Comparison of main models for size effect on shear strength of reinforced and prestressed concrete beams," *Struct. Concr.*, vol. 17, no. 5, pp. 778–789, 2016.

[18] Z. P. Bažant et al., "Justification of ACI 446 proposal for updating ACI code provisions for shear design of reinforced concrete beams," *ACI Struct. J.*, vol. 105, no. 4, pp. 512–515, 2008.

[19] B. El-Ariss, "Behavior of beams with dowel action," *Eng. Struct.*, vol. 29, no. 6, pp. 899–903, 2007.

[20] C. G. Hoover and Z. P. Bažant, "Cohesive crack, size effect, crack band and work of fracture compared to comprehensive concrete fracture tests," *Int. J. Fract. Mech.*, vol. 187, no. 1, pp. 133–143, 2014.

[21] M. S. Samora, A. C. D. Santos, L. M. Trautwein, and M. G. Marques, "Análise experimental da contribuição do concreto na resistência ao cisalhamento em vigas sem armadura transversal," *Rev. IBRACON Estrut. Mater.*, vol. 10, no. 1, pp. 160–172, Feb 2017.

[22] W. Krefeld and C. W. Thurston, "Contribution of longitudinal steel to shear resistance of reinforced concrete beams," *ACI Struct. J.*, no. 63, pp. 325–344, 1966.

Author contributions: JRCP: conceptualization, supervision, writing, methodology. TNB: Conceptualization, data curation, formal analysis, writing, methodology. IJSR: Conceptualization, data curation, formal analysis, writing, methodology

Editors: Edgar Bacarji, Guilherme Aris Parsekian.

ANNEX A

Data for Concrete Beams Without Stirrups

1. Adebar, P.E. (1989): Shear Design of Concrete Offshore Structures. A Thesis submitted in conformity with the requirements for the Degree of Doctor of Philosophy, University of Toronto 1989

2. Adebar, P.; Collins, M.P. (1994): Shear design of concrete offshore structures. ACI Structural Journ., V. 91, No. 3, May-June 1994, 324-335

3. Adebar, P.; Collins, M.P. (1996): Shear Strength of members without transverse reinforcement. Canadian Journal of Civil Engineering 23 (1996), No. 1, 30-41

4. Ahmad, S.H.; Khaloo, A.R.; Poveda, A. (1986): Shear Capacity of Reinforced High-Strength Concrete Beams. ACI-Journ. V.83 (1986), März/April, 297-305

5. Ahmad, S.H.; Park, F.; El-Dash, K. (1995): Web reinforcement effects on shear capacity of reinforced high-strength concrete beams. Magazine of Concrete Research 47 (Sep.1995), No. 172, 227-233

6. Al-Alusi, A.F. (1957): Diagonal tension strength of reinforced concrete T-beams with varying shear span, ACI Journal, May 1957, S. 1067-1077

7. Angelakos, D.; Bentz, E.C.; Collins, M.P. (2001): Effect of Concrete Strength and Minimum Stirrups on Shear Strength of Large Members. ACI Structural Journ. V.98 (2001), No.3, May/June, 290-300

8. Aster, H.; Koch, R. (1974): Schubtragfähigkeit dicker Stahlbetonplatten. BuStb 69 (1974), H.11, 266-270 Baldwin, J.W.; Viest, I.M. (1958): Effect of Axial Compression on Shear Strength of Reinforced Concrete Frame Members. ACI-Journ. V.30 (1958), Nov., 635-654

9. Bazant, Z.P., Kazemi, M.T. (1991): Size effect on diagonal shear failure of beams without stirrups.ACI-Struct. Journ. V.88 (1991), May-June, 268-276

10. Bentz, E. C.; Buckley, S. (2005): Repeating a classic set of experiments on size effect in shear of members without stirrups. ACI Structural Journal 102 (2005), Nov.-Dec., 832-838

11. Bernander, K. (1957): An investigation of the shear strength of concrete beams without stirrups or diagonal bars. RILEM-Symp., Stockholm, Vol.1, 1957

12. Bernhardt, C.J.; Fynboe, C.C. (1986): High strength concrete beams. Nordic Concrete Research, Norske Betongforening, Oslo 1986

13. Bhal, N.S. (1968): Über den Einfluß der Balkenhöhe auf die Schubtragfähigkeit von einfeldrigen Stahlbetonbalken mit und ohne Schubbewehrung. Otto-Graf-Institut, H.35, Stuttgart, 1968

14. Birrcher, D.; Tuchscherer, R.; Huizinga, M.; Bayrak, O.; Wood, S.; Jirsa, J. (2009): Strength and serviceability design of reinforced concrete deep beams. CTR Technical Report 0-5253-1, Center for Transportation Research, The University of Texas at Austin, April 2009. pp. 400

15. Bresler, B.; Scordelis, A.C. (1963): Shear strength of reinforced concrete beams. ACI-Journ. V.60 (1963), No.1, 51-74

16. Cladera Bohigas, A. (2002): Shear design of reinforced high-strength concrete beams. Dr.-thesis, Dep. dÉnginyeria de la Construcció, Universitat Politécnica de Catalunya, Barcelona, December 2002. pp. 168 and pages A.1-A.96, B.1-B3, C.1-C12, D.1-D.2; E.1-E.6

17. Cladera, A.; Marí, A.R. (2002): Shear Strength of Reinforced High –Strength and Normal –Strength Concrete Beams. A New Simplified Shear Design Method. Universitat Politécnica de Catalunya, 1-19, 2002

18. Cao, Shen (2000): Size Effect and the Influence of Longitudinal Reinforcement on the Shear Response of Large Reinforcement Concrete Members. A Thesis in conformity with the requirements for the degree of Master of Applied Science Graduate Department of Civil Engineering University of Toronto, 2000

19. Cederwall, K.; Hedman, O.; Losberg, A. (1970): Shear strength of partially prestressed beams with pretensioned reinforcement of high-grade deformed bars. Division of concrete structures, Chalmers University of Technology, Gothenburg, Sweden, Publikation 70/6

20. Cederwall, K.; Hedman, O.; Losberg, A. (1974): Shear strength of partially prestressed beams with pretensioned reinforcement of high-grade deformed bars. SP 42 - 9

21. Chana, P.S. (1981): Some aspects of modelling the behaviour of reinforced concrete under shear loading. Techn. Report 543, Cement and Concrete Association, Wexham Springs, 1981

22. Chang, T.S.; Kesler, C.E. (1958): Static and fatigue strength in shear of beams with tensile reinforcement, ACI- Journal, June 1958

23. Diaz de Cossio, R.; Siess, C.P. (1960): Behavior and strength in shear of beams and frames without web reinforcement. ACI-Journ. V.31 (1960), No.8, Feb., 695-735

24. Drangsholt, G.; Thorenfeldt, E. (1992): High Strength Concrete. SP2 – Plates and Shells. Report 2.1, Shear Capacity of High Strength Concrete Beams. SINTEF Structural Engineering – FCB, August 1992, STF70 A92125

25. Elzanaty, A.H.; Nilson, A.H; Slate, F.O. (1986): Shear Capacity of Reinforced Concrete Beams Using High-Strength Concrete. ACI-Journ.V.83 (1986), No.2, March-April, 290-296

26. Feldman, A.; Siess, C.P. (1955): Effect of Moment Shear Ratio on Diagonal Tension Cracking and Strength in Shear of Reinforced Concrete Beams. Univ. of Illinois Civil Eng. Studies, Struct. Research Series No. 107, 1955

27. Ferguson, P.M.; Thompson, J.N. (1953): Diagonal Tension in T-Beams without stirrups. Journal of the American Concrete Institute (Mar. 1953), S. 655-676

28. Ferguson, P. M. (1956): Some Implications of Recent Diagonal Tension Tests. ACI Journal V. 28, No. 2, Aug. 1956

29. Ghannoum, W.M. (1998): Size Effect on Shear Strength of Reinforced Concrete Beams. Department of Civil Engineering and Applied Mechanics, McGill University Montréal, Canada, November 1998

30. Grimm, R. (1996/97): Einfluß bruchmechanischer Kenngrößen auf das Biege- und Schubtragverhaltenhochfester Betone. Diss., Fachb. Konstr. Ingenieurbau der TH Darmstadt, 1996 und DafStb H.477, Beuth Verlag GmbH, Berlin 1997

31. Haddadin, M.J., Hong, S., Mattock, A.H. (1971): Stirrup Effectiveness in Reinforced Concrete Beams with Axial Force. Proceedings ASCE; V.97 ST9 (Sept. 1971), 2277-2297

32. Hallgren, M. (1994): Flexural and Shear Capacity of Reinforced High Strength Concrete Beams without Stirrups. KTH, Stockholm, TRITA-BKN. Bull.9, 1994, 1-49

33. Hallgren, M. (1996): Punching shear capacity of reinforced high strength concrete slabs. Doctoral thesis, KTH Stockholm und TRITA-BKN: Bulletin 23, Stockholm, 1996

34. Hamadi, Y.D. (1976): Force transfer across cracks in concrete structures. PhD-thesis, Polytechnic of Central London, 1976

35. Hanson, J.A. (1958): Shear Strength of Ligthweight Reinforced Concrete Beams. ACI, Title No. 55-24, (1958), 387- 403

36. Hanson, J.A. (1961): Tensile Strength and Diagonal tension resistance of Structural lightweight Concrete. ACI-Journ. V.58 (1961), No.1, July, 1-39

37. Injaganeri, S. S. (2007): Studies on size effect on design strength and ductility of reinforced concrete beams in shear. Thesis Doctor of Philosophy, Indian Institute of Technology, April 2007

38. Islam, M.S.; Pam, H.J.; Kwan, A.K.H. (1998): Shear Capacity of high-strength concrete beams with their point of inflection within the shear span. Proc. Instn Civ. Engrs Structs & Bldgs. 128 (Feb. 1998), 91-99

39. Johnson, M.K.; Ramirez, J.A. (1989): Minimum Shear Reinforcement in Beams with Higher Strength Concrete. ACI-Struct. Journ. V.86 (1989), No.4, 376-382

40. Kani, G.N.J. (1967): How safe are our large reinforced concrete beams? ACI-Journ. V.64 (1967), No.3, 128-141. Disc. in ACI-Journ., Sept. 1967, 602-613

41. Kani, M.W.; Huggins, M.W.; Wittkopp, R.R. (1979): Kani on shear in reinforced concrete. Dep. of Civil Engineering, Univ.of Toronto 1979

42. Kawano, H.; Watanabe, H. (1998): Shear strength of reinforced concrete columns – Effect of specimen size and load reversal. 141-154 in: Concrete Under Severe Conditions 2. Proceedings of the 2nd International Conference on CONSEC '98. Vol. III. Editors: Gjørv, O.E.; Sakai, K., Banthia, N. (1998), E & FN Spon, London and New York

43. Kim, J.-K.; Park, Y.-D. (1994): Shear strength of reinforcement high strength concrete beams without web reinforcement. Magazine of Concrete research 46 (1994), No. 166, 7-16

44. Krefeld, W.J.; Thurston, Ch.W. (1966): Studies of the shear and diagonal tension strength of simply supported r.c.-beams. ACI-Journ. V.63 (1966), April, 451-475

45. Kuhlmann, U. Ehmann, J. (2001): Versuche zur Ermittlung der Querkrafttragfähigkeit von Verbundplatten unter Längszug ohne Schubbewehrung- Versuchsbericht. Institut für Konstruktion und Entwurf Stahl-, Holz-, und Verbundbau, Universität Stuttgart, Nr. 2001- 6X, Februar 2001

46. Kuhlmann, U.; Zilch, K.; Ehmann, J.; Jähring, A.; Spitra, F. (2002): Querkraftabtragung in Verbundträgern mit schlaff bewehrter und aus Zugbeanspruchung gerissener Stahlbetonplatte ohne Schubbewehrung- Mitteilungen. Institut für Konstruktion und Entwurf Stahl-, Holz-, und Verbundbau, Universität Stuttgart, Nr. 2002- 2

47. Kulkarni, S.M.; Shah, S.P. (1998): Response of reinforced Concrete Beams at High Strain Rates. ACI Structural Journal V.95 (Nov.-Dec. 1998), No. 6, 705-714

48. Laupa, A.; Siess, C.P.; Newmark, N.M. (1953): The shear strength of simple-span reinforced concrete beams without web reinforcement. Univ. of Illinois, Struct. Research Series, No.52, 1953

49. Leonhardt, F.; Walther, R. (1962): Schubversuche an einfeldrigen Stahlbetonbalken mit und ohne Schubbewehrung. DAfStb H.151, Berlin, 1962

50. Lubell, A.; Sherwood, T.; Bentz, E.; Collins, M. (2004): Safe Shear Design of Large Wide Beams. Concrete International 26, January (2004), No.1, 62-78

51. Lubell, A. (2006): Shear in wide reinforced concrete beams. Dr.-thesis, Graduate Dep. of Civil Engineering, University of Toronto, 2006. pp. 455

52. Marti, P.; Pralong, J.; Thürlimann, B. (1977): Schubversuche an Stahlbeton-Platten. IBK-Bericht Nr. 7305-2, ETH Zürich, Sept. 1977

53. Mathey, R.G.; Watstein, D. (1963): Shear strength of beams without web reinforcement containing deformed bars of different yield strengthes. ACI-Journ. V.60 (1963), No.2, Febr. 1963, 183-207

54. Moayer, M.; Regan, P.E. (1974): Shear strength of prestressed and reinforced concrete T-beams. 183-214 in: Shear in reinforced concrete. Vol. 1, Publ. SP 42, ACI Detroit. 1974

55. Moody, K.G.; Viest, I.M.; Elstner, R.C.; Hognestad,E. (1954/1955): Shear strength of r.c.-beams. Part 1 – Tests of Simple Beams. ACI-Journal V.26, (1954), No.4, Dec. 1954, 317-332 Part 2 – Tests of Restrained Beams without Web Reinforcement. ACI-Journal V.26, (1955), No.5, Jan. 1955, 417-434 Part 3 – Tests of Restrained Beams with Web Reinforcement. ACI-Journal V.26, (1955), No.6, Febr. 1955, 525-539

56. Morrow, J.D.; Viest, F.M. (1957): Shear strength of r.c.-frame members without web reinforcement. ACI-Journ. V.28 (1957), No.9, March, 833-869

57. Mphonde, A.G.; Frantz, G.C. (1984): Shear tests of high- and low- strength concrete beams without stirrups. ACI-Journ. V.81 (1984), July-Aug., 350-357

58. Niwa, J.; Yamada, K.; Yokozawa, K.; Okamura, M. (1987): Revaluation of the equation for shear strength of r.c.-beams without web reinforcement. Proc. JSCE No.372/V-5 1986-8 Translation in: Concrete Library of JSCE, No. 9, June 1987

59. Podgorniak-Stanik, B.A. (1998): The Influence of Concrete Strength, Distribution of Longitudinal Reinforcement, Amount of Transverse Reinforcement and Member Size on Shear Strength of Reinforced Concrete Members. University of Toronto (1998)

60. Rajagopalan, K.S.; Ferguson, P.M. (1968): Exploratory shear tests emphasizing percentage of longitudinal reinforcement. ACI-Journ. V.65 (1968), No.8, 634-638

61. Regan, P.E. (1971 a): Shear in Reinforced Concrete – an analytical study. CIRIA-Report, a report to the Construction Research and Information Association. Imperial College of Science and Technology, Dep. of Civil Engineering, Concrete Section. April 1971

62. Regan, P.E. (1971 b): Shear in Reinforced Concrete – an experimental study. CIRIA-Report, a report to the Construction Research and Information Association. Imperial College of Science and Technology, Dep. of Civil Engineering, Concrete Section. April 1971

63. Regan, P.E. (1971 c): Behaviour of reinforced and prestressed concrete subjected to shear forces. Institution of civil engineers, Proceedings, Paper 7441S

64. Reineck, K.-H.; Koch, R.; Schlaich, J. (1978): Shear Tests on Reinforced Concrete Beams with axial compression for Offshore Structures – Final Test Report. Stuttgart, July 1978, Institut für Massivbau, Univ. Stuttgart (unveröffentlicht)

65. Remmel, G. (1991): Zum Zugtragverhalten hochfester Betone und seinem Einfluß auf die Querkrafttragfähigkeit von schlanken Bauteilen ohne Schubbewehrung. Diss., TH Darmstadt, 1992

66. Rosenbusch, J.; Teutsch, M. (2002): Trial Beams in Shear. Brite/Euram project 97-4163, Final Report Sub task 4.2, Institut für Baustoffe, Massivbau und Brandschutz, TU Braunschweig, January, 2002

67. Rosenbusch, J.; Zur Querkrafttragfähigkeit von Balken aus stahlfaserverstärkten Stahlbeton. Diss., Fachbereich Bauingenieurwesen, TU Braunschweig, Institut für Baustoffe, Massivbau und Brandschutz, Juni 2003. pp. 199

68. Rüsch, H.; Haugli, F.R.; Mayer, H. (1962): Schubversuche an Stahlbeton-Rechteckbalken mit gleichmäßig verteilter Belastung. DafStb H.145, W. Ernst & Sohn, Berlin, 1-30

69. Salandra, M.A.; Ahmad, S.H. (1989): Shear Capacity of reinforced Lightweight High-Strength Concrete Beams. ACI Structural Journal V86, (Nov-Dec. 1989), No. 6, 697-704

70. Scholz, H. (1994):Ein Querkrafttragmodell für Bauteile ohne Schubbewehrung im Bruchzustand aus normalfestem und hochfestem Beton. Berichte aus dem Konstruktiven Ingenieurbau Heft 21, Technische Universität Berlin 1994

71. Sherwood, E. G. (2008): One-way shear behaviour of large, lightly-reinforced concrete beams and slabs.Dr.-thesis, Dep. of Civil Engineering, University of Toronto, 2008. pp. 547

72. Shin, S-W.; Lee, K-S; Moon, J-I; Ghosh, S. K. (1999): Shear Strength of Reinforced High-Strength Concrete Beams with Shear Span-to-Depth Ratios between 1.5 and 2.5. ACI-Struct. Journ. V.96-S61 (1999), July-August, 549-556

73. Sneed, L.H. (2007): Influence of member depth on the shear strength of concrete beams. Dr. Dissertation, Fac. of Civil Engineering of Purdue University, West Lafayette, Indiana. December 2007. pp. 258

74. Sneed, L.H.; Ramirez, J.A. (2008): Effect of depth on the shear strength of concrete beams without shear reinforcement - experimental study. PCA Research and Development Information, PCA R&D SN2921. Portland cement Assoc., Skokie, Illinois, 2008. pp. 173

75. Sneed, L.H.; Ramirez, J.A. (2010): Influence of effective depth on shear strength of concrete beams - experimental study. ACI Structural Journal 107 (2010), Sept.-Oct., 554-562

76. Swamy, N.; Qureshi, S.A. (1971): Strength, cracking and deformation similitude in reinforced T-beams under bending and shear. ACI-Journ. V.68 (1971), March, 187-195 the Railway Technical Research Institute, V. 46 (2005), No. 1, Feb., 53-58

77. Tanimura, Y.; Sato, T. (2005): Evaluation of Shear Strength of Deep Beams with Stirrups. Quarterly Report of the Railway Technical Research Institute, V. 46 (2005), No. 1, Feb., 53-58

78. Taylor, H.P.J. (1968): Shear stress in reinforced concrete beams without shear reinforcement. Cement and Concrete Ass., Techn. Rep. No.407, Febr. 1968

79. Taylor, H.P.J. (1972): Shear strength of large beams. ASCE-Journ. of the Struct. Div., V.98 (1972), ST11, 2473-2490

80. Thiele, C. (2010): Bemessung von Stahlbetondecken ohne Querkraftbewehrung mit integrierten Leitungsführungen. 12 pp. in: Doktorandensymposium 2010 - 51. Forschungskolloquium des DAfStb, 11. und 12. November 2010, Kaiserslautern. DAfStb e.V., Berlin

81. Tureyen, A.K. (2001): Influence of longitudinal reinforcement type on the shear strength of reinforced concrete beams without transverse reinforcement. Diss. Purdue University, West Lafayette, IN. December 2001

82. Tureyen, A.K.; Frosch, R.J. (2002): Shear tests of FRP-reinforced concrete beams without stirrups.ACI Structural Journal 99 (2002), July-August, 427-434

83. Van den Berg, F.J. (1962): Shear Strength of Reinforced Concrete Beams without Web Reinforcement. ACI-Journ. V.59 (1962) 1467-1477, 1587-1600 u. 1849-1862

84. Walraven, J.C. (1978): The influence of depth on the shear strength of lightweight concrete beams without shear reinforcement. Report S-78-4, Stevin Lab., Delft Univ., 1978

85. Winkler, K. (2011): Querkraftversuche an maßstäblich skalierten, schubunbewehrten Stahlbetonbalken.Versuchsbericht 2011-1. Lehrstuhl für Massivbau, Ruhr Universität Bochum. 3. Feb. 2011. pp. 105

86. Xie, Y.; Ahmad S.H.; Yu, T.; Hino, S.; Chung, W. (1994): Shear Ductility of reinforced Concrete Beams of normal and high-strength concrete. ACI Structural Journal V.91 (Mar.-Apr. 1994), No. 2, 140-149

87. Yoon, Y.-S.; Cook, W.D.; Mitchell, D. (1996): Minimum Shear Reinforcement in Normal, Medium and High-Strength Concrete Beams. ACI-Journ., V.93 (1996), No.5, Sept.-Oct., 576-584

88. Yoshida, Y.; Bentz, E.; Collins, M.P. (2000): Results of Large Beam Tests. University of Toronto (2000)

ANNEX B – CONCLUSION SUMMARY

Parameter	Design Formulation			
	ABNT:NBR6118 (2014)	ACI 318 (2014)	ACI 318 (2019)	Frosch et al. (2017)
f_c'	There is a decrease trend over the dataset, slightly more prominent	A strong trend of decreasing in S/R mean as compressive strength increases	Decreasing in S/R mean as compressive strength increases	No trends are noted, and the approach is the more conservative
a/d	No trends concerning the mean, most of the results with S/R<1 is located next to inflection point of Kani's valley	No trends concerning the mean, most of the results with S/R<1 is located next to inflection point of Kani's valley	a slight decrease trend	No strong trends are present
ρ_L	Most of the values to which S/R<1 to light reinforced beams, with a strong increase trend	Most of the values to which S/R<1 to light reinforced beams, with a strong increase trend	Presents no notable trends regarding this parameter,	No trends are present, and the results are dispersed in a more uniform manner
d	A strong decrease trends occurs, with excessively conservative design for shallow beams, decreasing until non conservative results to higher beam depth	A strong decrease trends occurs, with excessively conservative design for shallow beams, decreasing until non conservative results to higher beam depth	Significantly corrects the model error in shallow beams, leading to smaller S/R, and increasing its value as the beam depth increases	This dispersion is like ACI 318:2019 but is more conservative, mainly to the smaller beam depths

IBRACON Structures and Materials Journal
Revista IBRACON de Estruturas e Materiais
ISSN 1983-4195 ismj.org

ORIGINAL ARTICLE

Modal P-delta – simplified geometric nonlinear method by using modal and buckling analysis

Modal P-delta – método no lineal geométrico simplificado mediante el uso del análisis modal y de pandeo

Wagner Almeida Ferreira[a]
Jeffer Roussell Cordova De La Cruz[a]
Iván Darío Gómez Araujo[a]
Jesús Antonio Garcia Sánchez[b]

[a]Universidade Federal da Integração Latino-Americana – UNILA, Departamento de Engenharia Civil e Infraestrutura, Foz do Iguaçu, PR, Brasil.
[b]Universidade Federal de Itajubá – UNIFEI, Instituto de Engenharia Mecânica, Itajubá, MG, Brasil.

Received 31 March 2022
Accepted 18 August 2022

Abstract: Recent works show that in structures, there is a relationship between the natural period of vibration and global second-order effects. This relationship occurs because both depend on the stiffness matrix and the mass matrix of the structure. In this work, a non-linear geometric method - modal P-delta – is proposed that takes advantage of the relationship between the dynamic parameters and the non-linear effects. The methodology establishes an association between the buckling instability modes and the structural vibration modes. An interpolation of the vibration modes without axial loading and vibration modes with critical axial loading is proposed to approximate the vibration modes and frequencies of the loaded structure. In this way, through a simple formulation, the vibration modes and the natural frequencies of the loaded structure can be used to evaluate the displacements of the structures including the non-linear effects. Several numerical examples were simulated in regular structures in the plane, such as a free-fixed column and a plane frame with two different loading configurations. The results generated with the modal P-delta method provide information about the nonlinear behavior of the pre-buckling equilibrium path. These results are different from the findings in the literature, where the relationship between dynamic parameters and non-linear effects is used as a simple indicator or amplification factors to determine non-linear effects. Furthermore, our results indicate that the modal P-delta reduces the computational time spent considerably compared to the traditional P-delta iterative method.

Keywords: geometric non-linearity, modal analysis, structural stability, p-delta.

Resumen: Trabajos recientes muestran que en las estructuras existe una relación entre el período natural de vibración y los efectos globales de segundo orden. Esta relación se da porque ambas dependen de la matriz de rigidez y de la matriz de masa de la estructura. Este trabajo propone un método geométrico no lineal - modal P-delta - que aprovecha una relación entre parámetros dinámicos y efectos no lineales. La metodología establece una asociación entre los modos de inestabilidad de pandeo y los modos de vibración estructural. Se propone una interpolación de los modos de vibración sin carga axial y modos de vibración con carga axial crítica para aproximar los modos y frecuencias de vibración de la estructura cargada. De esta manera, a través de una formulación simple, los modos de vibración y las frecuencias naturales de la estructura cargada pueden usarse para evaluar los desplazamientos de las estructuras incluyendo los efectos no lineales. Se simularon varios ejemplos numéricos en estructuras regulares tales como una columna libre-empotrada y un marco plano con dos configuraciones diferentes de carga. Los resultados generados con el método modal P-delta proporcionan información sobre el comportamiento no lineal de la trayectoria de equilibrio previa al pandeo. Estos resultados difieren de los hallazgos en la literatura, donde la relación entre los parámetros dinámicos y los efectos no lineales se utiliza como un indicador simple o factores de amplificación para determinar los efectos no lineales. Además, nuestros resultados indican que el P-delta modal reduce el tiempo computacional empleado considerablemente en comparación con el método iterativo P-delta tradicional.

Palabras clave: no linealidad geométrica, análisis modal, estabilidad estructural, P-delta.

Corresponding author: Iván Darío Gómez Araujo. E-mail: ivan.araujo@unila.edu.br
Financial support: None.
Conflict of interest: Nothing to declare.
Data Availability: Data-sharing is not applicable to this article as no new data were created or analyzed in this study.

How to cite: W. A. Ferreira, J. R. Cordova De La Cruz, I. D. G. Araújo, and J. A. Garcia Sánchez, "Modal P-delta – simplified geometric nonlinear method by using modal and buckling analysis," *Rev. IBRACON Estrut. Mater.*, vol. 16, no. 2, e16209, 2023, https://doi.org/10.1590/S1983-41952023000200009

1 INTRODUCTION

The movement of the structure to a deformed position in the analysis of structures subjected to vertical and lateral loads causes additional internal forces called second-order effects. According to Rutenberg [1], this type of additional effect is not considered in normal static analysis and can be important for structural analysis of tall and slender structures. The second-order effects are also called P-delta effects since additional internal moments of the structure can be evaluated by multiplying of structural weight "P" on each floor and the displacement "delta" caused by lateral loads.

Structures with lateral loads and high axial internal forces can require a non-linear geometric analysis – NLG for the correct evaluation of the internal forces in the structure. Traditionally, the NLG effects are evaluated in two ways: with iterative methods [2] or with direct methods [1]. Commonly, iterative methods have a high computational cost in the analysis of large structures and cannot be appropriate for dynamic analysis where there may be structural instability due to resonance vibrations and P-delta effects simultaneously [3]. These characteristics have made its use difficult in common engineering projects. Alternatively, direct methods try simplifying or approximate the geometric stiffness matrix to avoid iterations and reduce computational time with an acceptable degree of approximation [1]. Another alternative, that can be classified as direct methods, is the use of simplified amplification factors to the first-order values [4], [5]. Several works can be found in the literature exploring these two alternatives, detailed information of NL effects and methods can be found in Gaiotti and Smith [6]. Also, the work by Rezaiee-Pajand et al. [7], [8] presented a comparative study related to the formulation, characteristic, and efficiency of several well-known structural geometrical non-linear – NL – solutions in iterative methods.

Recently, new methodologies have emerged to consider the NLG effects in structures, based on changes in dynamic parameters by the axial loads in structures [9], [10]. These methodologies can be considered as direct methods and are mainly proposed with two aims 1) as a method to evaluate the amplification factors of first-order analysis to approximate second-order analysis and 2) as an indicator of the structure's susceptibility to second-order effects. Specifically, the work by Statler et al. [11] proposes using a single degree of freedom model of the structure to define second-order amplification factors from the first natural frequency of the system. In that work, it was considered that the stiffness of a single degree of freedom system can be modified by a moment amplification factor defined in a highly simplified linear deformed shape of a rigid structure. In this way, it is possible to evaluate the natural frequency of the structure as a function of the moment amplification factor. Reis et al. [12] uses a similar procedure applied in Statler [11], however, it uses a dynamic model of a flexible structure based on equivalent cantilever beam-column to estimate the first natural frequency. In another work by Leitão et al. [13], the proposed method by Reis et al. [12] was used to evaluate the applicability of the amplification factor based on natural frequencies in an asymmetric structure in which torsional vibration modes can become fundamental vibration modes.

The previous methodologies based on the natural frequency of the structure show facility to estimate the amplification factors due to second-order effects since that amplification factor depends only on the natural frequency and thus requires only a modal analysis. However, these methodologies are based on approximations of the amplification factors that are used to perform rapid verification of the susceptibility for second-order effects, commonly used in standards or codes for the design of reinforced concrete during preliminary stages of design. Therefore, this amplification factor is only valid for a particular type of structure (e.g. sway frame) and limited for small values of amplification, smaller than 1.3. Additionally, these methods cannot determine the equilibrium path curve before buckling load.

To overcome the various limitations of based methodologies on dynamic parameters to estimate second-order effects and the problems related to the computational cost in iterative methods, this paper proposed a *Modal P-delta method* to estimate second-order effects. The proposed methodology provides the NL pre-buckling equilibrium path, and not only an indication of the susceptibility to second-order effects or definition of an amplification factor. In this way, the proposed method takes advantage of the relationship between dynamical parameters and NL effects to create an alternative methodology, which can be computationally cheaper than iterative traditional methods. The Modal P-delta establishes structural displacements from natural frequencies and vibration modes of the loaded structure, including P-delta effects. These dynamic parameters of the structure can be approximated from an interpolation of vibration modes obtained with the unloaded structure and with the structures under the critical load. Different structural examples were addressed to demonstrate the capability of the proposed method to evaluate the pre-buckling equilibrium path. The results and computational time-consuming of the proposed method were compared with the iterative traditional P-delta method.

2 THEORETICAL BACKGROUND

This section contains a description of the theoretical bases to define the relationship between NLG, modal analysis, and the buckling phenomenon. First, the effects of axial load in the vibration modes and frequencies will be shown. With this, a relationship between the buckling mode with the vibration mode of the structure under the critical load can be established. Initially, these concepts in a simple example are presented – a column element – and later they are applied in a frame structure. In summary, it was shown that any vibration mode and natural frequency can be defined using the orthogonality properties of modes, and an interpolation of the vibration modes obtained using the unloaded structure and the vibration modes obtained using the structure under the critical load. Finally, with these concepts, the modal P-delta method will be proposed.

2.1 Effect of axial load on vibration modes and frequencies

Here will be shown as the vibration modes and natural frequencies are altered when the internal loads are increased in a Euler-Bernoulli beam element. A solution for this problem was presented by Shaker [14], however, some modifications were made to this work to obtain vibration modes and natural frequencies in a simple manner. The governing equation of the beam shown in Figure 1 is given as

$$p(x,t) = EIu(x,t)'^{v} + Pu(x,t)'' + \bar{m}\ddot{u}(x,t), \tag{2.1}$$

where $\tilde{u}(x,t)$ is the transverse deflection; $\ddot{u} = \partial^2 \mathrm{u}(x,t)/\,\partial \mathrm{t}^2$ is the acceleration; $u(x,t)''$ represents the second derivative related to x; $\bar{m} = \rho A$ is the mass per length unit; E is the Young modulus; I is the moment of inertia of the cross-section; P represents the axial load (in this case the internal axial load and the axial external load have the same value $N = P$); and $p(x,t)$ is the transverse external load. In Figure 1b V represents the shear load and M the bending moment.

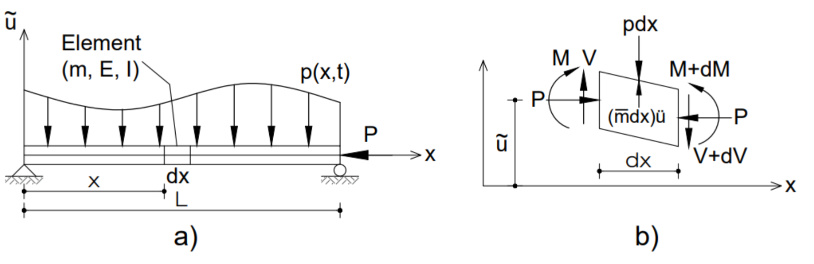

Figure 1. (a) Representation of coordinates for vibration in a beam; **(b)** Convention of signals for forces and moment under constant axial load, acting in an arbitrary element.

The dynamical characteristics of free vibration system are obtained with $p(x,t) = 0$. Applying in Equation 2.1, we obtained the following expression:

$$0 = EIu(x,t)'^{v} + Pu(x,t)'' + \bar{m}\ddot{u}(x,t), \tag{2.2}$$

The solution of Equation 2.2 according to Shaker [14] and Paz [17], is found by substituting $u(x,t) = \Phi(x)f(t)$, which correspond to a variable separation principle, then it can be obtained:

$$\Phi(x)'^{v} + \frac{P\Phi(x)''}{EI} - \frac{w^2\bar{m}\Phi(x)}{EI} = 0, \tag{2.3}$$

$$w^2 f(t) + \ddot{f}(t) = 0. \tag{2.4}$$

The solution of Equation 2.3 gives us the vibration modes for a natural frequency w. The solution of Equation 2.4 allows us to obtain the time behavior for each natural frequency.

Considering $\Phi(x) = Ce^{Dx}$ as a solution, then Equation 2.3 is rewritten as,

$$D^4 + D^2 \frac{P}{EI} - \frac{w^2 \bar{m}}{EI} = 0. \tag{2.5}$$

The roots of Equation 2.4 are,

$$\lambda_1 = \sqrt{-\frac{k^2}{2} + \sqrt{\frac{k^4}{4} + \beta^4}}\,;\ \lambda_3 = -\lambda_1, \tag{2.6}$$

$$i\lambda_2 = \sqrt{\frac{k^2}{2} + \sqrt{\frac{k^4}{4} + \beta^4}}\,;\ \lambda_4 = -i\lambda_2, \tag{2.7}$$

where,

$$k^2 = \frac{P}{EI} \tag{2.8}$$

$$\beta^4 = \frac{w^2 \bar{m}}{EI} \tag{2.9}$$

Then, considering Equations 2.6 and 2.7, the solution $\Phi(x)$ is rewrite as,

$$\Phi(x) = C_1 e^{\lambda_1 x} + C_3 e^{-\lambda_1 x} + C_2 e^{i\lambda_2 x} + C_4 e^{-i\lambda_2 x} \tag{2.10}$$

or,

$$\Phi(x) = A \cos\mathrm{h}(\lambda_1 x) + B senh(\lambda_1 x) + D \cos(\lambda_2 x) + E sen(\lambda_2 x), \tag{2.11}$$

where A, B, D and E are the constant of integration, that are determined using the boundary conditions of the beam.

Therefore, knowing Equation 2.11, it can be found a specific solution for the beam. The boundary conditions are those given for a column element as shown in Figure 2,

$$\begin{cases} u(0,t) = 0 \; or \; \Phi(0) = 0, \\ u'(0,t) = 0 \; or \; \Phi'(0) = 0, \\ \mathrm{M}(L,t) = \frac{-EI\, \partial^2 u(L,t)}{\partial x^2} = 0 \; or \; \Phi''^{(L)} = 0, \\ \mathrm{V}(L,\mathrm{t}) = -\mathrm{EI}\left[\frac{\partial^3 u(L,t)}{\partial x^3} - \frac{P}{EI}\frac{\partial u(L,\mathrm{t})}{\partial x}\right] = 0 \; or \; \Phi'''(L) + k^2 \Phi'(L) = 0. \end{cases} \tag{2.12}$$

The characteristic equation is obtained, which is the non-trivial solution, applying the boundary conditions, Equation 2.12, in Equation 2.11,

$$\left(-2\lambda_1 k^2 \lambda_2 + \lambda_1 {\lambda_2}^3 - {\lambda_1}^3 \lambda_2\right) senh(\lambda_1 L) sen(\lambda_2 L) + \left({\lambda_2}^2 k^2 + 2{\lambda_1}^2{\lambda_2}^2 - {\lambda_1}^2 k^2\right)\cosh(\lambda_1 L)\cos(\lambda_2 L) + {\lambda_2}^4 + {\lambda_1}^2 k^2 + {\lambda_1}^4 - {\lambda_2}^2 k^2 = 0. \tag{2.13}$$

The roots of Equation 2.13 allow the definition of the analytical natural frequencies of the column considering the effect of axial load on the element.

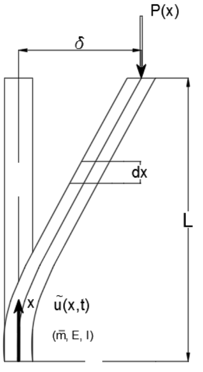

Figure 2. Free-fixed column with displacement association $\tilde{u}(x,t)$.

It is now intended to show that the characteristic equation, Equation 2.13, can be written as a function of a single variable, λ_1. Thus, operating in Equations 2.6 and 2.7 is obtained the following expressions.

$$\beta^4 = k^2{\lambda_1}^2 + {\lambda_1}^4\,, \tag{2.14}$$

$$\beta^4 = -k^2{\lambda_2}^2 + {\lambda_2}^4. \tag{2.15}$$

Operating in Equations 2.14 and 2.15, can be isolated the variable k^2, getting

$$k^2 = \frac{{\lambda_2}^4 - {\lambda_1}^4}{{\lambda_1}^2 + {\lambda_2}^2}. \tag{2.16}$$

Considering the positive root of Equation 2.16, it is possible to find the relationship between λ_1 and λ_2,

$$\lambda_2 = \sqrt{k^2 + {\lambda_1}^2}. \tag{2.17}$$

Combining Equation 2.17 and Equation 2.13, the characteristic equation can be obtained only as a function of a single variable, λ_1,

$$(-k^2\lambda_1) senh(L\lambda_1) sen\left(L\sqrt{k^2 + {\lambda_1}^2}\right)\sqrt{k^2 + {\lambda_1}^2} + \cosh(L\lambda_1)\cos\left(L\sqrt{k^2 + {\lambda_1}^2}\right)\left(k^4 + 2k^2{\lambda_1}^2 + 2{\lambda_1}^4\right) + 2{\lambda_1}^2\left(k^2 + {\lambda_1}^2\right) = 0. \tag{2.18}$$

The roots of Equation 2.18 represent the natural frequencies of a free-fixed column under axial load, which are expressed as

$$w = \sqrt{\frac{EI}{\bar{m}}\beta^4} = \sqrt{\frac{EI}{\bar{m}}(k^2{\lambda_1}^2 + {\lambda_1}^4)}. \tag{2.19}$$

Vibration modes are obtained considering the boundary conditions shown in Equations 2.12 and 2.11. Assuming the constant $A = 1$, rewrites Equation 2.11 as,

$$\Phi(x) = [\cos h(\lambda_1 x) - \cos(\lambda_2 x)] + B\left[senh(\lambda_1 x) - \frac{\lambda_1}{\lambda_2} sen(\lambda_2 x)\right], \tag{2.20}$$

where constant B is given by the expression,

$$B = \frac{-\lambda_2{}^2 cos(\lambda_2 L) - \lambda_1{}^2 \cos h(\lambda_1 L)}{\lambda_1 \lambda_2 sen(\lambda_2 L) + \lambda_1{}^2 senh(\lambda_1 L)}. \tag{2.21}$$

Thus, the expression (2.20) represents the vibration modes of the structure.

Equations 2.19 and 2.20 are used to analyze the effect of axial stress on the natural frequencies and vibration mode of a generic beam. Thus, in Figure 3 the variation of the first natural frequency is shown, w, as the load P increases. The values shown in the figure, in the vertical and horizontal directions, are normalized, for $wn1$ and by the critical load $Pcrit$, respectively. It can be noticed as the axial load increases, the frequency of the structure decreases, and when the equilibrium path approaches the bifurcation point ($P = Pcrit$), the frequency becomes zero.

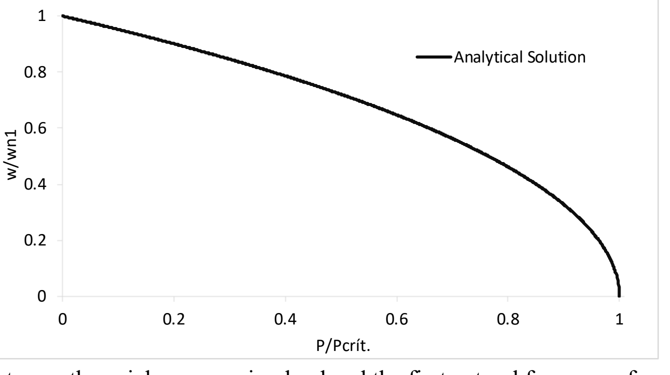

Figure 3. Relation between the axial compression load and the first natural frequency for a free-fixed column.

Figure 4 shows the first vibration mode of the column, normalized to the mass matrix, for different values of axial load. This figure shows the nodal displacement on the vertical axis at different points along the length of the column, x. The behaviors for five values of axial load P are shown, starting from the free vibration problem, $P = 0$, up to critical load $P = Pcrit$. Note that there is a change in the first vibration mode as the axial load is varied.

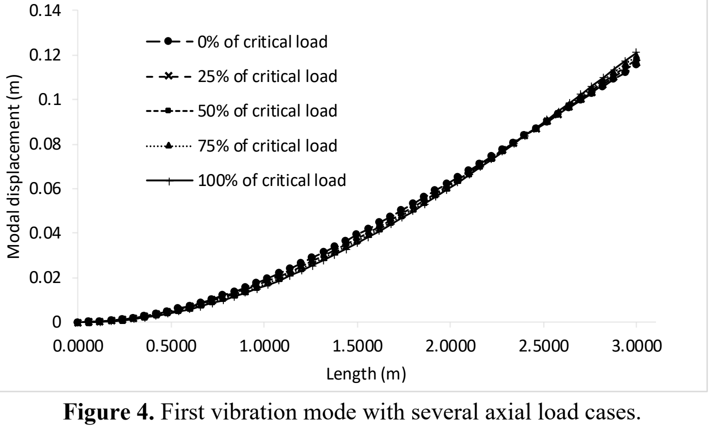

Figure 4. First vibration mode with several axial load cases.

2.2 Relationship between buckling mode and vibration mode in a free-fixed column

In this section a column will be analyzed, obtaining the first vibration mode for the critical buckling load and the first buckling mode, which will be compared to each other, showing the relationship between them. Initially, the first buckling mode will be analytically represented. Considering the column in Figure 2, the differential equation of deflection is given as,

$$\frac{p}{EI}\text{ä} = u(x)'' + \frac{P}{EI}u(x). \tag{2.22}$$

The solution of Equation 2.22 is,

$$u(x) = C_1 \sin\left(\sqrt{\frac{p}{EI}}x\right) + C_2 \cos\left(\sqrt{\frac{p}{EI}}x\right) + \text{ä}, \tag{2.23}$$

where C_1 and C_2 are integration constants and ä is the displacement at the top of the column. Considering the boundary conditions of the column the deflection curve is rewritten as

$$u(x) = \delta\left[1 - \cos\left(\sqrt{\frac{P}{EI}}x\right)\right]. \tag{2.24}$$

For the boundary condition to be satisfied $u(L) =$ ä, it is necessary that in Equation 2.24,

$$\delta \cos\left(\sqrt{\frac{P}{EI}}x\right) = 0. \tag{2.25}$$

The non-trivial solution of Equation 2.25 allows obtaining the critical buckling loads.

$$P_{cri} = \frac{(2\mathrm{n}-1)^2\pi^2 EI}{4L^2}. \tag{2.26}$$

Considering $P = P_{cri}$, the first buckling mode ($n = 1$) is written as,

$$u(x) = \delta\left[1 - \cos\left(\frac{\pi}{2L}x\right)\right]. \tag{2.27}$$

Now, with Equation 2.20 the first vibration mode will be found when the column is under the action of the first critical buckling load. When the axial load is equal to the critical load (P_{cri}), then $\beta^4 = 0$, which makes the first natural frequency equal to zero. With this result and considering Equation 2.6 it can be concluded that λ_1 is also equal to zero.

Substituting in Equation 2.8 the first critical buckling load, and considering Equation 2.17, it is shown that,

$$k = \lambda_2 = \frac{\pi}{2L}. \tag{2.28}$$

With the previous result, it is possible to find the first vibration mode by rewriting Equation 2.20, thus,

$$\Phi(x) = \left[1 - \cos\left(\frac{\pi}{2L}x\right)\right]. \tag{2.29}$$

Comparing the first buckling mode, Equation 2.27, with the first vibration mode at critical load, Equation 2.29, it is noted that the two equations are linearly dependent. This allows us to conclude that, in the case shown here, the first vibration mode in the critical load and the buckling mode are equivalent.

2.3 Modal analysis and linear-buckling analysis of a structure

In this section, the concepts described in sections 2.1 and 2.2 will be expanded to any reticular space structure.

2.3.1 Finite element model

The balance of the force of an element in the deformed condition is given by the following relationship [15],

$$\left[[K_e] + [K_g]\right]\{\delta_e\} = \{F_e\}, \tag{2.30}$$

where $[K_e]$ is elastic stiffness matrix, $[K_g]$ is the geometric matrix, $\{F_e\}$ is the nodal load vector of the element, $\{\delta_e\}$ is the nodal displacement vector $\{\delta_e\}$. In detail, the elastic stiffness matrix of the element is expressed as,

$$[K_e] = \int_0^L [B_e]^T [D][B_e]\, dx, \tag{2.31}$$

where $[B_e]$ represents a matrix containing the derivatives of the shape functions $[N_e]$ and $[D]$ describes the matrix material constitutive; $[K_g]$ the geometric matrix is given by,

$$[K_g] = \int_0^L P_\alpha [N'_e]\, [N'_e]\, dx\,; \tag{2.32}$$

Where P_α is the axial internal force, and finally, the vector $\{F_e\}$ is the nodal force vector of the element, it is written as,

$$\{F_e\} = \{F_n\} + \{F_{neq}\} \tag{2.33}$$

where $\{F_n\}$ is the nodal force vector applied directly to the nodes of the element $\{F_{neq}\}$ the equivalent nodal force vector due to distributed forces acting along of element.

2.3.2 Linear buckling analysis

In a buckling problem, internal axial loads are sought that cause the sum of the stiffness matrix and the geometric matrix to be a singular matrix [16], thus the problem is given by,

$$\left[[K_e] + \alpha[K_g]\right]\{\phi_{pn}\} = 0. \tag{2.34}$$

Equation 2.34 represents a homogeneous system of equations, which can be formulated as an eigenvalue problem. Where α are the eigenvalues and ϕ_p are the buckling modes. A load $\{F_e\}$ must be defined to estimate the geometric matrix that depends on the internal axial stresses. Following the definition of critical load, the magnitude of $\{F_e\}$ is not important since the critical load will be dimensioned by the load multipliers α.

2.3.3 Modal analysis

The modal analysis aims to obtain the response of the structure through vibration modes and frequencies [17]. In this way, it will be shown how these dynamic parameters are obtained when the geometrical matrix is included. Equation of motion can be written considering the geometrical matrix,

$$[M_e]\{\ddot{\delta_e}(t)\} + \left[[K_e] + [K_g]\right]\{\delta_e(t)\} = \{F_e(t)\}, \tag{2.35}$$

where $\{F_e(t)\}$ is the vector of nodal forces of the structure, $[M_e]$ is the mass matrix of the structure and $\{\delta_e(t)\}$ is the nodal displacement vector. Specifically, the mass matrix of the structure is given by,

$$[M_e] \; = -\left(\int_0^L \rho [N_e]^T [N_e] dx\right). \tag{2.36}$$

To study the natural vibration of the structure, the load vector applied to the structure must be null $\{F_e(t)\} = 0$ and it is assumed that the nodal displacements vector can be expressed as,

$$\{\delta_e(t)\} = \{A\} \sin(\omega t + \phi). \tag{2.37}$$

Considering Equation 2.37 and $\{F_e(t)\} = 0$, it is rewritten Equation 2.35 as,

$$\left([K_e] + [K_g] - \omega_{pn}^2 [M_e]\right)\{\widetilde{\phi_{pn}}\} = 0. \tag{2.38}$$

Equation 2.38 represents a homogeneous system of equations that can be represented as an eigenvalue problem. The eigenvalues ω_{pn} are the natural frequencies and ϕ_{pn} are the vibration modes of the structure. It can be noted that if the total stiffness matrix of the structure is singular $[K_e] + [K_g] = 0$, the natural frequency ω_{pn} of Equation 2.38 must be equal to zero.

The buckling problem shows that the total stiffness matrix is singular when the first critical buckling load is reached, therefore the buckling mode obtained for the first critical load $\{\phi_{pn}\}$ belongs to the vibration mode when the first natural frequency is equal to zero. Modal analysis can also be performed when the structure is completely unloaded, in which case the internal axial stresses in the elements do not exist and the geometric matrix is null, thus,

$$([K_e] - \omega_n^2 [M_e])\{\phi_n\} = 0, \tag{2.39}$$

where ϕ_n and ω_n are the vibration modes and natural frequencies for unloaded structure, respectively. It can be noted that the vibration modes of the structure vary between the vibration modes of the unloaded structure $\{\phi_n\}$ and the vibration modes of the structure when subjected to critical loading $\{\phi_{pn}\}$. By considering this aspect, in this work, it is proposed to approximate the vibration modes of the loaded structure $\{\widetilde{\phi_{pn}}\}$ from a simple linear interpolation between $\{\phi_n\}$ and $\{\phi_p\}$ in the following way,

$$\{\widetilde{\phi_{pn}}\} \approx \left(1 - \frac{\Delta}{\alpha}\right)\{\phi_n\} + \frac{\Delta}{\alpha}\{\phi_{pn}\}. \tag{2.40}$$

Where Δ is a parameter that indicates the internal load magnitude and varies between 0, when the structure is unloaded, and 1 when the structure is under the critical load. If the internal load is equal to the critical load, the vibration mode will be the buckling mode $\{\phi_{pn}\}$, while if the internal load is 0 then the vibration mode will be the vibration mode of unloaded structure $\{\phi_n\}$.

If both modes, ϕ_n and ϕ_{pn}, are normalized to the mass matrix, $\{\phi\}^T [M_e]\{\phi\} = 1$ and using the orthogonality property of vibration modes, the natural frequency of the loaded structure $\widetilde{\omega_{pn}}$ can be approximated, such as,

$$\widetilde{\omega_{pn}} \approx \sqrt{\{\widetilde{\phi_{pn}}\}^T \left[[K_e] + \Delta [K_g]\right]\{\widetilde{\phi_{pn}}\}}. \tag{2.41}$$

2.4 Static displacement from vibration modes and frequencies

Considering the dynamic equation of motion, static displacements can be calculated as a function of natural frequencies and vibration modes, as follows,

$$[M][\phi]\{\ddot{q}\} + [K_T][\phi]\{q\} = \{F_e\} \tag{2.42}$$

The displacements can be defined as a linear combination of modal displacements $\{q\}$, thus,

$$\{u\} = [\phi]\{q\}. \tag{2.43}$$

If the dynamic equation is pre-multiplied by $[\phi]^T$ and vibration modes are normalized to the mass matrix, n uncoupled motion equations for each vibration mode are obtained. Besides, for static loads, the acceleration vector is $\{\ddot{q}\} = 0$. In this way, the following equation is given by,

$$\begin{bmatrix} w^2{}_1 & \dots & 0 \\ \dots & \dots & \dots \\ 0 & \dots & w^2{}_n \end{bmatrix} \{q\} = [\phi]^T\{F_e\}. \tag{2.44}$$

Or n uncoupled equations,

$$q_1 = \frac{\{\phi_1\}^T\{F_e\}}{w^2{}_1}, \tag{2.45}$$

$$q_2 = \frac{\{\phi_2\}^T\{F_e\}}{w^2{}_2}, \tag{2.46}$$

$$q_n = \frac{\{\phi_n\}^T\{F_e\}}{w^2{}_n}. \tag{2.47}$$

Relating Equations 2.45-2.47 with Equation 2.43 can be obtained one equation capable of calculating the static displacements from the vibration modes and the natural frequencies of vibration:

$$\{u\} = \{\phi_1\}\frac{\{\phi_1\}^T\{F_e\}}{w^2{}_1} + \{\phi_2\}\frac{\{\phi_2\}^T\{F_e\}}{w^2{}_2} + \dots + \{\phi_n\}\frac{\{\phi_n\}^T\{F_e\}}{w^2{}_n}. \tag{2.48}$$

Considering the contribution of "n" vibration modes, the following formulation for the calculation of the static displacements is obtained,

$$\{u\} = \sum_{i=1}^{n}\{\phi_\mathrm{i}\}\frac{\{\phi_i\}^T\{F_e\}}{w^2{}_i}. \tag{2.49}$$

2.5 Modal p-delta analysis

It was shown through Equations 2.48 and 2.49 that it is possible to approximate the vibration modes and the natural frequencies of the loaded structure by interpolating the vibration modes between the state without axial load and the state with critical axial load. Therefore, it is possible to calculate the displacements of the structure for a determined load level using Equation 2.48 that depends on the vibration modes and natural frequencies. These displacements consider the effects of NLG. Based on these concepts, the method Modal P-delta is proposed, which uses modal and buckling analysis to perform a NLG analysis. This method allows us to obtain the behavior of the equilibrium path until the buckling of the structure occurs.

In this way, the basic routine for performing NLG analysis using the Modal P-delta method is described in Figure 5. The methodology is divided into two phases, pre-calculation, and calculation phase. In the first phase, some input parameters are determined and in the second, the displacements of the structure for each loading step are calculated.

In the first phase, the number of vibration modes “nmod” and the number of load steps “nstep” must be initially defined. After, the global stiffness matrix of the structure, the nodal force vector, and the global mass matrix of the structure must be calculated; the boundary conditions of the structure in all these parameters must be considered. With this, modal analysis can be performed to calculate the vibration modes of the unloaded structure $[\phi_n]$ and then calculate the geometric matrix $[K_g]$ by using the displacement due to external load $\{F_e\}$. With the geometric matrix can be performed a buckling analysis to calculate the buckling modes$\{\phi_{pn}\}$ and eigenvalues $\{\alpha\}$.

- Set the number of load steps, *nstep*.
- Set the number of vibration and buckling modes to use, *nmod*.
- Define the global stiffness matrix of the structure $[K_e]$ considering boundary conditions.
- Define nodal loads vector $\{F_e\}$, considering boundary conditions.
- Calculate the displacements for a first load delta, $\{F_{e1}\} = \frac{\{F_e\}}{nstep}$,
  $\{\delta T(:,1)\} = [K_e]^{-1}\{F_{e1}\}$.
- Define of the global mass matrix of the structure, considering boundary conditions$[M_e]$.
- Perform modal analysis to calculate the vibration modes of the unloaded structure $[\phi_n]$.
- Calculate the geometric matrix$[K_g]$ for load vector $\{F_e\}$.
- Perform buckling analysis to calculate buckling modes $[\phi_{pn}]$ and eigenvalues $\{\alpha\}$.
- For k=2:nstep
- Define the first displacement vector $\{\Delta\delta 1\} = \{0\}$

Calculate the approximate total stiffness matrix.

$$[K_T] = [K_e] + (k/nstep)[K_g]$$

For j=1:*nmod*

- Calculate the vibration mode of the loaded structure.

$$\{\widetilde{\phi_{pn}}\} = \left(1 - \frac{(k/nstep)}{\alpha(j)}\right)\{\phi_n(:,j)\} + \frac{(k/nstep)}{\alpha(j)}\{\phi_{pn}(:,j)\}$$

- Calculate the natural frequency for loaded structure.

$$\widetilde{\omega_{pn}} = \sqrt{\{\widetilde{\phi_{pn}}\}^T [K_T]\{\widetilde{\phi_{pn}}\}}$$

- Define the whole load vector $\{F_T\}$ to each load step.

$$\{F_T\} = \Delta\{F_{e1}\} = k/nstep\{F_{e1}\}$$

- Calculation of displacements.

$$\{\Delta\delta 2\} = \{\widetilde{\phi_{pn}}\}\left(\frac{\{\widetilde{\phi_{pn}}\}^T\{F_T\}}{\widetilde{\omega_{pn}}^2}\right)$$

End

Total displacement calculation in the load step.

$\{\delta T(:,i)\} = \{\Delta\delta 2\}$

End

Figure 5. Modal P-delta method, analysis routine.

The second phase begins with the definition of the total stiffness matrix of the structure that considers the contribution of the elastic matrix and the geometric matrix. The geometric matrix is considered to vary linearly between the unloaded case and the case of the fully-loaded structure, using the factor ($\Delta = k/nstep$), where k is the load step. For each load, the step must be calculated the following parameters: the vibration mode of the loaded structure using a linear interpolation between $\{\phi_n\}$ and $\{\phi_{pn}\}$ and the natural frequency for loaded structure. Thus, using Equation 2.48, the displacement in the current load step can be calculated. The previous procedure can be performed by adding various vibration and buckling modes, as shown in Figure 5.

3 RESULTS AND DISCUSSIONS

3.1 Analysis of a column

The purpose of this item is to use the proposed method, Modal P-delta, and apply it to a column as shown in Figure 2. The equilibrium path obtained with the Modal P-delta method will be compared with that obtained using the traditional iterative P-delta method [3]. Thus, the characteristics of the column are defined as: a length of $3\ m$, a cross-section of $0.04\ m^2$, a specific mass of $250\ kg/m3$, Young's modulus of $2.72 \times 10^{10}\ N/m^2$ and a moment of inertia equal to $0.000133\ m^4$. The number of load steps has been set as equal to 200 and there is a lateral load at the top of the element of $10\ kN$. The total axial load applied was $994.27\ kN$ which corresponds to the critical buckling load of the element. For numerical analysis, the discretized model was defined with 20 elements.

Figure 6 shows the displacements at the top of the column, using the iterative P-delta methods and the proposed method – varying the number of vibration and buckling modes. A simple analysis of this figure shows a total agreement between the results obtained with the delta-P method and the results obtained with the modal P-delta even when there is a variation in the amount of vibration and buckling modes. Additionally, it is important to report that the P-delta analysis demonstrated a computational processing time is approximately the tenth part of time spent by the traditional method. All analysis were developed on a computer with AMD Ryzen 7 1700 Eight-Core processor 3.00GHz, physical memory (RAM) 16 GB.

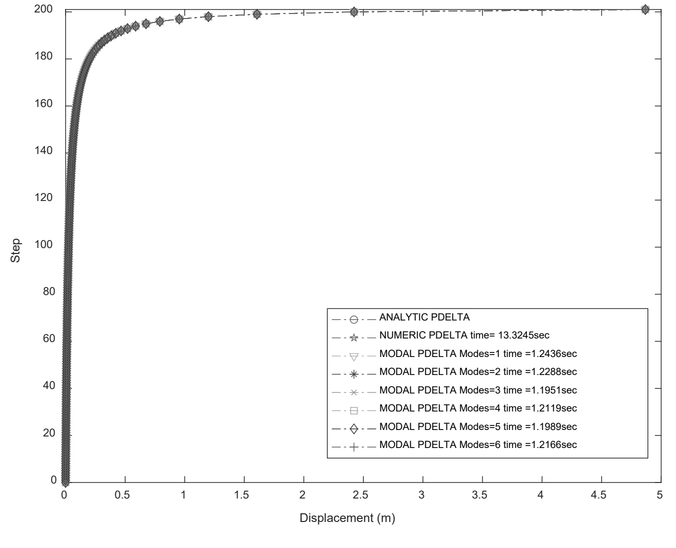

Figure 6. Relationship between Analytic P-Delta analysis and Modal P-Delta analysis - free-fixed column.

Figure 7 shows the error of the Modal P-delta method, taking as reference the analytic P-delta analysis, which formulation is in the Appendix A. The error consists of a difference between the displacements of the two methods. In the results of the modal P-delta method, the number of vibration and buckling modes was varied between 1 and 6 modes. The analysis of the error shows that, while is increasing the number of modes used, the error tends to decrease for the first load cases and converge to a constant value in the last ones, to this test the maximum average error is around 0.0002143m in the last case of load.

In general, it is noted that to the first load steps, the resulting error is less as the number of used modes increases, but to the last load steps, the increasing the number of modes makes the increasing of amount of error, which tends to be a constant value. However, despite the existence of error in the calculation of displacements in all situations, all of these are considered minimal, in the order of 1×10^{-4} m.

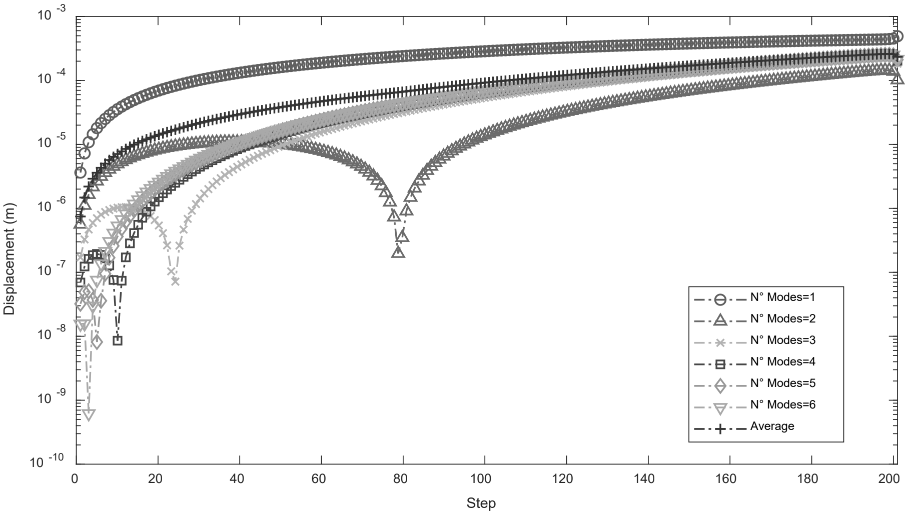

Figure 7. Error regarding the number of Modal P-Delta modes - free-fixed column.

3.2 Analysis of a plane frame

In this item, it is shown the applicability of the proposed modal P-delta method in a plane frame structure. The results were compared to the traditional iterative P-delta method.

Two analyses were performed on the same model, performing a modification of the external loads. The plane frame uses the properties shown in Table 1. The number of load steps used was equal to 200. The first type of applied loading, called test 01, were applied axial loads at the top in each of the columns P01, P02, and P03 with a load equal to 0.28, 0.5, and 0.28 of the calculated critical load of $8.215\times10^{7}\ N$, respectively. In test 01 there is also a lateral load of $100\ kN$, as shown in Figure 8.

Table 1 Properties of the plane frame

	Column P01	Column – P02	Column – P03	Beams (V01 – V09)	Beams (V10 – V19)
Lenght (m)	25.75	25.75	25.75	4.74	3.73
Young´s Module (N/m^2)	2.72E+10	2.72E+10	2.72E+10	2.72E+10	2.72E+10
Cross-Section (m^2)	0.1	0.1	0.1	0.12	0.12
Moment of inertia (m^4)	0.00208	0.00208	0.00208	0.00360	0.00360
Specific mass ? (kg/m^2)	250	250	250	300	300

Test 02 was generated with vertical loads distributed in the floor beams and lateral loads on each of the floors, the loads are shown in Figure 8. The loads are amplified with a multiplier factor of 10.5, to bring the structure to a condition of critical buckling loading.

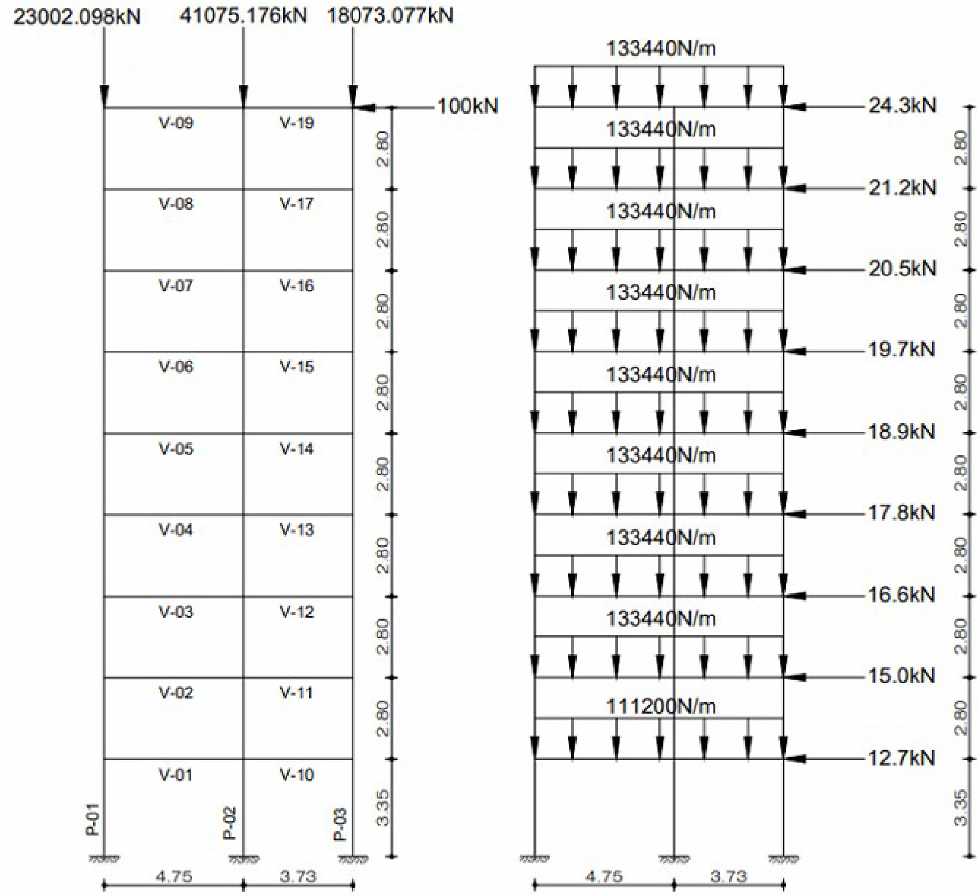

Figure 8. Test 01 (left) and Test 02 (Right) – Plane frame.

In both tests, the equilibrium path was constructed extracting the displacements at the top of the P03 column, with the P-delta and Modal P-delta methods. In the case of the Modal P-delta method, the number of vibration and buckling modes used was varied. The results of the analyses in both load tests are presented in Figures 9 and 10. In these figures, it can be noted that comparatively there are minimal differences between the use of P-delta and Modal P-delta.

In Figures 9 and 10, the calculation times of both load tests with p-delta and modal p-delta methodologies are also reported, where is possible to notice the considerable time reduction of the computational calculations using the proposed method opposite to the traditional P-delta method.

It is important to say that the calculation times for the iterative P-delta method have been verified in commercial computational software such as SAP-2000©, having a consideration that, the number of elements of discretization in each model tested with the proposed methodology was the same used in a verification with a software SAP-2000, which were 2 elements for the columns and beams. This verification shows calculation times like or greater than those shown with our computational code. These notable computational calculation time differences between P-delta and the proposed method are due to which the traditional P-delta method calculates an inverse of the global stiffness matrix to calculate the displacements at each load step or uses some optimization method. In contrast, the proposed method performs a single-time modal and buckling analysis for calculating displacements in each load step, the rest of the calculation procedures are simple multiplications and sums of vectors with no iterations.

Figures 11 and 12 shown the error of the P-delta modal analysis, considering as reference the iterative P-delta method. It can be noted, as in the case of the column, the error between the two methodologies is minor to the first steps loads also as the number of vibration modes are increased in the calculation, the error tends to converge to a constant value, to the test 01 the maximum relative error is around 0.02447m and to the test 02 the maximum relative error is around 0.071864m, and these values are almost the same from using 4 modes onwards, for both tests. However, for all situations of the number of vibration modes the maximum relative error was $1 \times 10^{-2}\ m$.

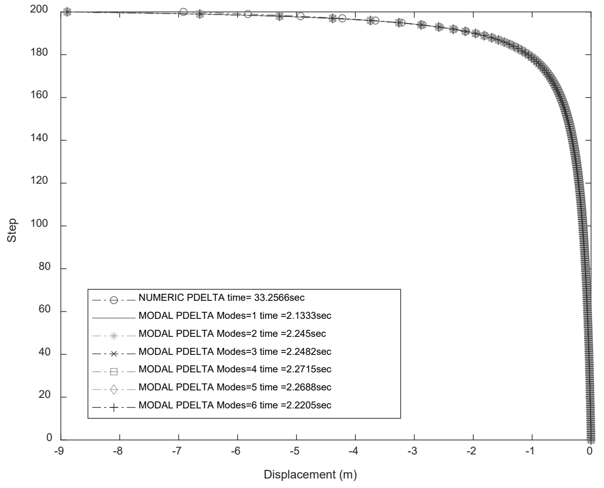

Figure 9. P-Delta analysis and Modal P-Delta analysis – test 01.

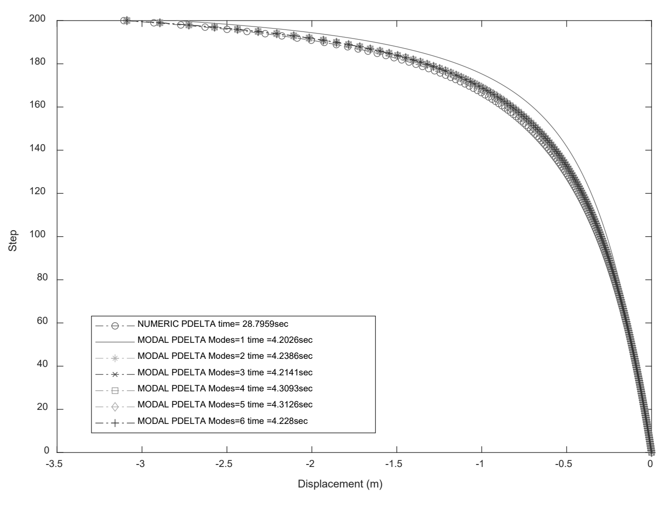

Figure 10. P-Delta analysis and Modal P-Delta analysis – test 02.

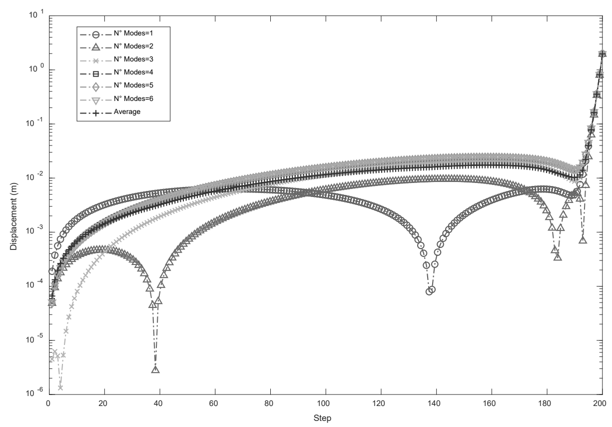

Figure 11. Error regarding the number of modal P-Delta modes – test 01.

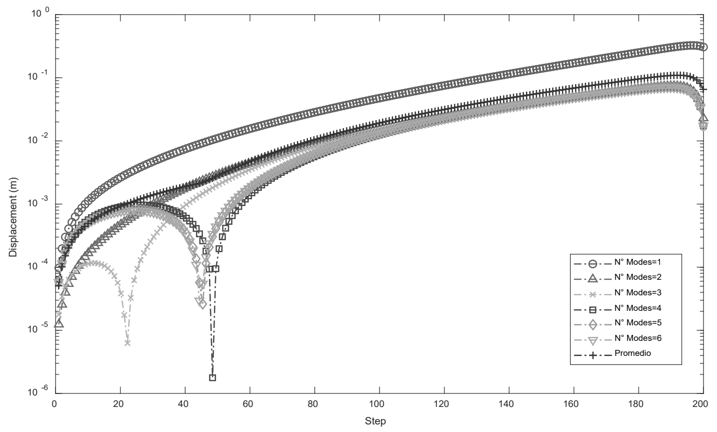

Figure 12. Error regarding the number of modal P-Delta modes – test 02.

As seen in the Figures 11 and 12, the first two or three vibration modes have a direct and rapid influence on the error reduction, however it is not yet clear the ideal number of vibration modes to use. Because the results show that with considering the first modes, the method proves to be efficient, with low error values, but when higher modes are added, the proposed method shows a relative stabilization of the error, without improvement, which allows conclude that the methodology cannot converge the error to zero with an increase in the number of vibration modes. This characteristic of the error is due to the approximation performed by the interpolation of the vibration modes (structure without load and at critical load) to establish the displacements of the structure. It is assumed that this interpolation has an intrinsic error in the interpolation of each vibration mode. It is necessary in future research with different structural problems to check the error behavior for different modes and try to understand what error is produced in the interpolation of the higher modes after the first load step. Another characteristic seen in the error graphs is the increase in error as the number of steps increases. This may be since in the upper steps there is an accumulation of error from the previous steps.

Finally, it is important to highlight that to make the interpolation of vibration modes and buckling modes, it is necessary to identify longitudinal modes which will be omitted in the calculation due these do not contribute to the lateral displacements. The identification of the longitudinal vibration modes was performed using the intensities of the amplitudes of the vibration modes, considering as a condition that the absolute value of the amplitudes of the transverse vibration modes are close to zero.

4 CONCLUSIONS

This paper describes a new methodology – Modal P-delta – for NLG analysis of structures. This method considers the relationship between dynamic parameters (vibration modes and natural frequencies) and geometrical NL effects. It has been shown that the vibration mode in the critical buckling load and the buckling mode are linearly dependent. In this way, the vibration modes of the loaded structure were approximated by performing a linear interpolation of vibration modes between these two states of load, without and critical buckling load. Furthermore, the natural frequencies were approximated using the orthogonal properties of the approximate vibration modes of the loaded structure. With the approximate vibration modes and frequencies of the loaded structure, NL displacements were calculated.

Several examples were simulated on regular structures in the plane, showing the effectiveness of the proposed method. A column and a plane frame with two load cases were used to build the pre-buckling equilibrium path. Compared with the traditional iterative P-delta method, the results showed maximum errors in the order of $1 \times 10^{-2}\ m$ for the frames and $1 \times 10^{-4}\ m$ for the column analyzed. The Modal P-delta method allowed adding a certain number of vibration modes in the analyses and it was found that in the cases analyzed, while major will be the number of modes used, the error will tend to be a constant value, in this way using a maximum of six vibration modes is enough to obtain satisfactory results. Therefore, the use of higher vibration modes in the analyzed cases does not result in an error reduction.

The proposed method can be classified as a direct method since it approximates the displacements without an iterative process. Therefore, a relevant feature of the proposed methodology, compared to the traditional iterative P-delta method, is the reduction of computational time. In the different simulations it is showed a great reduction in the computational time. This is due to a drastic reduction in complex calculations that uses the iterative P-delta method at each loading step to obtain the displacement, such as the inverse of matrices or optimization methods (e.g., Newton-Raphson).

The efficiency of the modal P-delta method in irregular three-dimensional structures will be tested shortly. These future analyses will aim to understand the behavior of the method when the superior vibration and buckling modes have a greater influence on the displacements. Another interesting idea would be to analyze the computational time testing the proposed methodology in larger dynamical NL problems.

ACKNOWLEDGE

This work was conducted with the economic support of the Social Demand Program – UNILA, Strict Sense Postgraduate Scholarships.

REFERENCES

[1] A. Rutenberg, "A direct p-delta analysis using standard plane frame computer programs," *Comput. Struc.*, vol. 14, no. 1–2, pp. 97–102, 1981.

[2] H. Singh and G. M. Singh, "Non-linear analysis of frames," *Comput. Struc.*, vol. 44, no. 6, pp. 1377–1379, Sep 1992, http://dx.doi.org/10.1016/0045-7949(92)90379-E.

[3] E. L. Wilson and A. Habibullah, "Static and dynamic analysis of multi-story buildings, including P-delta effects," *Earthq. Spectra*, vol. 3, no. 2, pp. 289–298, 1987.

[4] W. J. LeMessurier, "Practical method of second order analysis. Part I and II," *Eng. J. AISC*, vol. 4, no. 2, pp. 49–67, 1976.

[5] D. W. White, A. E. Surovek, and C.-J. Chang, "Direct analysis and design using amplified first-order analysis. Part 2 – moment frames and general rectangular framing systems," *Eng. J.*, vol. 44, no. 4, pp. 323–340, 2007.

[6] B. R. Gaiotti and S. Smith, "P-delta analysis of building structures," *J. Struct. Eng.*, vol. 115, no. 4, pp. 755–770, 1989.

[7] M. Rezaiee-Pajand, M. Ghalishooyan, and M. Salehi-Ahmadabad, "Comprehensive evaluation of structural geometrical nonlinear solution techniques part I: formulation and characteristics of the methods," *Struct. Eng. Mech.*, vol. 48, no. 6, pp. 849–878, 2013, http://dx.doi.org/10.12989/sem.2013.48.6.849.

[8] M. Rezaiee-Pajand, M. Ghalishooyan, and M. Salehi-Ahmadabad, "Comprehensive evaluation of structural geometrical nonlinear solution techniques. Part II: comparing efficiencies of the methods," *Struct. Eng. Mech.*, vol. 48, no. 6, pp. 879–914, 2013, http://dx.doi.org/10.12989/sem.2013.48.6.879.

[9] J. Valle, D. Fernández, and J. Madrenas, "Closed-form equation for natural frequencies of beams under full range of axial loads modeled with a spring-mass system," *Int. J. Mech. Sci.*, vol. 153–154, pp. 380–390, Apr 2019, http://dx.doi.org/10.1016/j.ijmecsci.2019.02.014.

[10] A. Bokaian, "Natural frequencies of beams under tensile axial loads," *J. Sound Vibrat.*, vol. 142, no. 3, pp. 481–498, Nov 1990, http://dx.doi.org/10.1016/0022-460X(90)90663-K.

[11] D. E. Statler, R. D. Ziemian, and L. E. Robertson, "The natural period as an indicator of second-order effects," in *Proc. Struct. Stab. Res. Counc. Annu. Stab. Conf. 2011, ASC*, 2011, pp. 136–147.

[12] D. G. Reis, G. H. Siqueira, L. C. M. Vieira Jr., and R. D. Ziemian, "Simplified approach based on the natural period of vibration for considering second-order effects on reinforced concrete frames," *Int. J. Struct. Stab. Dyn.*, vol. 18, no. 5, pp. 1850074, 2018, http://dx.doi.org/10.1142/S0219455418500748.

[13] F. F. Leitão, G. H. Siqueira, L. C. M. Vieira Jr., and S. J. C. Almeida, "Analysis of the global second-order effects on irregular reinforced concrete structures using the natural period of vibration," *Rev. IBRACON Estrut. Mater.*, vol. 12, no. 2, pp. 408–428, 2019, http://dx.doi.org/10.1590/s1983-41952019000200012.

[14] F. J. Shaker, *Effect of Axial Load on Mode Shapes and Frequencies of Beams*. Washington: NASA, 1975.

[15] T. J. R. Hughes, *The Finite Element Method: Linear Static and Dynamic Finite Element Analysis.* New York: Dover Publ. Inc., 2000.

[16] J. Hutchinson and W. Koiter, "Postbuckling theory," *Appl. Mech. Rev.*, vol. 23, no. 12, pp. 1353–1366, 1970.

[17] M. Paz, *Structural Dynamics: Theory and Computation.* Cham: Springer, 2012.

Author contributions: IDGA: Supervision, Conceptualization, Formal analysis, Investigation, Numerical tests, Writing. WAF: Formal analysis, Investigation, Numerical tests, Writing. JRCDLC: Formal analysis, Investigation, Numerical tests, Writing. JAGS: Supervision, Formal analysis, Investigation, Numerical tests, Writing.

Editors: Mauro de Vasconcellos Real, Guilherme Aris Parsekian.

APPENDIX A

ANALYTIC SOLUTION ANALYSIS P-DELTA FOR A COLUMN

Considering the compressed column as shown in Figure 1A-a, and considering the equilibrium equation in relation to the fixed support (Figure 1A-b), that is:

$$M(x) = F(L-x) + P\delta - Pu(x) + p\frac{x^2}{2} - pLx + p\frac{L^2}{2} + M \tag{A.1}$$

We can obtain a differential equation of simplified equilibrium using the relation between the curvature and the bending moment:

$$\frac{EI\partial^2 u(L,t)}{\partial x^2} + Pu(x) = F(L-x) + P\delta + p\frac{x^2}{2} - pLx + p\frac{L^2}{2} + M \tag{A.2}$$

With the boundary conditions of the element shown in Figure 3, applying the Laplace transform in Equation A2 and showing u (s), we obtain:

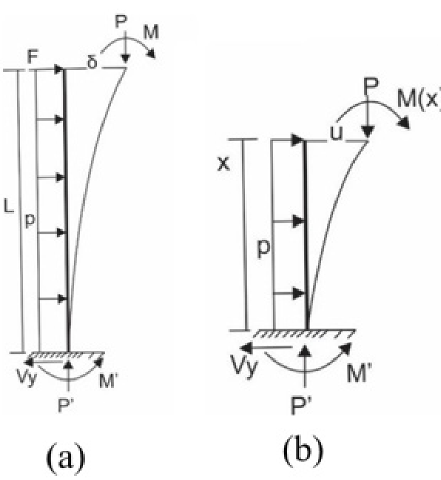

Figure 1A: (a) Representation of the free-fixed column in the undisturbed condition (b) deformed condition of the free-fixed column

$$\boldsymbol{u(s)} = \frac{z^2\left(\frac{L}{s}-\frac{1}{s^2}\right)}{(s^2+k^2)} + \frac{k^2\delta\frac{1}{s}}{(s^2+k^2)} + \frac{d^2\left(\frac{L^2}{2s}-\frac{L}{s^2}+\frac{1}{s^3}\right)}{(s^2+k^2)} + \frac{\frac{j^2}{s}}{(s^2+k^2)} \tag{A.3}$$

where:

$$z^2 = \frac{F}{EI}\ ; k^2 = \frac{P}{EI}\ ;\ d^2 = \frac{p}{EI}\ ;\ j^2 = \frac{M}{EI} \tag{A.4}$$

The solution of this equation is given by applying the inverse Laplace transform. Being plot A related to lateral load F, plot B to top displacement, plot C to M' and plot D to load p, the equation of lateral deflection of a compressed bar in plots is defined:

$$A(x) = z^2\frac{kL-kx+sen(kx)-kLcos(kx)}{k^3} \tag{A.5}$$

$$B(x) = \delta[1 - cos(kx)] \tag{A.6}$$

$$C(x) = -\frac{1}{2}d^2\,\frac{(-k^2)L^2 + 2 + 2Lxk^2 - x^2k^2 + k^2L^2\,cos(kx) - 2\,cos(kx) - 2Lksen(kx)}{k^4} \tag{A.7}$$

$$D(x) = (-j^2)\,\frac{(-1) + cos\,(kx)}{k^2} \tag{A.8}$$

$$u(x) = A(x) + B(x) + C(x) + D(x) \tag{A.9}$$

To obtain δ from Equation A.5 it is necessary to evaluate at x = L, considering that at x = L the value of u (L) must be equal to δ, thus obtaining the value of the same. However, to obtain the value of δ, an optimization method is necessary, considering that the equation is nonlinear.

$$u(L) = \delta = A(L) + B(L) + C(L) + D(L) \tag{A.10}$$

IBRACON Structures and Materials Journal
Revista IBRACON de Estruturas e Materiais
ISSN 1983-4195 ismj.org

ORIGINAL ARTICLE

Effect of prehydration of Portland cement on the superplasticizer consumption and the impact on the rheological properties and chemical reaction

Efeito da pré-hidratação do cimento Portland no consumo de superplastificante e o impacto nas propriedades reológicas e na reação química

Danila Fabiane Ferraz[a]
Ariane Carolina Rodrigues Martho[a]
Elizabeth Gertrude Burns[b]
Roberto Cesar de Oliveira Romano[c]
Rafael Giuliano Pileggi[c]

[a]GCP Applied Technologies, Sorocaba, SP, Brasil
[b]GCP Applied Technologies, Cambridge, MA, United States
[c]Universidade de São Paulo – USP, Escola de Engenharia, Departamento de Engenharia Civil, São Paulo, SP, Brasil

Received 13 September 2021
Accepted 20 August 2022

Abstract: The use of pre-hydrated cement in formulation of mortar and concrete is common because there is not always effective control on the cement production, grinding, transportation and subsequent storage. This paper presents a case study on the optimization of admixture for use with prehydrated cement by assessing changes in the rheological properties of Portland cement artificially pre-hydrated. The cement was artificially pre-hydrated by exposure to relative humidity (RHs) of 90%, in an environment of NH_4Cl saturated solution. Additionally, the cement pastes were evaluated with and without superplasticizer. Stepped flow test using a parallel-plate geometry was the method choose to evaluate the rheological behavior, apparent viscosity, yield stress and hysteresis area of each paste at the early age. Oscillatory rheometry was conducted to evaluate the storage modulus (G'), comparing the consolidation with the hydration kinetics obtained by calorimetric evaluation of the same suspensions. Initial rheometer results indicate that the pre-hydrated sample presents lower level of shear stress than the reference sample, because of the higher reactivity of the non-pre-hydrated sample.

Keywords: Portland cement, prehydration, chemical reaction, rheology, superplasticizer.

Resumo: A utilização de cimento pré-hidratado na formulação de argamassas e concretos é comum, pois nem sempre há um controle efetivo na produção do cimento, moagem, transporte e posterior armazenamento. Este trabalho apresenta um estudo de caso sobre a otimização de aditivo para uso com cimento pré-hidratado, avaliando as mudanças nas propriedades reológicas do cimento Portland pré-hidratado artificialmente. O cimento foi pré-hidratado artificialmente por exposição à umidade relativa (URs) de 90%, em ambiente de solução saturada de NH4Cl. Adicionalmente, as pastas de cimento foram avaliadas com e sem superplastificante. O teste de fluxo escalonado usando uma geometria de placas paralelas foi o método escolhido para avaliar o comportamento reológico, viscosidade aparente, tensão de escoamento e área de histerese de cada pasta em idade precoce. A reometria oscilatória foi realizada para avaliar o módulo de armazenamento (G'), comparando a consolidação com a cinética de hidratação obtida pela avaliação calorimétrica das mesmas suspensões. Os resultados iniciais do reômetro indicam que a amostra pré-hidratada apresenta menor nível de tensão de cisalhamento do que a amostra de referência, devido à maior reatividade da amostra não pré-hidratada.

Palavras-chave: cimento Portland, pré-hidratação, reação química, reologia, superplastificante.

Corresponding author: Danila Fabiane Ferraz. E-mail: Danila.f.ferraz@gcpat.com
Financial support: None.
Conflict of interest: Nothing to declare.
Data Availability: The data that support the findings of this study are available from the corresponding author, DFF, upon reasonable request.

How to cite: D. F. Ferraz, A. C. R. Martho, E. G. Burns, R. C. O. Romano, and R. G. Pileggi, "Effect of prehydration of Portland cement on the superplasticizer consumption and the impact on the rheological properties and chemical reaction," *Rev. IBRACON Estrut. Mater.*, vol. 16, no. 2, e16210, 2023, https://doi.org/10.1590/S1983-41952023000200010

1 INTRODUCTION

Cement prehydration is the inadvertent reaction of anhydrous cement with water, causing the partial hydration of the particle cement surface [1]. The prehydration of the cement includes the physical adsorption of water on the cement particle and the chemical reaction to form hydration products such as calcium silicate hydrate, portlandite, gypsum, ettringite and syngenite [2]. Among these ettringite and syngenite are preferably formed [3].

Many factors affect the degree of cement pre-hydration, for example temperature, relative humidity (RH), time of exposure and particle fineness [4] and prehydration can occur during the cement manufacture, transportation or storage of cement [5], [6].

The cement surface hydration can also occur during the manufacture as a consequence of the dehydration of gypsum during the grinding process in the cement mill. In addition, some producers add water into the ball mill in order to keep the temperature of the mill feed below 115ºC or add into the vertical mill to stabilize it [4]. Prehydration of cement due to gypsum dehydration may also occur during the transportation and storage.

Cements tend to sorb different quantities of water vapor depending on their phase compositions, according to [4], cements containing high levels of free lime, orthorhombic C_3A and ß-$CaSO_4.1/2H_2O$ are more sensitive to moisture.

In practice, pre-hydrated cements tend to show adverse effects on the engineering properties of cement and concrete, affecting at different levels the reactivity of each phase of hydration [4], [5] These effects include compressive strength reduction, decreased workability, open-time and setting time. According to [2], cement prehydration, measured as "corrected loss-on-ignition, (Wk)" values above 0.3% can significantly reduce compressive strength.

The changes at the cement particle due to prehydration can also affect the admixtures performance [4]. Depending of the composition of the admixtures the effects are different, for example, in one study using superplasticizer the rheological measurements of cement suspensions revealed better performance with the pre-hydrated cement than with the fresh cement [3], [7]. However, the best efficiency of each admixture depends on the synergy with the cement used in the concrete formulation since each binder is produced with distinct physical, chemical, mineralogical and surface characteristics.

The desired performance for each admixture depends on the mixing demand, transport application, workability and the stability of workability with time. In some cases, there is a need for greater workability without the need for stability over time and in other cases the opposite result is adequate [7]. Therefore, for each scenario, the appropriate evaluation of the parameters and the rheological profile of each cement composition in association with the specific admixtures is extremely important. This work seeks to add to the limited body of work discussing such interactions.

1.1 Dispersing agents (Superplasticizers)

Water-reducing admixtures for concrete are chemicals that are intentionally added to the concrete to modify concrete to suit specific applications [7]. Typical admixtures are superplasticizers, that is, they have dispersion properties, either by electrostatic effect or by electro-steric effect, and this dispersion releases trapped water allowing the mixture to flow.

Generally, the use of such chemical admixtures promotes the increase of final strength in the concrete by reducing water, improves slump retention, and in some cases, when the composition is carefully balanced, increases the initial strength. Currently, the most efficient admixtures for this purpose are the third-generation superplasticizers, generally formulated based on polycarboxylate or polyacrylate [8].

In this work, two types of polycarboxylate base dispersants were used to obtain the desired rheological properties as shown in Figure 1. The variation of the polycarboxylate content influences directly the rheological properties of the mix [3]. The increase of the admixture content in the viscosity, the shear stress and the hysteresis area (area inscribed between the stress curves vs. rate) are reduced, showing the dispersion capacity of the admixture.

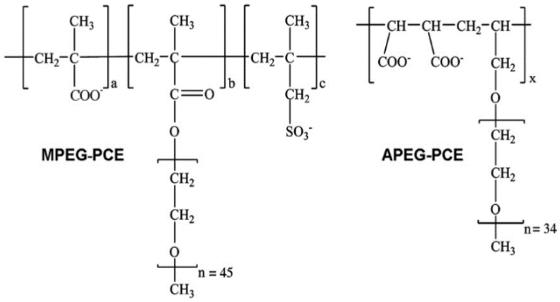

Figure 1. Structure of the chemical composition in the comb polymer of a sodium polycarboxylate molecule: PCE-methacrylic to the left and PCE of allylic ether to the right [8].

The mode of action of the polycarboxylates is based on the dispersion of the cement particles by electro-steric effect. The main chain of the admixture has anionic charges that are attracted by the positive charges present on the surface of the cement at the beginning of the hydration. The chain is deposited/adsorbed on the cement surface, while the side chains are extended from the surface, pushing the particles apart. Different dispersion efficiencies are obtained from the use of the different types of polymers and are dependent on the type of cement. After the cement particles are dispersed, hydration products begin to grow, and the polycarboxylate polymers are covered up and entrapped.

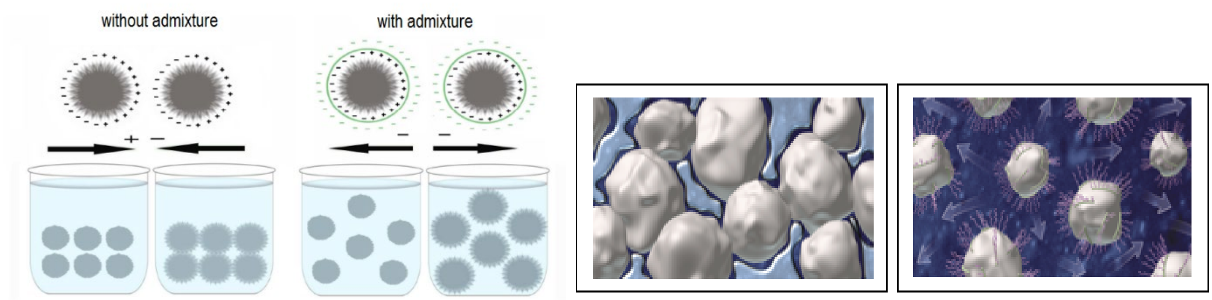

Figure 2. Simulation of cement particles dispersion electrostatic effect (left) and polycarboxylate adsorption (right). GCP Applied Technologies rights.

Cement particles have a natural tendency to agglomerate when mixed with water due to their polarity and Van Der Waals attraction force between these cement particles. Water is entrapped between them reducing the flowability of the concrete [9]. With the use of dispersing agents, the cement particles are deflocculated and dispersed, releasing the water and increasing the fluidity of the concrete (Figure 2). Since the cement particles cannot approach one another, the energy required to induce the flow in the system is reduced. The dispersed cement also lubricates the aggregates of the concrete mix, further improving the pumpability. Dispersed particles disturb the flow less than the agglomerated particles, so the water is free to hydrate the surface of the cement and fluidize the mixture [7].

The variation of the admixture content also results in alteration of the properties of the concrete under flow which affects the transport and the application of the concrete [8]. In addition, the amount of water in the system is reduced considerably which generates a dense, less permeable matrix, enhancing the durability of the concrete. In the experiments below, superplasticizer content is systematically increased, the time of the concrete flow is reduced until the saturation point is reached, this point being considered as the *optimum content* [10]. In the conditions of this study, this optimum content varies according to the physical, chemical and mineralogical composition of each cement using the same admixture; in addition, polymer type, water-to-solids ratio, and other variables can alter the flow of concrete, many studies are necessary to conclusively define the optimum type and content of each admixture for a particular cement [10].

1.2 Portland cement and admixtures interactions

The rheological properties of the concrete are modified by the interaction of cement and admixtures [10]. Other factors such as mode and time of addition of the admixture or water/cement ratio may also affect the performance of the concrete in the fresh state [10].

Among properties of the cement, surface area, particle size and porosity, prehydration and chemical/mineralogical composition are factors that affect rheological properties and hydration kinetics of the paste [11]. The chemical nature of each cement influences the interaction with superplasticizer mainly in the fresh state [12]. Other factors such as alkali-soluble sulfate content, admixture addition time (normal or delayed addition) [12], and temperature of the concrete, influence the hydration process of cement mixtures and many of them have a synergistic effect [12]. The structure of each polycarboxylate polymer also influences the hydration of cement, with the length of the main and lateral chain of each molecule of polycarboxylate, and molecular weight, being important parameters. To understand the system, it is important to study the cement-admixture “pairs” [10].

The superplasticizers react with the cement particle and interfere with the hydration in the early stages, either in the nucleation process, hydration reaction rate or both [10], [13]. Because of the strong interaction with the various mineral phases of the cement, the admixture interferes in several phenomena. The SO_4^{-2} ions added intentionally in the cement manufacture act as hydration controllers reacting with the aluminate phases preferentially, and the polynaphthalene sulfonate base admixture or polycarboxylate also have higher affinity for the aluminate phases, competing with the sulfates for surface area on the aluminate phases [14]. Moreover, the PCE can intercalate on hydration compounds formation by different mechanisms, it can explain the distinct content of the same admixture on pre-hydrated and non-pre-hydrated mixes. The undersulfated systems allows the PCE intercalation, where the quick soluble sulphate to stoichiometrically transform all the C_3A into AFm and Aft [13], [11].

Studies have shown that the prehydration directly affects the fluidity of the concrete in the presence of polycarboxylate, since the cement particle size is reduced by the formation of hydration products, increasing the specific area of the cement [13], [11]. Some problems such as rapid loss of workability or increased rigidity, excessive delay or pumping difficulties are common when there is incompatibility between cement and admixture[11]. Studies have shown that polycarboxylate are better compatible with different types of cement, and cement / admixture compatibility is more affected by the amounts of alkali sulphates in the cement [13]. However, these studies have not included the detailed rheological studies described here.

The multiphase characteristics of the cement and its hydration products are essential factors for the affinity of the organic admixtures however, undesirable side effects can be seen during the preparation of the concrete in the fresh state [13], [11]. If not studied and compensated for, the interaction between cement–admixture these side effects can adversely affect the final performance [11]. The particle size also influences admixture interaction; the smaller the particle size of cement or larger the specific area higher the amount of admixture to obtain the same dispersion of a bigger particle [13]. Modifications in the admixture addition time also affect the rheological properties of the concrete. Delayed addition leads to a reduction in the heterogeneous adsorption of the system, so the admixture is more adsorbed by the alite [12].

For all the reasons cited above, it is important that new admixtures are constantly developed, improving the interaction with the cement, anticipating the interaction problems and correcting them with the adjustment of specific admixtures for each type of cement. This will allow optimization of the content, avoiding waste which brings both economic and environmental benefits.

2 MATERIALS

The cement chosen to carry out this work is a CPV-ARI according to the Brazilian standard, collected directly at the cement plant, and was named in this work as a *non-pre-hydrated*. This is the Brazilian cement with lower content of additions and is like to the CEM I cement defined in the European standard EN 197–1, which is also called OPC (ordinary Portland cement) in the technical-scientific literature.

A polycarboxylate-base admixture containing 2 types of polymers blended, as shown in Figure 1 was the superplasticizer adopted to evaluate the changes when the system is dispersed.

3 METHODS

3.1 Cement characterization

Particle size distribution: equipment used: Malvern Instruments model Mastersizer 2000/2000E. The test was performed wet, in absolute ethyl alcohol.

X-ray fluorescence: according to ISO/FDIS 29581-2:2009 (E) - equipment used: Panalytical model Minipal Cement, from melt pellets on a Claisse model M4 melting machine using melt-based lithium tetraborate / lithium metaborate mixtures MAXXIFLUX (66.67% Li_2B4O_7, 32.83% $LiBO_2$ and 0.50% LiBr), with a ratio of 1g of sample), 6.75g of flux.

X-ray diffraction: according to [15] - equipment used: Rigaku model Windmax 1000, operating on copper Kα radiation with 40kV - 20mA and scanning of 2°/min. Identification of the compounds was performed using Panalytical X-pert High Score Plus software (version 3.0) and diffraction patterns provided by the International Center for Diffraction Data (ICDD).

The Figure 3 presents the particle size distribution of each sample, Table 1 shows the chemical species of the binders, obtained by X-ray fluorescence, and Table 2 illustrates the mineralogical composition.

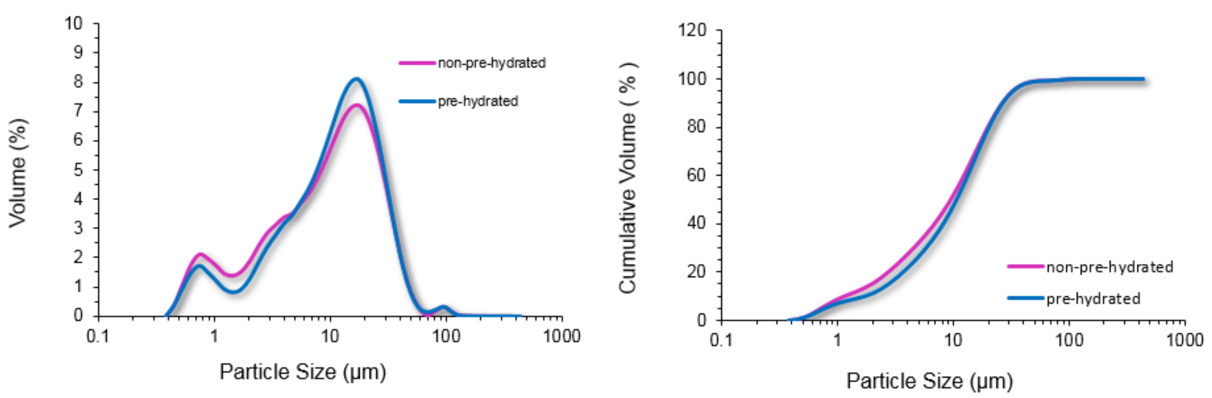

Figure 3. Left: Particle size distribution of the cement samples Right: Cumulative particle size distribution.

Table 1. Chemical composition by X-ray fluorescence.

Analyte, %	Non-pre-hydrated	Pre-hydrated	Standard 16697-2018 Requirements
Loss on ignition – LOI	2.19	3.50	≤ 6.5
Silicic Anhydride (SiO_2)	18.5	18.3	-
Aluminum oxide (Al_2O_3)	3.99	3.93	-
Ferric oxide (Fe_2O_3)	2.71	0.68	-
Calcium oxide (CaO)	61.1	61.5	-
Magnesium oxide (MgO)	5.82	5.83	≤ 6.5
Sulfuric anhydride (SO_3)	3.31	3.28	≤ 4.5
Potassium oxide (K_2O)	1.17	1.15	-
Titanium oxide (TiO_2)	0.22	0.21	-
Manganese oxide (Mn_2O_3)	0.10	0.10	-
Strontium oxide (SrO)	0.07	0.07	-
Phosphorus oxide (P_2O_5)	0.17	0.18	-
Others	2.84	3.77	-

Table 2. Mineralogical composition calculated by Rietveld refinement using the data of X-ray diffractometry.

Analyte, %	Non-pre-hydrated	Pre-hydrated
C_3S	63.8	61.0
C_2S	8.00	9.00
C_3A cubic	5.90	4.70
C_3A orthorhombic	0.40	0.50
Gypsum	1.90	0.80
Bassanite	3.30	2.50
Periclase	6.10	6.10
Brownmillerite	7.60	7.40
Calcite	1.70	1.70
Portlandite	1.30	1.50
Syngenite	-	2.60
Ettringite	-	2.10

Syngenite and ettringite were detected by X-ray diffraction, characteristic phases of pre-hydrated cements. According to Silva et al. [1], normally commercial cements presents prehydration (Wk) ≈ 0.15 to 0.3% when leaving the cement mill; values above 0.3% can significantly impact the cement performance properties. The pre-hydrated cement presented fewer fines particles than the reference cement, which indicates the agglomeration of the particles of the pre-hydrated sample. These characteristics affect the packing and the distance between the particles.

The pre-hydration was carried out at 23±2 °C and ≥ 90% relative humidity in a plastic hermetic container for 7 days and indicated as a *pre-hydrated* sample using ammonium chloride, this level of pre-hydration was adopted considering as an worse condition that the cement is submitted in field.

3.2 Mixing Procedure

The dry powder was weighed in a beaker and the water plus admixture in another, keeping the water-to-cement ratio at 0.35. The mixture was run on a Eurostar P1, IKA mechanical stirrer for 2 min keeping the rotational speed at 1200 rpm. Then, the rotation was increased to 2000 rpm for a further 1 min, totaling 3 minutes of homogenization / dispersion [16].

The suspensions were used in the spreading (Kantro cone), rotational and oscillatory rheometry and isothermal conduction calorimetry tests [16], [17].

The same samples were subjected to the test at the same time to reduce variability on the results.

3.3 Paste characterization

Rotational rheometry

The rheological behavior of cement pastes or concrete is influenced by several factors, some of them mentioned above, other factors are the volumetric concentration of the particles, physical-chemical and mineralogical characteristics of the cement, interparticle separation distance (IPS), and surface interactions [10]. Rheology is a science in which the flow and deformation of materials are studied. In this case the interaction between materials in suspension, cement particles with water and in some cases admixture, which are homogeneously distributed, is being studied [13], [11]. The cement reacts over time with the water forming crystals of hydration, modifying the stiffness of the cement-water- admixture set [16]. In this paper, rheometry helps to understand the interaction between the different types of cements with the admixture.

The rheological and strength properties of concrete are essential parameters required for concrete performance, so it is necessary to study the interaction between cement and admixture, since not all admixture/cement pairs function optimally together, even if both meet the published standards. For example, especially at low water/cement ratios incompatibility between cement and admixture can be detected with rheology before concrete is made, avoiding concrete that exhibit problems such as false set, fast flowability loss, handle retardation, excessive air entrainment [10], [11].

The rheological methods chosen for this study were rotational and oscillatory rheometry. Rotational test indicates the rheological behavior of pastes, viscosity, hysteresis profile, and others, always in function of changes on the shear rate. For oscillatory methods, the information is obtained over time, or in function of changes in strain, or even frequency applied, depending on the kind of application desired for the products or monitoring the hardening stage after application.

Rotational rheometers are high precision equipment, and accurate results can be obtained regarding the behavior of the material [16].

The cementitious pastes were mixed as described above and added to an Anton-Paar rheometer, model MCR302, shown in Figure 4. The tests were performed using cross-hatched stainless-steel parallel plate geometry with Diameter of 25mm (PP25/P2), to guarantee shear without slipping during the tests. A stepped flow test was used for the determination of rheological parameters and the type of behavior under flow request. The shear rate was increased from $0.1s^{-1}$ to $50s^{-1}$ (acceleration period) and then returned to $0.1s^{-1}$ (deceleration period). It was applied 10 steps by each period, each one with 10s. These results were used to obtain the optimal content of admixture [16], [18].

Oscillatory Rheometry: The mixed oscillatory test was applied using strain/time sweep tests. During the first stage, the amplitude was changed from 10^{-5} to 10^{-1}, keeping the frequency constant at 1Hz, while in the time sweep test the frequency was maintained at 1Hz and strain at 10^{-4}. In this second case the test was performed for 30 minutes. The strain/time cycle was repeated 8 times, totaling almost 3 hours of testing. An illustration of the schedule is shown in Figure 5 . However, the results presented are equivalent to the time sweep test. This strategy was adopted to try to maintain a correlation with the flow test as a function of time, after breaking down the microstructure under formation [16], [18].

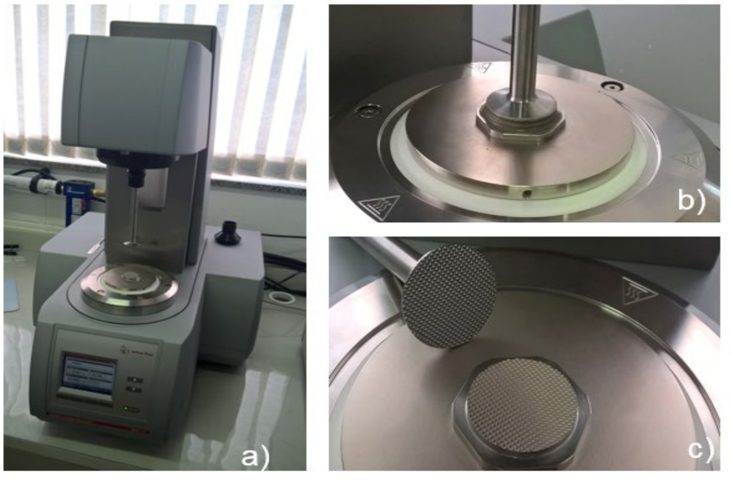

Figure 4. a) rheometer; b) addition of the paste c) geometry - cross hatched.

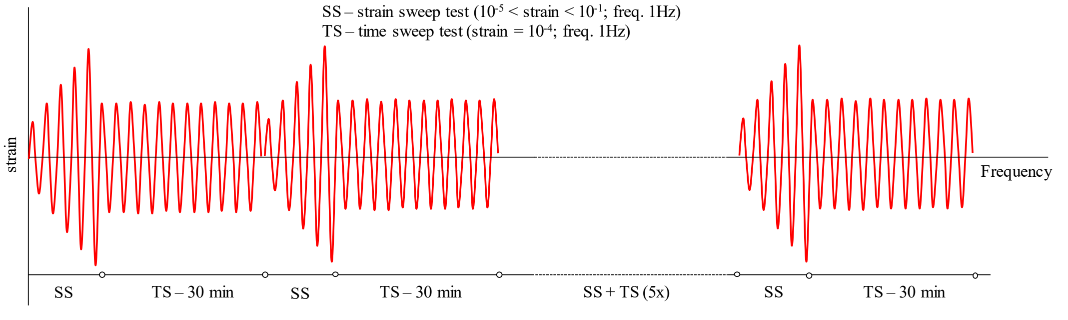

Figure 5. Illustration of oscillatory rheometer programming with mixed tests of strain sweep and time sweep. (For the discussion were used only the results of time sweep test) [11], [16].

Kantro Cone Test: The Kantro test, also known as a miniature cone test, is a simple method to evaluate the comparative dispersing effect of an admixture, it is a mini stainless-steel cone, and this method allows to evaluate only the interaction of the cement - admixture + water, since only paste is used, without the influence of aggregates [17].

The process involves filling a cone set on a metal plate well leveled horizontally with cement paste, and then removing the excess paste with a spatula for the surface levelling. After this, the cone is removed, thus the paste flows by the action of gravity and weight of its own body to the equilibrium in the state of rest. The parameters of spreading of the sample are measured, such results are compared with the yield stress data obtained by the paste rheometer [16], [17].

The test was performed according to Kantro *apud* Bucher [19]. About 100g of paste was added to the Kantro mini cone and the spreading is performed on a wet metal base, quantified when spreading ceases after removal of the mold. The Kantro cone test is used to evaluate the paste spread with the use of the admixture, with small amounts of paste it is possible to evaluate the sample spread parameters, thus determining the fluidity of the mixture with the different contents and types of admixture, which can often be related to the flow voltage data obtained by the rheometer [17].

Isothermal calorimetry: equipment used: TA Instrument isothermal calorimeter model Thermometric TAM AIR. The results of this technique allow the evaluation of the kinetics of the chemical reactions that occur during the first 72 hours of hydration of the cement [1], [20].

4 RESULTS AND DISCUSSION

A portion of cement was pre-hydrated for comparison with cement without prehydration. Paste was prepared from pre-hydrated cement and the reference cement and analyzed in rotational and oscillatory rheometry. The optimal content of the admixture was determined for cement with and without prehydration using the Kantro cone test and rotational rheometry. In this case, the prehydrated cement required less admixture. In the Kantro cone test, the spread is associated with the gravity action (single point test), the results of rotational rheometry are obtained for different shear conditions (multipoint test). These data make possible the quantification of a rheological profile, viscosity, yield stress and hysteresis area. Results obtained using each method will be presented in sequence.

The isothermal conduction calorimetry test was carried out to evaluate the flow heat during Portland cement hydration reaction without and with pre-hydration, with and without superplasticizer in the optimal contents found through the rotational rheometry test. The same paste sample was used to run the tests in rheometry and Kantro cone test, another paste was prepared on the same conditions to run calorimetry tests.

4.1 Admixture Optimization

The results obtained from rotational rheometry are usually presented in the form of shear stress versus shear rate graphs, but for the determination of the optimal admixture content, the results are presented in terms of apparent viscosity, yield stress and hysteresis area depending on the percentage of admixture used [21]. The yield stress was quantified as the shear stress value at the lowest rate used in the test. As the tests are performed in two steps (acceleration and deceleration), the result obtained in the deceleration was used, since the material had already undergone the condition of greater imposed shear and there is a natural tendency of re-agglomerate. The apparent viscosity was estimated at the maximum shear rate [21]. The hysteresis area is equivalent to the area inscribed between the acceleration and deceleration curves in the stress graph vs. shear rate. A well dispersed suspension should have low flow stress and apparent viscosity, and hysteresis area close to zero. Positive hysteresis areas (thixotropic profile) indicate that the material that was deagglomerated during the acceleration step (increase in shear rate) showed slower re-agglomeration during deceleration. The variation in the apparent viscosity and in the yield stress of the pastes is indicated as a function of the type of mixing procedure, Figure 6 shows an schematic illustration on how the apparent viscosity data and yield stress data was obtained. There are different ways to get these values [22]. One of them is from the application of rheological modeling, such as from Herschel-Bulkley, Casson, Bingham, etc . In these cases the viscosity obtained is plastic, but care must be taken with the model parameters, as they often result in negative flow values, very low plastic viscosity and very high modeling errors . Another way of comparing the values is to collect raw data directly in the graph. In this scenario, the values of apparent viscosity was obtained at the maximum shear rate applied in the test, since it is the state of greater dispersion of the particles. In the graph of stress vs. shear rate, viscosity is the ratio of both. The yield stress was quantified as the shear stress value at the lowest rate used in the test: as the tests were performed in two stages (acceleration and deceleration) the results of the deceleration step were adopted, since the material had already passed through the higher imposed shear condition, and there is a natural tendency for re-bonding [21].

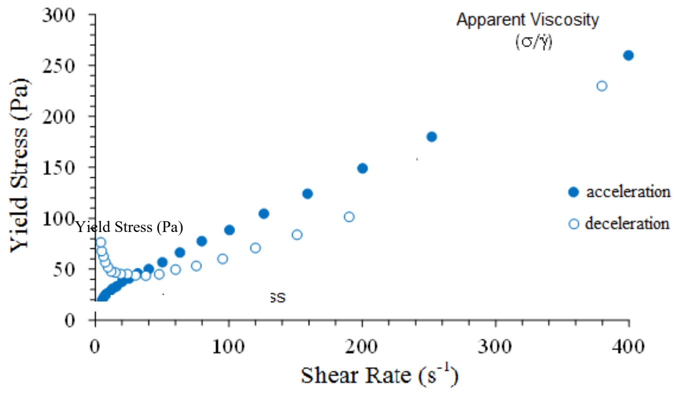

Figure 6. Schematic illustration of apparent viscosity and yield stress [21].

In the case of negative hysteresis areas, the rate of re-agglomeration is more pronounced than the deagglomeration of the particles, and the profile of rheopexy is observed. The data obtained in these experiments is shown in Figure 7. The variation in the apparent viscosity, in the yield stress and in the hysteresis area of the pastes is indicated as a function of the variation of the content of admixture. It was not used any model to represent the results obtained on this work, the data was treated using graphical method as per previous work done by Romano et al. [21].The optimal content of the admixture was quantified based on yield stress, apparent viscosity and hysteresis area, considering the lower hysteresis area, the point that the yield stress and viscosity keeps constant and lower values [21].

In the pastes with pre-hydrated cement the content of the admixture to reach the optimum was lower when compared to the cement not pre-hydrated, this happens due to the formation of crystals of hydration that has greater affinity for the polycarboxylate admixture thus requiring a lower content [22].

The optimized contents are described in the table within Figure 7 (0.5% for non-prehydrated and 0.3% for prehydrated) based on 3 tests of each dosage and were used for stability evaluation over time, presented later.

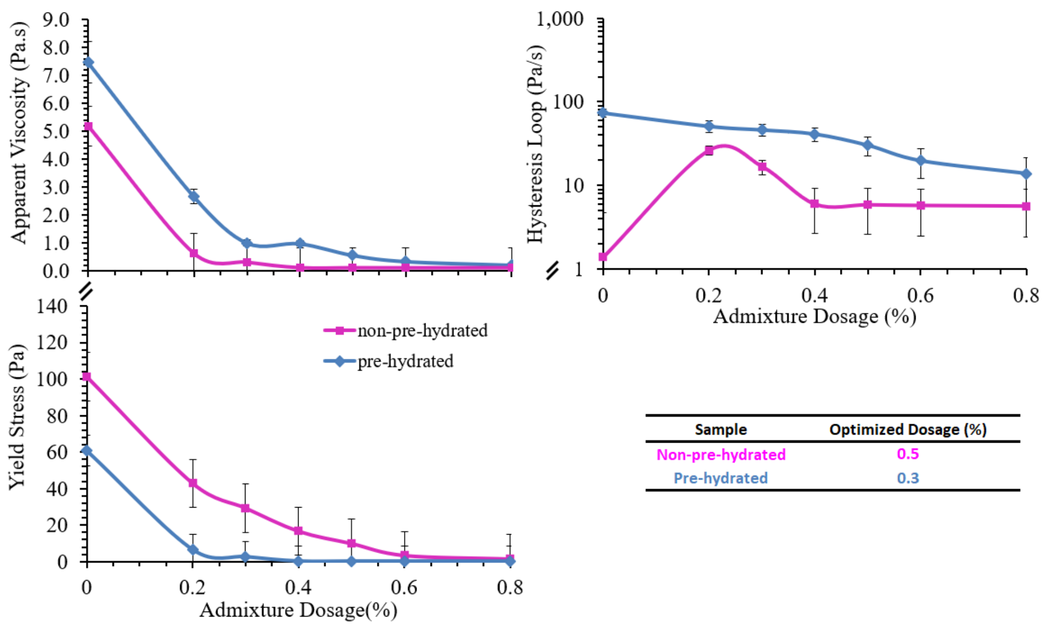

Sample	Optimized Dosage (%)
Non-pre-hydrated	0.5
Pre-hydrated	0.3

Figure 7. Apparent viscosity (Pa·s), Yield stress (Pa) and Hysteresis loop (Pa/s) of each sample in function of admixture content. Table represents the optimized content, with error bars.

In this work, the optimized contents of the admixtures were obtained from rotational rheometry tests, but it is known that companies or technical centers do not always have rheometers for the study of admixtures. Therefore, it is customary to use the Kantro cone test. Thus, the same paste was evaluated from the spreading and the results are presented in the sequence. The results presented are an average of three measurements of each sample [23].

4.2 Free flow according the Kantro's cone test

The results of a series of slurries obtained by Kantro cone test are shown in Figure 8. In the pastes with the non-pre-hydrated cement a higher the amount of polymer was required to have greater the flow. Based on the Kantro cone tests, it was difficult to define an optimal content for the admixture, and the values were from 0.4 and 0.6% for both cements [23].

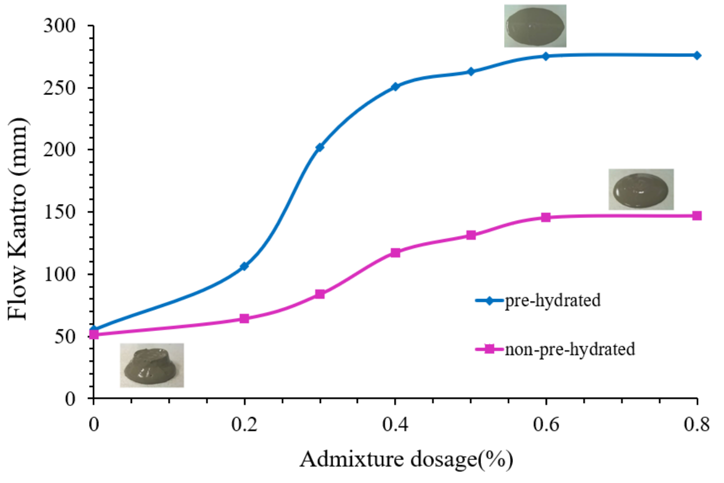

Figure 8. Flow variation at Kantro cone test.

Additionally, there is a correlation between the increase of the admixture content and the increase of the flow, but this result can be masked by the segregation in the paste and by the heterogeneous flow during the spreading. Although it is possible to measure the spread of the sample visually it is possible to verify a phase separation halo, but from the normalization it is possible to obtain an average value of the spreading diameter. With the increase of the content of the admixture and the migration of water to the surface and formation of the halo, this separation will also occur during the application, making it difficult to handle the cementitious material. This phenomena was observed on the higher content of the admixture (0.8%) [24].

In practice, such a single point test is used based on the need for each application, but it is known that the results have a good correlation with the yield stress and viscosity.

In this way, it can be inferred that:

- Both by rotational rheometry and from the Kantro cone spreading, it was possible to observe differences caused by the admixtures in the pastes with the cement with and without prehydration. The highest amount of admixture was required for non-pre-hydrated cement, the higher adsorption of the admixture is reached by higher fineness of cement particle, thus polymer molecules exhibits higher affinity to the available C_3A and hydration products, once the superplasticizer shows different adsorption affinity by the surface of different hydration products and mineral surfaces [2].
- The results of rotational rheometry enabled definition of optimal admixture content for each sample, which the Kantro cone test did not adequatelly;
- Correlating the flow results with the rheological parameters, it was confirmed that the change in spread is governed by both the viscosity and the yield stress, according illustrated in Figure 9, previously.
- The higher difference is that using rotational rheometry it is possible to obtain, beside of the rheological parameters, the rheological behaviour of each composition during the flow, because the fresh state properties are evaluated in different shear conditions, which can be close related to many practical applications.

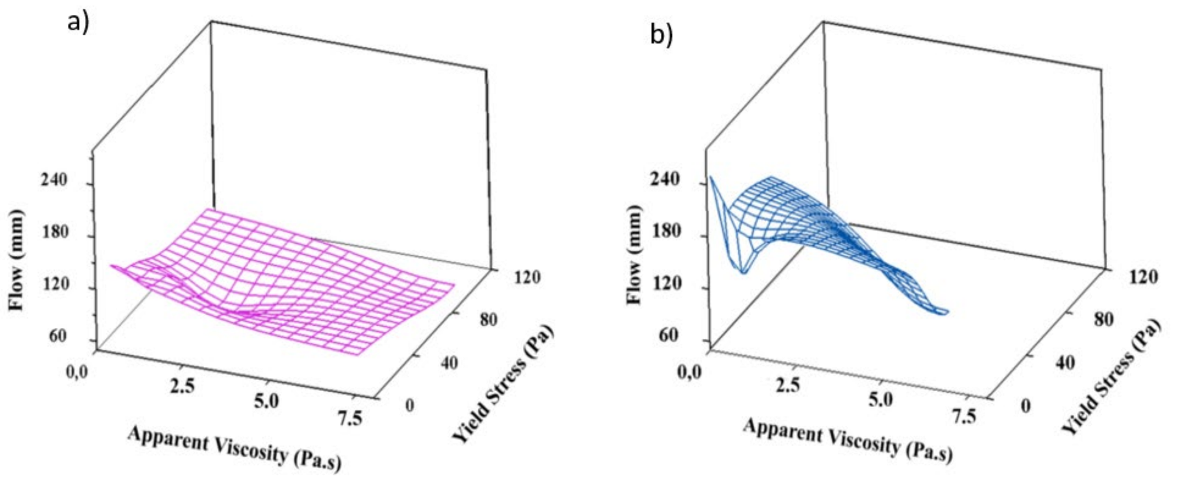

Figure 9. Flow vs Apparent Viscosity vs Yield stress for both cements changing the admixture content (a) non-prehydrated and b)pre-hydrated).

With the results presented so far, only information about the characteristics of the paste in the early age of cement hydration were obtained, since the tests were carried out 5 minutes after mixing. However, no information was obtained about the stability over time. For this, oscillatory rheometry tests were performed and the results are presented next. In this step the tests were carried out only with the admixtures in the optimal contents for each type of cement with and without the addition of superplasticizer [24].

4.3 Stability over time

During hydration, the hydrated product form a three dimensional network which makes more rigid the suspension over the time, to monitor the stiffening it's used the oscilatory rheometry [25]. Figure 10 presents the change in flow and in the storage modulus (G') from oscillatory rheometry over time. The monitoring of G' using the mixed oscillatory test illustrates the gain on consistency over time, after breaking down the agglomerates in the strain sweep test.

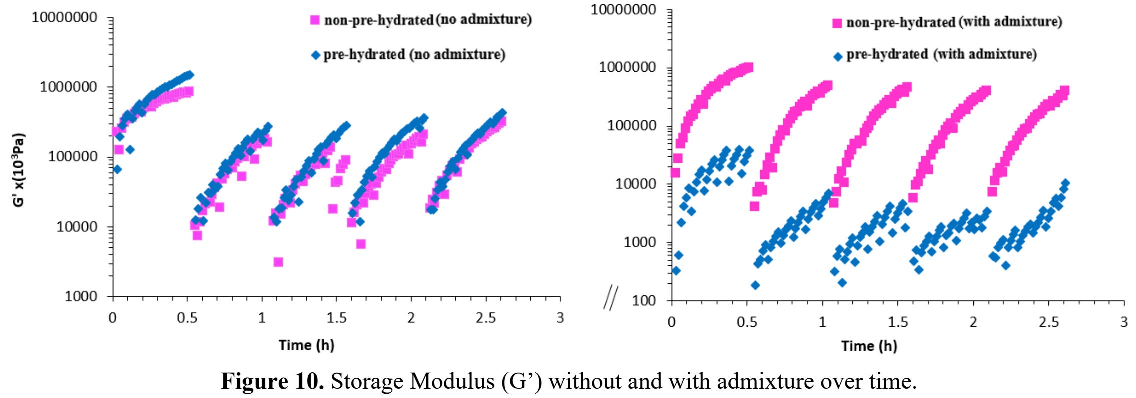

Figure 10. Storage Modulus (G') without and with admixture over time.

Without admixture, no significative differences were observed between the pastes made from prehydrated and reference cements, the pre-hidrated sample only increased the G' value at the first 2 hours slightly. In the presence of admixture, the prehyrated and reference cements show different interactions with the admixture [25]. There is a noticeable increase in final G 'in each stage of the time sweep, which indicates that the restructuring of the microstructure is occurring in an most intensive way, increasing the forces of attraction. By using admixture, the differences between non-pre-hydrated and pre-hydrated was significant, however the stability over time was 2.5 hours for both [26].

The admixture effect on pre-hydrated sample indicates that the consolidation of the paste occurs based on a physical contribution by particles reaglomeration, in addition the pre-hydrated sample shows higher amount of ettringite and smaller amount of C_3A cubic, showing that the amount of admixture for this reduced quantity of cubic C_3A is higher than the non-prehydrated cement allowing better fluidity of the paste over the time improving the cement-adimixture interaction [25], [26].

4.4 Isothermal calorimetry

The curves presented in Figure 11 and the stages of hydration reaction presented in Table 3 show how the cement reaction is affected by prehydration and use of admixture.

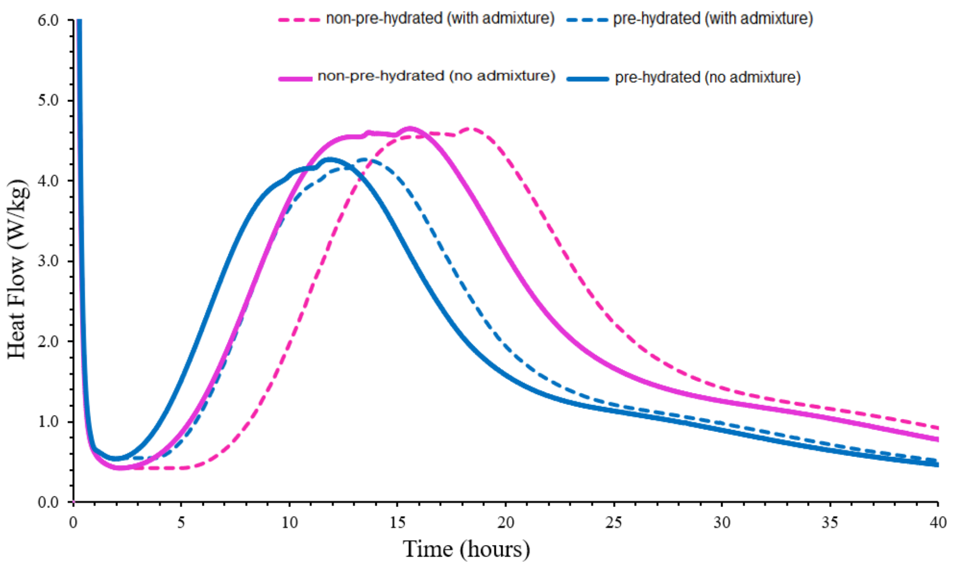

Figure 11. Heat flow over the time.

Table 3. Reaction rate, cumulative heat at initial setting, time of induction period, end of acceleration period and setting time by Vicat.

Composition	Induction period (h:min)	Reaction rate (mW/g·h)	Setting time (h:min)	Cumulative heat at initial setting (J/g)	End of acceleration period (h:min)
non-pre-hydrated	3:10	0.64	7:00	35.2	13:00
non-pre-hydrated (with admixture)	5:35	0.28	9:00	30.9	17:00
pre-hydrated	2:15	0.61	5:00	37.6	10:00
pre-hydrated (with admixture)	4:35	0.68	6:00	34.6	12:00

In general, the pre-hydrated sample affected the chemical hydration reaction, caused an acceleration in the induction period and a considerable displacement in the time of formation of the main silicate peak [25]. The pre-hydration of the cement particles results in the formation of nanoscale ettringite needles on the surface of the cement, this fenomena can affect the interaction with the superplasticizer, as observed by Winnefeld [22], the cement aging can increase the performance of polycarboxylate, it depends on the chemical and mineralogical composition of the cement used.

The differences observed between pre-hydrated and non pre-hydrated hydration kinetics, are probably associated to the degree and type of reactions at silicate surfaces once C-S-H shows enhanced growth rates in the presence of silicate hydrate seeds that provide preferred nucleation sites and thus accelerate reactions in Ca_3SiO_5 and shorten induction period [25]. The silicate surface reactions result in the generation of a type of C-S-H that generates sites for nucleation of typical C-S-H during normal hydration [25], [26].

The surface of the pre-hydrated cement particles is initially covered by an enhanced C-S-H amount, which can have the following effects:

- Reduced the exposed surface area of the anhydrous phases available for dissolution,
- Cause an earlier transition to a diffusion-controlled mechanism when a continuous C-S-H layer on the anhydrous grains has grown thick enough to limit the transport of dissolved ions to-and-from the bulk solution,
- In contrast, silicate phase surface modifications caused by the cement prehydration are gradually etched away upon normal [25], [26].

Based on the geochemical theory of dissolution, the development of chemical reaction of cement occurs even without calcium oversaturation. The C-S-H in formation acts as a point of nucleation and starts the acceleration period. So, the induced prehydration of cement presented an intense heat flow released comparing with the anhydrous cement: the balance between dissolution of anhydrous phases of cement and the precipitation of hydrated products is energetically favorable for etch pits to form [25], [26].

The use of admixture on the other hand, increases the induction period, independently of the prehydration process, but the kinetics have the same behaviour, similar that it was observed by Rojas and Cincotto [27]. This effect is expected, since the polycarboxylate admixtures improve the workability of pastes, mortars and concretes by facilitating the dispersion of cement particles by electro-repulsion, keeping the stability of the system over the time [23].

Admixtures are not homogeneously adsorbed by the cement: the C_3A and C_4AF phases are the ones with the highest affinity for the dispersants [23], so they adsorb the higher amount of admixture when compared to the C_3S and C_2S. These are also the phases most active in the initial hydration processes [25], [26].

5 CONCLUSIONS

The results showed that small percentages of prehydration can strongly impact the engineering properties of the cement, specially changing the rheological behavior of the cement.

The results obtained from the Kantro cone test do not allow us to define the optimal content of superplasticizer, while the rotational rheometry test gives us a deflocculating curve and it is possible to identify the optimum admixture content for each cement sample. Although the information obtained from the single-point test is commonly used in the market it can only serve as a comparative parameter.

For the oscillatory rheometry tests, it is possible to identify the characteristics of better stability over time for the pre-hydrated cement with the addition of superplasticizer was the best combination when compared to the cement without prehydration and with the combinations without the use of admixture.

However, the change in cement prehydration resulted in different interaction with the evaluated admixture.

In this way, the use of an admixture cannot be defined as optimal all for types of binders. The choice depends, in addition to the type of application desired, of the correct content evaluation for each type of cement and the prehydration affects the rheological and mechanical properties.

For this, it’s necessary to use a better tool for the correct understanding of the causes of the variations and not only of the effects in the spreading. The calorimetry showed that only the induction period increased by using the admixture on the pre-hydrated and non-pre-hydrated cements, but the kinetics remains the same.

6 ACKNOWLEDGEMENTS

The authors wish to thank the Laboratory of Microstructure and Eco-efficiency in Materials– LME of University of São Paulo, and GCP Applied Technologies for the support during the development of this research.

7 REFERENCES

[1] D. Silva, J. Thomas, D. Kazmierczak, and J. Cheung, "Pre-hydration of cement: global survey and laboratory results," *ZKG Int.*, vol. 71, no. 6, pp. 1–6, 2018.

[2] J. Stoian et al., "New insights into the prehydration of cement and its mitigation," *Cement Concr. Res.*, vol. 70, pp. 94–103, 2015.

[3] F. Winnefeld, "Influence of cement ageing and addition time on the performance of superplasticizers," *ZKG Int.*, vol. 61, no. 11, pp. 68–77, 2008.

[4] M. Whittaker, “The effects of cement prehydration of engineering properties,” in *Proc. 30th Cem. Concr. Sci. Conf.*, Birmingham, 2010.

[5] M. Whittaker, E. Dubina, F. Al-Mutawa, L. Arkless, J. Plank, and L. Black, "The effects of prehydration on the engineering properties of CEM I Portland cement," *Adv. Cement Res.*, vol. 25, no. 1, pp. 12–20, 2013.

[6] K. Vance, M. Aguayo, T. Oey, G. Sant, and N. Neithalath, "Hydration and strength development in ternary portland cement blends containing limestone and fly ash or metakaolin," *Cement Concr. Compos.*, vol. 39, pp. 93–103, 2013.

[7] H. Uchikawa, S. Hanehara, and D. Sawaki, "The role of steric repulsive force in the dispersion of cement particles in fresh paste prepared with organic admixture," *Cement Concr. Res.*, vol. 27, no. 1, pp. 37–50, 1997.

[8] C. Chomyn, “Synthesis, characterization and dispersing properties of anionic and zwitterionic polycarboxylate superplasticizers prepared via different synthetic methods,” Ph.D. dissertation, Tech. Univ. München. München, 2020.

[9] M. Ilg and J. Plank, "Effect of non-ionic auxiliary dispersants on the rheological properties of mortars and concretes of low water-to-cement ratio," *Constr. Build. Mater.*, vol. 259, pp. 119780, 2020.

[10] J. Plank, D. Zhimin, H. Keller, F. V. Hossle, and W. Seidl, "Fundamental mechanisms for polycarboxylate intercalation into C3A hydrate phases and the role of sulphate present in cement," *Cement Concr. Res.*, vol. 40, no. 1, pp. 45–57, 2010.

[11] F. A. Hartmann and J. Plank, "New insights into the effects of aging on Portland cement hydration and on retarder performance," *Constr. Build. Mater.*, vol. 274, pp. 122104, 2021.

[12] H. Uchikawa, S. Hanehara, and D. Sawaki, "Influence of kind and added timing organic admixture type and addition time on the composition, structure, and property of fresh cement paste," *Cement Concr. Res.*, vol. 25, no. 2, pp. 353–364, Feb 1995.

[13] S. Hanehara and K. Yamada, "Interaction between cement and chemical admixture from the point of cement hydration, absorption behavior of admixture, and paste rheology," *Cement Concr. Res.*, vol. 29, no. 8, pp. 1159–1165, 1999.

[14] S. Hassan, H. Salah, and N. Shehata, "Effect of alternative calcium sulphate-bearing materials on cement characteristics in vertical mill and storing," *Case Stud. Constr. Mater.*, vol. 14, e00489, 2021.

[15] American Society for Testing and Materials, *Standard Test Method for Determination of the Proportion of Phases in Portland Cement and Portland-Cement Clinker Using X-Ray Powder Diffraction Analysis*, ASTM C1365-06, 2011.

[16] D. F. Ferraz, A. C. R. Martho, E. G. Burns, R. C. O. Romano, and R. G. Pileggi, “Effect of mixing procedure on the rheological properties and hydration kinetics of portland cement paste,” in *Rheology and Processing of Construction Materials*, V. Mechtcherine, K. Khayat, and E. Secrieru, Eds., Cham: Springer Int. Publ., 2020, pp. 311–319.

[17] D. L. Kantro, "Influence of water-reducing admixtures on properties of cement paste-Miniature slump test," *Cem. Concr. Aggreg.*, vol. 2, no. 2, pp. 95–102, 1980.

[18] D. Ferraz, A. C. R. Martho, E. Burns, R. C. O. Romano, and R. G. Pileggi, “The effect of dispersing agent on the rheological properties of different types of Portland cement from Latin América,” in *Proc. Concr. Solut. 7th Int. Conf. Concr. Repair*, Cluj Napoca, Romania, 2019.

[19] H. R. E. Bucher, "Desempenho de aditivos redutores de água de alta eficiência em pastas, argamassas ou concretos", in *REIBRAC*, 30, Rio de Janeiro, 1988, pp. 609-625.

[20] V. A. Quarcioni, “Influência da cal hidratada nas idades iniciais da hidratação do cimento Portland – estudo em pasta,” Ph.D. dissertation, Esc. Politéc., USP, São Paulo, 2008, 172 p.

[21] R. C. O. Romano and R. G. Pileggi, "Use of rheological models for the evaluation of cement pastes with air-entraining agent in different temperatures," *Annu. Trans. Nordic Rheol. Soc.*, vol. 25, pp. 341–348, 2017.

[22] A. Zingg, F. Winnefeld, L. Holzer, J. Pakusch, S. Becker, and L. Gauckler, "Adsorption of polyelectrolytes and its influence on the rheology, zeta potential, and microstructure of various cement and hydrate phases," *J. Colloid Interface Sci.*, vol. 323, no. 2, pp. 301–312, 2008.

[23] J. Liu, C. Yu, X. Shu, Q. Ran, and Y. Yang, "Recent advance of chemical admixtures in concrete," *Cement Concr. Res.*, vol. 124, pp. 105834, 2019.

[24] D. Jiao, C. Shi, Q. Yuan, X. An, Y. Liu, and H. Li., "Effect of constituents on rheological properties of fresh concrete: a review," *Cement Concr. Compos.*, vol. 83, pp. 146–159, 2017.

[25] Dubina, E. and Plank, J., *Influence of Moisture – and CO_2 – Induced Ageing in Cement on the Performance of Admixtures Used in Construction Chemistry*. München: Tech. Univ. München, 2012.

[26] E. Dubina, R. Sieber, and J. Plank, “Effects of prehydration on hydraulic properties on Portland cement and synthetic clinker phases,” in *Proc. 28th Cem. Concr. Sci. Conf.*, Manchester, 2010.

[27] Rojas, C. M., and Cincotto, M. A., and, Influência da estrutura dos policarboxilato na hidratação do cimento Portland. *Ambient. Constr.*, vol. 13, no. 3, pp. 267-283, 2013.

Author contributions: DFF: conceptualization, funding acquisition, supervision, data curation, methodology, writing; ACRM: data curation, formal analysis, methodology; EGB: data curation, formal analysis; RCOR: data curation, formal analysis; RGP: data curation, formal analysis.

Editors: Lia Lorena Pimentel, Guilherme Aris Parsekian.